Modelling the ultrasonic scatter of complex microstructures in heavy rotor forgings

By Daniel Neumann

A thesis submitted to
the University of Birmingham
for the degree of
DOCTOR OF ENGINEERING

School of Metallurgy & Materials
College of Engineering and Physical Sciences
University of Birmingham
December 2019

Abstract

This thesis sets out to establish a quantitative model of ultrasonic scattering caused by the martensitic microstructure associated with power generation steel. An established model from the literature, which is designed for pearlite microstructure, is extended for the martensitic model. A mechanism is established to predict the reflective ability of microstructural features based on their acoustical impedance and relative size, which is based on the principles of acoustic theory.

A series of samples are generated and quantified covering a range of microstructure feature sizes and phases, including pearlite, mixed martensite and bainite and fully martensitic microstructures. The measured attenuation of the generated samples is used to validate, and ultimately disprove the pearlitic scattering model and also the martensitic extension. The quantified microstructure is used in combination with expected (from orientation relationships) and measured (from EBSD measurements) crystallographic orientation mismatches of the martensitic microstructure features to estimate scattering significance based on the boundary reflectivity method. These predictions, and further hardness measurements, appear to be in agreement with other qualitative assessments of martensitic scatter mechanisms in the literature. The scattering associated with martensitic microstructure is shown to be dominated by prior austenite grain boundaries due to their size.

Acknowledgement

This work would not have been possible without the love and support of a great number of people, all of whom contributed in their own unique and special way, largely without any knowledge of the significance of their actions. As a comprehensive account of every smile, kind deed and the priceless shared experiences would be far too involved, I shall merely say: to every friend, relative and loved one I hope you know who you are and how very dear to me every moment shared will always remain. May your love never end and your dreams never fade.

In addition a large number of individuals, groups and organisations contributed to the content of this work; be that by way of discussion, assistance or providing equipment or workspace. First of all I would like to thank all the guys in the University of Birmingham Met and Mat workshop, without whom the quality of sample preparation so important during the ultrasonic testing stage could not have been achieved. No matter how busy the schedule you always make time for a laugh, as well as a friendly discussion accompanied by a smile. The technicians and support staff tend to be the unsung heroes of any well run organisation and so I would like to thank everyone who contributed along the way. In particular Jasminder Singh and Paul Osborn should be commended for their friendly and welcoming attitudes whenever encountered. A pleasant and friendly demeanour can do wonders for moral and community spirit. Theresa Morris proved to be invaluable in obtaining the EBSD data and her patience and level of support is commendable given her busy schedule.

Many organisations outside of my member universities were also invaluable during this process. I am thankful for the many valuable discussions with Gary Lowton from Sonatest, your assistance in testing the limits of the equipment setup proved critical in assessing the

structural errors associated with the testing process and the samples. The ultrasonics group from the University of Warwick allowed for the development of the best testing technique with their generous assistance with time and equipment. And especially to the optics group at King's college London who enabled the majority of testing to take place in their labs, with use of their oscilloscope after the EPSRC loan pool was shut down. In particular Mr William (Bill) Lockhurst should be thanked for his friendly and helpful attitude, and always ensuring they remain as accommodative as possible.

This project is sponsored by Alstom power (now GE power) who I would like to thank for their support and the material provided (via Saarschmiede). As this project is part of a network linking the University of Birmingham, Loughborough University and the University of Nottingham, a vast network of both people and resources has been provided, which was greatly appreciated. We should all try to be more open to collaboration as the benefits are innumerable.

Finally, the most significant contribution of all was provided by the guidance and support of my supervisors, Dr Martin Strangwood and Prof Claire Davis. Your patience with my often unorthodox ideas cannot be overstated and our far ranging discussions were appreciated. Your vast knowledge and insight into the metallurgical processes were invaluable and the solid grounding of discussions across the range of other topics managed to keep some of my more eccentric and grandiose ideas in check. Without your support and feedback, the successful completion of this project could not have been achieved.

Contents

1. Introduction

1.1. Industrial context and scientific challenge

The power generation industry is in a constant state of development, as indicated by Figure 1.1, which illustrates past and potential future advancements in steam conditions and corresponding technologies. The increasing temperature and pressure levels these components are required to withstand lead to ever more stringent physical requirements which are summarised in table 1.1.

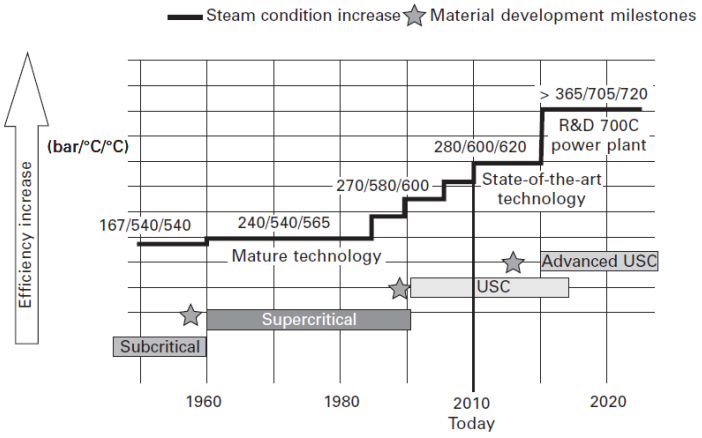

Figure 1.1: Chart indicating the constant drive for the power generation industry to innovate, leading to ever greater temperature and pressure requirements to improve efficiency. USC – ultra super-critical and Advanced USC – Advanced ultra super-critical are used to describe categories of temperature and pressure. [Osgerby, 2014]

Table 1.1: A summary of the required mechanical characteristics for individual components advanced power generation facilities [Osgerby, 2014]

Component	Creep strain	Creep rupture	Creep crack initiation and growth	High cycle fatigue	Low cycle fatigue and cyclic hold endurance	Fracture toughness	Creep relation
Rotors	✓	✓	✓	✓	✓	✓	
Casings	✓	✓	✓		✓	✓	
Rotating blades	✓	✓		✓	✓		
Stationary blades/ diaphragm rings					✓	✓	
Bolts		✓					✓

The requirements placed on the current generation of rotor steels are being achieved by a martensitic microstructure of guaranteed cleanness [Abe, 2017], meaning free from defects above a given threshold. This is achieved through a process of ingot casting, homogenisation, forging and heat treatment to achieve the required microstructure; the component is then inspected ultrasonically to ensure the component is free from defects over a given size and the attenuation/back wall reflection is within tolerance. These topics are all addressed in a family of EngD and PhD projects at the University of Birmingham looking at the casting [Dally, 2017], forging [Watson, 2017], heat treatment [Kalinowski, 2017], with this project considering the ultrasonic non-destructive testing aspect.

The ability to inspect these large components is restricted by the fact that the sheer size (diameter of several meters), combined with cleanness requirements, brings the technique to the limit of what is achievable. The standard method to compensate for this would be to adjust the wavelength of the inspection signal; however, this would then increase the minimum size of the detectable defect, and thereby restricting the ultimate level of guaranteed cleanness achievable. Variations of ultrasonic testing methods such as pitch/catch or phased array testing can be used to overcome some of these challenges, but are not always appropriate solutions. It is known that the microstructure is responsible for the detectability issues of new components [Donth et al., 2011]; however, a complete quantitative description as to why some components are uninspectable to the quality required remains elusive.

Therefore, the scientific problem can be formulated as seeking to address the problem of quantitatively linking the attenuation of a propagating ultrasonic wave to the microstructure of a component. The primary aim is to predict the level of scatter, a major contributor of

attenuation, from the microstructure itself. By providing a predictive model ultrasonic inspection characteristics could be more actively considered during the development of new high temperature alloys, rather than being checked retrospectively on a trial rotor forging. Trial rotors developed as part of the COST research program appear promising for high temperature applications but have encountered difficulties due to unsatisfactory ultrasonic detectability [Donth et al., 2011]. A recent paper provides such a scattering model for pearlite microstructures [Du and Turner, 2014], which is extended to martensitic microstructures as is applicable to power generation steels.

As the topics covered as part of this project cover several fields it is assumed the reader is not overly familiar with all aspects and so more focus is placed on providing a solid understanding throughout. This thesis attempts to lead the reader through the thought processes involved which hopefully proves useful to people from industry, materials scientists, as well as those involved in either the theoretical or the practical application of ultrasonic testing.

1.2. Aims and objectives

The main objectives of this project are:

- To develop a suitable testing methodology to examine scatter induced attenuation for complex microstructures in rotor steels
- To understand the mechanisms by which scatter is induced in complex microstructures
- To create a model by which this process can be quantitatively predicted based on microstructural features

- To generate samples with suitable microstructure to validate the model
- To quantify the microstructure of these samples
- To understand the potential limitations of the model
- To be able to quantitatively predict the influence of microstructural parameters on ultrasonic signal attenuation relative to total attenuation

2. Power generation and materials overview

2.1. Industry requirements

2.1.1. Operating conditions of a power generation plant

The process of power generation is remarkably similar across most mainstream technology types. With the exception of solar photovoltaics, all processes use a generator, which can be reduced in its simplest form to a rotating coil of wire in a magnetic field which induces a current. In order to generate this rotation, kinetic energy from a variety of sources is used, such as water, wind or heat via the expansion of a “working fluid”. In a gas turbine this working fluid would be air, but in most other scenarios this would be steam.

As is the case with any combustion process the constraints are determined by the laws of thermodynamics, specifically the heat engine [Smith, 2017]. The most common method to increase the efficiency of a heat engine is to increase the initial temperature (source) or to reduce the final temperature (sink), which increases the useful work done by the system. There are many variations of power generation facilities currently in use around the world; however, the greatest inlet temperature and pressure of a steam turbine are associated with a thermal facility (most likely coal) closely followed by that in a combined-cycle gas plant [Tanuma, 2017]. Table 2.1 indicates a range of inlet temperatures and pressures, the higher values are associated with improved efficiencies with the final entry (a) currently under development.

Table 2.1: Table indicating a range of steam turbine inlet temperatures. Final entry (superscript a) currently under development. [Ohji and Haraguchi, 2017].

Inlet pressure (MPa g)	Inlet temperature (°C)
2.0	320–350
4.1	400–440
6.0	440–480
8.6	480–510
10.0	510–538
12.5	510–538
16.6	538–566
24.1	538–566
25.0	600–620
31.0[a]	700–725

A combined-cycle gas facility is somewhat counterintuitive in that it does not typically maximise the efficiency of the gas turbine nor of the steam cycle, due simply to the fact the greatest overall efficiency is generated by combining slightly suboptimal conditions for both stages [Breeze, 2016; 2019]. As the waste heat from the primary stage becomes the main heat component input for the secondary stage, the overall optimum efficiency is achieved by considering the entire system rather than optimising the individual stages. Figure 2.1 depicts a general layout associated with a thermal power station indicating the different possible fuel sources. This work does not consider the fuel source, nor the burn pattern or boiler conditions, the only consideration is that of the steam turbine material associated with the highest possible temperature and pressure requirements.

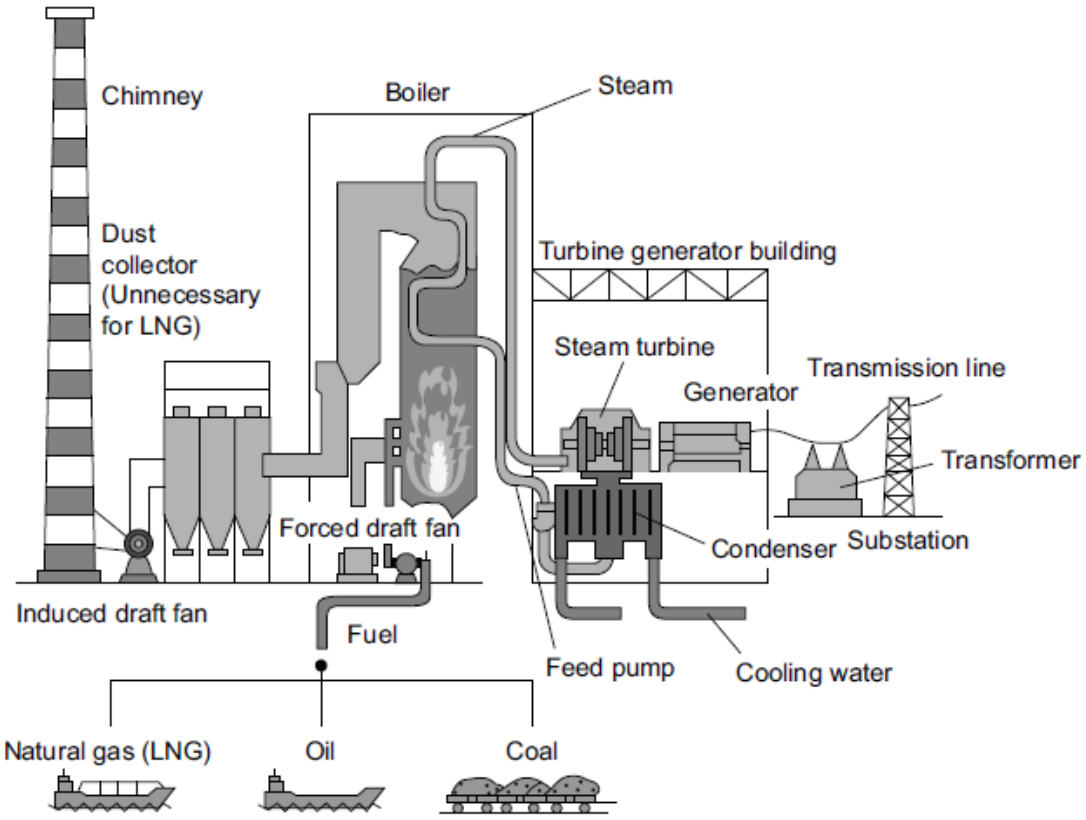

Figure 2.1: General image of a typical thermal power station. [Ohji and Haraguchi, 2017]

A point is reached at a steam temperature of 374.2°C and pressure of 22.12MPa where the steam turns supercritical, which avoids the formation of bubbles by forcing the liquid water directly into steam which then has liquid-like qualities. As the phase transition stage is itself very energy intensive, achieving supercritical steam conditions provides a dramatic boost in efficiency. Above this critical threshold, raising steam inlet pressure further increases the efficiency of the conversion process but also increases wetness losses. Wetness losses occur as a result of energy absorption by the moisture and the water droplets causing erosion of the leading edge of low pressure turbine blades [Li et al., 2014a; Joseph et al., 2016]. Therefore, both temperature and pressure are typically increased in conjunction to combine the respective efficiency improvements whilst simultaneously avoiding the wetness losses [Ohji and Haraguchi, 2017].

There are many steps which can be taken to improve the efficiency of the energy conversion associated with a thermal power station; the most obvious is simply to increase the temperature and pressure of the steam [Tominaga, 2017] and so the combination of these parameters is typically maximised in practice and constrained by the materials which are economically viable [Smith, 2017]. However, many other elements are also considered, from burn characteristics of the initial fuel to reducing losses in the conversion process with multiple turbines and reheat and regeneration cycles; Figure 2.2 indicates just how complicated it can get.

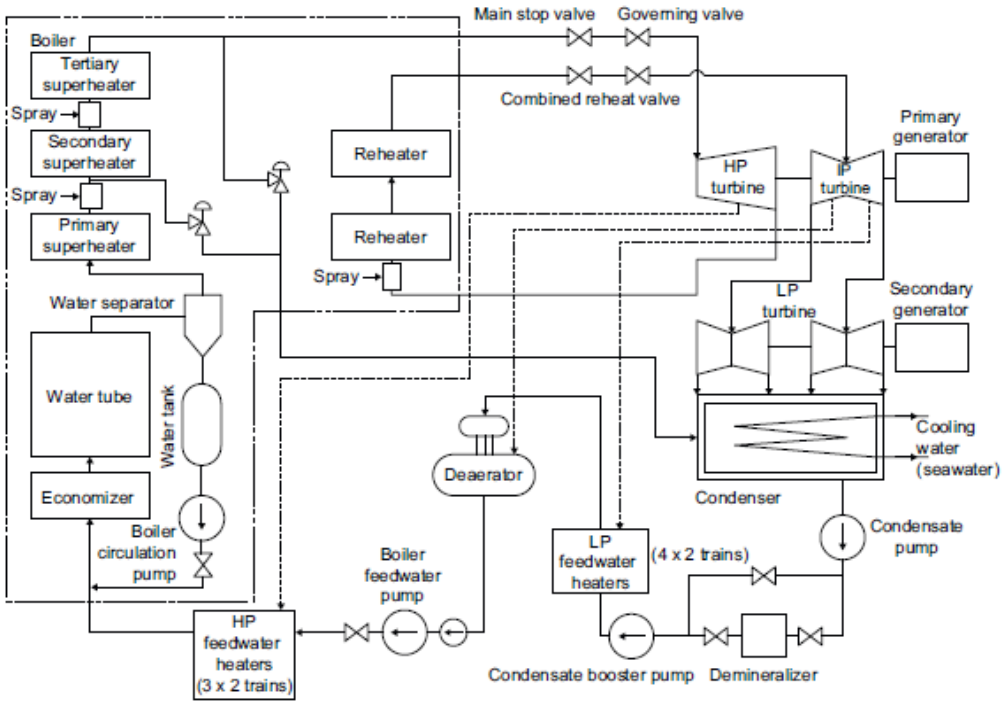

Figure 2.2: Image showing the complexity of an efficient thermal power plant [Ohji and Haraguchi, 2017].

It is important to note the combustion temperature in the boiler is around 1700 – 1800 °C and so in theory there is still large scope for thermal efficiency improvements. This does not translate easily into reality however due to the material limitations associated with the components handling the steam inlet temperatures. Current and future materials are expected to safely allow a steam inlet temperature of 600 – 700 °C to be used [Ohji and

Haraguchi, 2017]. At first glance this vast temperature difference seems like a major missed opportunity to increase thermal efficiency, especially as gas turbines have been operating above 1300 °C for virtually half a century and now regularly exceed 1500 °C [Fadok, 2010; Bontempo and Manna, 2019]. This discrepancy must therefore be due to a valid consideration, and to fully understand it the material properties must be understood in terms of the requirements placed upon them.

Given the extreme temperature conditions of a gas turbine it is perhaps surprising to discover the materials used are largely similar to those of a steam turbine. The substrate is predominantly steel-based for lower temperature, less critical sections and Ni-based superalloy for higher temperature areas [Fadok, 2010]. There are several summaries which discuss the development and need for high temperature superalloys in great detail [Betteridge and Shaw, 1987; Reed, 2006; Nowotnik et al., 2014]. The main advancements which have allowed operating temperatures to increase so significantly can be categorised into two subgroups, cooling technologies [Scalzo and Bannister, 1994] and thermal barrier coatings [Reed, 2006]. As the names suggest these techniques allow the substrate to operate at far higher temperatures than otherwise possible. The difference between the gas flow temperature and the substrate can reach 600 °C in advanced turbines, meaning the operating temperature easily exceeds the solidus temperature (the maximal temperature at which the alloy is no longer completely solid) of the substrate material [Fadok, 2010]. The cooling elements are therefore critical for safety and component longevity and so coating adhesion and durability are essential. A further issue to consider is any air or steam used to cool the component will also interfere with the working fluid itself, resulting in reduced efficiency [Breeze, 2019]. Therefore an evaluation must be made during the turbine design

stage as to how much cooling is gaining in terms of overall efficiency and whether it is likely to be economically viable.

Table 2.2: A table to summarise the expected operating conditions of a typical gas and steam turbine.

Turbine type	Expected operating temperature (°C)	Expected operating pressure	Material associated with modern turbines
Gas turbine	1500 +	Compression ratio typically under 20	Nickel / iron based alloys
Steam turbine	~ 700	350 bar	Nickel / iron based alloys

The data summarised in table 2.2 indicate there are no major material differences causing the big temperature differences between gas turbine and steam turbine operating conditions. Therefore the combination of thermal insulation and cooling associated with gas turbines prove significantly more effective than for steam turbines. The discrepancy between the two turbine types can be accounted for by large differences in mass flow rates, which leads to the respective differences in heat transfer capabilities. This same mass flow increase results in a reduced operating temperature requirement for gas turbines running on partial hydrogen fuels [Fadok, 2010].

2.1.2. Rotor/turbine design considerations

The requirements placed on these materials depend on a number of factors which are designed for in advance of the manufacturing process, and so an element of “locking in” the material characteristics is associated with each turbine. An obvious aspect which determines the overall category of the turbine is the operating temperature, which is why turbines are rated to run under certain temperature and pressure conditions. The aspects which determine whether or not the components can safely run under those operating conditions are a combination of the expected operating lifetime and the forces experienced during service. Traditionally, steam turbines were expected to operate for extended periods of

time at high temperature (baseload), whereas simple gas turbines often cycle their output frequently (peaking). The typical failure mechanisms would differ under these conditions, peaking plants would typically be limited by low cycle fatigue whereas baseload would be more creep limited. This traditional gas turbine/steam turbine divide has been further complicated by the addition of renewables onto modern day grids. As a consequence turbines which were designed with baseload operations in mind are required to cycle their respective outputs frequently creating low cycle fatigue issues for which they were not designed. To further complicate the issue these failure mechanisms are not independent from one another, with creep and fatigue mechanisms interacting, known as thermal mechanical fatigue [Fadok, 2010].

The failure mechanism associated with steam turbines is predominantly determined through creep-related fatigue, hence the desire for superior creep strength development as part of many research programs developing more advanced materials. The failure mechanism is thought to occur via cavities forming at grain boundaries due to slip (intergranular creep damage) whilst under high stress [Sklenička et al. 2003]. These initially small voids would grow over time, merging with one another and eventually developing into a crack which is the ultimate cause of component failure. Figure 2.3 indicates the progression of these failure stages with the majority of time spent under the early phase until an ultimately fairly rapid progression until failure. Figure 2.4 displays a series of micrographs showing the increasing creep cavitation associated with creep life fraction evolution. It is evident from the images that with increased cavitation there is an associated trend of increased clustering, with image (f) indicating clear interaction and growth of cavity clusters.

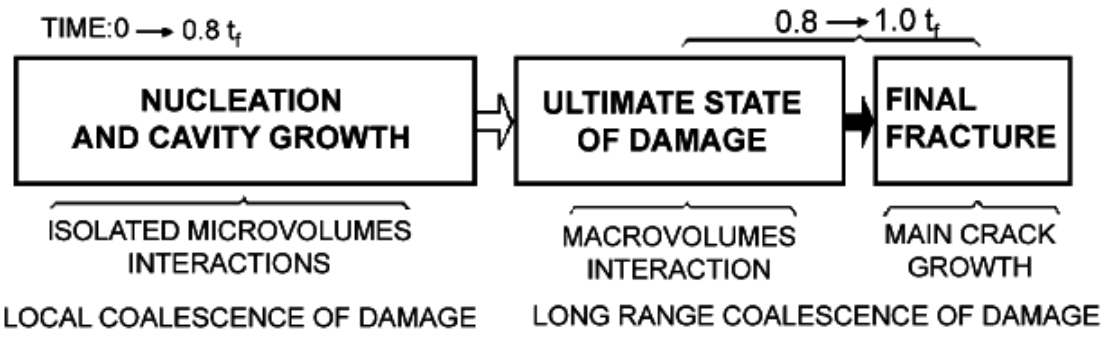

Figure 2.3: Crack development and failure mechanism [Sklenička et al., 2003]

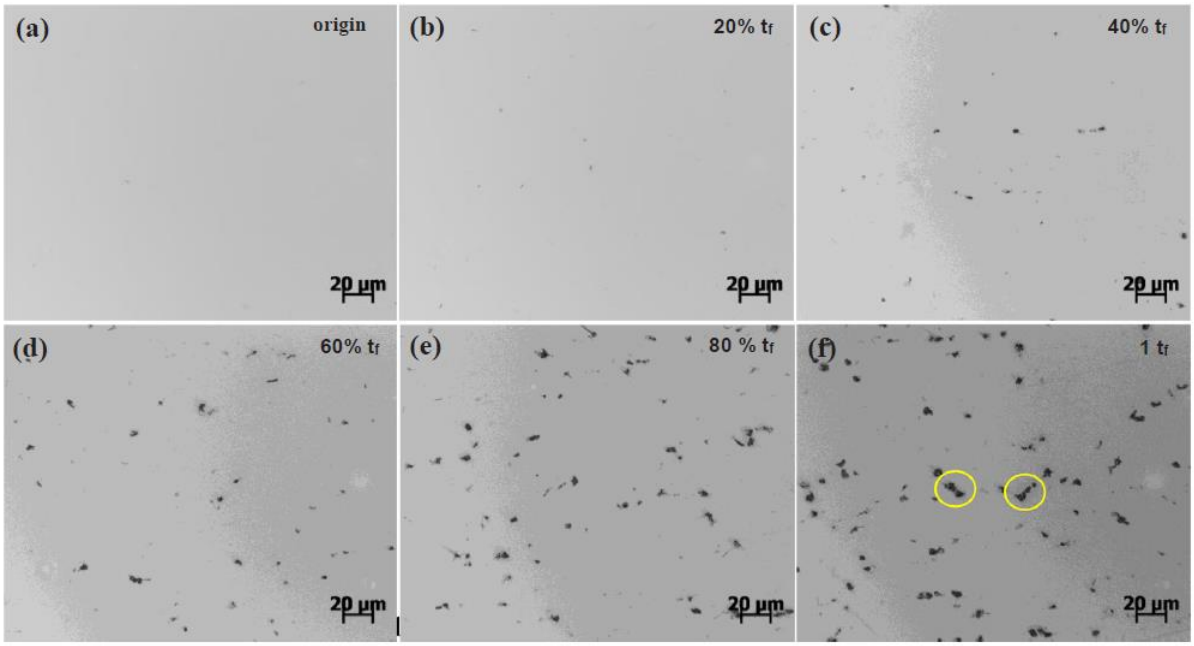

Figure 2.4: Images of creep cavitation in increasing stages of creep life fraction. From the fine-grained heat affected zone (FGHAZ) of ASME T/P 92 weld. (a) initial; (b) 20 % t_f; (c) 40 % t_f; (d) 60 % t_f; (e) 80 % t_f; (f) 1 t_f [Wang et al., 2018]

In order to delay this failure mechanism for as long as possible during service life, many of the alloying elements are specifically selected with the express purpose of minimising this cavitation process; this is done by solid solution hardening, precipitation hardening, dislocation hardening and boundary or sub-boundary hardening [Abe, 2014a; 2004]. By delaying the onset of creep damage mechanisms the early stage of the damage process is prolonged, with the result of a disproportionate effect on the time until failure [Wang et al., 2019].

In addition to avoiding these failure mechanisms the rotor/turbine components would ideally be cheap, easily manufactured (machinability and forging) and welded (weldability), avoid/reduce solid particle erosion or corrosion, resist oxidation and be easily inspected for defects and other safety concerns (ultrasonic detectability).

2.1.3. Alloy types

Current material design is between the abilities of two different material types, advanced heat resistant steel grades used in ultra-supercritical turbines up to steam temperatures around 620 °C and nickel-based superalloys capable of temperature above 700 °C in advanced ultra-supercritical turbines [Tominaga, 2017]. The situation is not as clear cut as it may initially appear, with the higher temperature nickel-based alloy being significantly more expensive than its steel predecessor. Therefore it is advantageous to use a combination of both materials across a turbine section, with higher temperature nickel-based alloys used towards the start of the turbine and the lower temperature steel welded on part way through [Tominaga, 2017]. This is made possible by the temperature dropping with each stage of the turbine as more energy is extracted from the working fluid (steam), as indicated in Figure 2.5. This trend adds significant complexity in turbine design to balance both efficiency and economics. As a result material based development is following the duel path of improving both material types simultaneously. This work predominantly focusses on the steel grades of rotor steels, with many aspects likely being applicable to other turbine components or nickel-based material components.

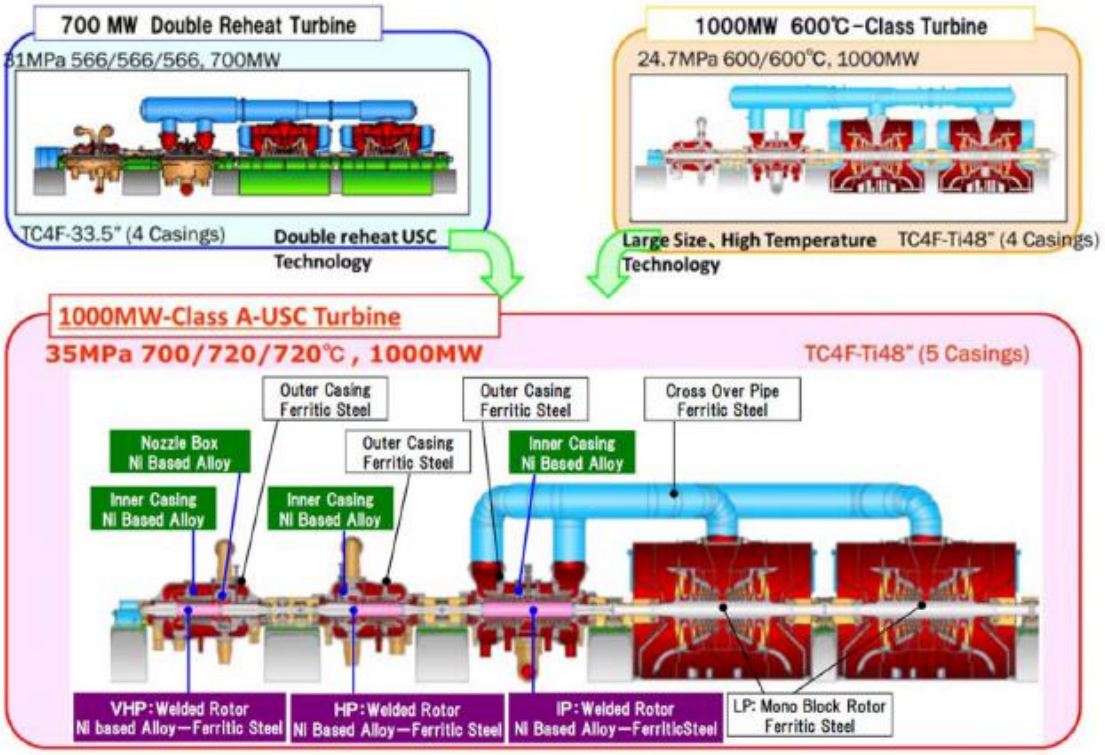

Figure 2.5: Image indicating the mixed use of a nickel-based alloy and steel as determined by temperature exposure of individual components. Also showing how lessons have been learned from previous (USC) generations of turbine and are incorporated into the new generation designs (A-USC), such as the double reheat technology combined with large and high temperature system. [Tominaga, 2017]

Generally new alloy developments are first introduced for smaller components, such as blades, and then the larger components - rotor or casings - are introduced later [Nomoto, 2017]. This leads to blades typically having the highest creep rupture strength of the turbine section, conveniently this marries well with blades typically being exposed to the highest temperatures. A significant difference between the blades and the rotor are the thermal gradients which they are exposed to. As rotors have such a large mass, the outer surface often presents a significant temperature difference to the inner regions; this process then introduces thermal stress which induces low-cycle fatigue [Nomoto, 2017]. Conversely the direct steam exposure of rotating blades introduces high-cycle fatigue issues as a result of the excitation forces of the high pressure steam [Nomoto, 2017]. Fatigue issues are important considerations in the failure mechanisms of components, with the distinction

between high - and low – cycle fatigue being made to designate elastic and plastic deformation respectively [DeLuca, 2001].

2.1.4. Alloy composition

There have been many grades of rotor steel used over the years (Table 2.3), a common current commercial grade is FB2 and so this is the primary consideration of this work. FB2 is a composition developed as part of the European COST (European Cooperation in Science and Technology) program [Di Gianfrancesco et al., 2008], which had the aim to find alloys with improved material properties and so withstand the higher temperature and pressure of more demanding operating conditions. Table 2.4 summarises alloys which are closely linked to FB2 in the COST research program, B2 was the precursor grade which subsequently developed into FB2 and this was further adapted to create FB4.

Table 2.3: The composition of several typical rotor steels (all wt% compositions) [Cowen et al., 2012]

Summary of Major 9-12% Cr Steels Used for Steam Turbine Rotors

Chemistry														
Material	C	Mn	Si	Ni	Cr	Mo	V	Nb	N	W	B	Co	Fe	Other
COST FB2	0.13	0.30	0.08	0.05	9.30	1.50	0.20	0.05	0.026		0.01	1.00	Bal	
COST E	0.12	0.45	0.10	0.74	10.40	1.10	0.18	0.045	0.05	1.00			Bal	
TOS107	0.15	0.55	0.05	0.70	10.00	1.00	0.18	0.04	0.04	1.00			Bal	0.005 Al
TOS110	0.11	0.08	0.10	0.20	10.00	0.70	0.20	0.05	0.02	1.80	0.01	3.00	Bal	
TMK2 (TR1150)	0.13	0.50	0.05	0.70	10.20	0.40	0.17	0.06	0.05	1.80			Bal	
TR1200	0.12	0.50	0.05	0.80	11.20	0.30	0.20	0.08	0.06	1.80			Bal	
HR1200	0.10	0.55	0.06	0.50	11.00	0.23	0.22	0.07	0.02	2.70	0.020	2.70	Bal	
GE 10Cr	0.16	0.70	0.30	0.50	11.00	1.00	0.20	0.08	0.04				Bal	0.005 Al

Table 2.4: Comparison of advanced rotor steel compositions as part of the COST program. B2 lead to the development of FB2, which then subsequently developed into FB4. (all wt% compositions) [Blaes et al., 2011]

	C	Mn	Cr	Ni	Mo	V	N	Nb	B	Co
Cost B2	0.2	0.75	9	0.1	0	0.2	0.02	0.05	0.01	
Cost FB4	0.18	0.3	9.25	0.15	1.5	0.3	0.015	0.06	0.01	
Cost FB2	0.13	0.35	9.25	0.15	1.5	0.2	0.023	0.05	0.01	1.3

Table 2.5: Composition of P91 and P92 steel grades by wt%. These compositions are typically used for steam pipe applications; they are also closely related to FB2 rotor steel. [Saad et al., 2013]

	Cr	Mo	C	Si	S	P	Al	V	Nb	N	W	B
P91	8.60	1.02	0.12	0.34	<0.002	0.017	0.007	0.24	0.070	0.060	0.03	-
P92	8.62	0.33	0.10	0.45	0.002	0.015	0.019	0.21	0.076	0.047	1.86	0.0034

Table 2.5 presents the chemical composition of two steel grades typically used in steam piping type applications. It is of relevance for this work due to the close relation to common rotor steel grades, principally FB2. Due to the considerably greater literature available for these steel grades and the many parallels with the rotor steels, it is useful to draw on this where appropriate.

2.1.5. Microstructure required for good creep resistance

The industrial requirements clearly place a high importance on the creep strength of power generation components. As Figure 2.6 indicates however, this is not a static attribute and so the evolution of creep strength over time is an important area of research. It is also clear there are many contributory factors to overall creep strength and trying to optimise this leads to the addition of many alloying elements.

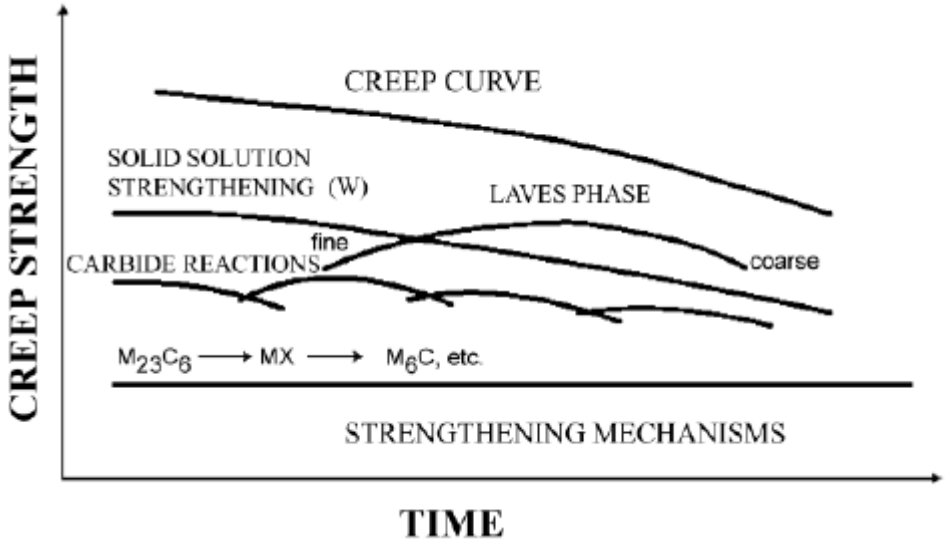

Figure 2.6: The evolution of creep strength contributory aspects over time [Sklenička et al., 2003]

Figure 2.7 indicates the process in determining the maximum operating temperature of a particular alloy. Here the maximum temperature is obtained where the alloy has average stress rupture strength of 100 MPa after 100,000 hours. The Figure shows the large differences across a range of power generation steel alloys. Figure 2.8 shows the creep rupture strength of several alloys which were part of the COST development program. Here it is clear that FB2 did not in fact exhibit the highest creep rupture strength of all of the developed alloys; however it did prove to be the most consistent over time. This proved to be the determining characteristic of FB2 over other grades, as rotors steels are designed with a very long operating life in mind.

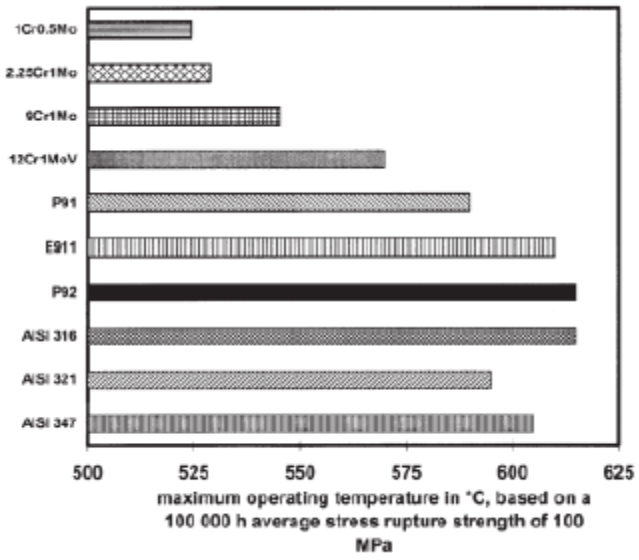

Figure 2.7: Summary of the maximum operating temperatures across a range of power generation steels. Figures based on stress rupture strength tests. [Ennis and Czyrska-Filemonowicz, 2003]

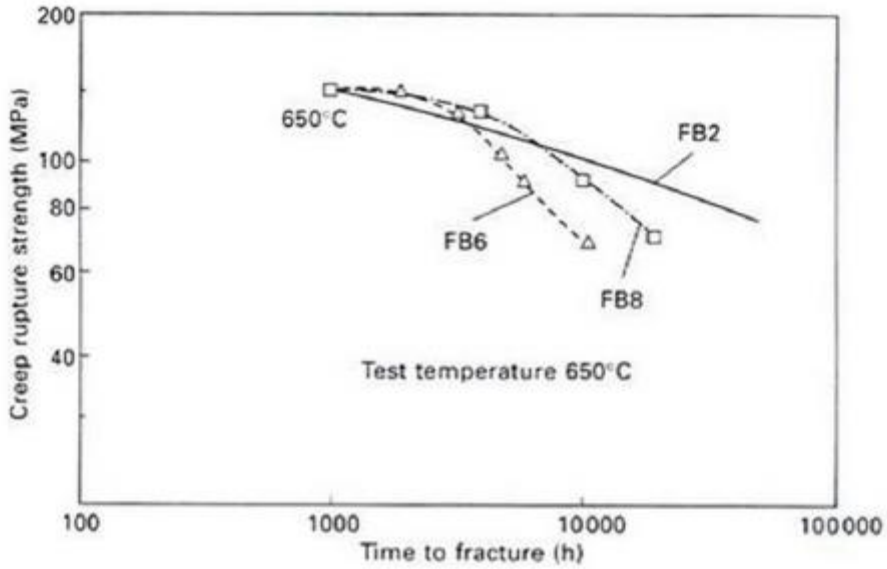

Figure 2.8: Comparison of the creep rupture strength of several test alloys developed as part of the COST program. [Mayer and Masuyama, 2008]

The superior creep characteristics of this material are generated by the stability of the tempered martensite microstructure with $M_{23}C_6$ carbide precipitates, especially under high temperature and load [Zeiler, 2017].

2.1.6. Martensitic microstructure

The microstructure of these alloys is a tempered martensite, which is desirable due to its combination of good hardness and toughness and superior creep resistance characteristics [Vanstone et al., 2013]. [Ma et al., 2019] Investigates the tempering of $M_{23}C_6$ precipitates in CB2 (the non-forged variant of FB2) and finds a significant increase in precipitate coarsening as a result of a higher tempering temperature. Average precipitate diameter of 132 nm was associated with 2 hours tempering at 690 ° C, whereas an average precipitate diameter of 198 nm was found for 2 hours tempering at 790 ° C. It is known that $M_{23}C_6$ precipitates play a significant role in the stability of the subgrain boundaries and subsequently creep strength [Ma et al., 2019]. Therefore the coarsening of these important precipitates has a negative influence on overall creep strength properties. As the precipitates coarsen, the associated

lath width increases and recovery of the martensitic structure leads to a reduction in tensile and yield strength [Ma et al., 2019]. The data in Figure 2.9 show the clear decrease of Brinell hardness of the CB2 steel associated with different tempering temperatures over a 2 hour time period with subsequent air cooling.

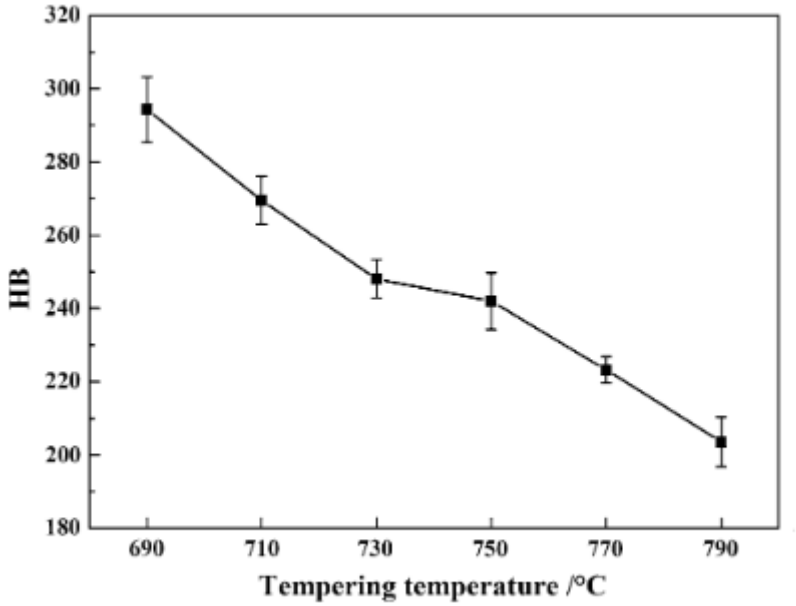

Figure 2.9: The Brinell hardness of CB2 steel as a result of different tempering temperatures (over 2 hours) [Ma et al., 2019]

A martensitic microstructure forms by cooling from the austenitic phase, estimates made for 9 Cr steels show a 5 K min^{-1} critical cooling rate is the minimum required for a martensitic rather than bainitic transformation [Raju et al., 2010; Ganesh et al., 2011]. This would result in a martensitic transformation of 9-12 Cr steels under air-cooled conditions [Bhadeshia, 2001a]. As the martensitic transformation is a diffusionless process the transformation takes place due to a deformation of the austenite lattice to form a body-centred tetragonal (BCT) structure. This deformation is related to the Bain strain, which is a 17% compression in the z-axis and approximately 17% uniform expansion in the x and y axis [Dally, 2017]. The martensitic start temperature, M_s, is heavily dependent on the composition involved in the transformation and so must be calculated on an individual

basis. Equation 2.1 [Ganesh et al., 2011], considers low carbon and high chromium steels (such as FB2) and so provides a useful oversight for power generation rotor steels.

$$M_s / K = 908 - 474(C + 0.86(N - 0.15(Nb - Zr)) - 0.66Ta) - ((17Cr + 33Mn + 21Mo + 20Ni + 39V + 5W) - 45Mn^2 - 25Ni^2 - 100V^2 + 10Co + 20Cu) - 47.4Si \quad (2.1)$$

The martensite finish temperature (equation 2.2) is the temperature at which the martensitic transformation is complete with the resultant material being fully martensitic. [Steven and Haynes, 1956]

$$M_f = M_s - 387 \quad (2.2)$$

A martensitic structure, in low carbon steels, is defined by a group of laths, all of similar orientation in what is known as a packet. Higher levels of carbon result in plate and twin martensite. Figure 2.10 shows a transmission electron micrograph, optical micrograph and a diagram of the microstructure associated with lath martensite. From image c it is evident that there are many different boundary types present within a single austenite grain. Figure 2.11 shows the evolution of expected lath martensite microstructure with increasing carbon content. A progressively finer lath structure with increased carbon content and by 0.8 wt% carbon lenticular martensite also starts to form with the lath martensite.

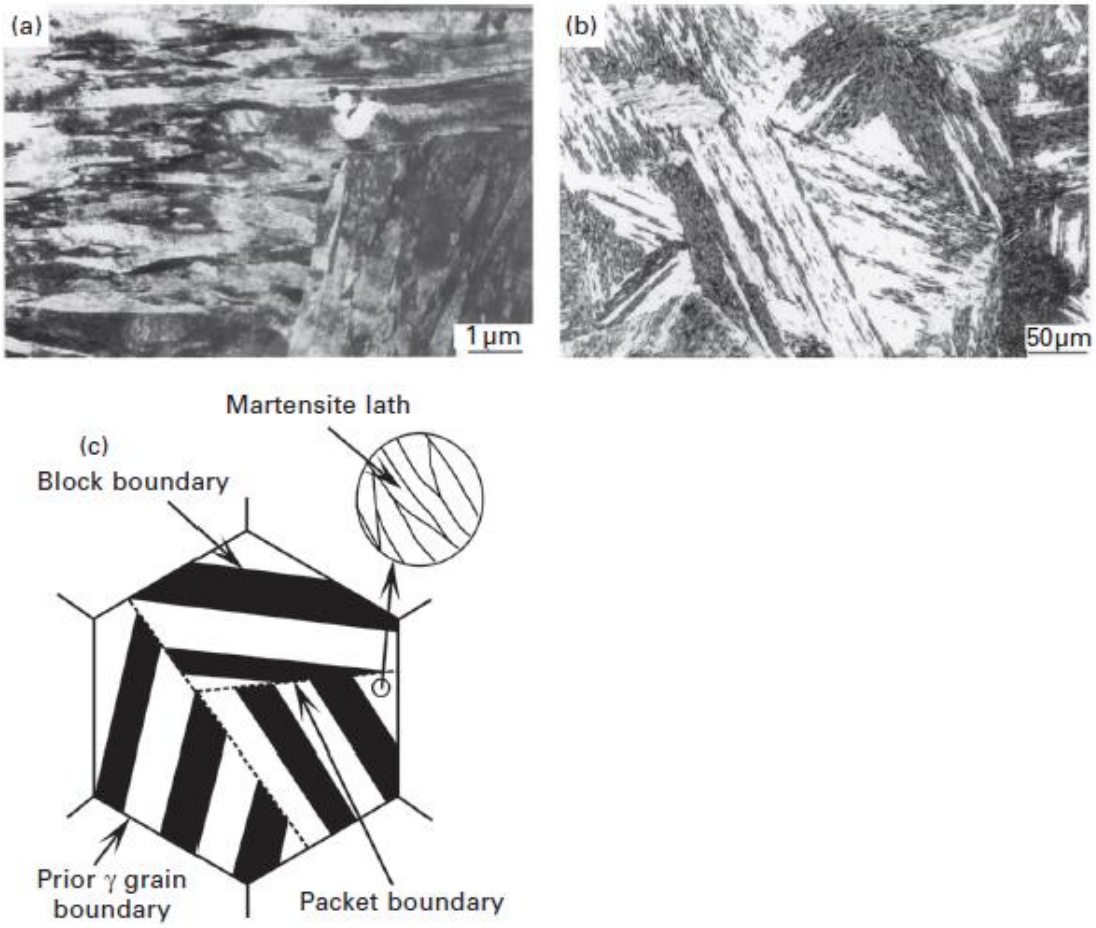

Figure 2.10: (a) Transmission electron micrograph of lath martensite in Fe-0.2%C alloy, (b) optical micrograph of lath martensite in Fe-0.2%C alloy and (c) schematic indicating the structure of lath martensite in an austenite grain. [Marder and Marder, 1969; Inoue *et al.*, 1970; Matsuda *et al.*, 1972] from [Maki, 2012]

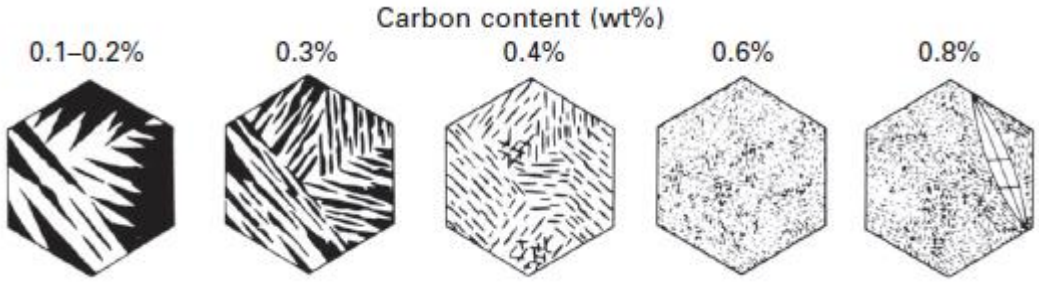

Figure 2.11: Diagram indicating the expected change of martensitic microstructure with carbon content in Fe – C alloys. The laths become finer and more difficult to distinguish with increased carbon content and by 0.8 wt% carbon lenticular martensite also forms with the lath martensite [Maki et al., 1980; Maki, 2012]

2.1.7. Orientation relationships

A characteristic of the formation of polycrystalline materials is the crystallographic rules they adhere to. As many laths form within the boundaries of a prior austenite grain,

grouped into packets, they have specific orientations relative to one another. These are known as crystallographic orientation relationships with those of martensite known as Kurdjumov-Sachs (K-S), Nishiyama-Wassermann (N-W) and Greninger-Troiano (G-T) orientation relationships (OR). These orientation relationships apply between BCC (body centred cubic) and FCC (face centred cubic) and so they relate the martensitic lath orientation to the parent austenite grain. A good overview is found in [Bhadeshia, 2001b] and explains how the orientation relations are formed as a result of the strain during the martensitic transformation.

2.1.8. Alloying elements

The composition of the alloy used is a major determinant of the properties the component will exhibit and how it will perform throughout its service life. The alloying elements used for modern rotor forgings generate a complex mix of both positive and negative impacts. During the alloy development the relative impact of each alloying element is considered and can be offset against one another in order to achieve an overall desired outcome. Most elements contribute both positive and negative impacts and so must be carefully considered. Table 2.6 aims to provide a summary of the important properties of the typical alloying elements found in rotor steel grades.

Table 2.6: Summary of contributions provided by commonly used rotor steel elements

Element	Positive	Negative	Notes
Carbon	Carbides are used to pin grain boundaries and increase strength, hardenability and creep resistance	Carbides are essentially small inclusions which could interact with ultrasonic wave propagation (the relative significance of this statement shall be explored in subsequent sections of this thesis) Carbide coarsening reduces the regularity of carbide distribution reducing the	Carbide former Determines the degree of tetragonality of martensite structure

		overall pinning effect	
Chromium	Improves oxidation and corrosion resistance Aids in achieving martensitic microstructure Cr-rich carbides pin grain boundaries (see carbon)	Ferrite formers need to be balanced with austenite stabilisers to form austenite rather than delta - ferrite during heat - treatment Carbides potential UT influence Carbide coarsening	Forms oxide layer Increases likelihood of martensitic rather than bainitic transformation Ferrite stabiliser Carbide former
Molybdenum	Mo-rich carbides pin grain boundaries (see carbon)	Solid solution strengthening only true at lower temperatures of previous generations of rotor steels [Hald, 2008] Carbides potential UT influence Carbide coarsening Ferrite stabiliser needs to be balanced (see chromium) Laves phase formation reduces creep strength [Abe, 2014a; 2014b]	Solid solution strengthening [Swindman and Klueh, 1977] Carbide former Laves phase former Ferrite stabiliser
Nickel	Balances out ferrite stabilisers	Can reduce A1 temp leading to alpha ferrite formation [Masuyama, 2001] Reduced creep strength due to Laves phase [Lun Wang, 2010] and destabilising $M_{23}C_6$ by promoting M_6C [Dally, 2017]	Austenite stabiliser Laves phase former Limited to below 0.4 wt % in P91, P92 and FB2 Also limited due to expense
Manganese	Improves hardenability, toughness, hot working properties and strength	Reduces A1 temp Forms manganese sulphides which exhibits low interfacial cohesion and leads to cavitation	Austenite stabiliser
Cobalt	Does not reduce A1 temp and increases martensite start temperature [Klueh, 2005] Increases creep strength		Austenite stabiliser Reduces diffusion rate leading to increased stability of MX particles and so improved creep strength [Cipolla, 2010]
Boron	Increases hardenability and slows δ – ferrite formation [Klueh, 2005] Contributes to carbide and carbonitride formation which can reduce prior austenite grain boundary particle coarsening [Abe, 2008] Negates negative effects of phosphorus and sulphur	Boron nitride formation which removes boron from solution decreasing the positive effects Large boron nitride particles could be a problematic initiation area of fatigue failure by reducing creep life [Dally, 2017]	

	boundary segregation [Yamaguchi et al., 2007]		
Nitrogen	Austenite stabiliser Forms small precipitates pinning grain boundaries [Masuyama, 2001]	Can evaporate in ferrite leading to pores – can be mitigated by controlling Ni solubility with Co additions [Klotz et al., 2008] Removed from solution to form boron nitrides which can be detrimental when large	Forms small precipitates
Niobium	MX precipitates are small and stable, can pin grain boundaries leading to increased creep resistance [Danielsen, 2015] Promotes a fine grain structure improving strength and toughness by limiting austenite recrystallization [Dally, 2017]		Forms small precipitates Ferrite stabiliser
Vanadium			Ferrite stabiliser Carbide former
Silicon	Improves steam oxidation resistance	Laves phase former Ferrite stabiliser reducing toughness and causing fabrication issues [Ennis and Cyzrska-Filemonowicz, 2002]	Increases carbon activity Can improve casting by forming a protective oxide layer helping prevent carburisation [Hu, 2012]
Copper	Austenite stabiliser Reduces A1 temperature decrease if above 0.5 wt %		Forms copper-rich precipitates on lath boundaries [Cipolla, 2010], which can prevent significant grain growth
Sulphur		Detrimental to weldability of steel Forms manganese sulphide particles which exhibits low interfacial cohesion and lead to cavitation	Limited to 0.01 wt % [Hu, 2012]
Phosphorus		Segregates to grain boundary causing embrittlement and loss of ductility [Hu, 2012]	
Aluminium		Reduces creep strength	

2.1.9. Precipitates

Power generation rotor steels contain a high number density of precipitates that are present to provide the high strength and creep resistance. The precipitates are typically iron carbides (cementite) or alloy carbides and can be present in the laths (intralath), on the lath boundaries (interlath) and on the packet / grain boundaries. Tables 2.7 and 2.8 provide a summary of precipitates found in P91 and P92 grade steels respectively. These steel grades were precursors and with similar composition to FB2, and so are useful to gain an insight into expected precipitate formation from the extensive literature available.

Table 2.7: Precipitates found in P91 grade steel [Hald and Korcakova, 2003]

Steel grade	Precipitate	Composition
P91	$M_{23}C_6$	$(Cr,Fe,Mo)_{23}C_6$
	MX	(Nb,V)(N,C)
	Laves phase	$(Fe,Cr)_2Mo$

Table 2.8: Precipitates found in P92 grade steel [Hald and Korcakova, 2003]

Steel grade	Precipitate	Composition
P92	$M_{23}C_6$	$(Cr,Fe,Mo,W)_{23}C_6$
	MX	(Nb,V)(N,C)
	Laves phase	$(Fe,Cr)_2(Mo,W)$

Figure 2.12 indicates the typical expected precipitate distribution and relative size. As these precipitates coarsen their relative benefit reduces as their overall distribution becomes increasingly uneven. This evolution of precipitation is an important aspect of the creep curve development as seen previously in Figure 2.6.

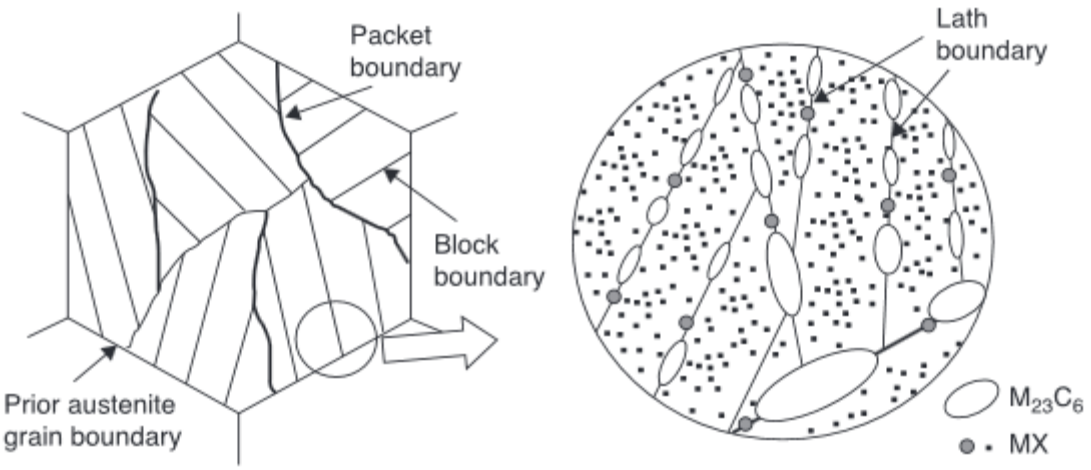

Figure 2.12: Diagram indicating the typical distribution of precipitates in a prior austenite grain. [Abe, 2014b]

2.1.10. Processing route

It is not simply the alloy composition and resulting microstructure which determine the properties a given component exhibits, the processing methods are also of critical importance. The first stage in the manufacturing route is the casting of the ingot, which primarily determines the segregation and cleanness associated with the ingot. There are many variations of the casting process which are determined by the company technology available, ingot size requirement and ingot properties required. Segregation and casting techniques shall be discussed in greater detail in a subsequent section (section 2.3).

Once the solidification process is completed the ingot is heated to a high temperature (1050 -1100 °C) and held at temperature for long periods (~48 hours for large rotors) [Watson, 2017]. This long and high temperature process is a diffusion-based homogenisation heat-treatment. The high temperature exposure encourages grain growth, which is detrimental to the material properties and so requires grain refinement via thermo-mechanical working. Here a series of upsetting, cogging and final forging press operations are used to achieve a final desired shape and microstructure. Initially, upsetting is used to generate the required

height, and then through a series of 45 and 90 degree turns the component is incrementally forged in the cogging process, typically this involves 20 to 30 deformations [Watson, 2017]. During this forging process the temperature is held above the recrystallization temperature (the temperature at which new grains can form), firstly to allow the metal to be easily manipulated but also to achieve the desired recrystallization and grain refinement induced through strain. As the temperature of the component drops during forging it is typical for a reheat treatment to be applied; this then brings the component back into the temperature window allowing for further stages of upsetting and cogging taking place. Finally the component is stamped into a preform to achieve the desired shape.

An issue with this open die forging process is the uneven distribution of recrystallization rates throughout, an example of the uneven strain distribution during upsetting is shown in Figure 2.13. Strain, strain rates and temperature throughout the component are used to predict recrystallization and to develop potential mitigation steps. As a result the component is frequently pressed from a series of predefined angles which have been calculated by use of modelling techniques, these intend to optimise the forging process and improve reproducibility [Kang et al., 2005]. These models can be based on finite difference (FD) [Rübenkönig, 2006; Morton and Mayers, 2005], finite volume (FV) [LeVeque, 2002] or finite element (FE) [Zienkiewicz, 1973; Strang and Fix, 1973] methods; the specifics of these methods shall not be covered here but are found across many alternative sources such as the references provided. The most problematic areas are typically those directly in the region of the die-workpiece interface (point of contact), as indicated in Figure 2.13. Therefore, by rotating this point of contact frequently the most serious issues can be avoided.

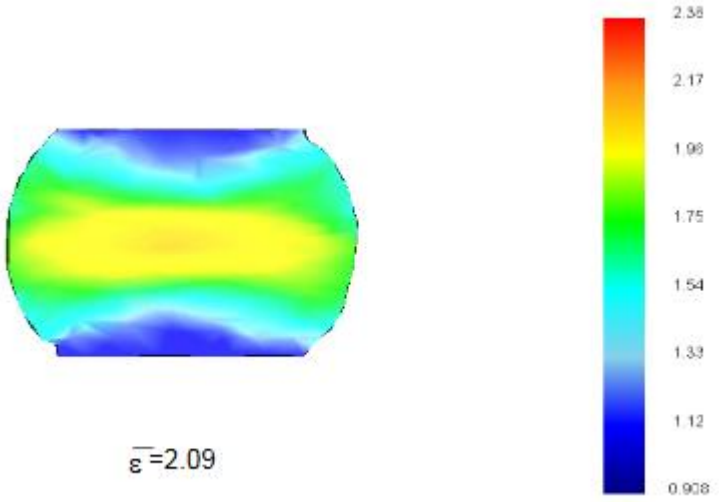

Figure 2.13: Prediction of the expected strain distribution during the upsetting process. [Kang et al., 2005]

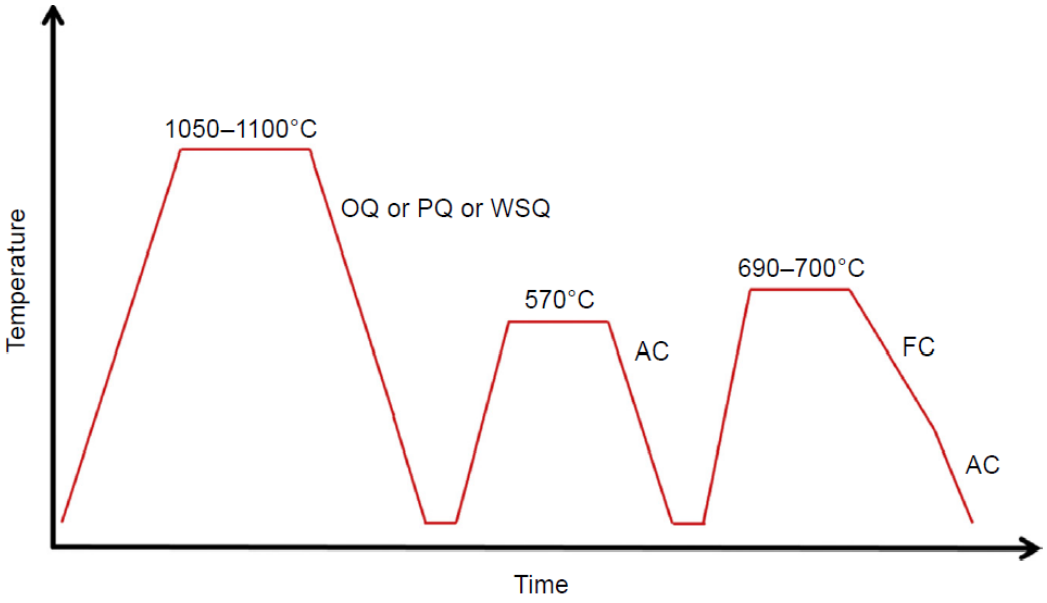

Figure 2.14: Typical quality heat treatment associated with modern rotor forgings. Note: Air cooled (AC), Furnace cooled (FC), Oil/polymer/water-spray quench (O/P/WS – Q). [Zeiler, 2017]

A typical quality heat treatment procedure is shown in Figure 2.14. Here there are three distinct phases shown, the first phase is taken above the austenitizing temperature to ensure uniformity of grains throughout. This first heat treatment phase is a normalisation heat treatment (preliminary heat treatment in Figure 2.15) and is designed with sufficient temperature and time for full austenitic transformation to take place; this is to ensure a uniform microstructural transformation is achieved upon quenching. Once the required

temperature is achieved the austenitic transformation occurs quickly (from seconds to minutes), although large components require significantly longer to ensure that the transformation is complete throughout due to temperature gradients. Reducing the time at temperature has proven beneficial to generating finer heat treated microstructures along with slight improvement to tensile and impact properties [Voigt et al., 2004]. Precise heat treatment procedures are often not readily available for commercially sensitive alloy grades [Watson, 2017], however extensive literature is available on similar grades such as P91 [Shrestha et al., 2015; Yoshino et al., 2008; Totemeier et al., 2006; Dudko et al., 2012; Sawada et al., 2008]. The second and third parts of the heat treatment in Figure 2.14 are the first and second tempering phases (or quality heat treatment), where a fully tempered martensitic microstructure is achieved with the desired precipitation and growth of carbides.

2.2. Ultrasonic testing during manufacturing

An essential part of the manufacture process is the testing; this ensures the desired characteristics have indeed been generated. As this process must by necessity be non-destructive, ultrasonic testing is the main method to achieve this. These days the ultrasonic testing process is so essential to product quality and safety requirements it is unthinkable that a component could be delivered without being tested during the manufacturing process. Due to these vigorous testing requirements the process is highly automated with a wide range of advanced testing methods applied [Zimmer et al., 2010] – these techniques shall be introduced in chapter 3. Figure 2.15 provides a flow chart of the manufacturing procedure associated with a trial rotor forging; a typical service rotor procedure is

essentially the same although an extra ultrasonic testing stage is introduced before quality heat treatment as well as during final inspection [Zeiler, 2017].

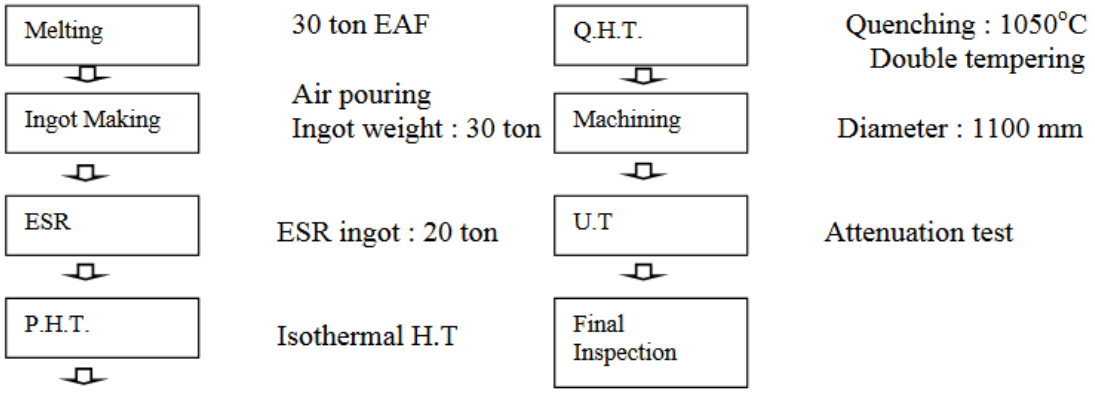

Figure 2.15: The processing route associated with a trial rotor forging. [Kang et al., 2005]

Ultrasonic testing has long been concerned with finding defects above a given risk threshold, depending on the size of the defect and expected failure mechanics of the component [Mayer et al., 1996]. These defects are known to cause problems during the component service life, analysis of brittle failures of low pressure turbines and generators were found to be caused in large part (70%) due to forging defects [Mayer et al., 1996], Figure 2.16 provides a record of these failures over time. The exact limits are dependent on the location and requirements of that specific component location, some areas have higher defect thresholds than others within the component; Figure 2.19 provides a summary of the flaw assessment process. As flaws can be comprised of an individual large reflector or the congregation of multiple smaller ones, a standardisation process (typically industry specific) is used where the indication is evaluated as an equivalent reflection by a standardised flat bottom hole as shown in Figure 2.18. Much effort is made to ensure the defects are correctly sized, with multiple ultrasonic tests using angled transducers made in roughly 7° increments; Figure 2.17 provides a full overview of how this is typically conducted. This

complicated testing process is the result of prior testing oversights. A complete rotor failure in 1988, the result of an angled defect being undersized, led to an overhaul of the testing procedure; testing processes and correction tables are now standard in order to avoid similar mistakes [Zimmer et al., 2010]. The other aspect which is monitored is the ultrasonic detectability of a given region, which again has differing limits based on requirements. The process is driven by the requirement to detect any defects above a certain size threshold, if there is some restriction on this ability the component cannot be safely authorised to enter service. This is the reason for both attenuation and back-wall echo reduction to be monitored as part of the standard testing procedure (Figure 2.19).

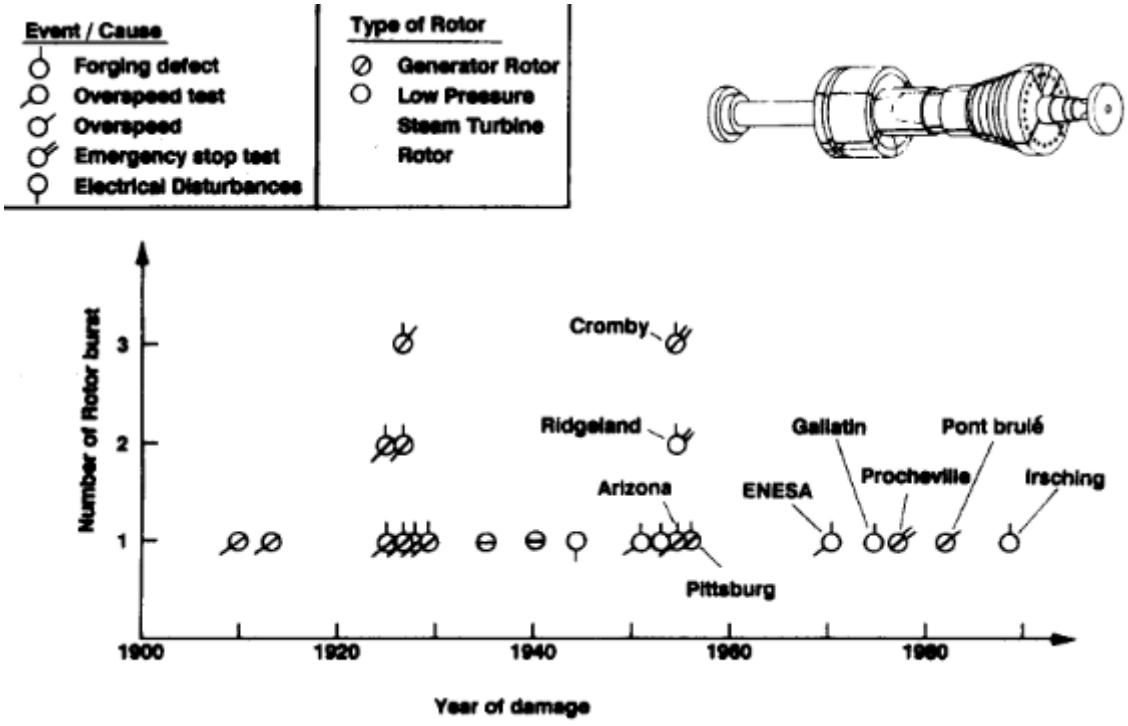

Figure 2.16: Summary of rotor damage history. [Mayer et al., 1993]

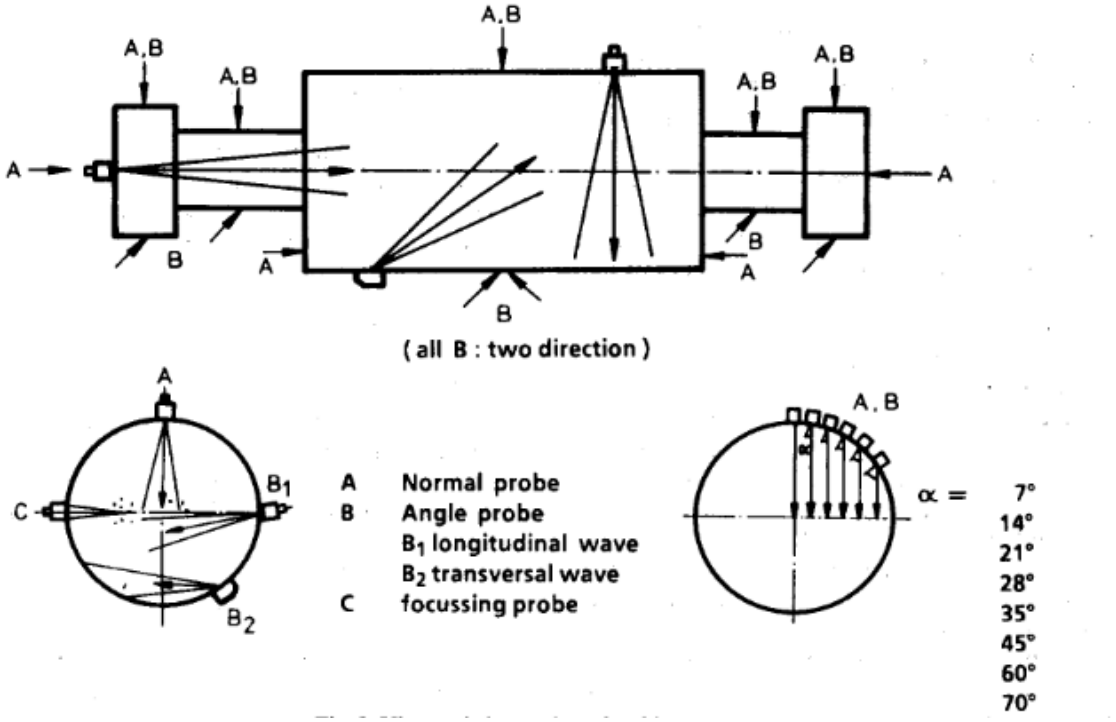

Figure 2.17: Typical ultrasonic inspection routine of rotor forgings. [Mayer et al., 1993]

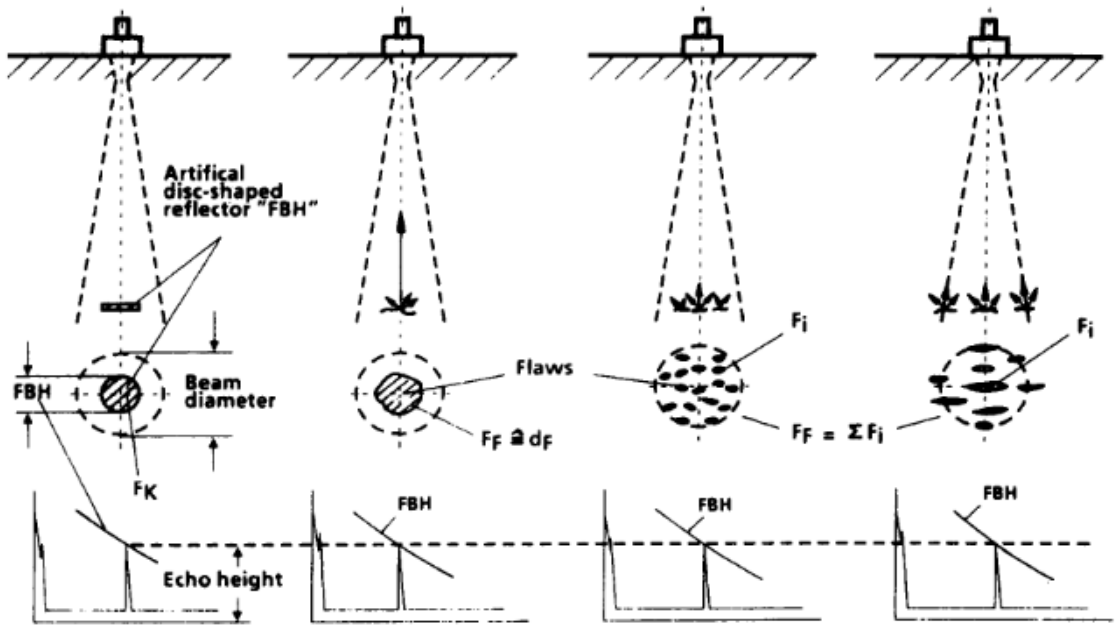

Figure 2.18: Comparison of different flaws standardised with an "equivalent reflector size" as compared against a standard flat bottom hole. [Mayer et al., 1993]

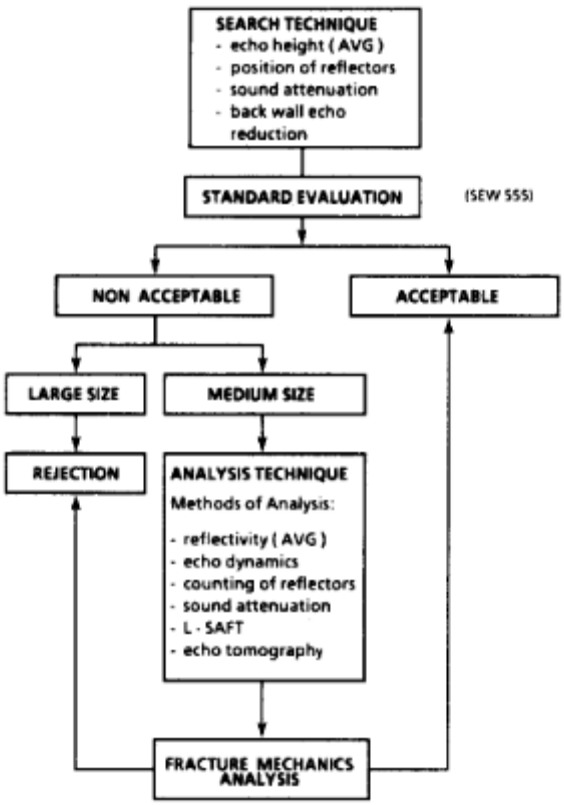

Figure 2.19: Typically ultrasonic testing and evaluation procedure of a rotor forging. [Mayer et al., 1993]

2.3. Ingot casting segregation review

2.3.1. Overview

Segregation is an inherent part of the ingot casting procedure. It occurs due to the uneven distribution of alloying elements during the casting process, via the sideways rejection of solute out of a growing dendrite into a solute rich “mushy zone” [Dally, 2017]. It has been shown that the formation of macro scale segregation is a direct consequence of fluid motion in the inter-dendritic region [Li et al., 2012a; 2012b; Mcdonald and Hunt, 1970; Sarazin and Hellawell, 1988]. Micro-segregation can be reduced somewhat during the homogenisation heat treatment; however the macro-segregation still largely remains [Pickering, 2014]. The homogenisation heat treatment is effective at relieving micro-segregation but largely ineffective against macro-segregation due to their differences in relative scales. As the

names suggest, micro-segregation involves the segregation of alloying elements over small relative distances (on the micron scale) whereas macro-segregation is the segregation across an area the order of the ingot itself (a macro scale). As a result the diffusion process over the timescale of a homogenisation heat treatment does not have the capacity to remedy macro scale segregation, whereas it does on a micro scale. This retained inhomogeneity, associated with macro-segregation, can detrimentally impact the quality of the finished product by altering expected microstructures along with the associated variation in mechanical properties [Pickering and Bhadeshia, 2014; Ghosh, 2001], and so must be understood or, better yet, controlled [Medina et al., 2004]. The severity of this macro-segregation can also be monitored ultrasonically [Gusarova et al., 2015] and is a potential cause of ultrasonic quality control rejection [Bogdan, 2018; Sarnet, 2009].

There are many controllable aspects which contribute to segregation within ingots. For instance [Ge et al., 2018a] discusses the impact of ingot size, with larger ingots exhibiting more severe segregation in general. This trend does level off however as it reaches a critical size (ingot weight of 25 tons) where limits to packing restrict any further negative segregation forming. Pouring temperature and velocity of the molten liquid into the mould influence the grain formation and turbulence and so should be tightly controlled to limit segregation [Maduriya and Yadav, 2018].

2.3.2. Micro-segregation

The solidification of an ingot consists of three stages; initially there is the liquid phase which has a high degree of solute mixing. As the liquid cools it begins to solidify, however this forms a type of solidification front or “mushy zone” and consists of a solid dendritic mesh with a liquid flowing through this dendrite network (Figure 2.20). Once further cooling has

taken place this dendritic network/inter-dendritic liquid solidifies further to form the fully solidified bulk material.

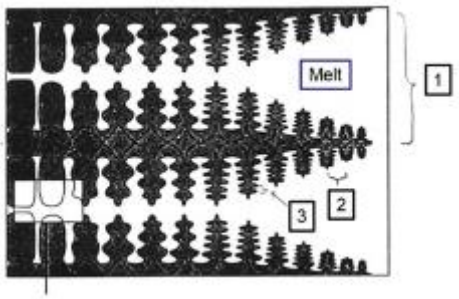

Figure 2.20: Image depicting an ideal columnar dendrite. (1) indicates primary dendrite arm spacing, (2) indicates secondary dendrite arm spacing and (3) indicates tertiary dendrite arm spacing. [Louhenkilpi, 2014]

Micro-segregation forms as the result of solutes being unevenly distributed, which is primarily influenced by two main factors, the equilibrium partition coefficient and the diffusion coefficient of the element in the solid phase [Louhenkilpi, 2014]. The equilibrium partition coefficient is determined by the ratio of solid to liquid concentration which corresponds to the solidus and liquidus lines of the equilibrium phase diagram. This determines the maximum magnitude of total micro-segregation, which would be associated with zero diffusion. However, it is typically reduced somewhat by subsequent diffusion, which is determined by the diffusion rate of each individual element in the solid phase (known as back diffusion). An infinite, or sufficiently large, diffusion coefficient could eliminate the micro-segregation across the dendritic network, which is the reason behind certain elements tending to segregate rather than others. The basis of this work is discussed in detail by [Dally, 2017] and comprehensively examines the different underlying assumptions of the lever rule and Scheil model, Brody-Flemings model and the Clyne-Kurz model. The differences between the models consists of their scope with respect to back-diffusion occurring. The lever rule is achieved by considering the equilibrium case of infinite back diffusion. By contrast a non-equilibrium model which assumes no back-diffusion is

known as the Scheil model. These differ from the other models which consider the more complex levels of back-diffusion providing an intermediate stage between the two limiting cases. The validity of any particular model is dependent on the solidification characteristics of each particular case, particularly in regards to solute transfer kinetics, although in general it is fair to say the Scheil model tends to break down for nickel based superalloys or steel [backdiffusion, Sentesoftware]. Work which is specifically focussed on the micro-segregation of high alloy steels such as FB2 indicate the complexity involved with the segregation of the many solute types. [Dally, 2017] has shown the Scheil model is most applicable for a small number of elements (Mo and partially Cr and V). However, no single model definitively predicts the segregation of every element and so a combination of different models may prove to be the best approach. Furthermore, it appears as though the use of a constant partition coefficient does not seem appropriate for all elements, particularly for the austenite stabilising elements.

Although ultrasonic techniques are used to detect macroscopic segregation in steels [Gusarova et al., 2015], micro-segregation is typically too small to appear as conventional defects. However, the consequences of material property variation as a result of this micro-segregation could well be observed as part of NDE techniques. Variations in Young's modulus are algebraically linked with ultrasonic velocity, as verified with micro-tensile testing in a sample from a large bainitic steel ingot which had been forged and heat-treated [Dupont-Marillia et al., 2017].

The work linking macro and micro segregations was first presented by Flemings and colleagues [Flemings, 2000; 1974; Flemings and Nerco, 1967; 1968a; 1968b; Fuji et al., 1979], where they discussed the significance of convection in the mushy zone of ingot

solidification. Here inter-dendritic flows are used to predict macro-segregation formation and form the basis of the predictive modelling work conducted today.

2.3.3. Macro-segregation

The macro-segregation of ingots is caused by the flow of solute-rich liquid in solute-depleted regions during solidification. These can occur in numerous ways such as by solidification shrinkage, buoyancy-related flows from thermal or solutal gradients, forced flows (e.g. via pouring, stirring, rotation or movement of gas bubbles), movement of free (equiaxed) grains or solid fragments, or the deformation of the solid network [Beckermann, 2001].

The segregation which forms in a typical ingot has several distinct forms: cones of negative segregation, hot top segregation, V and A segregates and vertical bands. These segregation types are potential causes of defects found during the ultrasonic testing process (Figure 2.21), and so would ideally be avoided. [Zaloznik and Combeau, 2010] show the formation of meso-segregates (channel segregates/ V and A segregates) does not require local remelting, as was previously thought but can result from the instability of the solidification front.

[Ge et al., 2018a] shows the dominant factor for small ingot castings is thermal-solutal buoyancy, however the sedimentation of equiaxed grains becomes more significant for larger ingot size. The segregation severity also tends to increase with ingot size and therefore is of particular relevance to large ingots such as those used for rotor forgings.

The applicability of these general segregation characteristics depends on the casting process used, which was also a consideration of the previously mentioned COST research programs.

The techniques trialled included conventional ingot casting, the BEST (Bohler Electro Slag Topping) process and ESR (Electro Slag Remelting) over a range of ingot sizes up to 154 metric tonnes [Blaes et al., 2003]. The BEST technique (ingots of up to 48 metric tonnes achieved) is specifically designed to improve ingot homogeneity over conventional casting techniques. This is done by using a water-cooled ring at the top of the mould, with the mould filled by a bottom pouring process. A slag of special chemical composition is used with a consumable electrode immersed within it. Once a current is applied the slag heats, the electrode melts, ultimately dripping into the solidifying ingot compensating for shrinkage and positively influencing the solidification process [Zeiler, 2017]. This process avoids V - segregation and has similar levels of A - segregation to ESR – ingots; the levels of homogeneity and cleanness are better than conventional casts but not as good as ESR – ingots [Zeiler, 2017]. A similar approach to the BEST procedure was also used as part of the Japanese rotor steel test forgings, this was known as ESHT (Electro Slag Hot Topping) and exhibits similarly good results [Mikami et al., 2000; Nozu et al., 2003]. For components which require a very high level of cleanness a process known as PESR (Protective gas Electro Slag Remelting) is used, where a protective atmosphere of argon and nitrogen is used in combination with the ESR process in order to avoid oxidation issues which would compromise cleanness.

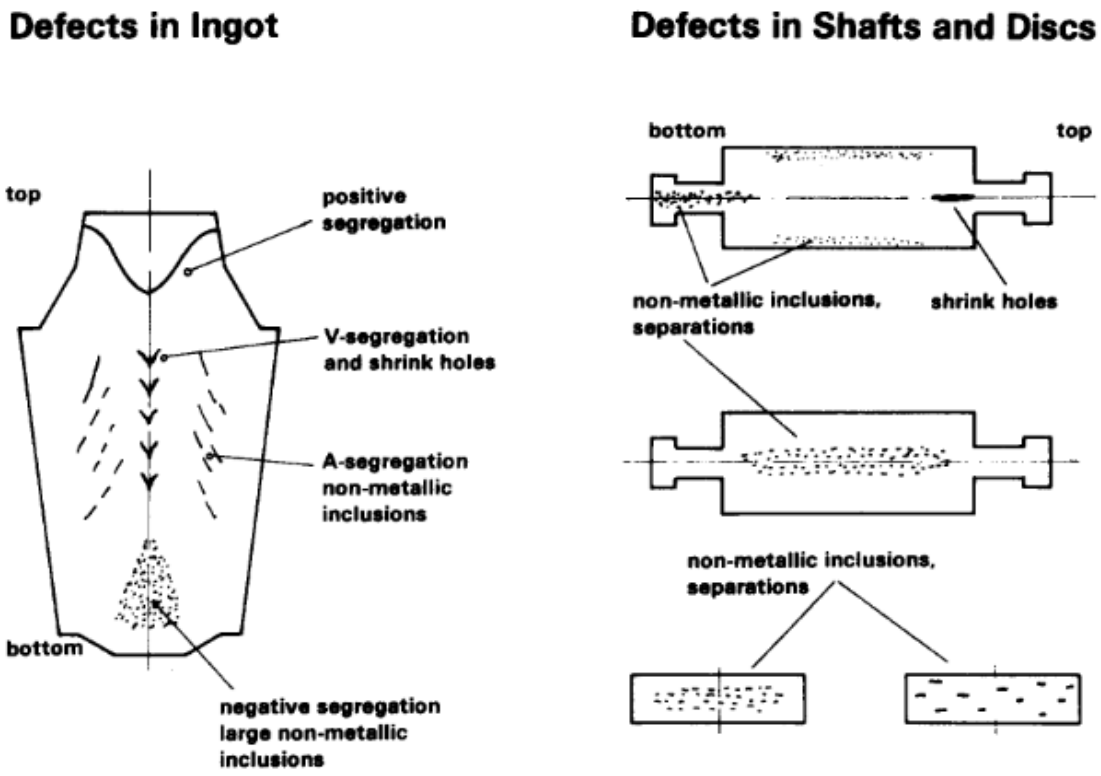

Figure 2.21: Distribution of defects which occur during the manufacturing process. [Mayer et al., 1993]

2.3.4. Alternative methods to reduce segregation

There are several methods suggested to reduce macro-segregation in large ingots. [Sang et al., 2010] suggest adding balls of the same composition as the melt liquid in order to increase the cooling rate leading to more rapid solidification and refined grain structure. The presented results comparing a steel ball ingot with a reference ingot seem to support the assertions with an apparent refinement of the microstructure, reduction in macro segregation (A segregation is prevented), and an improvement in subsequent mechanical properties.

The gradual cooling approach [Ge et al., 2018b], introduces the method of cooling the melt liquid in stages by removing layers of insulation around the mould when the solid fraction

had reached 70% of the previous section (16 sections were used in total). The simulated results showed drastic improvements in overall segregation levels.

2.4. Microstructure variations (Bainite) and tempering

Martensite is typically expected to form carbides only upon tempering, which can include either auto or artificial tempering. This is the main distinction between martensite and bainite, as it is a requirement of the bainitic transformation for the carbon to partition. As lower bainite is formed at a lower temperature (than upper bainite) the carbon partitioning occurs at a slower rate, therefore some of the carbon has the opportunity to finely precipitate, in a single orientation, within the bainitic ferrite lath. The remainder of the partitioned carbon precipitates out as carbides at the bainitic ferrite lath boundary (Figure 2.22), which is where the entirety of the carbides form in upper bainite. Further detail can be found elsewhere [Bhadeshia and Christian, 1990; Bhadeshia, 2015; Bhadeshia, 2002].

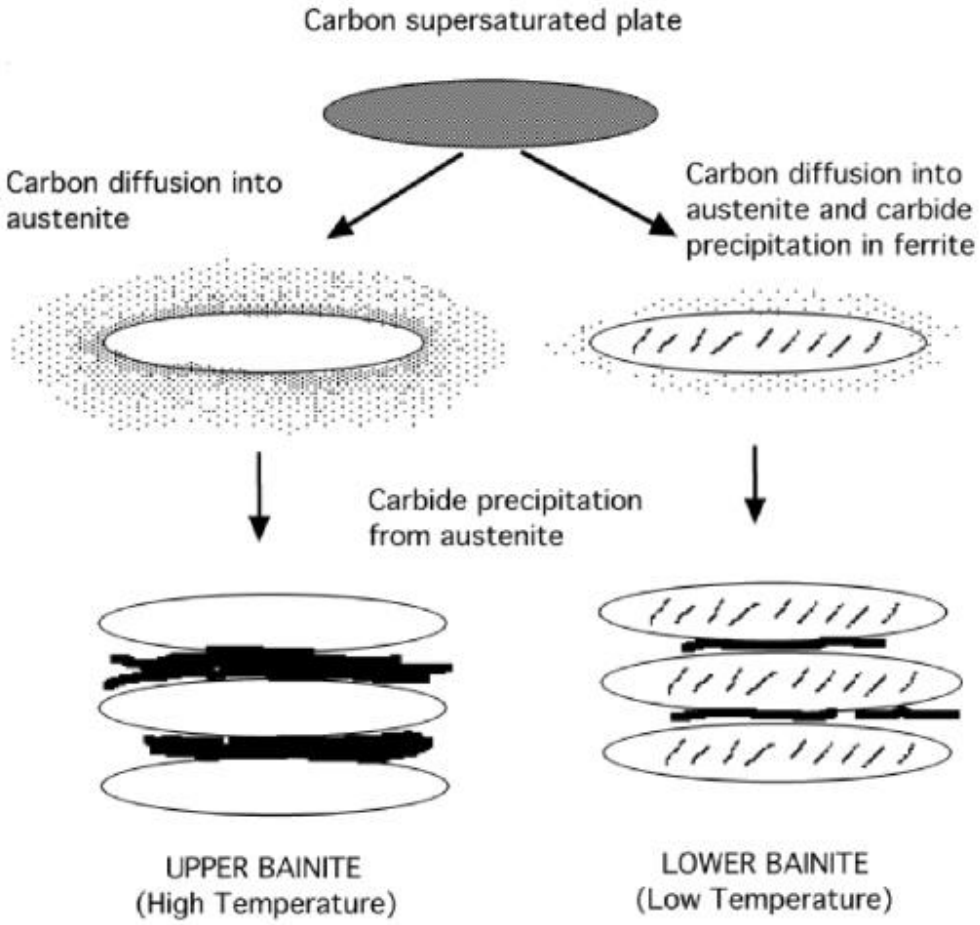

Figure 2.22: A depiction of the formation of upper and lower bainite highlighting the difference in carbide precipitation sequence. [Bhadeshia, 2008]

3. Ultrasonic testing review

3.1. Ultrasonic testing important details

3.1.1. General overview

The need for ultrasonic testing during the manufacturing of power generation components was introduced in chapter 2, and is nicely summarised in [Zimmer et al., 2010], this testing has traditionally been the domain of conventional ultrasonic testing techniques. By conventional ultrasonic testing we typically mean volumetric inspections using a pulse/echo type setup. However as the requirements for safety, reproducibility and speed of the testing techniques, and requirements of the components themselves, continued to be improved the conventional techniques were no longer sufficient. An example of this would be the use of focused phased array techniques in dissimilar metal welds (DMWs) to improve upon the low probability of crack detection due to distortion and beam splitting associated with the anisotropic weld media [Kim et al., 2016].

A key attribute of ultrasonic flaw detection is that an elongated defect exhibits the highest reflectivity at normal incidence, not accounting for this led to major component failures and angle probe testing was more thoroughly introduced. [Arakawa et al., 1985] published work indicating the potential misjudgement of defects due to the incidence angle and suggest a systematic approach of multiple angle tests varied by 15 ° increments. This is capable of providing coverage with minimal reflected signal loss due to any possible elongated defect orientation angle.

Reproducibility, speed and safety can all be improved by incorporating automated testing procedures wherever possible, rather than manual alternatives. These techniques allow for regular testing to be conducted throughout the manufacturing process, within pre-defined

error bounds and a detailed record of every test automatically generated and stored digitally. This conveniently avoids the many human related issues of manual testing (human dexterity, fatigue, operator variability etc.), whilst simultaneously creating a superior quality control process [Zimmer et al., 2010].

The introduction of automated testing allowed for far more detailed ultrasonic maps to be generated. These advances ranged from more detailed data presentation (B-scan, C-scan, D-scan) to more advanced testing hardware (phased array and full matrix capture), to digital image enhancement techniques (total focussing method - TFM, synthetic aperture focussing technique – SAFT, common source method – CSM). The combination of these advances in testing procedures coupled with the systematic and comparable testing made throughout the manufacturing process allow for detailed insights to be generated as standard practice, which would simply have been unimaginable in the recent past [Zimmer et al., 2010]. This allows for more certainty in material testing and ultimately, more confidence in the capability of advanced components. The combined improvements led to a reduction in rotor forging detection size capabilities from the equivalent of a 5 mm flat bottomed hole (FBH) to one of 0.7 mm [Vrana et al., 2016].

The fundamental elements determining the ultrasonic process are based on the selection of ultrasonic transducer. The frequency associated with the standard ultrasonic transducer is determined by the piezoelectric element, which converts an electric current into an ultrasonic pulse by the way of physical displacement. Other than the standard technique it is possible to generate ultrasonic signals using lasers, EMAT probes, immersion baths and phased array. Although the capabilities of these technologies are now widely accepted the overall benefit over conventional techniques were not quite as clear-cut earlier [McNab and

Campbell, 1987], generally the biggest advances for all of these methods are cost and computing power improvements. This cost/benefit improvement then resulted in initially marginal techniques becoming widely accepted for a range of applications in the NDT community.

As a generalisation direct contact techniques are the simplest to carry out and cheapest technique to use. The different techniques in fact only change the initial generation of the pulse and do not alter the propagation of the waves within the testing media. They can however, allow for the interaction of several generated pulses with one another in a controlled manner. These “controlled interactions” are the essence on which the phased array is built (and full matrix capture technique being similar). The core principle is for multiple signals to be generated from individual elements, which are delayed from one another to account for the longer propagation distance. The end result being these multiple signals will then converge perfectly on a given position within the sample, allowing for far better resolution than would otherwise be achievable through conventional testing techniques. The equipment required in order to generate and control these perfectly timed pulses means this technique is more expensive and involves extra layers of complexity. Conversely, it does also allow for enhanced resolution at controllable depths of the sample. This ability is itself invaluable in many flaw detection scenarios, particularly where specific regions are more critical than others.

The coupling procedure seems like the most basic and unglamorous element of ultrasonic testing, but even this has undergone changes. Due to environmental considerations [Zimmer et al., 2010], oil is no longer used as the primary couplant being replaced by water coupling. Ultimately it makes little difference which medium is used as a couplant as long as

it adequately displaces any air boundary which limits transmission of ultrasonic signal into the test medium [Nde-ed].

The above introduction is a summary of the advances in industrial ultrasonic testing procedures as applied predominantly to heavy rotor forgings in the power generation industry. The subsequent sections of this chapter will cover in greater detail some of the more relevant aspects to this work and then focus more specifically on the scattered ultrasonic signal as caused by microstructural interactions.

3.1.2. Coupling

Similarly to conventional direct contact testing, phased array and full matrix capture techniques also require a direct physical contact with the sample being tested. This is facilitated by the use of a coupling agent, which is usually some form of water-based solution. The importance of any particular coupling agent is for the solution to be readily applicable between the testing area and the transducer and it must remove any potential air barriers between the two media. Any significant air barrier between the transducer and the sample presents a major problem for the transfer of ultrasonic energy, as virtually all of the incident energy is internally reflected at the boundary due to the impedance mismatch. However Figure 3.1 does also show that even good couplants lose the majority of signal at the interface (explicit calculations made as part of chapter 5), although this should not be considered a problem.

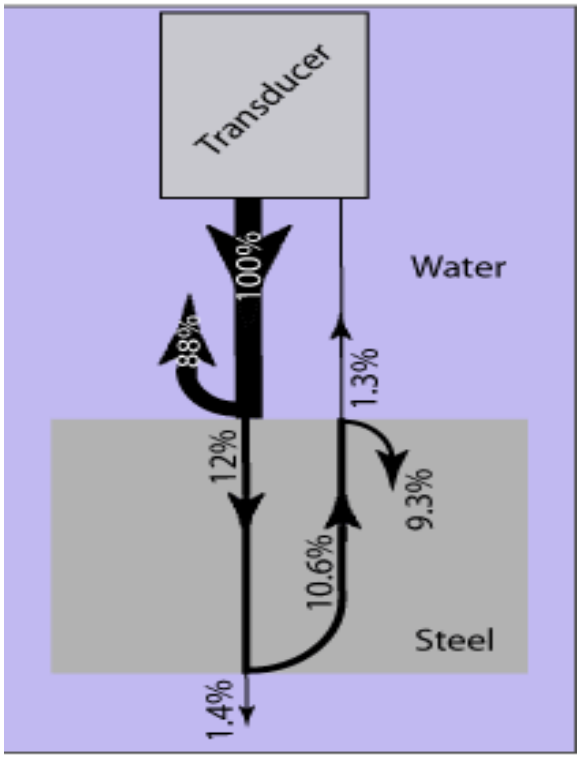

Figure 3.1: Diagram indicating the energy transmitted/ losses during UT inspection of steel. From [El-Ali, 2011]

Figure 3.1 is a schematic representation of the drastic signal losses which can occur during the detection process. The vast majority of the transmitted energy never enters the intended testing material and significantly less returns. The amount of energy lost in the initial phase, between the transducer and the initial material interface, although large, is similar across couplant types. A study [Dugmore et al., 2002] did consider variation across a range of common couplants used for composite structures where “settling time” was considered, the time to wait until maximum signal amplitude was reached, which could lead to variation across couplant types. The conclusion was that glycerine (a common couplant also for steels) required no settling time and exhibited the least variation over multiple tests, but other types did benefit from a settling time period. Ultimately, the amount of transmitted signal is dependent on the acoustic impedance mismatch between the coupling agent and the test specimen and so consistency should be maintained, which could include a settling period if appropriate.

A further important consideration is the coupling layer thickness, as a thin enough layer would show no reflection of the ultrasonic wave; this concept is explored in [Krautkramer and Krautkramer, 1990]. They describe how even a thin layer of air, which essentially allows for no ultrasonic wave propagation, can have no influence with a small enough boundary layer (Figure 3.2).

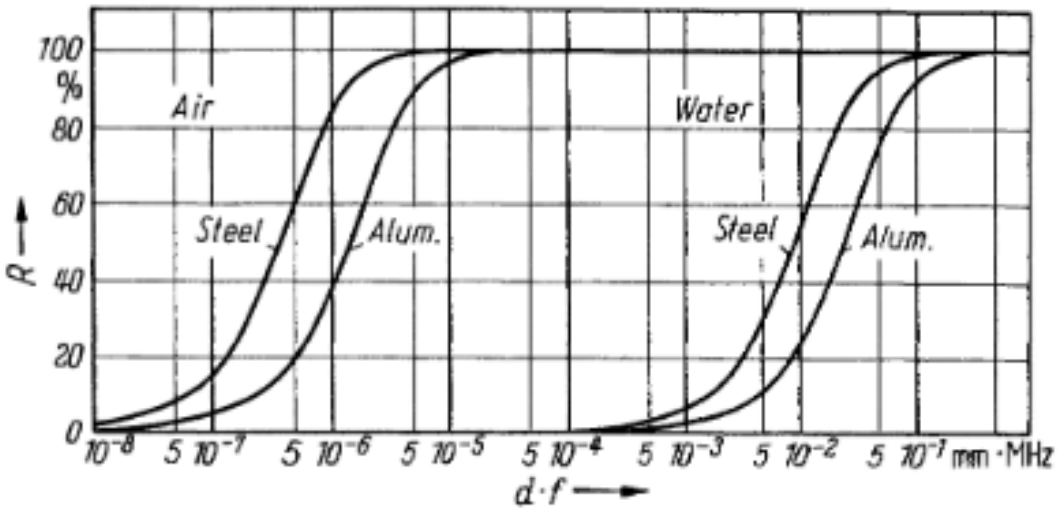

Figure 3.2: A chart taken from [Krautkramer and Krautkramer, 1990] showing the drop off in reflection coefficient with layer thickness for steel and aluminium in both water and air.

R is equal to the proportion of the maximum reflected signal, i.e. waters reflection coefficient (relative to steel) of 0.88 (88 %) would be equivalent to an R of 100 %, any reduction of this R number would be relative to this maximum. Therefor an R value of 50 % would reduce this value to 0.44 (44 %). This is the primary reason why the ultrasonic signal reflection of a coupling medium is not typically discussed, as the small layer thickness minimises this influence. Note a typical couplant should be roughly equivalent to the water curve in Figure 3.2. The units of the x – axis (layer thickness multiplied by frequency) are used to standardise the results across ultrasonic frequencies, therefore representing all the data in only one chart.

The equation used to calculate these curves [Clark and Chaskelis, 1981] is provided by equation 3.1:

$$R = \frac{\frac{1}{4}\left(r - \frac{1}{r}\right)^2 sin^2 kd}{1 + \frac{1}{4}\left(r - \frac{1}{r}\right)^2 sin^2 kd} \tag{3.1}$$

Note the result will be in the form of a decimal rather than a percentage. Here $r = \frac{Z_l}{Z_m}$, with Z_l being the acoustic impedance of the layer (such as water or air) and Z_m the acoustic impedance of the bounding media (such as steel); the mathematical definition of acoustic impedance is provided in equation 3.2. K corresponds to the acoustic wavenumber within the layer, as defined in equation 3.3. v is the wave velocity, d is the layer's thickness, ρ is the density, and λ the wavelength.

$$z = \rho v \tag{3.2}$$

$$k = \frac{2\pi}{\lambda} \tag{3.3}$$

This is valid for an ultrasonic wave at normal incidence to a semi-infinite boundary layer relative to the ultrasonic wavelength within the bounding medium (meaning the layer is of effectively infinite length and width but of limited thickness).

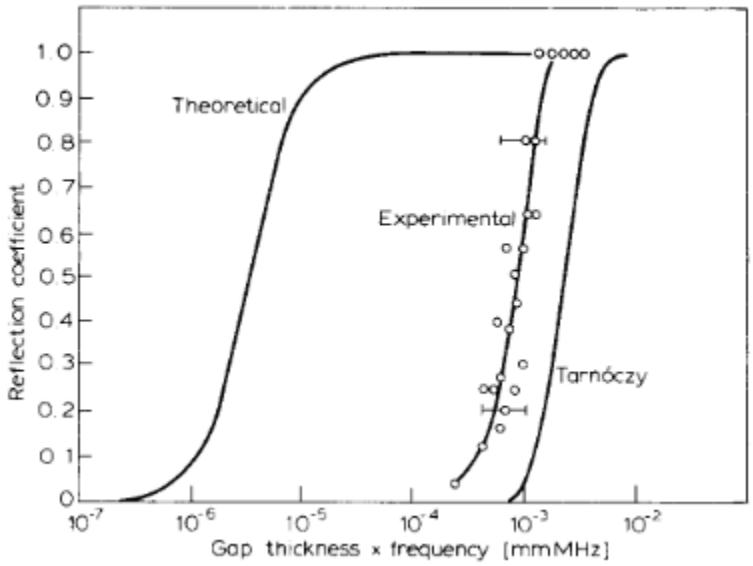

Figure 3.3: Comparing theoretical predictions with experimental values of the reflection coefficient for an air gap measured at 2.5 MHz [Clark and Chaskelis, 1982; Tarndczy, 1956]

[Szilard, 1963] suggested reasons for the discrepancy between the theoretical and experimental results (Figure 3.3) such as the application of acoustic theory being inappropriate for such small gaps and the expectation of non-linear effects, however these were subsequently deemed to not have significant influence [Clark and Chaskelis, 1981; Gustafson, 1978]. A further study [Clark and Chaskelis, 1982] provides reasons for the experimental results to significantly differ from the theoretical prediction of equation 3.1; the main conclusion being dirt in the boundary layer. More micro-bridges than expected and intermolecular forces were also considered but deemed not significant. Any matter present within the boundary gap layer, would have significantly closer density to the main media (steel or aluminium) than that of water or air. As a result the curves would shift from left to right, just as the curve for water has relative to air in Figure 3.2, and so account for the experimentally observed deviation from theoretical predictions.

3.1.3. Signal-to-noise

An estimate of the quality of a signal within a particular experimental setup, which is often used in industry, is known as the signal-to-noise ratio. Here any spurious, undesired signals are grouped together by the term “noise”, which itself can be the source of valuable additional information such as is used in ultrasonic backscatter [Huang et al., 2019; Kube et al., 2018].

Ultrasonic noise can generally be split into two core aspects of the total “noise”; these are material-based sources and beam related sources. These two categories are represented by the following equation [nde-ed]:

$$\frac{S}{N} = \sqrt{\frac{16}{\rho \cdot v \cdot w_x \cdot w_y \cdot \Delta t}} \cdot \frac{A(f_0)}{FOM(f_0)} \tag{3.4}$$

The signal to noise ratio $\left(\frac{S}{N}\right)$ is therefore inversely proportional to the square root of the density of the material (ρ), the velocity of the wave propagating through the material (v), the lateral beam width at the point of the flaw in the x and y directions respectively $\left(w_x \cdot w_y\right)$ and the pulse width (Δt). Additionally, it is dependent on the ratio of the amplitude $\left(A(f_0)\right)$ and the Figure of merit $\left(FOM(f_0)\right)$, using the centre frequency of the pulse at the point of the flaw. As the test material and the ultrasonic testing equipment typically cannot be altered at the point of testing, signal to noise ratios are improved by maximising the signal amplitude, such as by using sufficient and appropriate couplant or achieving normal incidence reflection. Another possibility is to reduce the lateral beam width (i.e. beam spread) by using an increased frequency or to reduce the pulse width which is typically a variable setting on ultrasonic testing equipment.

3.1.4. Minimum detectable defect size

As discussed in chapter 2 the core element of the ultrasonic testing process is the identification and sizing of defects. But this is not a foregone conclusion, as the ultrasonic detectability varies between materials, component size and shape, and so the ultrasonic test frequency (by this we typically mean the centre frequency of the generated pulse) must be tailored to the ultimate testing requirements. This is illustrated by Figures 3.4 and 3.5, where trial rotor forgings as part of the COST FB2 development program are compared by manufacturer and melting process. Here the minimum detectable defect size varies with segment dimensions and melting process, but no process appears superior across all individual sections. A defect is only observable as a distinct feature if it is of a sufficient size large enough to reflect a detectable portion of the ultrasonic signal, as well as satisfying the signal-to-noise requirements. Therefore the cleanness of the melting process is an important consideration and the reason for testing different techniques for the trial rotor forgings.

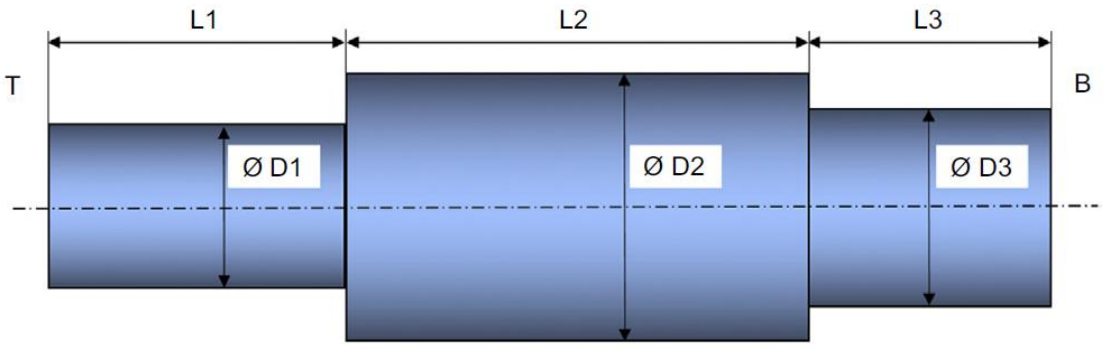

Figure 3.4: Example diagram of trial forgings used in the development of FB2. [Zeiler, 2017]

Manufacturer	Melting process	D1 (mm)	D2 (mm)	D3 (mm)	L1 (mm)	L2 (mm)	L3 (mm)	MDDS (mm) D1/D2/D3
Bohler Kapfenberg (Austria)	BEST	770	1180	865	1350	930	1110	1.2/1.8/1.3
Societa delle Fucine Terni (Italy)	EAF/VCD	925	1110	790	800	2750	830	1.0/1.5/1.5
Saarschmiede Voelklingen (Germany)	ESR	800	1215	1050	1085	2130	800	1.5/2.0/1.7

MDDS, minimal detectable defect size

Figure 3.5: Summary of the dimensions and minimum detectable defect size (MDDS) of COST FB2 trial rotor forging by different manufacturers and melting processes [Zeiler, 2017].

The limitation of discontinuity detection of ultrasonic inspection is known as the minimum detectable defect size (mdds). The mdds is proportional to the wavelength. A smaller wavelength, that is a higher frequency, allows for smaller defect resolution capabilities. However, this brings with it penetration depth issues, as the greater scatter, which allows for better resolution of the defect, applies to all scattering boundaries therefore leading to increased signal loss (attenuation) overall. So the frequency selection is critical in order to balance the resolution with volume inspection requirements. This is due to the two facets of ultrasonic testing being fundamentally opposed to one another; in order to improve resolution the frequency should be increased, but to improve signal penetration in large components frequency should be decreased. The exact dependency is determined by the scattering regime within which the interactions take place; these shall be introduced in a subsequent section. This dilemma, of balancing resolution with penetration depth, is a fundamental attribute of ultrasonic testing which has determined the ideal frequency selection for many ultrasonic testing practices. Whilst this fundamental truth of ultrasonic testing will always be present some of the new testing techniques, as discussed at the start

of this chapter, offer a potential mitigation of the problem. They all essentially work by either improving the signal at a given point or reducing the noise, thereby improving the signal-to-noise ratio and achieving impressive results in flaw detection capabilities.

Table 3.1: Table indicating the minimum detectable defect size (mdds) in millimetres varying by transducer frequency in MHz. Author calculated, based on expected detection of a defect of half the ultrasonic wavelength.

Transducer frequency	Minimum detectable defect size (mdds)
2 MHz	1.5 mm
5 MHz	0.6 mm
10 MHz	0.3 mm

As a rule of thumb, it is typically said defects of half wavelength are distinguishable, as this relates to a common resolution limit (known as the Rayleigh diffraction limit). However, it is possible to detect defects below this point, such as [Huang et al., 2019] using enhanced techniques to reliably find defects of 0.305 the size of the wavelength in the difficult to detect near-surface region.

3.1.5. Beam refracting

A propagating ultrasonic signal can deviate from the expected propagation path within the test sample, known as beam refracting. This results in a potential for lower signal strength at a specific test location within the sample. This phenomenon can have a range of potential causes and indeed consequences. The most obvious consequence is the reduction in the overall signal strength at a given location, and hence the reduced signal-to-noise ratio, potentially leading to indistinguishable signals from the background noise. If beam refracting is significant and is not accounted for it can also lead to a perceived lack of signal

due to the receiving transducer simply being positioned in an unsuitable location, with poor locating or sizing of defects as a potential consequence [Nowers et al., 2016].

Beam refracting is typically attributed to material microstructure. The microstructure allows for a preferential propagation path which deviates from the neutral route. This could be caused by texture or microstructural inhomogeneity, and can range from barely detectable to extremely problematic scenarios, although typically a large grain size would be required. The degree to which beam refracting influences the propagation path is largely dependent on whether the features cancel one another out on aggregate or reinforce the effect. For a sufficiently large testing medium, with an approximately random distribution of microstructural features, the overall influence will essentially be negligible, even though it will undoubtedly occur on a local scale. These local scale influences form a major part of the contributions to the work in subsequent chapters, although it should be noted that large beam refracting issues across the bulk of a component are not of particular interest here.

3.2. Ultrasonic waves

3.2.1. Ultrasonic wave velocities

There are several important physical differences between longitudinal and transverse waves, the two main wave-modes in conventional ultrasonic testing. Firstly, the displacement of the propagating wave is in the direction of travel for a longitudinal wave mode, whereas it is perpendicular to the propagating direction for transverse waves. As a consequence of their displacement characteristics, transverse waves can be polarised whereas longitudinal waves cannot. It is also important to note that longitudinal waves have an ultrasonic velocity roughly double that of transverse waves. Therefore, propagating waves originating at roughly the same position will overlap at approximately every other

longitudinal reflection (or every transverse reflection). This phenomenon could potentially prove problematic when measuring reflected signals, as is the case in this work, and so experimental work should bear this in mind.

Longitudinal wave velocity is defined by:

$$V_l = \sqrt{\frac{E(1-\mu)}{\rho(1+\mu)(1-2\mu)}} \tag{3.5}$$

And similarly the transverse wave equation is determined by:

$$V_t = \sqrt{\frac{E}{2\rho(1+\mu)}} \tag{3.6}$$

Where E is the Young's modulus of the material, ρ is the material density and μ represents Poisson's ratio. V_l and V_t are the longitudinal and transverse wave velocities.

The wave equation, which is the foundation of waves in classical physics, is a second order partial differential equation and the general form in one space dimension is

$$\frac{\partial^2 u}{\partial t^2} = c^2 \frac{\partial^2 u}{\partial x^2} \tag{3.7}$$

If the medium considered is isotropic the equation of motion of a propagating elastic wave in three dimensions can be represented as

$$\rho \frac{\partial^2 u_1}{\partial t^2} = \left(\frac{E\mu}{(1+\mu)(1-2\mu)} + \frac{E}{2(1+\mu)}\right) \frac{\partial}{\partial x_1}\left(\frac{\partial u_1}{\partial x_1} + \frac{\partial u_2}{\partial x_2} + \frac{\partial u_3}{\partial x_3}\right) + \frac{E}{2(1+\mu)}\left(\frac{\partial^2 u_1}{\partial {x_1}^2} + \frac{\partial^2 u_1}{\partial {x_2}^2} + \frac{\partial^2 u_1}{\partial {x_3}^2}\right) \tag{3.8}$$

$$\rho \frac{\partial^2 u_2}{\partial t^2} = \left(\frac{E\mu}{(1+\mu)(1-2\mu)} + \frac{E}{2(1+\mu)}\right) \frac{\partial}{\partial x_2}\left(\frac{\partial u_1}{\partial x_1} + \frac{\partial u_2}{\partial x_2} + \frac{\partial u_3}{\partial x_3}\right) + \frac{E}{2(1+\mu)}\left(\frac{\partial^2 u_2}{\partial {x_1}^2} + \frac{\partial^2 u_2}{\partial {x_2}^2} + \frac{\partial^2 u_2}{\partial {x_3}^2}\right) \tag{3.9}$$

$$\rho \frac{\partial^2 u_3}{\partial t^2} = \left(\frac{E\mu}{(1+\mu)(1-2\mu)} + \frac{E}{2(1+\mu)}\right) \frac{\partial}{\partial x_3}\left(\frac{\partial u_1}{\partial x_1} + \frac{\partial u_2}{\partial x_2} + \frac{\partial u_3}{\partial x_3}\right) + \frac{E}{2(1+\mu)}\left(\frac{\partial^2 u_3}{\partial {x_1}^2} + \frac{\partial^2 u_3}{\partial {x_2}^2} + \frac{\partial^2 u_3}{\partial {x_3}^2}\right) \tag{3.10}$$

The constants $\frac{E\mu}{(1+\mu)(1-2\mu)}$ and $\frac{E}{2(1+\mu)}$ are also known as Lamé constants and are sometimes abbreviated for convenience (as λ and μ respectively). By using the Helmholtz decomposition, taking the divergence and curl of equations 3.8 - 3.10, the longitudinal and transverse wave velocities (equations 3.5 and 3.6) are found from equations 3.11 and 3.12; the full derivation of which can be found in [Connolly, 2009]. Equations 3.11 and 3.12 are the two wavefield potentials, with the scalar function Θ representing the longitudinal wave and the vector function $\boldsymbol{\Psi}$ representing the transverse wave. (Note the constants λ and μ in equations 3.11 and 3.12 are Lamé constants in the abbreviated form)

$$\nabla^2\Theta = \frac{\rho}{\lambda+2\mu}\frac{\partial^2\Theta}{\partial t^2} \tag{3.11}$$

$$\nabla^2\boldsymbol{\Psi} = \frac{\rho}{\mu}\frac{\partial^2\boldsymbol{\Psi}}{\partial t^2} \tag{3.12}$$

As is evident from equations 3.5 and 3.6, the wave velocity is merely a function of the wave type and the material characteristics (in a non-dispersive medium). These properties are assumed isotropic when calculating velocity of a bulk medium, although there is often a significant amount of insight to be gained from the anisotropy [Davis et al., 2008; Wiskel et al., 2016]. For this reason the time until the signal is detected is an accurate method to approximate propagation distance and forms the basis of many practical applications, one such method is time - of - flight diffraction (TOFD) which is considered a sensitive and reliable method in determining crack depth [Silk and Lidington, 1975; Charlesworth and Temple, 2001].

3.2.2. Wave/boundary interaction

The transducers used as part of a pulse echo setup mainly generate longitudinal rather than transverse waves; however they can be subsequently converted (from longitudinal to transverse) given the right circumstance. Transverse waves can be generated at any interface encountered during propagation by a process known as mode conversion. Transverse wave ultrasonic probes can also be used and are formed by changing the alignment of the piezoelectric element and do not necessitate a mode conversion step.

As the waveform is not restricted as it propagates through a given medium it is important to define the terms by which mode conversion takes place. Mode conversion can only occur at a boundary, such as the transducer/sample interface or any subsequent boundary which delineates a change in acoustic properties. The number of scattering sites considered is a point of approximation in some scattering models, although not all [Bai et al., 2018]; this is based on the Born approximation being used to consider only first order scattering events and so simplify the calculation. The first order Born approximation is only valid for weak scattering materials, however any number of terms of the Born expansion can be used with the n+1th term representing the nth scattering event [Blugel, 2012].

In order to account for mode conversion occurrence at interface boundaries it is necessary to understand general wave interaction at the interface. Accounting for the three potential incident waves (longitudinal and both transverse waves) at the boundary between two media with distinct acoustic properties, there is a possible total of twelve waves at the interface; the general diagram of a 12-point interface is included in Figure 3.6. It is important to note that of the twelve identified waves at the interface, some of these waves would be eliminated as they would not be valid options as highlighted in Figure 3.7. Detailed

analytical calculation can be found elsewhere [Connolly, 2009]; here the Snell constant is a shared characteristic between all of the waves at the interface. Phase vectors can be calculated from the slowness vectors which intersect the slowness surface.

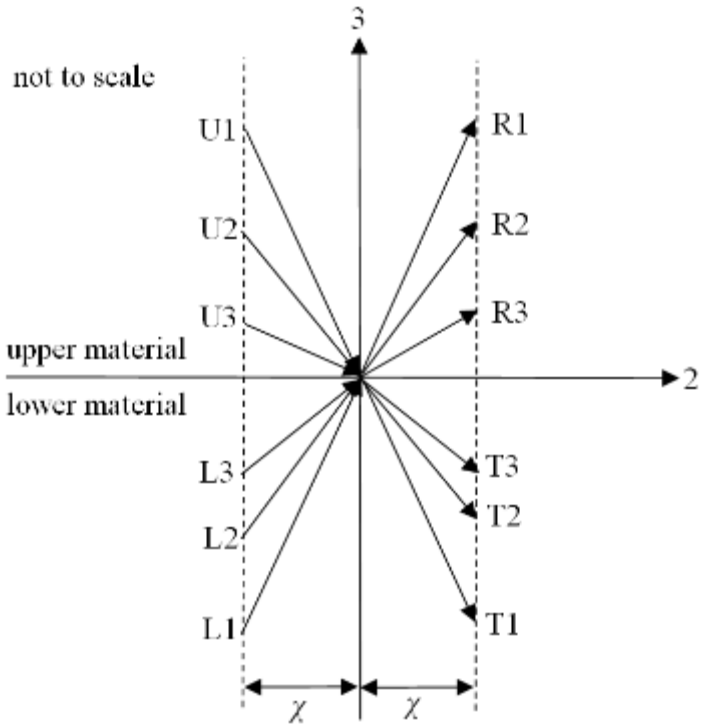

Figure 3.6: Diagram depicting a general 12-point interface of six incident and six scattered waves. The letter χ represents the Snell constant which each wave at the interface share. [Connolly, 2009]

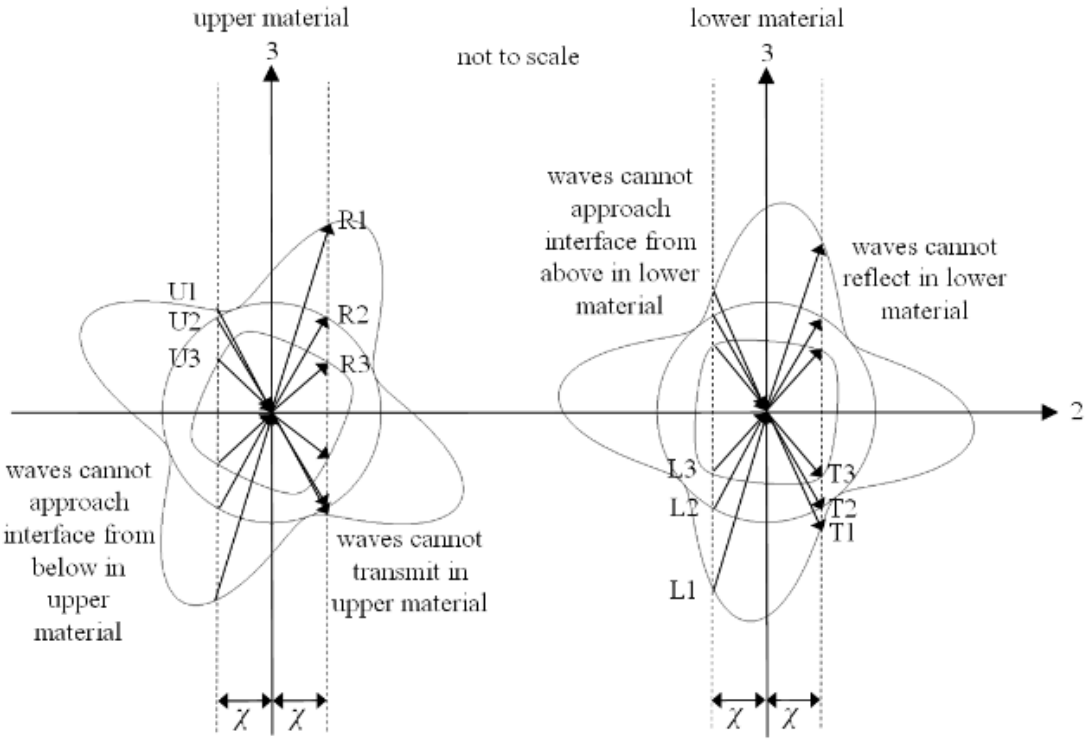

Figure 3.7: Diagram of the general 12-point interface with invalid options indicated. The slowness surface is included to highlight the origin of the Snell constant χ. [Connolly, 2009]

For some readers a more intuitive representation of Snell's law is presented in Figure 3.8. It is important to note the fixed nature of each boundary interaction. Snell's law dictates the angle of either reflection or refraction based on the velocity and type of wave at the interface. As discussed above the velocity of either a longitudinal or transverse wave is determined by the properties of the media in which it travels, the exact nature of the boundary wave interaction is determined by the acoustic properties of the media forming the interface itself. The result of the boundary interaction is determined by all scattered waves valid under Snell's law.

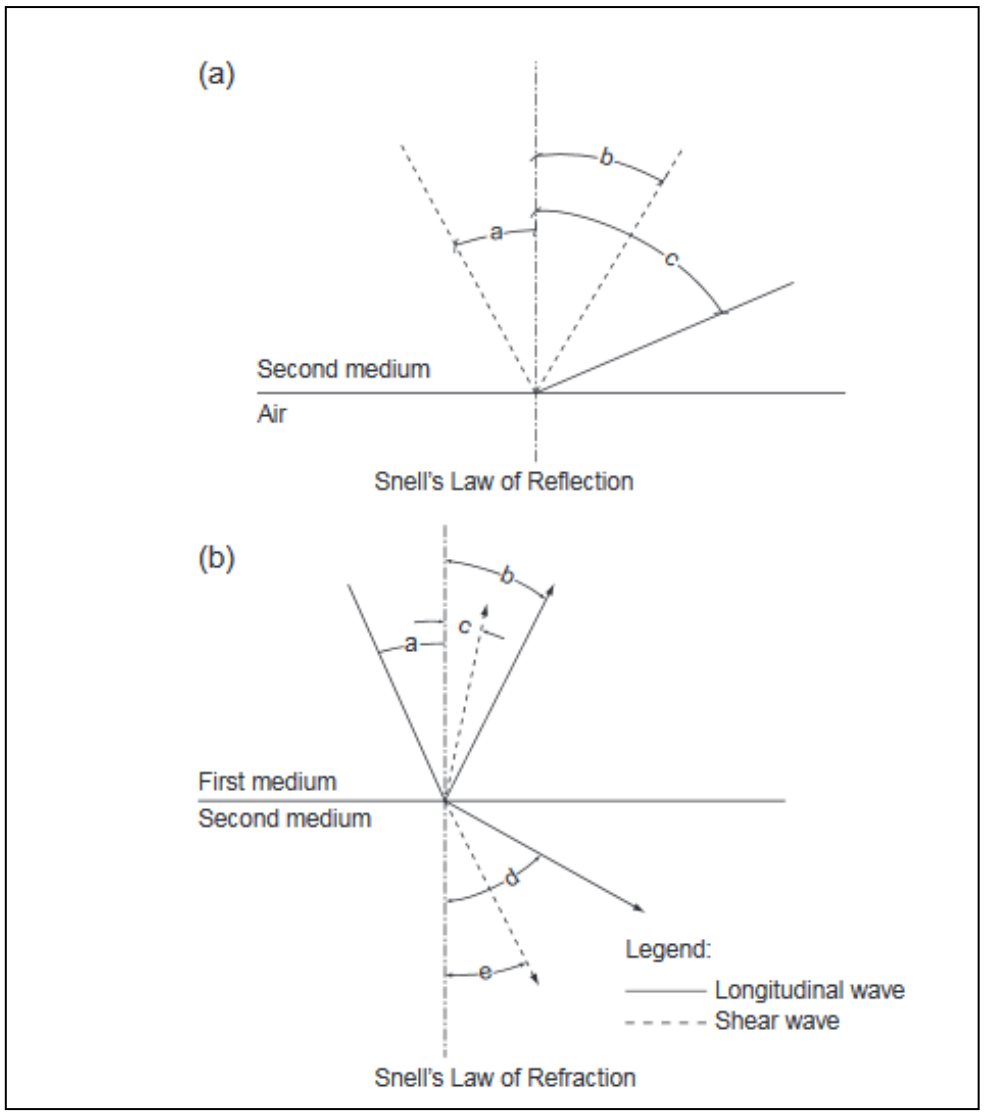

Figure 3.8: (a) shows a boundary with air; here the entire signal is reflected internally. (b) shows a boundary with more balanced physical properties on either side of the interface, this leads to partial internal reflection as well as refraction into the second medium. From [Singh, 2016]

Figure 3.8 illustrates the potential situations which can arise during boundary interactions. The exact situation is determined by the properties of the second medium relative to the first, the specifics are determined in Snell's law via the velocity and incidence angle, as in equation 3.13. Here the ratio between the sine of the angle of the incident wave, θ_1, and the sine of the scattered wave, θ_2, is equal to the ratio of their respective velocities, V_1 and V_2.

$$\frac{Sin\ \theta_1}{V_1} = \frac{Sin\ \theta_2}{V_2} \tag{3.13}$$

When an interface consists of a higher to lower acoustic impedance medium a critical angle exists. This critical angle is the minimum angle where total internal reflection occurs. Just as with reflection, transmission and mode conversion the specific angle depends on the acoustic impedance mismatch at the interface. Detailed example calculations for all potential scenarios are available to further aid understanding or specific calculations [Krautkramer and Krautkramer, 1990].

3.2.3. Signal losses and attenuation

Attenuation is the measure of amplitude loss of the pulse over time and propagation distance. There are many mechanisms by which the energy is no longer contained within the measurable pulse itself, and so the various causes are required to be considered independently from one another. In its simplest form ultrasonic wave propagation can be reduced to an oscillating system, formed by the sequence of oscillating atoms which allow the energy of the wave to be transferred along the direction of propagation. Attenuation would correspond to the damping term involved in this propagating wave.

Beam spread is the distribution of signal over an area of increasing radius with propagation distance. As the signal originates and culminates in the same area, that of the pulse-echo transducer surface plate, any signal which falls beyond these boundaries are, for all intents and purposes, lost. However, this lost signal is a natural component of ultrasonic testing and so must be taken into account when measuring the specific losses attributable to microstructural interactions.

There are many factors which determine the ultimate signal strength at any given point, [Goni and Rousseau, 2014] distil this into the following equations (3.14-3.16) and illustrated

in Figure 3.9. These equations quite simply establish every contribution to the reduction of the original ultrasonic signal, and so provide a real foundation to base any attenuation calculations on.

$$V'_0 = V_0 R_A D(S'_0) \tag{3.14}$$

$$V_1 = V_0 T^2{}_A R_B D(S_1) \exp(-2h\alpha) \tag{3.15}$$

$$V_2 = V_0 T^2{}_A R^2{}_B R_A D(S_2) \exp(-4h\alpha) \tag{3.16}$$

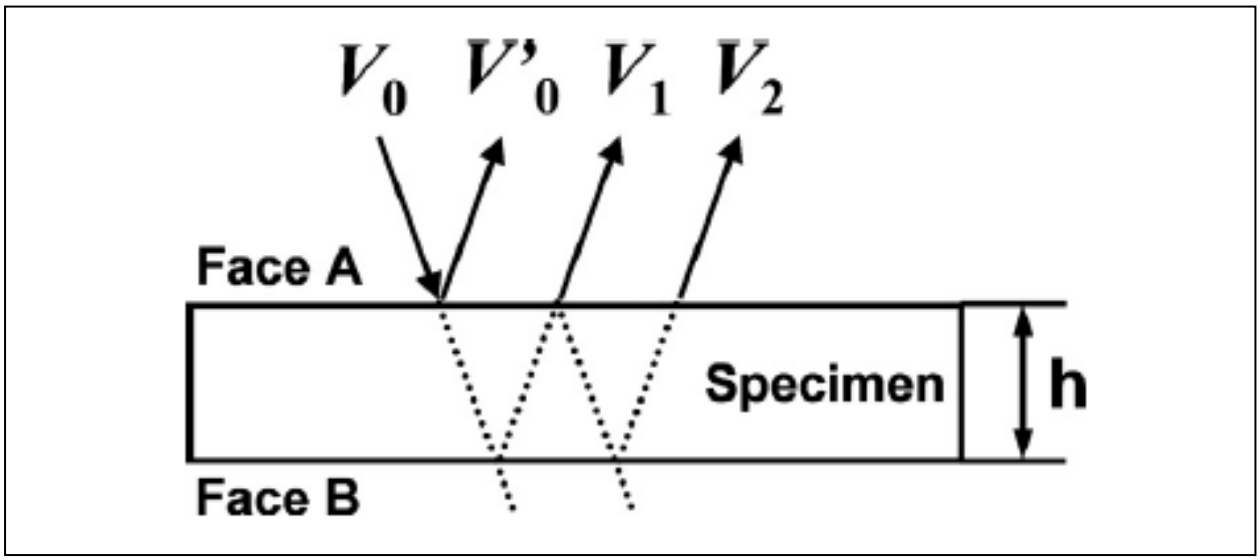

Figure 3.9: Image identifying the origins of equations 3.14-3.16. [Goni and Rousseau, 2014]

Where V_0 is the original signal amplitude; V'_0,V_1, V_2 are front-wall echo, 1st and 2nd back-wall echoes respectively. R corresponds to the proportion of the signal which is reflected from the various faces (the intensity reflection coefficient), and so conversely T is the proportion of the signal which is allowed through (the intensity transmission coefficient), as they are related by equation 3.17.

$$R^2 = 1 - T^2 \tag{3.17}$$

Here it is assumed that the entire signal is either reflected or transmitted, with no losses as part of the process. $D(S)$ relates to the beam spread estimation as calculated in [Rogers and Van Buren, 1974]. The equation estimates the proportion of the original signal which remains within the confines of the transducer radius (determined by the exposed area of the piezoelectric element); any signal outside of this hypothetical region is considered lost signal as there is no possibility to detect the signal spread outside of the transducer radius directly.

$$D(s) = \sqrt{\left[\cos\left(\frac{2\pi}{s}\right) - J_0\left(\frac{2\pi}{s}\right)\right]^2 + \left[\sin\left(\frac{2\pi}{s}\right) - J_1\left(\frac{2\pi}{s}\right)\right]^2} \tag{3.18}$$

Where

$$S(n) = \frac{2nh\lambda_s}{a^2} \tag{3.19}$$

This equation is written in a format in order to estimate the relevant proportion of signal at the nth back-wall reflection. As a result the values of s, which are used as inputs into equation 3.18, follow a regular pattern, which correspond to each back-wall echo rather than some point in between. Equation 3.19 depends only on the sample height (h), the wavelength within the sample (λ_s) and the transducer radius (a), so maintaining a degree of consistency between tests results in the only factor to consider being the back-wall reflection number applicable to the calculation.

Equation 3.18, the beam spread correction factor, is made up of a series of periodic functions which are offset from one another. In the equation J_0 and J_1correspond to Bessel

functions of the first kind of 0^{th} and 1^{st} order respectively. These Bessel functions are essentially tapering off trigonometric functions and so, depending on the input value s, the combination of periodic functions lead to counterintuitive results. Figure 3.10 shows a graph of the results as calculated by [Rogers and Buren, 1974]; here the same trend is shown as predicted by the equation. This is entirely expected as it coincides with the inconsistencies of the near field region. This is easily explained with the Huygens-Fresnel principle, which considers a wavefront to be the product of multiple spherical waves of the wavefront at a previous instance [Huygens' principle, Mathpages.com]. Fresnel elaborated on Huygens' principle by suggesting the amplitude of the wave would be provided by the summation of all secondary waves at that point. The resulting interference pattern explains the undulating nature of the wave amplitude and why it effectively disappears after a given propagation distance. This initial phase is known as the near-field region (or sometimes Fresnel region) and the second more stable part is known as the far-field region (or Fraunhofer region).

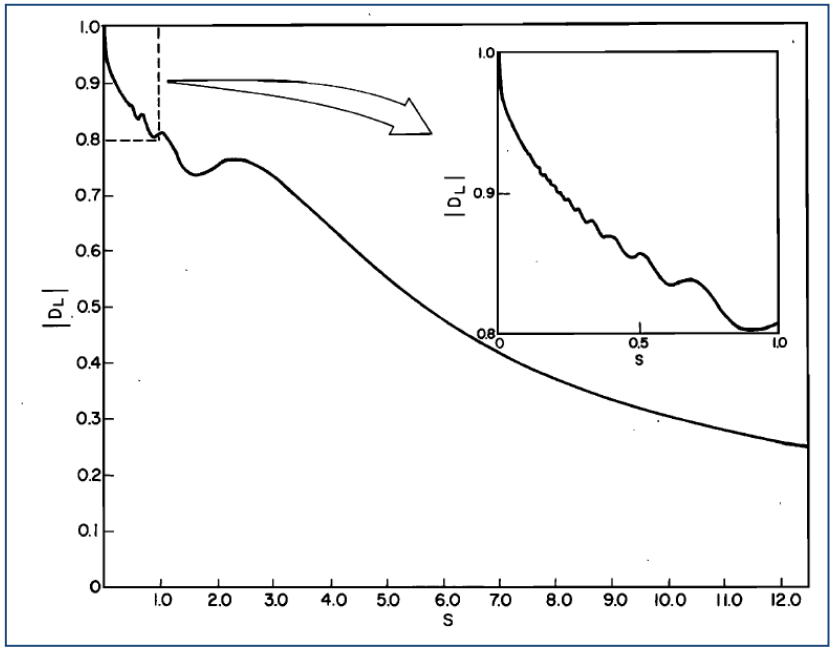

Figure 3.10: Graph of calculated results of eq 3.18 [Rogers and Van Buren, 1974], indicating the interference pattern of the near-field region and the subsequent stability of the far-field region.

The beam deviation correction is only one aspect of the attenuation calculation, and so in order to calculate the attenuation, manipulation of equations 3.15 and 3.16 (or any other sequential equations) is required. Dividing equation 3.16 by equation 3.15 and rearranging for attenuation leads to:

$$\alpha = \frac{1}{2h} \ln \left[\frac{V_1}{V_2} R_A R_B \frac{D(S_2)}{D(S_1)} \right] \tag{3.20}$$

Equation 3.20 presents the attenuation coefficient with a correction term for the reflection at both surfaces of the test piece and a correction term for the beam deviation. By applying these corrections, the known elements which affect signal amplitude are removed from the calculation and so will not skew the results. The reflection terms are typically only relevant for immersion testing techniques or other such scenarios with large signal loss at the sample interface. For typical contact testing this aspect is largely deemed insignificant, for the reasons described in the section on couplant.

3.2.4. Frequency dependence

Given the frequency dependence of attenuation [He and Zheng, 2001], a natural spread of attenuation of different frequency components around that of the centre frequency occurs. Therefore neglecting to consider the superimposed nature of waves, which constitute an ultrasonic pulse [Povey, 1997], leads to a limited understanding of the fuller picture of experimental results. As shall be elaborated on in section 3.3, the scatter of a propagating ultrasonic wave is frequency dependent and is categorised into distinct scattering regimes. Therefore, for a given size scattering centre, a higher frequency wave would have a larger degree of scatter than that of a smaller frequency. As the propagating wavefront

encounters a great number of scattering centres in polycrystalline materials, the ultrasonic pulse becomes increasingly distorted with propagation distance (as illustrated in Figure 3.11). Figure 3.11 is produced from a simulated pulse propagating in an 8.33 mm Plexiglas sample with the resultant echoes depicted in figure 3.12. Details of the precise methodology used can be found in the original paper [Zhao et al., 2005].

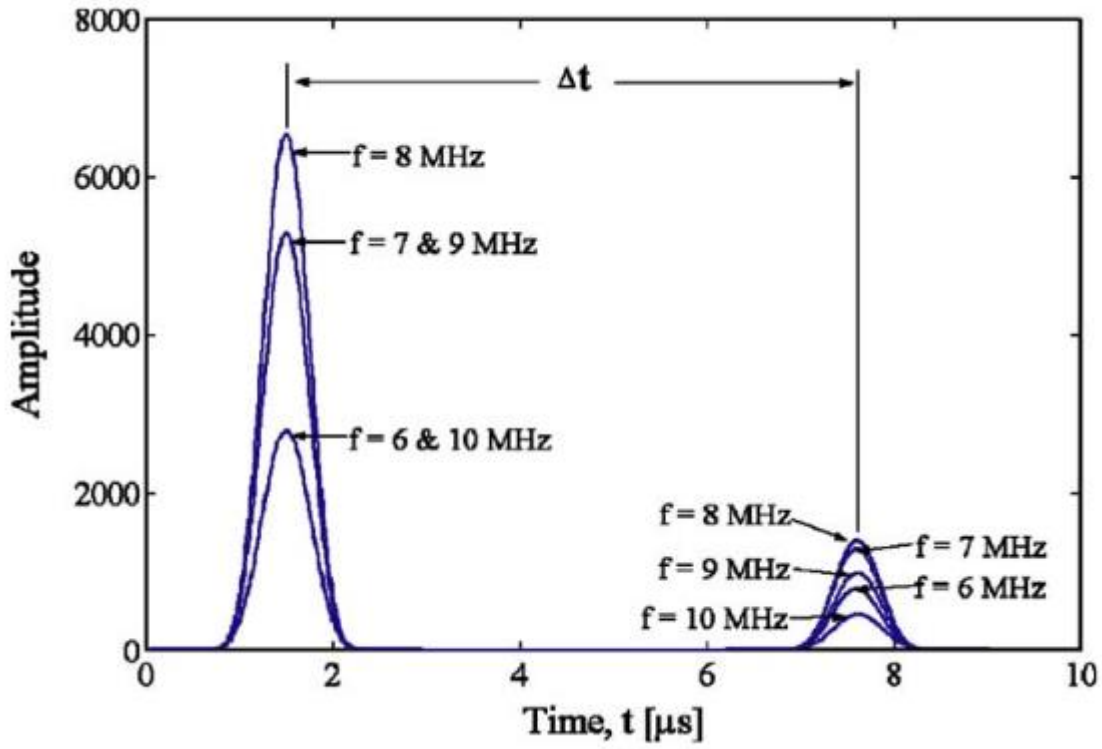

Figure 3.11: Indication of the shift in centre frequency with propagation distance; the wave's amplitudes are no longer symmetric around the (original) centre frequency [Zhao et al., 2005]

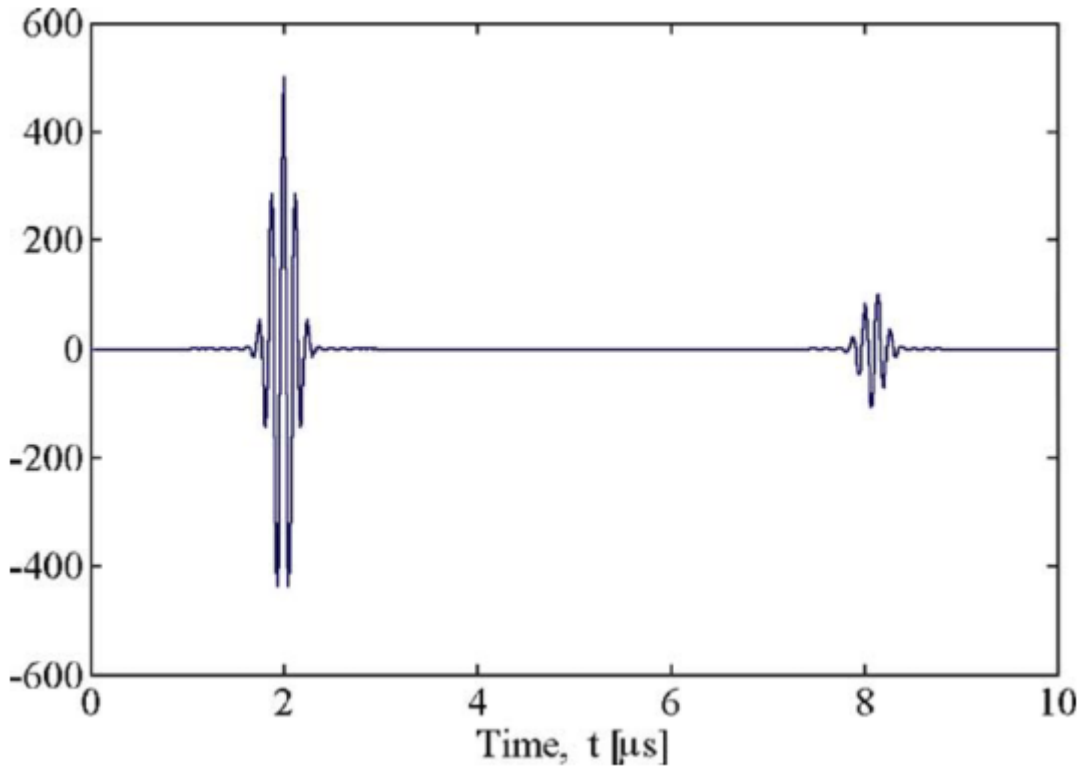

Figure 3.12: Simulated echoes of a propagating pulse in an 8.33 mm Plexiglas sample used to show the asymmetric propagation of different frequency components in figure 3.11 [Zhao et al., 2005]

Previous work [He, 1999; He and Zheng, 2001] has shown the frequency dependence of attenuation and phase velocity to be:

$$c_i = c_0 + f \cdot \left(\frac{dc}{df}\right) \tag{3.21}$$

$$\alpha_i = \alpha_0 + f \cdot \left(\frac{d\alpha}{df}\right) \tag{3.22}$$

Where c_i is the phase velocity, α_i is the attenuation coefficient.

This frequency dependent view of the pulse is achieved by applying a Fourier transformation to the signal. The signal's Fourier transform results in amplitude spectra, which can then be compared for two pulses in order to calculate the attenuation of each individual frequency component of the original ultrasonic pulse, similarly to any other general attenuation measurement.

For dispersive media ultrasonic velocity is dependent on frequency. Therefore the phase velocity will differ from the overall group velocity, leading to the equation above (3.21). The phase spectrum is often used to calculate the phase velocities constituting an ultrasonic pulse [He, 1999; He and Zheng, 2001]; however this often leads to complications relating to calculation ambiguities in the phase unwrapping process [Zhao et al., 2005]. This can be avoided with an alternate process based on the amplitude spectra (as in Figure 3.11). By measuring the time between relative amplitude maxima of a given frequency component and applying a simple correction, an accurate phase velocity measurement can be performed. The paper validated this by simulation and compared against results of the conventional method, which proved the accuracy of the technique.

3.2.5. Slowness profile

A slowness surface is a graphical representation of the inverse of the phase velocity over an anisotropic media. As the phase and group velocity depend on direction in anisotropic media, a slowness surface can be a useful tool in determining ultrasonic beam refraction and beam profile effects [Huang et al., 2005]. These are important elements in the ultrasonic testing process, with the potential to limit ultrasonic detectability in components.

As the shape of the slowness surface is determined by the phase velocity, which is in turn dependent on direction in anisotropic media, the texture and orientation relationships of the material are important considerations. As introduced in chapter 2, the orientation relationship of a given microstructural transformation limits the resultant possible crystallographic orientations in the subsequent anisotropic media. The fact there are a limited range of possible orientations, rather than a random distribution, allow for

predictions to be made which inform the understanding of wave propagation within these media and can be expressed as a slowness surface to aid understanding and calculation.

3.3. Relationship between ultrasonic signals and material microstructures

3.3.1. Attenuation

Ultrasonic attenuation in materials was shown to comprise of two components; one a term linearly dependent on frequency and another with 4th power dependence [Mason and McSkimin, 1947]. Initially the linear term was referred to as the elastic hysteresis loss associated with most solids, although now it would be more commonly known as dissipation or absorption. The second part, with 4th power frequency dependence is based on the work described by Lord Rayleigh, now known as Rayleigh scattering. He wrote extensively on the subject, laying much of the foundations in the field, in his two volume book "The theory of sound" [Rayleigh, 1877; 1878].

$$\alpha_{total} = \alpha_{scatter} + \alpha_{dissipation} \tag{3.23}$$

The dissipation losses are generally attributed to conversion of energy into heat via damping and viscosity; many papers explore these in detail [Wegel and Walther, 1935; Gemant, 1943; Lyons and Prettyman, 1948; Fusfeld, 1950; Roderick and Truell, 1952; Papadakis and Reed, 1961]; although these are important contributions in their own right, this shall be largely ignored as part of this work.

3.3.2. Scattering

The scattering component of attenuation has proven to be of particular interest. [Bhatia, 1959; Papadakis, 1964b] are some of the works which built on the first suggestions of scattered energy losses by [Mason and McSkimin, 1947] and [Rayleigh, 1877; 1878]; this all then subsequently led to [Stanke and Kino, 1984] writing a unifying theory of scattering. The scattering of ultrasonic waves by grain boundaries in polycrystalline materials is typically divided into three categories, or scattering regimes. These are categorised by the ratio of the wavelength to the diameter of the grain as there are three distinct scattering relations (equations 3.24 – 3.26), the Rayleigh regime (α_R), stochastic regime (α_S) and the geometric regime (α_G).

$$\alpha_R \propto D^3 f^4 \qquad \lambda_R \gg D \tag{3.24}$$

$$\alpha_S \propto D^1 f^2 \qquad \lambda_R \approx D \tag{3.25}$$

$$\alpha_G \propto D^{-1} f^0 \qquad \lambda_R \ll D \tag{3.26}$$

A problem with the early scattering models was the use of the Born approximation, which restricted calculation to single scattering events and so to weakly scattering materials. The first to incorporate a multiple scattering model was [Hirsekorn, 1982], where ultrasonic propagation in polycrystalline material of random or preferred grain orientation is described. A calculation, based on the assumption of low elastic constant and density variation between grains, uses second order perturbation theory to consider the case of random grain orientation and cubic symmetry. Issues remained due to single- size grain approximation and more general solutions, therefore the unified theory of Stanke and Kino subsequently became the preferred solution [Van Pamel, 2015].

The work by Stanke and Kino [Stanke and Kino, 1984] excellently explores these difficulties in analytic formulation, examining in great detail the work presented by others. They managed to avoid the single scattering restriction of the Born approximation by using the second order Keller approximation [Karal and Keller, 1964]. [Stanke, 1986] aptly described the concept of a statistical probability of two points falling within the same area to represent the shape of the object. This was known as the two-point autocorrelation function and allowed a clear and mathematically succinct way of representing the effective grain size and shape in polycrystalline materials. These two aspects greatly simplified the calculations of scattering models, and the regular stream of citations indicates it remains a well-established technique to this day.

[Weaver, 1990] used the Dyson equation to account for multiple scattering, and so provided an alternative approach. However, in so doing he uses the Born approximation to simplify the solution and therefore limits applicability to below the geometric regime. This approach was further developed [Turner, 1999], by the use of Green's function for anisotropic materials.

Although most of the research conducted in the field has been concentrated on a simple grain structure, more recently work has considered a secondary microstructural feature [Lobkis and Rokhlin, 2010]. Here a term known as the m-factor is introduced in order to balance the contributions of each aspect of the duplex microstructure. This concept has then been used to consider the influence of more complex microstructures than the typical simple grain model, have on ultrasonic propagation, in this case a pearlitic microstructure [Du and Turner, 2014], where contributions from a colony size (effective 'grain' size of the

pearlite lamellae) and lamellae spacing (separation between the ferrite and cementite plates) are considered as the two phases.

Whilst this reference paper provides an ideal starting point to use as part of this work, a few points of clarification should be made. The experimental data used [Du and Turner, 2014] were based on quench depth of rail steel, with microstructure only being introduced by general trends rather than any firm measurements. This approach seemed to provide adequate results against the predicted values of the model; however it is important to note the use of "fitting parameters" as part of the model calculations and so the ultimate validity of these results should be questioned. Furthermore, the assumptions made for the links between the microstructure and quench depth are in fact impossible to achieve in the extreme case. It is unrealistic to assume lamellae spacing approaches colony size and would be completely unachievable in physical samples. Nonetheless, the original estimates relating quench depth and lamellae spacing in a previous paper [Du et al., 2013] seem to be far more realistic than the trends used in their model, and is based on actual microstructural measurements via optical micrographs. Therefore, the foundation of the work is deemed reasonable with the physically unrealistic extreme considered more of a thought experiment to develop the model than actual prediction.

With this base of mathematical vigour established it has been possible for a number of publications to broaden the scope of applicability for ultrasonic scattering models. For instance, work has been published to include texture [Li et al., 2014b], this work specifically looked at texture of polycrystalline materials of orthotropic and trigonal grains which exhibit an ellipsoidal grain shape. They used a modified Gaussian orientation distribution function to describe the crystallographic orientation of the grains. This contrasts with previous work

which considers textured polycrystalline materials with equiaxed grains [Hirsekorn, 1985; 1986; Ahmed and Thompson, 1996; Turner, 1999; Yang et al., 2007]. A couple of studies have considered other grain shapes [Ahmed and Thompson, 1995; Yang and Rokhlin, 2013] and these only covered cubic grain symmetry and were limited in applicability.

The crystallographic symmetry was a further area of investigation. These studies covered hexagonal [Yang et al., 2011a; 2012], triclinic [Li and Rokhlin, 2015] and orthorhombic [Yang et al., 2013] crystallite symmetry, rather than just cubic. Further the grain shape influence was also amended by altering the spatial correlation function as discussed previously for spherical grains. This ellipsoidal specific spatial correlation function has been utilised by a range of authors [Li et al., 2016; Yang et al., 2011b; Lobkis et al., 2012]. [Kube et al., 2017] Used a ray -based scattering model to measure the grain elongation based on backscattered ultrasonic signal from polycrystalline materials.

Work by Papadakis provides a useful examination of ultrasonic attenuation across a range of material microstructures, with the work summarised in [Papadakis, 1981]. [Papadakis, 1961; 1964a] outlined a statistical approach for finding the appropriate grain size, as the typically log normal distribution of grain size resulted in an average grain diameter being larger than the median grain diameter by a factor of 1.45 [Papadakis, 1964a]. [Papadakis, 1981] also describes how “polyphase or multiparticle structure within grains” can be discussed quantitatively but has not been worked out in detail. He goes on to say that overall contribution to ultrasonic scatter would result from two sources, the individual scatter of each region of the structure (within the grain) and the original scatter of the grain unit, and the overall scattering would be a summation of these contributions. In a series of experiments [Papadakis, 1981], an attenuation comparison was made between

microstructures. Here different cooling techniques were used to generate steels with pearlitic (with ferrite), bainitic, martensitic and tempered martensitic microstructures. These microstructures, with grain size held constant, showed considerable differences in scattering behaviour; the attenuation in order of highest to lowest was associated with the pearlitic, bainitic, martensitic and the tempered martensitic microstructures. This was attributed to the increased substructure of the grain "breaking up" the associated anisotropy, and hence reduces the contributions to overall scatter.

An experiment using a low-alloy, 0.5 wt% carbon steel (SAE 4150) [Papadakis, 1964b], found an f^4 relationship between the attenuation of pearlite and bainite and bainite and martensite but an f^2 relationship between martensite and tempered martensite (Figure 3.13). The suggested, but unverified, reasons for the f^2 relationship are dislocation damping, atomic relaxations or magnetic boundary effects. The attenuation was therefore written as equation 3.27.

$$\alpha_i = A_i{}^{(R)} f^4 + C_i f^2 \tag{3.27}$$

Where I represents the different microstructures, R for Rayleigh scattering, and A and C being constants determined experimentally. As part of the experiment it was found A had a significantly greater difference between microstructures than C, associated with a factor 225 and a factor 10 difference respectively.

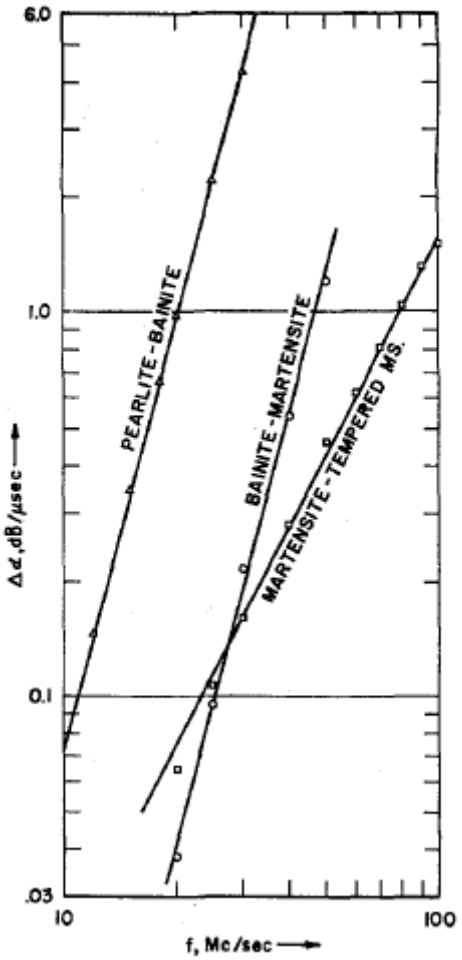

Figure 3.13: A Figure showing the longitudinal wave attenuation difference between microstructures generated in Papadakis' attenuation experiment. An f^4 relationship between pearlite and bainite and bainite and martensite is found but an f^2 relationship between martensite and tempered martensite [Papadakis, 1964b]

3.3.3. Other model methods

There are also other methods used to investigate ultrasonic signal interaction with material microstructure. Computationally intensive methods have come into focus over recent years as the capabilities of these techniques continue to improve with increasing computing power [Van Pamel et al., 2017]. Explicit and implicit finite element methods, spectral element methods, finite volume methods and finite difference methods are all numerical techniques which can be implemented [Packo, 2013]. The most developed of these techniques are finite-difference (FD) and finite-element (FE) modelling. These are techniques where the differential equations are discretised over the spatial domain

[Temple, 1993; Van Pamel et al., 2017]. An alternative approach to discretising the spatial domain is to discretise the boundary, such as the boundary element method [Brebbia and Dominguez, 1992]. Additional techniques include the Gaussian beam model, distributed point source method and ray tracing method. A distributed point source method can be advantageous as they are less computationally intensive [Fooladi and Kundu, 2019].

These models can be hugely beneficial in advancing ultrasonic scatter or back-scatter research fields; however it is important to note all of these models are only as good as their underlying assumptions. This means any generated model, whilst undoubtedly providing useful insights in their own right, must also be based on validated mechanisms. Therefore it is crucial to avoid the self-confirmation trap of comparing with other models of the same or similar assumptions. The best validation technique would of course be to compare against physical experiments.

3.4. Aspects requiring further investigation

A great deal of work has already been covered in investigating ultrasonic scatter induced by steel microstructures; particularly in regard to theoretical models. This work therefore intends to build on this already established knowledge base and aims to address some of the missing elements. As this work has an industrial drive to it, a particular emphasis is placed on industrial relevance. This includes testing equipment and methodologies, a focus on microstructures relevant to the power generation industry, and industrially relevant sample preparation and testing.

A primary area of investigation is to address the lack of quantitative model available for predicting scatter induced attenuation in the complex microstructures associated with

power generation relevant steels. Therefore the potential framework for such a model must be established, and then experimental work should be used for validation in order to establish the models overall viability. As the majority of established ultrasonic scattering work in the literature is predominantly theoretical, an emphasis is placed on experimental validation as part of this work. It is likely that there is significant amount of relevant data held by industry which is not made available in the literature due to commercial sensitivity (or simply a perceived lack of necessity).

A further aspect to address is the scattering associated with a particular boundary relative to another. There is currently no established practice whereby the reflection coefficient of one boundary relative to another (of the same size and shape) can be quantitatively predicted. In the few experimental investigations conducted “fitting parameters” have been used rather than any sort of first principles-based calculations. Using the principles of acoustic theory it should be possible to broadly predict the reflection coefficient of different boundaries and with this to compare the influence of different boundary types on a propagating wave.

By investigating these topics and generating the experimental data required, it is hoped valuable insights can be gained, helping to further the overall field. It is understood that not all aspects can be fully investigated and there will likely be even more questions upon completion of this project. Therefore, it is hoped the outcomes of this project, whatever they may be, can help inspire and develop future areas of investigation. A section which briefly discusses the possibilities of future work is included in the hopes it will be of relevance.

4. Experimental setup, methods and error analysis

4.1. Sample selection and composition

Initial work focussed on material of type FB2. The material used to generate an analogous martensitic microstructure, as is present in FB2 grade rotor steels, was of grade BS S156, with the composition as presented in table 4.1. BS S156 is a commercial high strength gear steel.

Table 4.1: Composition of the BS S156 sample in weight % compared to desired specification ranges.

Element	C	Si	Mn	P	S	Cr	Mo	Ni	Cu	Sn	Al	Fe
Target	0.14-0.18	0.10-0.35	0.25-0.55	<=0.015	<=0.012	1.0-1.4	0.20-0.30	3.8-4.3	-	-	-	Bal
Actual	0.155	0.18	0.39	0.007	0.0008	1.16	0.22	3.9	0.12	0.013	0.015	Bal

A rail steel, with composition provided in table 4.2, was used to generate the desired pearlitic microstructures.

Table 4.2: Composition of the rail steel sample in weight %

Element	C	Si	Mn	P	S	Cr	V	Al	Fe
Composition	0.76	0.3	1.02	<0.025	0.01	<0.15	<0.03	<0.004	Bal

4.2. Sample preparation

Samples with an initial size of approximately 30 * 30 * 30 mm^3 were cut from the as-received steel blocks (FB2 rotor forging, BS S156 hot rolled billet and hot rolled rail) for heat treatment and ultrasonic measurements. Sample size was determined by a balance of initial block dimensions; the need for rapid but controlled heat treatments with uniform sample temperature; to allow a sufficient propagation path to avoid any near-field interference; and to allow for a suitable bulk of material to be tested using the 10 MHz transducer. Only once lower frequencies (2-5 MHz range) were deemed necessary, to avoid scattering regime issues, did it become apparent that beam spread was a major issue leading to erroneous

attenuation results (discussed further in the results section). The only feasible option to solve this issue was for samples with a larger surface area to length ratio to be used, however this was not an option given the material available.

Cutting was conducted with standard cutting equipment in the University workshop, although the hardness of the samples did result in a little difficulty. Heat treatments were conducted using the schedules listed in tables (4.3, 4.4 and 4.5).

Table 4.3: Details of heat treatment procedures used to prepare each of the tested pearlitic (rail steel) samples. Each sample is given a designator in order to simplify discussion and to avoid any potential confusion between samples

Sample name	Heat treatment procedure
A	1100°C for 1.5 hours and air cooled (RT)
A_1	850°C for 0.5 hours and 600°C for 1 hour and air cooled (RT)
B	1100°C for 1.5 hours and 600°C for 1 hour and air cooled (RT)
B_1	850°C for 0.5 hours and air cooled (RT)

Table 4.4: Heat treatment procedures for the mixed martensitic/bainite (hot rolled BS S156) samples. Similarly to Table 4.3, they have also been given a code to aid differentiation in further discussion.

Sample name	Heat treatment procedure
C	900°C for 1 hour and air cool (RT)
C1	900°C for 1 hour and 500°C for 4 hours and air cool (RT)
C2	1000°C for 0.5 hours and air cool (RT)
C3	1050°C for 0.5 hours and air cool (RT)
D	1100°C for 1 hour and air cool (RT)
D1	1100°C for 1 hour and 500°C for 4 hours and air cool (RT)

Table 4.5: Heat-treatment procedures for the final set of fully martensitic (hot rolled BS S156) samples. They are largely formed by reheating the previous samples from table 4.4 after testing, but quenching in water (wq) in order to ensure a full martensitic microstructure.

Sample name	Heat treatment procedure
M1	Fresh sample - 1000°C for 0.5 hours + wq (RT) and 600°C for 1 hours + wq (RT)
M2	Sample C [900°C for 1 hour and air cool (RT)] Re-heat [900°C for 10 mins + wq (RT)]
M3	Sample C1 [900°C for 1 hour and 500°C for 4 hours and air cool (RT)] Re-heat [900°C for 10 mins + wq (RT) and 500°C for 1 hour + wq (RT)]
M4	Sample D [1100°C for 1 hour and air cool (RT)] Re-heat [1100°C for 10 mins + wq (RT)]
M5	Sample D1 [1100°C for 1 hour and 500°C for 4 hours and air cool (RT)] Re-heat [1100°C for 10 mins and + wq (RT) and 500°C for 1 hour + wq (RT)]
M6	Sample C3 [1050°C for 0.5 hours and air cool (RT)] Re-heat [1050°C for 10 mins + wq (RT)]
M7	Sample C2 [1000°C for 0.5 hours and air cool (RT)] Re-heat [1000°C for 10 mins + wq (RT)]

Air cooling (air cool) and water quenching (wq) were used to control the cooling rate between heat treatments, they both resulted in the samples being cooled back to room temperature and are indicated by (RT). Furnace cool (or where no intermediate cooling procedure was used) resulted in the sample being transferred from a hotter furnace to a cooler furnace and then gradually reaching the new equilibrium temperature.

The temperature selection was based on generating a range of samples with differing microstructures. These target microstructures were selected to coincide with the overall aims of this project. Firstly, the pearlite microstructures with differing colony size and lamellae spacing were intended to test the initial model previously presented in the literature. The bainitic and martensitic samples were generated with the intention of varying the prior austenite grain size, and then to combine this with tempering heat treatment in order to generate carbide coarsening as well as an increase in lath width. This was to enable the individual microstructural contributions to overall attenuation to be identified. Ideally, each variable would be altered in one sample and have a directly comparable sample as a baseline. This intention proved difficult however, due to the natural variation in sample microstructure, as well as the intertwined nature of microstructural features.

For the pearlitic samples (table 4.3) the initial furnace temperature was selected with the intention of allowing for pearlite colony growth. The difference of the temperature and time in the furnace was deemed sufficient for a significant difference in colony size between the two groups of samples. The second phase was designed with the intention of allowing lamellae coarsening to occur, with significant measureable differences intended.

Similarly to the pearlitic samples, the initial furnace temperature (above the austenitising temperature) of the martensitic and bainitic samples (table 4.4 and 4.5) was varied in order to allow for a range in prior austenite grain sizes. With more grain growth associated with higher heat treatment temperature. The second heat treatment phase intended to recreate a tempering heat-treatment program. The intention was to enable a variation in lath growth as well as carbide precipitation and coarsening.

Once heat treatment and quenching had been completed to achieve the desired microstructure, a thin slice was removed from one of the surfaces of the cube, of approximately 3 - 5 mm thickness so as to avoid the decarburised layer which forms in the top 1 mm or so of the sample surface. This slice was then further cut, removing a further ~2 mm from each edge, once again to remove the decarburised layer. The remaining section was typically cut in half (to a size suitable for the mounting press) and hot mounted in conducting Bakelite. Final sizes of the mounted samples were approximately 12 mm * 8 mm.

The remaining (block) samples were machined, using a Jones and Shipman 540 surface grinder with an aluminium oxide wheel, to ensure the surfaces were parallel, and sufficiently smooth for ultrasonic testing. The surface conditions exceed the smoothness mostly found in industry conditions.

4.3. Microstructural analysis

4.3.1. Sample preparation and microstructure analysis

The samples, mounted in Bakelite, were ground and polished to a final 1 µm diamond paste finish before being etched. To adequately etch the prior austenite grain boundaries a

saturated picric solution heated to 60 °C was required, and they still proved difficult to reveal at times, requiring multiple rounds of etching. A 2% nital solution was used to etch all of the other sample features; this included pearlite colony and lamellae boundaries, as well as the laths/packets of both bainite and martensite. It should be noted however that carbide size was not explicitly measured as part of this work.

An optical microscope (Carl Zeiss Axioskop 2) was used to observe pearlite colony size and the prior austenite grain size of both the martensitic and mixed martensite/bainite samples. They were imaged using Axiovision software and analysed using the image analysis software ImageJ. Grains were measured by manually drawing a boundary around the feature with the area within this boundary being equivalent to the area of the measured grain. The area of the measured grain was converted to an equivalent circle diameter with a correction factor of 1.61 applied to account for the underestimate of size associated with a three-dimensional object being measured in two-dimensions (stereology) [Underwood, 1970]. The conversion to an equivalent circle diameter allows an analytical comparison to be made for grains of many varying shapes. This conversion was deemed appropriate for the measurement of pearlite colonies and prior austenite grains due to their approximately equiaxed nature, however any strong tendency of elongation in a dominant orientation would invalidate this assumption. Therefore, this process would not be appropriate for the measurement of lamellae or lath features, nor of any grains with a clear tendency for elongation in a preferred orientation (such as along the rolling direction).

The remainder of the microstructural features, lamellae spacing, lath width and packet size, were all measured from scanning electron microscopy (SEM) images taken on a Philips XL30 using 20 kV accelerating voltage. The packet size was also measured directly, in the same

way as the grain sizes, therefore the 1.61 correction factor was applied here as well. Both the lamellae spacing and the lath width were measured using the linear intercept method. The method is described by [Vander Voort, 1984] for pearlite and uses a correction factor of (π/4) to convert to the mean true spacing. This is a factor which takes the angle of pearlite colonies into account, as an oblique viewing angle would give the appearance of a larger lamellae spacing. Whilst this is not directly transferable to the measurement of a lath due to the slight difference in shape compared to lamellae (it is more of an ellipse), it has been deemed close enough in order to use here to also correct for any oblique viewing angles. The reasoning for this assumption is the large number of aggregated laths which form a packet with specific orientation. Therefore, whilst an individual lath would be dominated by its respective shape, the aggregate nature of the numerous laths in a packet would function ultrasonically in much the same way as a colony of lamellae.

Crystallographic orientation was measured using EBSD on a FIB-SEM. Sample preparation with a greater degree of care was required as the internal strain of the sample can reduce the ability of the software to index successfully. The (HKL Channel 5) software uses Kikuchi lines to identify the crystallographic orientation and within a given tolerance assigns a phase when it matches with a database of pre-set expected phases. The expected phase against which the measured crystallographic orientation should be compared is required to complete a scan; a standard value for BCC iron was selected here. The reason for this selection was to simplify the process, as whilst it is known the crystallography of martensite is body-centered tetragonal (BCT) rather than body-centered cubic (BCC) the degree of tetragonality is mainly dependent on carbon in solution. As the carbon in solution precipitates out to form carbides, a key attribute of tempered martensite, estimating the

tetragonality is no simple task. Also the relatively low levels of carbon present in the alloys results in a low level of tetragonality, and so is expected to be similar to the standard database value for BCC iron.

Obtaining tests with sufficiently high indexing rate proved to be problematic for these samples, especially given the number of internal boundaries which seemed to impair the software's ability to index successfully. An additional issue can be caused by internal strain, which can be introduced during the polishing stage of sample preparation, and can distort, and so obscure the Kikuchi bands. A method used to reduce this internal strain is to etch the sample in 2% nital solution and then to subsequently remove this etched surface layer. Approximately 2 or 3 cycles of etching and polishing were sufficient to achieve a suitable indexing rate as part of this work. [Zhang et al., 2019] provide an analysis of testing parameters and determine the accuracy of measurement (in their case detecting retained austenite), the key points are a high indexing rate is better but benefits plateau above a certain value (~86%-92%) depending on material; and an optimal step size would be below a threshold value (~1/5 of feature size).

The polishing of EBSD (electron backscatter diffraction) samples was similar to that of the other microstructural analyses up to the 1 micron diamond paste finish, ensuring that loads on the samples were not too high, in order to reduce the amount of strain introduced. Appropriate load levels were estimated with the information provided by the equipment manufacturer [Struers preparation guide], and were matched to sample size, number and material hardness levels (~10N/sample). The final stage of polishing used colloidal silica (OPS) or alumina (OPA)-based solutions, with a significantly reduced loading (~0-5N/sample) in order to approximate vibration polishing methods. This stage can be kept on for longer

than the previous stages due to the reduced load (~30 mins). Care was taken that sufficient lubricant is present throughout to avoid the formation of further scratches.

4.3.2. EBSD (electron backscatter diffraction) analysis

A variety of software packages were used to evaluate the EBSD data. Tango, a standard EBSD visualisation software package, proved a useful tool to quickly generate a map in either Euler angle or IPF colour. A comprehensive variety of other features are also available as part of this software package, but this was predominantly not used other than for quick visualisations. The preferred software to analyse the EBSD data and to present as part of this work was the MTEX open source toolbox which is available for Matlab. The advantage of using this package over the Tango software is the extreme versatility of using a Matlab package, where the functions can simply be adapted to suit a particular purpose rather than being limited by preformed functions. As a wide range of functions have been developed as part of the toolbox, and used in many previous works [Nolze and Hielscher, 2016; Krakow et al., 2017; MTEX website], it is simple to make the required selections. A further benefit of the Matlab script format is the repeatability over any number of datasets, with little to no individual inputs required.

4.3.3. Vickers hardness testing

Hardness testing was conducted on an Indentec 5030 SKV. Samples previously mounted in Bakelite were used and had all previously been polished to ensure a flat surface. A load of 20 kg was selected (therefore a Vickers hardness 20 – HV 20 number was generated). As the

samples exhibited a low variability of hardness across the test piece a total of 10 tests were conducted and then averaged.

4.4. Ultrasonic testing

The ultrasonic testing experimental setup was chosen to take a form which was as simple as possible (Figure 4.1), in order to fit with standard industry testing methodology, as discussed in chapter 3.

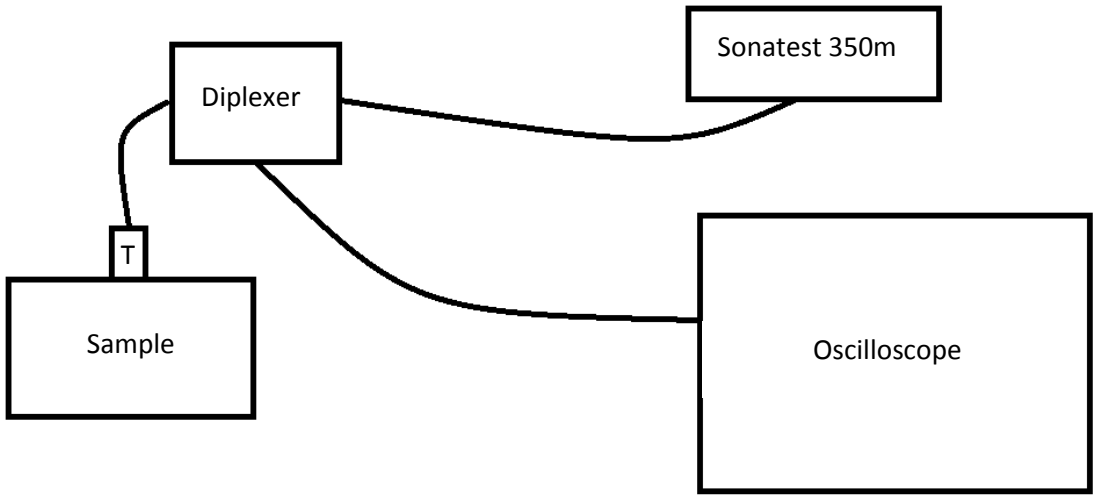

Figure 4.1: Diagram indicating experimental setup, with T representing the transducer position during testing.

The equipment used for this project was the Sonatest 350m, with 3 unfocussed, zero angle transducers (10 MHz, 5 MHz and 2.25 MHz). As the equipment does not output digital data it was necessary to record the data on a LeCroy LC574AL oscilloscope via the use of a custom-made diplexer.

Whilst a better set-up would be to conduct the tests in a full immersion ultrasonic testing bath to allow for the best repeatability and control of experimental parameters, this process was not possible within the scope of this project. Most industrial use of ultrasonic testing

would also have the same constraint, particularly with in-service components, therefore it was decided to use an industry standard testing setup here as well.

An important consideration for oscilloscope specifications was the sampling rate at which the data were measured. A sufficient number of data points must be taken in a given period of time for the sampled data to provide an adequate representation of the true data curve. An insufficient sampling rate, n, can lead to the details of any sudden changes in data being entirely removed from the sampled result. For instance a sampling rate of n=f, i.e. where the sampling rate is equal to the frequency, f, could reduce a sine wave down to a perfectly straight line. In order to estimate the minimum sampling rate to adequately represent the data, the Nyquist frequency was used. The Nyquist frequency is described as the minimum sampling frequency which can be used without introducing errors and is twice the maximum frequency contained within the data being sampled. The sampling rate as part of this work was 2 Gs/s, well above the minimum level indicated by the Nyquist frequency (50 - 100 MHz).

Standard unfocussed transducers of frequency 10 MHz, 5 MHz and 2.25 MHz were used which are slightly above typical industry frequencies, although still comparable. Industrial test frequencies are typically in the range of 1 – 4 MHz, purely to account for the increased sample size to ensure sufficient penetration.

Figure 4.2: Image indicating the decay pattern of multiple back-wall-reflections. The Sonatest equipment is a common brand used for ultrasonic testing in industry. Source Sonatest 350M user guide [Sonatest 350M]

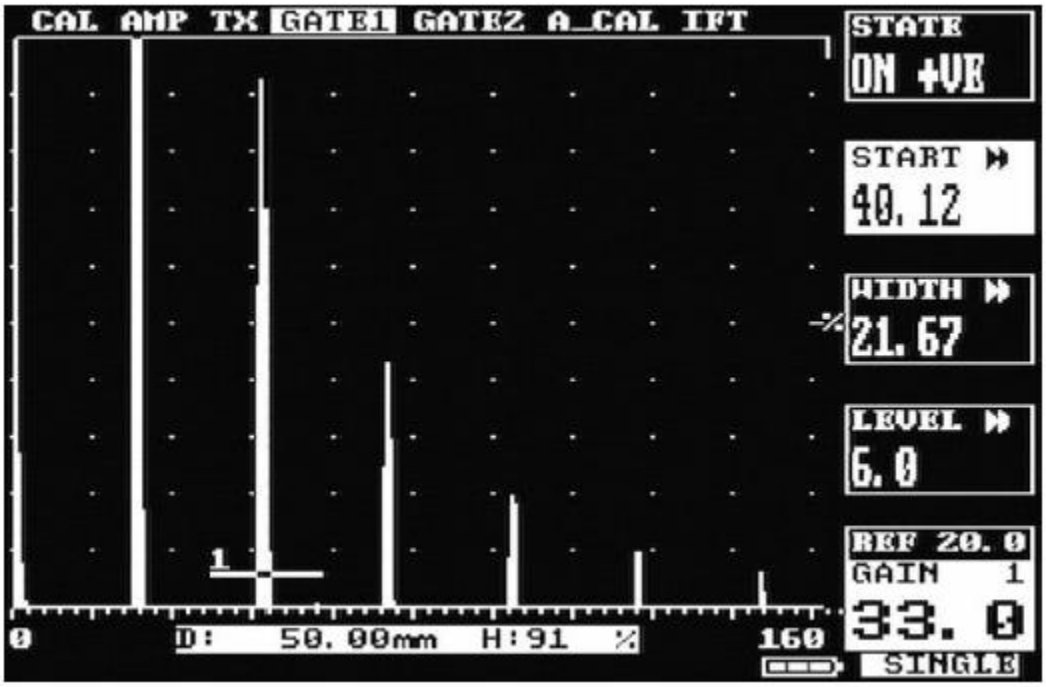

Figure 4.3: Image indicating the display screen of multiple back-wall-reflections by Sonatest 350M direct contact ultrasonic testing equipment. The display range is set to 160mm in order to observe a number of reflections, typically used to calibrate the equipment. Source Sonatest 350M user guide [Sonatest 350M]

Figures 4.2 and 4.3 represent an ultrasonic signal being generated using a direct contact zero angle, unfocussed ultrasonic transducer, in this case that of Sonatest 350M.

As introduced in section 3.2.3., the far field region describes how the beam spreads over a given propagation distance. Equation 4.1 is the far field equation which predicts this phenomenon.

$$\sin(\theta) = 1.2\frac{\lambda}{D} \tag{4.1}$$

Where θ represents the angle associated with beam spread, D is the diameter of the transducer and $\lambda$the wavelength of the signal.

Substituting the respective values of a 2.25 MHz, 5 MHz and 10 MHz transducer into equation 4.1 respectively yields the angle of spread in the far field region (equations 4.2 – 4.4).

For 2.25 MHz transducer of diameter 6 mm

$$\theta = 22.33° \tag{4.2}$$

For 5 MHz transducer of diameter 6 mm

$$\theta = 10.95° \tag{4.3}$$

For 10 MHz transducer of diameter 6 mm

$$\theta = 5.41° \tag{4.4}$$

As is clearly indicated by these results beam spread is heavily weighted towards the lower frequency transducers. This proved to be of particular concern as part of this project, given

the limited sample sizes available and the distortion of attenuation reading of the lower frequency (2.25 MHz and 5 MHz) tests by side wall reflections. Therefore any future sample size selection should consider these aspects from the outset; surface area (length and width) rather than depth are likely to be limiting factors. It may prove beneficial to favour higher frequencies to avoid any side-wall interference issues if sample size is an issue, although it should be noted this leads to a naturally higher level of attenuation.

The near field region can be calculated using equation 4.5

$$N = \frac{D^2}{4\lambda} \tag{4.5}$$

Where D and λ once again represent transducer diameter and wavelength respectively. N is the length of the near field region. Once again the corresponding near field region is calculated for a transducer with associated frequency of 2.25 MHz, 5 MHz and 10 MHz and a diameter of 6mm.

For 2.25 MHz transducer of diameter 6 mm

$$N = 3.6 \text{ mm} \tag{4.6}$$

For 5 MHz transducer of diameter 6 mm

$$N = 7.9 \text{ mm} \tag{4.7}$$

For 10 MHz transducer of diameter 6 mm

$$N = 15.8 \text{ mm} \tag{4.8}$$

Ultrasonic testing was always conducted with the transducer in the centre of the sample surface in order to minimise potential sidewall interference. Sonagel D1, part of Sonatest's

Sonagel series was used as a couplant. For this work a standard error of the mean of approximately 1% was deemed an adequate target threshold and is discussed in more detail in the error section at the end of this chapter (section 4.6). Numerous repeat tests were taken to easily satisfy the target error threshold. The typical number of tests for each sample was approximately 50, with multiple stages of complete couplant reapplication.

4.5. Data acquisition

The raw data were in the form of a time series dataset as measured by the oscilloscope; with the setup used here there were 200,000 data points corresponding to 0.1 milliseconds of data measured at a sampling rate of 2 GHz. These data were saved by the oscilloscope in a binary format and were then converted to a Matlab data file using a conversion script (Appendix A). The file was then saved in a folder which was readable by Matlab and was readily accessible by the evaluation script.

To evaluate the converted oscilloscope data Matlab was used to Fourier transform the data from the spatial to the frequency domain. By doing so, the broadband ultrasonic pulse was split into the respective contributing frequencies. The relative amplitude was used to calculate the attenuation between the first and second back-wall echo, with the appropriate correction terms applied, in this case to account for the beam spread, with equation 3.16 from chapter 3.

The script itself (Appendix B) was separated into three distinct sections: user input, calculation and output. The user input data were the details necessary for the calculation; these were made up of hardware parameters: transducer width and frequency, as well as oscilloscope sampling rate. The only other requirement was the sample size (along the

propagation direction); the numbering parameter (N) was adjusted in order to ensure only one back-wall echo features per window. The “window” in fact applied no correction to the data itself but was merely used to segment the data as the position of each echo varied with propagation path length and average ultrasonic velocity associated with the sample. When the condition of one echo per window was met, then the attenuation was output in the array AlphaStar in nepers/meter. Using the attenuation associated with the first and second back-wall echoes was recommended as this would provide the most accurate results as it contained the least amount of interference.

4.6. Errors

The error associated with the equipment was an important consideration when evaluating the data. Firstly, as the transducers are handmade, they have a large uncertainty range associated with the specified centre frequency (±10%), however the true centre frequency can be determined with far greater accuracy by inspecting the frequency output of the measured signal. The true centre frequency of the 10 MHz transducer was approximately 9.2 MHz, towards the lower end of the uncertainty range but still within the supplier specified tolerances.

Oscilloscope uncertainty was accounted for in two parts, the uncertainty in time and in measured voltage. The time component of uncertainty was given by ± ((0.06 * sample interval) + (1 ppm of measured interval)). The latter term was negligible over such a short time period as was the case here (0.1 milliseconds per measurement), and the former was also vanishingly small (of the order 10^{-10}). Therefore, the ultrasonic measurement error was associated with the voltage measurement error and the pulse generation error of the flaw detector (Sonatest 350M in Figure 4.2).

The Sonatest 350M has a vertical and horizontal screen uncertainty of 1% and 0.4% respectively, but as the oscilloscope was used rather than the flaw detector screen the oscilloscope measurement error supersedes this flaw detector error. The amplifier error of the flaw detector was rated as ± 0.1 dB but was also avoided as the amplifier did not influence the oscilloscope measurement. Therefore the only consideration of error for the flaw detector itself was associated with the pulser, here the equipment was rated as having a rise/fall time of <10 ns into 50 ohms at 200 V. This uncertainty was deemed negligible as it was less than the increment associated with each measured time interval of the oscilloscope.

The uncertainty of the oscilloscope voltage measurement was dependent on the full scale voltage used as this impacted the smallest voltage step measured. For the oscilloscope used here the error was ± 2 voltage steps. This translated to ± (2 * 625 µV) for a full scale voltage of 160 mV and 8-bit resolution. As this error consisted of a fixed set of values, with equal probability of a positive or negative occurrence, it was advantageous to use repeated readings in order to minimise the relative impact on the final result.

The number of test results required to obtain a reasonable representation of population statistics from a number of samples was calculated using a standard error calculation.

$$SE_{\bar{x}} = \frac{s}{\sqrt{n}} \tag{4.9}$$

Equation 4.9 is used to calculate the standard error in the mean. Here $SE_{\bar{x}}$ represents the standard error, s is the standard deviation of the sample set and n represents the number of tests which constituted the sample size. Therefore the standard error of the mean ($\bar{x}$) is proportional to $\frac{1}{\sqrt{n}}$

Using a set of ultrasonic testing results formed of n=103 tests, $\bar{x} = 27.148$ and s=0.875, it was possible to alter the value of n in order to see how this influenced the standard error of the mean. Values of n equal to 103 (equation 4.10 – 4.12), 50 (equation 4.13 – 4.15), 25 (equation 4.16 – 4.18) and 10 (equation 4.19 – 4.21) are represented below:

$$SE_{27.148} = \frac{0.875}{\sqrt{103}} \tag{4.10}$$

$$SE_{27.148} = 0.0862 \tag{4.11}$$

$$\therefore \ \bar{x} = 27.148 \pm 0.0862(0.318\%) \tag{4.12}$$

$$SE_{27.148} = \frac{0.875}{\sqrt{50}} \tag{4.13}$$

$$SE_{27.148} = 0.1237 \tag{4.14}$$

$$\therefore \ \bar{x} = 27.148 \pm 0.1237(0.456\%) \tag{4.15}$$

$$SE_{27.148} = \frac{0.8750}{\sqrt{25}} \tag{4.16}$$

$$SE_{27.148} = 0.175 \tag{4.17}$$

$$\therefore\ \bar{x} = 27.148 \pm 0.175(0.645\%) \tag{4.18}$$

$$SE_{27.148} = \frac{0.875}{\sqrt{10}} \tag{4.19}$$

$$SE_{27.148} = 0.2770 \tag{4.20}$$

$$\therefore\ \bar{x} = 27.148 \pm 0.277(1.020\%) \tag{4.21}$$

As is evident from these examples, a larger number of tests which contribute to the sample dataset provided a more robust estimate of results. From these estimates it was decided to use a total number of 49 tests (multiples of 7 were beneficial for data transfer as the oscilloscope required a floppy disk) for a sample when obtaining ultrasonic testing data. This allowed for an estimated upper bound of the standard error of 1% of the mean. By limiting the required number of tests, it was possible to ensure the reliability of the data whilst minimising the required testing time.

Similarly to the ultrasonic testing measurements, a specific number (10) of tests were conducted for the hardness testing of each sample. This allowed for the standard error of the mean to be controlled (typically falling in the 1% - 3% range), whilst ensuring adequate space between test indentation sites in order to avoid distortion.

A large number of measurements were taken in order to measure the microstructures of the generated samples. The upper bounds were set at a 5% standard error in the mean associated with prior austenite grain size; packets were set at 4% and lath width at below

3%. Colony size was associated with an upper bound of 3% and lamellae spacing was within 1.5%. The majority of sample measurement sets were well within these upper bounds, however a few seemed to push up the upper bound requirement for the entire set. This was typically seen amongst the largest variants of the set and proved to remain after multiple etching attempts. This is likely due to the natural variation of microstructural feature size coupled with the large feature size limiting the number of readings possible for a given sample. The data presented as part of the materials quantification section (chapter 6) have been presented with an error range consisting of 1 standard error either side of the mean value used for a particular data-point.

5. Modelling and Calculations

5.1. Modelling Approaches

The modelling work undertaken builds upon existing models to account for ultrasonic scatter from grain boundaries and pearlitic lamellae boundaries, discussed in chapter 3, to consider the complex martensitic microstructures used in the power generation industry. The equation developed considers scattering from the different microstructural elements and has been reduced down to a series of simple-to-use scripts, with minimal input parameters. The aim is to keep these models as simple as possible in order to aid in future applicability potential, with the bulk of complexity in self-contained calculation segments. Therefore a user who wishes to use the calculation for a specific microstructure could simply focus on the input and output sections without needing to consider the underlying complex mathematics.

The final goal of the work would be the development of a user-friendly software interface, with a selection of several possible calculation variants depending on the applicable scenario. However, this requires the underlying mathematical calculations to be robustly developed and verified. This project has focussed on developing the mathematical calculations and applying them to exemplar microstructures initially. For a usable software interface to be practical, virtually all of the potential issues and limiting factors should be fully identified and ideally be resolved. These tasks fall firmly beyond the scope of this work but could be carried out subsequently to allow large scale commercial adoption.

The software with which the models are created and equations calculated are either MATLAB or MAPLE, selected depending on the suitability for the particular application. The majority of coding was written specifically for the purpose of solving the given problem.

However, wherever applicable a pre-existing script or subroutine was implemented. This predominantly consisted of standard tasks which are used in a multitude of fields and so code is freely available on the internet. Examples include a conversion script to convert the binary oscilloscope readings into a Matlab data file, and a rotation calculation around a three-dimensional rotational axis - see appendix for full script.

5.2. Boundary Reflectivity Coefficients

5.2.1. Introduction

Macroscopically the process of boundary reflection and transmission of ultrasonic signals is well understood (previously covered in chapter 3). It is governed for instance by Snell's law and the impedance mismatch between one medium and the other, as introduced in section 3.1.2. This inherent mismatch between the media, which creates the boundary itself, determines the characteristics of the transmission and reflection of the wave. These theories are applicable to boundaries between two infinite plates, and so are merely approximations in reality. However, on a macroscopic level these approximations are also valid as the effective size of the plate, in comparison to the wavelength, is so large that it could be considered infinite for the purpose of calculation. The criteria for these size relationships would be the same as those used for the scattering regimes as outlined in section 3.3. The scattering regime associated with large scattering centres, the optical or geometric regime, represents the conditions under which the afore-mentioned "macroscopic" reflection conditions hold.

Microscopically it has long been suggested that these same principles are the causes for much of the influence of microstructure on wave propagation [Bhatia, 1959; Guo, 2003;

Wiskel et al., 2016]. The difficulty arises when applying these principles to small microstructural features relative to the wavelength. As the macroscopic approach is limited to scattering in the geometric regime it requires adjustment to account for the smaller features of either the stochastic or Rayleigh regimes. However, as this would add significant degrees of complexity a simplifying assumption is made by continuing to use the same approach without the adjustment. The consequence of this simplification would be the direction and angle of the boundary reflection being incorrect; but this behaviour would not influence the reflection coefficient. Therefore, this simplifying assumption will not interfere with the investigation and so is deemed appropriate to use as part of this work.

5.2.2. Acoustic impedance

The impact on a UT signal caused by a transition from one medium to another is determined by the change in material constants between them. Therefore, if the microstructures are properly characterised, it is possible to determine analytically how significant any boundary would be, ultrasonically speaking. The most important factor to consider is the ultrasonic wave velocity of a particular wave mode, which was first discussed in section 3.2.1.

$$V_l = \sqrt{\frac{E(1-\mu)}{\rho(1+\mu)(2-\mu)}} \tag{5.1}$$

Where E is Young's modulus, ρ is the material density and μ is the Poisson's ratio. Equation 5.1 indicates how the anisotropy of the microstructure directly influences the ultrasonic velocity, thereby also the acoustic impedance. As the longitudinal wave velocity is

dependent on the Young's modulus, density and Poisson's ratio the velocity reflects the material's acoustic properties. Therefore, by basing a scattering model on velocity, a simple, measurable and well understood metric is used to consider all of the potential contributions to acoustic property variation throughout the sample microstructure. Longitudinal wave velocity, V_l, is used here as it is the dominant propagating wave in this work. This is due to the transducer used in the overall experimental setup (section 4.4). However, any wave type could be considered as long as consistency is maintained, between experimental and analytical practice, and any mode conversions are adequately considered (section 3.3.2).

The velocity of a propagating elastic wave is dependent on the density and elastic modulus of the medium itself and so is a good indication of whether an ultrasonic mismatch exists. Poisson's ratio does vary for different material types, although they are generally well known. Poisson's ratio values of 0.3 and 0.25 have been used for steel matrix and ceramics (representative of the carbides present in rotor steels) respectively as part of this work. Care does have to be taken in an industrial context, however, as the Poisson's ratio does vary with temperature [Garcin, 2016], and so this must be taken into account with high temperature in-situ monitoring.

The full measure of acoustic impedance Z is determined by the product of the wave velocity and the material density.

$$Z = \rho \cdot V_l \tag{5.2}$$

The reflection coefficient, determined by the acoustic impedance mismatch between medium 1 and medium 2, would be

$$R = \frac{(Z_2 - Z_1)^2}{(Z_2 + Z_1)^2} \tag{5.3}$$

Therefore it is theoretically possible for two media to have different wave velocities and yet have the same acoustic impedance values. This would be caused when a difference in elastic constants perfectly counters a difference in the material density, but this is more of an interesting curiosity rather than a vital element to consider. It should also be noted that whilst the velocity of a propagating wave shows inverse dependence on the material density, this is more than compensated for with the linear dependence on density in the acoustic impedance equation (eq 5.2).

The material constants, which determine the acoustic impedance mismatch, are known well on a macroscopic level, but far less is known about the variations at a microstructural level. The standard materials constants are all merely the averages over the bulk of the sample. This means these values remain fairly consistent due to the large number of data points contributing to the total. The problem here is that the consistently averaged value masks large variations which occur at a microstructural level, for example within grains due to anisotropy with crystallographic orientation, which can manifest itself in bulk samples with strong crystallographic texture [Davis et al., 2008]. The average is entirely suitable for most materials research topics, where the bulk of the sample is of interest. But in this research context the ultrasonic signal is dependent on each individual variation at every interface, and merely considering the bulk ignores the subtlety of microstructural interactions. For the remainder of this chapter the values C11=229.3, C12=134.1, C44=116.7 shall be used, these being the single crystal moduli for iron in GPa [Du and Turner, 2014].

5.2.3. Calculation

To determine ultrasonic scattering due to elastic modulus mismatch across a boundary interface it is important to be able to calculate the elastic constants for any combination of crystallographic plane orientations across the interface. As part of this work a script was developed in order to calculate the elastic constants for any combination of rotations of one plane to another. This is calculated by rotating the crystallographic orientation direction vector around an axis normal to the plane. Rotating the secondary plane by the misorientation angle around the misorientation axis allows the elastic constants to be calculated relative to the initial plane, and so allowing a comparison to be made across the interface. To ensure clear visualisation of the elastic constant variation the calculation is carried out in 1 degree increments across the full range of 360 degrees regardless of any repetition, thereby guaranteeing at least one full cycle has been considered. It should however be noted that symmetry conditions lead to repetitions of calculated results at smaller intervals than the full 360 degree rotation, Figures 5.1 and 5.2 display results which repeat with a 180 degree interval for instance.

It is important to note that a simplification has been made in the calculation of the longitudinal velocity (figure 5.2) from the calculated elastic constants (figure 5.1). It is assumed the isotropic longitudinal velocity equation (equation 5.1) holds, thereby using a first-order approximation. In reality the Christoffel equation should be used; however this has been omitted due to the increased complexity.

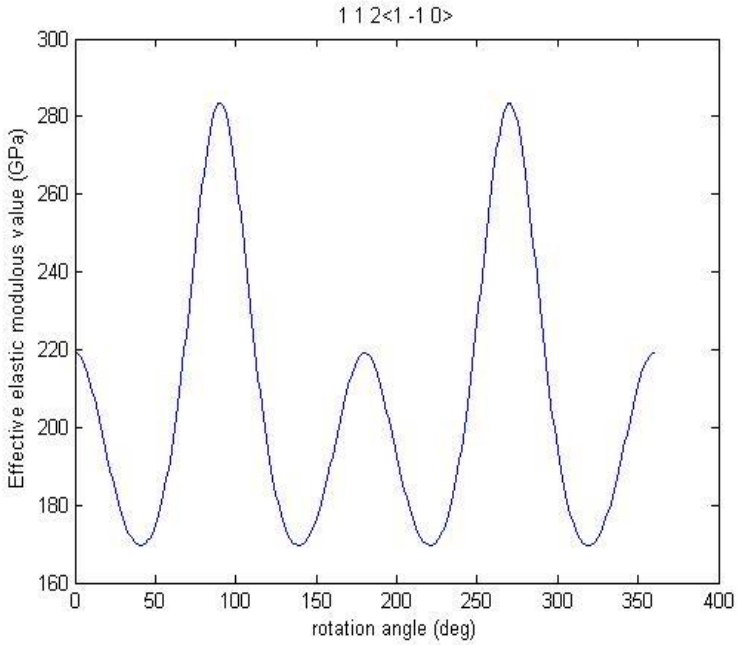

Figure 5.1: Elastic modulus variation relative to the rolling direction for the {112} <1 -1 0> texture component. Recreating a graph from [Davis et al., 2008] using the script in appendix D.

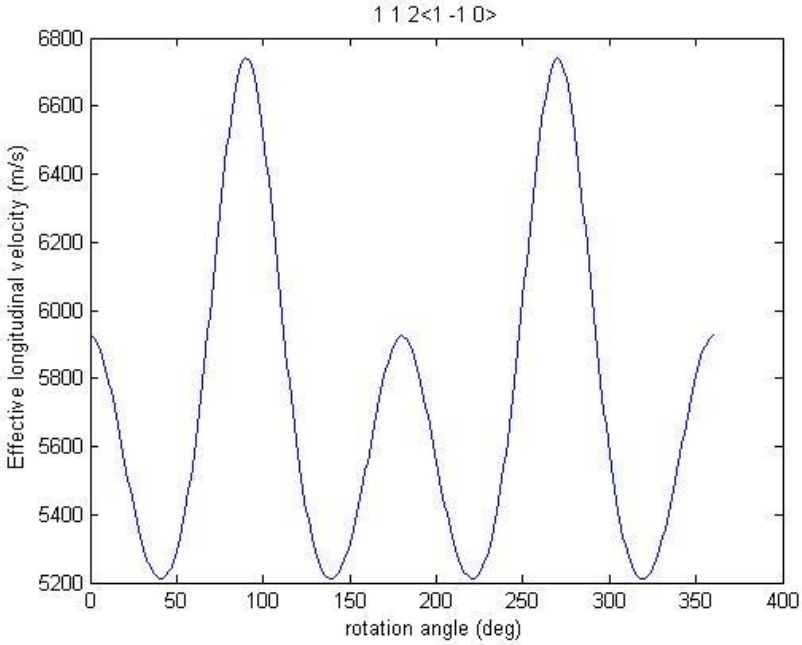

Figure 5.2: the elastic modulus variation of Figure 5.1 has been used to show the resultant change in longitudinal velocity.

The elastic modulus varies considerably depending on the crystallographic orientation, as demonstrated in Figure 5.1. It is critical to understand the mismatch at the transition from one orientation to another across a boundary. In order to achieve this, the script compares

the values from both sides of the transition separated by a given angle, which corresponds to the misorientation axis/angle pair between the respective directions of each crystallographic plane; this is determined by the orientation relationship for that type of microstructure.

The calculation itself is based on the work by Bunge [Bunge, 1982], showing the calculation of the elastic modulus values for different textures in a cubic crystalline structure. It should be noted that y_1, y_2 and y_3 are the directional components (directional cosines) of the arbitrary direction y, the reference direction for the particular microstructural feature.

$$\frac{1}{\tilde{E}(y)} = {y_1}^4 \cdot \tilde{s}_{1111} + {y_2}^4 \cdot \tilde{s}_{2222} + {y_3}^4 \cdot \tilde{s}_{3333} + 2 \cdot {y_1}^2 \cdot {y_2}^2 \cdot (\tilde{s}_{1122} + 2 \cdot \tilde{s}_{1212}) + 2 \cdot {y_1}^2 \cdot {y_3}^2 \cdot (\tilde{s}_{1133} + 2 \cdot \tilde{s}_{1313}) + 2 \cdot {y_2}^2 \cdot {y_3}^2 \cdot (\tilde{s}_{2233} + 2 \cdot \tilde{s}_{2323}) \quad (5.4)$$

This is then factorised down using the equivalencies in their condensed form

$$s_{1111} = S_{11} \quad (5.5)$$

$$s_{2222} = S_{22} \quad (5.6)$$

$$s_{3333} = S_{33} \quad (5.7)$$

$$s_{1122} = S_{12} \quad (5.8)$$

$$s_{1212} = S_{66} \tag{5.9}$$

$$s_{1133} = S_{13} \tag{5.10}$$

$$s_{1313} = s_{3113} = s_{3131} = S_{55} \tag{5.11}$$

$$s_{2233} = S_{23} \tag{5.12}$$

$$s_{2323} = S_{44} \tag{5.13}$$

As well as the following equivalencies for cubic symmetries:

$$S_{44} = S_{55} = S_{66} \tag{5.14}$$

$$S_{11} = S_{22} = S_{33} \tag{5.15}$$

$$S_{12} = S_{13} = S_{23} \tag{5.16}$$

Resulting in the equation in its final form

$$\frac{1}{E(y)} = {y_1}^4 \cdot S_{11} + {y_2}^4 \cdot S_{11} + {y_3}^4 \cdot S_{11} + 2 \cdot {y_1}^2 \cdot {y_2}^2 \cdot \left(S_{12} + \frac{S_{44}}{2}\right) + 2 \cdot {y_1}^2 \cdot {y_3}^2 \cdot \left(S_{13} + \frac{S_{44}}{2}\right) + 2 \cdot {y_2}^2 \cdot {y_3}^2 \cdot \left(S_{23} + \frac{S_{44}}{2}\right) \quad (5.17)$$

Using the following equations to calculate the compliance constants:

$$S_{11} = \frac{C_{11} + C_{12}}{{C_{11}}^2 + C_{11} \cdot C_{12} - 2 \cdot {C_{12}}^2} \quad (5.18)$$

$$S_{12} = \frac{-C_{12}}{{C_{11}}^2 + C_{11} \cdot C_{12} - 2 \cdot {C_{12}}^2} \quad (5.19)$$

$$S_{44} = \frac{1}{C_{44}} \quad (5.20)$$

This equation allows for the elastic modulus to be calculated for cubic crystals for any angle within a given plane (texture). The only requirement being the knowledge of standard material constants (C11=229.3, C12=134.1, C44=116.7 are the single crystal moduli for iron in GPa) and the textures expected in steels. All Figures have been recreated from [Davis et al., 2008], using the script in appendix D, implying both the script and the calculation are correct.

5.2.4. Application

With the use of the above calculation it is possible to compare the scattering induced by each boundary interface individually and use this knowledge to make a direct comparison with other boundaries. In order to appropriately interpret the results of this exercise it is

advantageous to generate some standard results to act as a reference. As boundary reflection is dependent on differences in acoustic impedance which in turn depends on density and/or acoustic velocity, the large differences associated with water and air compared to steel can be used. As the acoustic impedance mismatch is already so large the variations presented by the crystallography of the steel are so small as to be merely a rounding error, and so can be ignored for now to aid understanding.

Table 5.1 shows the calculated results for a boundary between the aggregate (bulk) values for a steel/water and steel/air boundary. It should be noted that these values are simplified by omitting the temperature and humidity variation of acoustic propagation velocity of air or the temperature and salinity aspect of water. The steel/water interface is the explicit calculation of an example used to illustrate the ultrasonic signal loss at the steel interface in an immersion bath test setup (Figure 3.1).

Table 5.1: Calculated values for boundary reflection coefficient for standard acoustic interface scenarios.

Interface	Density (kg/m^3)	Acoustic velocity (m/s)	Boundary reflection coefficient (equation 5.3)
Steel/air	7700/1.225	5960/343	0.999963
Steel/water	7700/997	5960/1482	0.87912

The values presented in table 5.1 are just as were expected with virtually total reflection between a steel/air interface. These example values can be used as a reference point when examining the other boundaries of this work. As the acoustic impedance mismatch is not nearly as extreme across a grain boundary (or other microstructural feature) it is expected the boundary reflection influence to be less severe.

Boundary reflection coefficients for various orientation relations can be calculated for all variations with the use of the methods described above. Using the information provided in

[Suikkanen et al., 2011], it is possible to now compute the boundary reflection coefficients associated with the Nishiyama-Wassermann orientation relationship (N-W OR). This orientation relationship was chosen primarily due to the already established misorientation angle/axis calculation between all variants (tables 5.2 and 5.3), as this simplifies the process and removes further possibility for error. Both N- W OR and K-S OR (Kurdjumov– Sachs orientation relationship) are the most common relationships used to describe bcc- fcc systems [Kral, 2012], as is the case for martensite and bainite. It should be noted that the N-W OR and K- S OR are in fact closely related to one another, with a small rigid body rotation (5.26°) around a common axis transforming one into the other [Strangwood, 2012; Dahmen, 1982]. Comparisons between the variants V2- V12 of the N- W OR are made relative to variant V1. The details of the variants and misorientation associated with every possible permutation of the N-W OR are provided in tables 5.2 and 5.3, with resultant boundary reflection coefficients presented in table 5.4.

Table 5.2: Table showing the 12 variants associated with the N-W OR and the misorientation relative to variant 1 [Suikkanen et al., 2011]

Variant	Orientation $(hkl)[uvw]$	Relative orientation in respect to Variant 1	
		Misorientation angle,	Misorientation axis
V1	(-0.71 0.70 0.12) [0.00 -0.17 0.99]	–	–
V2	(-0.71 0.12 0.70) [0.71 -0.12 0.70]	60.0	[0.00 -0.71 -0.71]
V3	(0.00 0.99 -0.17) [-0.71 0.12 0.70]	60.0	[0.00 0.71 0.71]
V4	(-0.71 0.99 -0.17) [-0.00 0.169 0.99]	19.5	[1.00 0.00 0.00]
V5	(-0.70 0.12 0.71) [0.70 -0.12 0.71]	53.7	[-0.22 -0.70 0.68]
V6	(-0.17 0.99 0.00) [-0.70 -0.12 0.70]	53.7	[-0.22 0.70 0.68]
V7	(-0.70 0.71 0.12) [0.17 0.00 0.99]	13.7	[0.71 -0.71 -0.06]
V8	(-0.12 0.71 .070) [-0.12 -0.71 0.70]	53.7	[0.68 -0.22 0.70]
V9	(-0.99 0.17 0.00) [-0.12 -0.70 0.71]	50.0	[-0.62 0.47 -0.62]
V10	(-0.12 0.70 0.71) [-0.17 0.00 0.99]	13.7	[0.71 0.71 0.06]
V11	(-0.12 0.70 0.71) [0.12 -0.70 0.71]	50.0	[-0.62 0.47 0.62]
V12	(-0.99 0.00 0.17) [0.12 -0.71 0.70]	53.7	[-0.68 0.22 0.70]

Table 5.3: Table showing the full list of possible misorientations of the N-W OR [Suikkanen et al., 2011]

Op	Misorientation	Axis	Axis (low-index Miller indices)	Between variants*
O_1	60.0°	<0.00 0.71 0.71>	<011>	V1–V2, V1–V3, V2–V3, V4–V5, V4–V6, V4–V5 V7–V8, V7–V9, V8–V9, V10–V11, V10–V12, V11–V12
O_2	53.7°	<0.22 0.70 0.68>	< 133 >	V1–V5, V1–V6, V1–V8, V1–V12, V2–V4, V2–V7, V2–V9, V2–V12, V3–V4, V3–V8, V3–V10, V3–V11, V4–V9, V4–V11, V5–V9, V5–V10, V5–V12, V6–V7, V6–V8 V6–V11, V7–V11,V7–V12, V8–10, V9–V10
O_3	50.0°	<0.63 0.47 0.63>	< 434 >	V1–V9, V1–V11, V2–V6, V2–V10, V3–V5, V3–V7, V4-V8, V4-V12, V5-V7, V6–V10, V8–V12, V9–V11
O_4	19.5°	<1.00 0.00 0.00>	< 100 >	V1–V4, V2–V8, V3–12, V5–V11, V6–V9, V7–V10
O_5	13.8°	<0.06 0.68 0.70>	< 011 >	V1–V7, V1–10, V2–V5, V2–V11, V3–V6, V3–V9, V4–V7, V4–V10, V5–V8, V6–12, V8–V11, V9–V12

Note: ∗ for example V1–V2 and V2–V1

Table 5.4: Table showing the calculated boundary reflection coefficients of each variant relative to variant V1. Misorientation angle and axis from table 5.2 is used.

Variant	Misorientation angle	Misorientation axis	Boundary reflection coefficient
V2	60°	[0.00 -0.71 -0.71]	0.0058
V3	60°	[0.00 0.71 0.71]	0.0039
V4	19.5°	[1.00 0.00 0.00]	0.0020
V5	53.7°	[-0.22 -0.70 0.68]	0.0048
V6	53.7°	[-0.22 0.70 0.68]	0.0043
V7	13.7°	[0.71 -0.71 -0.06]	~0
V8	53.7°	[0.68 -0.22 0.70]	0.0051
V9	50°	[-0.62 0.47 -0.62]	0.0048
V10	13.7°	[0.71 0.71 0.06]	0.0026
V11	50°	[-0.62 0.47 0.62]	0.0070
V12	53.7°	[-0.68 0.22 0.70]	0.0040

Table 5.5: Table 5.4 restated in decreasing order of misorientation angle.

Variant	Misorientation angle	Misorientation axis	Boundary reflection coefficient
V2	60°	[0.00 -0.71 -0.71]	0.0058
V3	60°	[0.00 0.71 0.71]	0.0039
V8	53.7°	[0.68 -0.22 0.70]	0.0051
V5	53.7°	[-0.22 -0.70 0.68]	0.0048
V6	53.7°	[-0.22 0.70 0.68]	0.0043
V12	53.7°	[-0.68 0.22 0.70]	0.0040
V11	50°	[-0.62 0.47 0.62]	0.0070
V9	50°	[-0.62 0.47 -0.62]	0.0048
V4	19.5°	[1.00 0.00 0.00]	0.0020
V10	13.7°	[0.71 0.71 0.06]	0.0026
V7	13.7°	[0.71 -0.71 -0.06]	~0

As is evident from tables 5.4 and 5.5 there is a clear distinction by misorientation angle in terms of the calculated “boundary reflection coefficient”. This term is used in this work to signify the scattering significance of a microstructural feature. There appears to be a clear tendency towards a larger boundary reflection coefficient for the variant combinations

associated with a large misorientation angle. Whilst the cut-off between a high and low angle grain boundary is typically assumed to be 15 °, this does not seem an appropriate distinction to make here. The two groupings, above 50 ° and below 20 °, seem to suggest the cut-off is somewhere between these values. Whilst it may be appealing to simply alter the cut-off associated with “high-angle/low-angle” designation, this would seem dubious given the relatively small range of data points.

Table 5.6: Table listing the 24 total variants of K-S OR, along with the misorientation angle/axis relative to variant V1 [Kitahara et al., 2006]

Variant no.	Crystal orientations of martensite variants									Misorientation angle from V1 (°)	Misorientation axis between V1 and other variants			
	(	*h*	*k*	*l*	)	[	*u*	*v*	*w*	]		[			]
V1	(	−0.075	−0.167	0.983	)	[	0.742	0.650	0.167	]	–	[	–	–	–	]
V2	(	−0.650	0.167	0.742	)	[	0.167	0.983	−0.074	]	60.00	[	0.577	0.577	−0.577	]
V3	(	−0.742	0.167	0.650	)	[	0.667	0.075	0.742	]	60.00	[	0.000	0.707	0.707	]
V4	(	0.075	−0.167	0.983	)	[	0.667	0.742	0.075	]	10.53	[	0.000	−0.707	−0.707	]
V5	(	0.667	0.075	0.742	)	[	0.075	0.983	−0.167	]	60.00	[	0.000	−0.707	−0.707	]
V6	(	−0.667	0.075	0.742	)	[	0.742	0.167	0.650	]	49.47	[	0.000	0.707	0.707	]
V7	(	0.167	−0.650	0.742	)	[	0.983	0.167	−0.075	]	49.47	[	−0.577	−0.577	0.577	]
V8	(	−0.167	−0.075	0.983	)	[	0.650	0.742	0.167	]	10.53	[	0.577	0.577	−0.577	]
V9	(	0.075	−0.667	0.742	)	[	0.167	0.742	0.650	]	50.51	[	−0.615	0.186	−0.767	]
V10	(	0.075	−0.742	0.667	)	[	0.983	0.167	0.075	]	50.51	[	−0.739	−0.462	0.490	]
V11	(	−0.167	0.075	0.983	)	[	0.742	0.667	0.075	]	14.88	[	0.933	0.354	0.065	]
V12	(	−0.742	−0.167	0.650	)	[	0.667	−0.075	0.742	]	57.21	[	−0.357	0.603	0.714	]
V13	(	0.167	−0.075	0.983	)	[	0.742	0.667	−0.075	]	14.88	[	0.354	−0.933	−0.065	]
V14	(	−0.167	−0.650	0.742	)	[	0.075	0.742	0.667	]	50.51	[	−0.490	0.462	−0.739	]
V15	(	−0.167	−0.742	0.650	)	[	0.983	−0.075	0.167	]	57.21	[	−0.738	−0.246	0.628	]
V16	(	0.167	0.075	0.983	)	[	0.650	0.742	−0.167	]	20.61	[	0.659	−0.659	−0.363	]
V17	(	−0.075	−0.742	0.667	)	[	0.167	0.650	0.742	]	51.73	[	−0.659	0.363	−0.659	]
V18	(	−0.075	−0.667	0.742	)	[	0.983	0.075	0.167	]	47.11	[	−0.719	−0.302	0.626	]
V19	(	−0.742	−0.075	0.667	)	[	0.650	0.167	0.742	]	50.51	[	−0.186	0.767	0.615	]
V20	(	−0.667	−0.075	0.742	)	[	0.075	0.983	0.167	]	57.21	[	0.357	0.714	−0.603	]
V21	(	−0.075	0.167	0.983	)	[	0.667	0.742	−0.075	]	20.61	[	0.955	0.000	−0.296	]
V22	(	−0.650	−0.167	0.742	)	[	0.742	0.075	0.667	]	47.11	[	−0.302	0.626	0.719	]
V23	(	0.650	−0.167	0.742	)	[	0.167	0.983	0.075	]	57.21	[	−0.246	−0.628	−0.738	]
V24	(	0.075	0.167	0.983	)	[	0.742	0.650	−0.167	]	21.06	[	0.912	−0.410	0.000	]

Table 5.6 lists the full 24 crystallographic variants associated with the Kurdjumov-Sachs Orientation Relation. All variant misorientation, relative to variant V1, have been listed by angle/axis pair, and so these shall also be calculated in order to determine the similarity to the N- W OR boundary reflection calculations.

Table 5.7: Table showing the calculated boundary reflection coefficients of each variant V2 - V24 compared with variant V1 of the Kurdjumov-Sachs Orientation Relation (K-S OR) ordered by misorientation angle – highest to lowest.

Variant	Misorientation angle	Misorientation axis	Boundary reflection coefficient
V1-V2	60°	0.577 0.577 -0.577	0.0032
V1-V3	60°	0 0.707 0.707	0.0027
V1-V5	60°	0 -0.707 -0.707	0.0052
V1-V12	57.21°	-0.357 0.603 0.714	0.0032
V1-V15	57.21°	-0.738 -0.246 0.628	0.0030
V1-V20	57.21°	0.357 0.714 -0.603	0.0015
V1-V23	57.21°	-0.246 -0.628 -0.738	0.0036
V1-V17	51.73°	-0.659 0.363 -0.659	0.0017
V1-V9	50.51°	-0.615 0.186 -0.767	0.0024
V1-V10	50.51°	-0.739 -0.462 0.490	0.0019
V1-V14	50.51°	-0.490 0.462 -0.739	0.0023
V1-V19	50.51°	-0.186 0.767 0.615	0.0019
V1-V6	49.47°	0.000 0.707 0.707	0.0019
V1-V7	49.47°	-0.577 -0.577 0.577	0.0036
V1-V18	47.11°	-0.719 -0.302 0.626	0.0015
V1-V22	47.11°	-0.302 0.626 0.719	0.0024
V1-V24	21.06°	0.912 -0.410 0.000	0.0018
V1-V16	20.61°	0.659 -0.659 -0.363	0.0020
V1-V21	20.61°	0.955 0.000 -0.296	0.0007
V1-V11	14.88°	0.933 0.354 0.065	0.0002
V1-V13	14.88°	0.354 -0.933 -0.065	0.0009
V1-V4	10.53°	0.000 -0.707 -0.707	0.0002
V1-V8	10.53°	0.577 0.577 -0.577	0.0001

Broadly speaking, table 5.7 shows the same trend as discussed for the N-W OR in tables 5.4 and 5.5, a decreasing boundary reflection coefficient with decreasing misorientation angle. This trend is as expected, however the values associated with the K-S OR in table 5.7 appear to be somewhat lower than that of the N-W OR values. As a result of the more narrow range of boundary reflection coefficient of the K-S OR than for the N-W OR, there does not appear to be the same degree of separation between low angle and high angle boundaries. However the more general trend of a positive correlation between misorientation angle and calculated boundary reflection coefficient does appear to hold across both orientation relations. The overall reasonable agreement would be expected as the two orientation relations are reasonable close to one another.

5.2.5. Limitations of the Boundary reflection coefficient presented in this form

It should be noted that each of the coefficients presented above is the arithmetic average (mean) of each reflection coefficient of the various pairs rotated in 1 degree increments. This may at first appear to add unnecessary confusion, but is required to account for the ultrasonic wave propagation path being arbitrary with respect to the pre-set unrotated orientation axis of the microstructure it interacts with. However, by using the equally weighted average of each rotational angle a simplifying assumption is made. The propagating wave would tend towards a slight refraction at the scattering boundaries, resulting in the tendency to favour alignment along certain propagation angles and avoid others. This self-selective action would be the same principle as that of beam refraction effects (chapter 3.1.5.), and so there is likely to be a tendency towards lower reflection coefficient pathways selection.

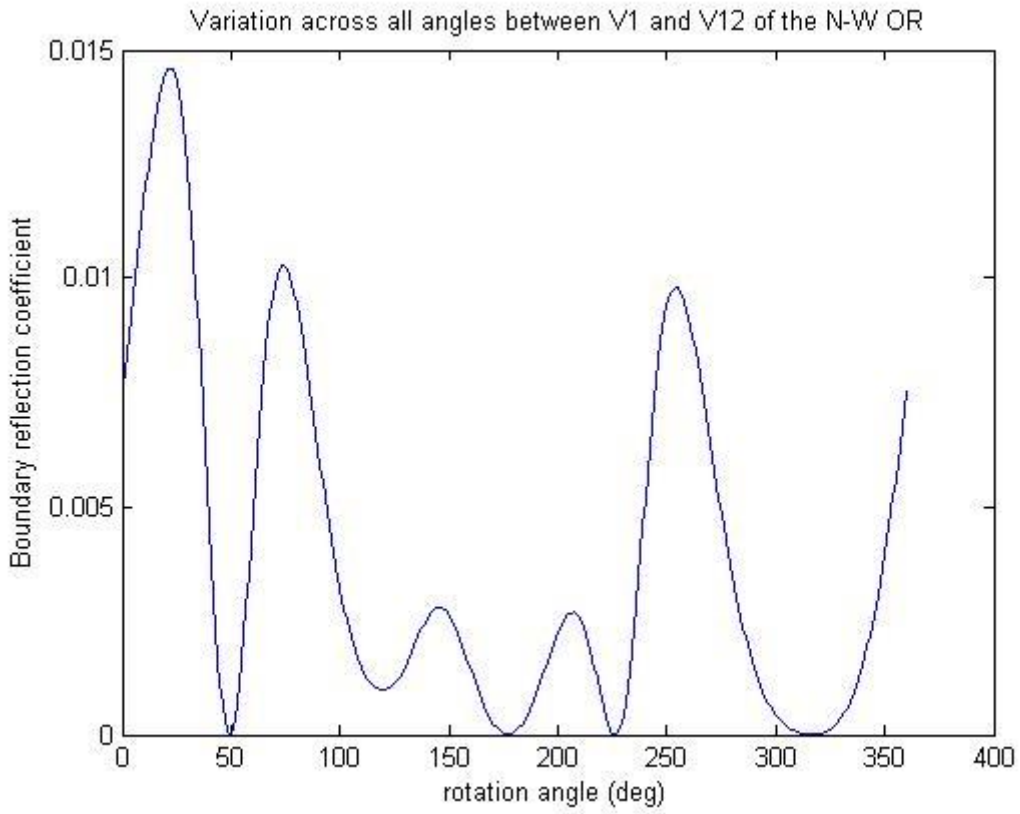

Figure 5.3: Generated boundary reflection coefficients across the full range of potential propagation path encounters. The image indicates the large range which is possible for a given variant pair (V1 and V12 which is the final row in table 5.4), the average being 0.0040, but a low of 0 and high of nearly 0.015 are also found.

Figure 5.3 shows the full range of boundary reflection coefficient values in 1 degree increments. This differs from the same entry of the same variants in table 5.4 as the Figure plots the variation of potential wave propagation direction, whereas the table entry is simply the average (mean) of all of these points. Figure 5.3 indicates a large range of potential scattering of a boundary. Each point in the plot represents the same boundary, which in this particular example represents a misorientation of 53.7° along the misorientation axis [-0.68 0.22 0.70], but every variation of initial wave propagation path is accounted for. As there is no simple method for prediction of which is more likely, due to preferential selection, they have all being given an equal probability weighting. Therefore the average values produced in the tables above are merely an attempt to represent this complexity. The preferential path selection question would be an interesting topic in its own

right but is not pursued as part of this work. It would potentially be well suited to a computer modelling extension as part of future work (potentially using a ray tracing model to simulate the refraction at each interface due to the acoustic impedance mismatch). But the additional complexity would put this beyond the scope of this project. It is important to be aware of the fact the misorientation angle between the two variants remains the same throughout Figure 5.3; it is in fact the ultrasonic wave propagation path which is being varied by calculating every one of the 360 possible (integer) angles.

5.2.6. Small feature cut-off

It is generally known (see discussion in chapter 3 for details) that large features tend to have a greater impact on ultrasonic scattering than smaller ones. But how small would a feature have to be for it to be considered too small? For instance carbides tend to be small, of the order of a micron or below, so are they even of sufficient size to contribute to overall scatter? A potential mechanism was introduced in section 3.1.2, whereby ultrasonic significance could be calculated in terms of feature size (equation 3.1). The equation was originally intended to calculate the significance of a bounding layer, or even a band of air, with a small enough layer being completely invisible from an ultrasonic perspective.

Equation 3.1 allows the scattering significance to be calculated directly from the acoustic impedance ratio between the respective media on either side of the interface, and the feature size, and can therefore be adapted to any material type. It should be noted that strictly speaking this calculation assumes a narrow band of infinite length, encountered at a perfectly perpendicular angle of incidence. As this condition can never be satisfied in reality, it is important to understand that a simplifying assumption is made in this regard. However, that being said, a direct attempt to account for all of the necessary amendments would

require adding significant levels of complexity, and so is beyond the scope of this project. The two main issues which would need to be compensated for are the angle of incidence, which has been done on a macro scale for the main interface boundary categories [Krautkramer and Krautkramer, 1990], and the intermittency of the encountered carbides. The experimental work used to verify the original air gap theoretical predictions (fig 3.2), showed the potential impact of an imperfect boundary layer, in this case it was suggested to be a cleanness issue [Clark and Chaskelis, 1982]. The results show a clear trend to decreasing feature significance as it deviates from the perfect theoretical value. Figure 3.3 indicates that the true experimental values result in an air gap of several orders of magnitude larger than the theoretical prediction required for the reflection to be of relevance. Therefore, it is logical to conclude any deviation of the carbide layer (or any other feature) away from the perfect theoretical value of an infinite band would also result in a reduced significance of the feature. However, without the ability to estimate the extent of the theoretical to experimental deviation (due to imperfection etc.), the theoretical value shall be adopted as predicted by acoustic theory. The ability to put a limiting bound on the significance of carbides based on size and density would in fact prove extremely valuable and shall now be developed below.

The original equation (eq 3.1) has been adapted into a simple Matlab script to predict feature significance, the code can be found in appendix F. The inputs for the script being the impedance ratio of the first medium (steel) relative to the second (carbide layer), in this case r=0.771, the velocity of the medium is assumed to be 5300 m/s for carbides and 5960 m/s for steel, along with density of 6680 kg/m^3 and 7700 kg/m^3 respectively.

There are two key trends to understand with this calculation; these are with respect to feature size/wavelength ratio and similarity of the two impedance values associated with the primary medium and the boundary layer. Firstly, all things being equal a larger feature size to wavelength ratio will present more significant scatter up to the full value associated with the boundary reflection coefficient. Secondly, the closer the respective density and velocity levels of the two media are, the lower the proportion of reflected signal; this is due to the reduced overall scattering potential of the boundary, as is calculated with the boundary reflection coefficient.

Table 5.8: Calculated values for boundary reflection coefficient for standard acoustic interface scenarios of steel/air and steel/water, alongside the steel/carbide interface value used in conjunction with Figure 5.4.

Interface	Density (kg/m^3)	Acoustic velocity (m/s)	Boundary reflection coefficient (equation 5.3)
Steel/air	7700/1.225	5960/343	0.999963
Steel/water	7700/997	5960/1482	0.87912
Steel/carbide	7700/6680	5960/5300	0.0166

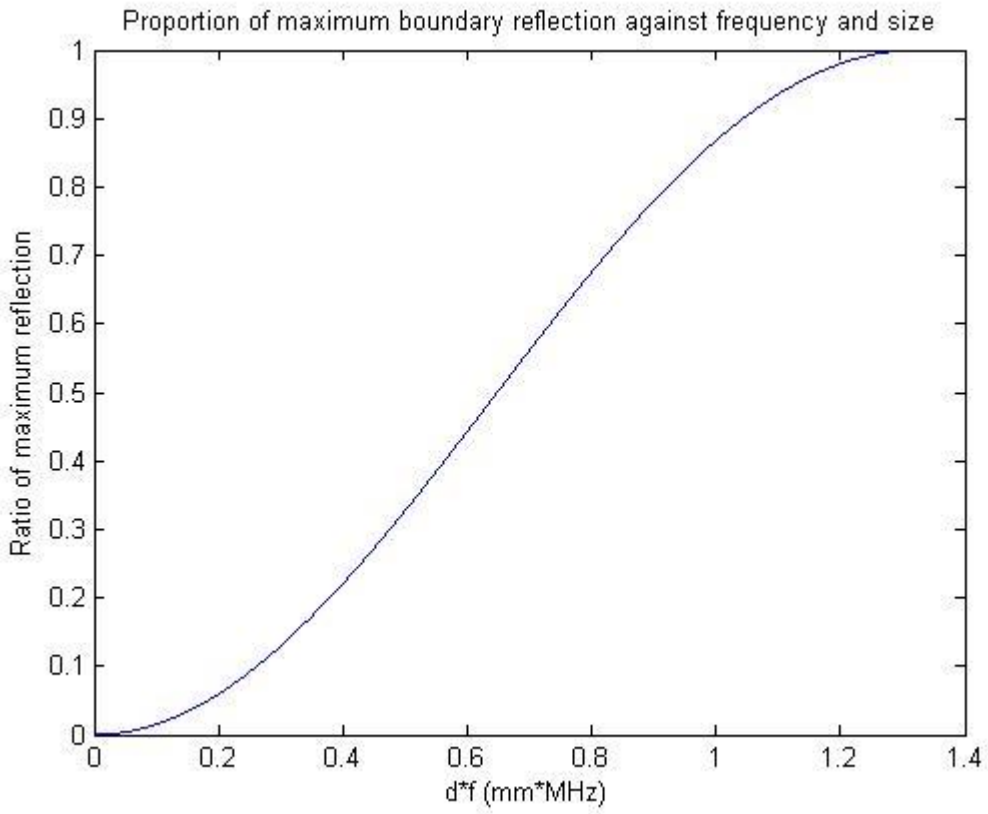

Figure 5.4: Proportion of maximum boundary reflection of carbide by size and frequency.

As is evident from the results of Figure 5.4, where d is boundary layer thickness and f is frequency, the results are dependent on the frequency of the ultrasonic signal. This is reasonable as it is the relative size of the reflective layer to the wavelength which determines boundary reflectivity. It should be noted that the peak reflectivity ratio (the boundary reflectivity coefficient), is determined by the relative impedance values of the two media, as was used in the previous section. In this case it is 1.66% (or 0.0166); for comparison the values for a steel/water interface and a steel/air interface (first shown in table 5.1) are restated in table 5.8 alongside the steel/carbide interface. As is evident from table 5.8, the far smaller acoustic impedance mismatch associated with the steel/carbide interface results in a significantly reduced scattering potential of this boundary relative to air or water.

The results presented in Figure 5.4 show how even reasonably strong ultrasonic scattering features (boundary reflection coefficient of 0.0166) can have severely reduced influence due to the relatively small feature size. As an example, a 10 MHz ultrasonic wave would have to encounter a steel/carbide boundary which is associated with a ~100 µm carbide layer thickness for ~1.5 % incident wave energy reflection. For the more realistic carbide size of 1 µm, this reflected signal value would be reduced to a rounding error (0.01 on the x- axis of Figure 5.4). Therefore it appears as though the scatter induced by carbide precipitation is negligible for realistic size distributions (approximately a micron or below). From Figure 5.4 it appears as though reflectivity reaches a maximum at approximately a quarter wavelength, which seems reasonable as it would fall into the upper region of the Rayleigh regime precisely where the transition region begins [Van Pamel, 2015].

Similarly to the analysis of carbides, other microstructural features can be examined for their influence when encountered at a small scale, such as martensitic lath boundaries. The resultant graph (Figure 5.5) appears very similar to the carbide calculation (Figure 5.4), but on closer examination it is evident the curve has shifted slightly towards the right. This is due to the slightly closer impedance mismatch. The values for variant 1-23 of the K-S OR were used to generate this curve, with a boundary reflection coefficient of 0.0036, impedance ratio (r) of 1.0569 and an average longitudinal velocity of 5510 ms^{-1}, as generated by the boundary reflection calculation (Appendix E).

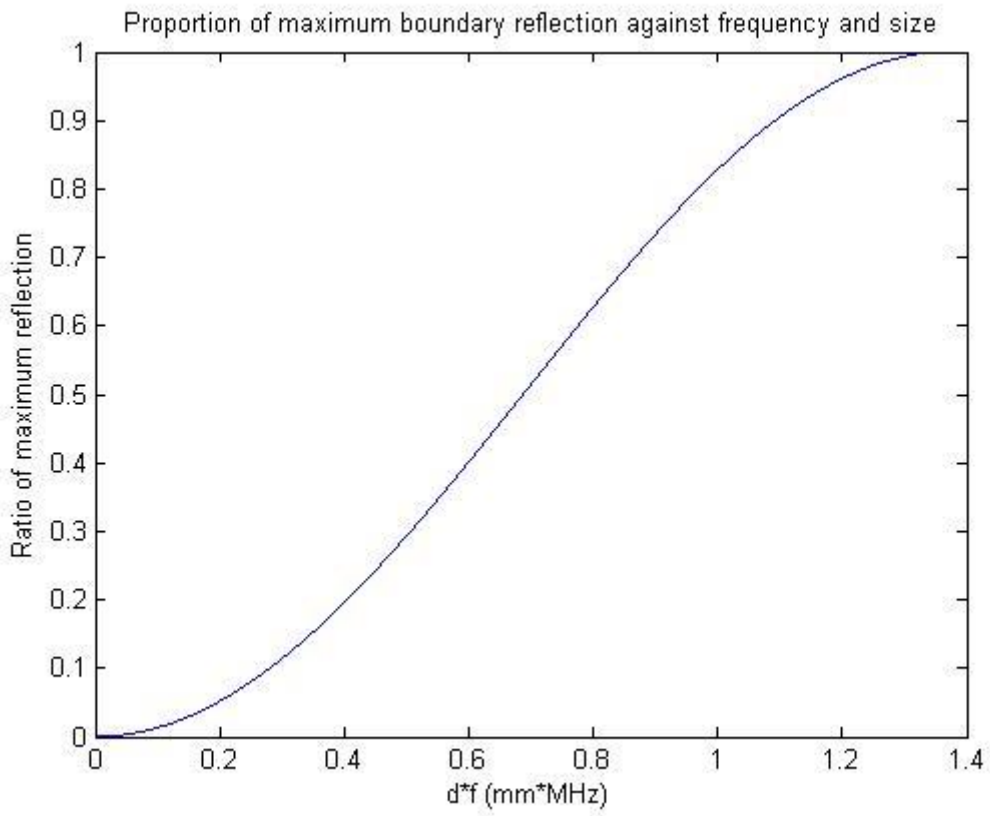

Figure 5.5: Proportion of maximum boundary reflection of variant 1 and 23 of K-S OR by size and frequency.

Once again Figure 5.5 indicates maximum reflection around the quarter wavelength point (wavelength equivalent to a normalised feature size of ~ 5.5 mm * MHz), the curve also tends towards zero below approximately $\frac{1}{40}$ of the wavelength. This rough wavelength based estimate provides some indication as to the significance of the reduction in scattering as a result of small boundary interfaces. It also indicates that smaller microstructural features (carbides, laths, lamellae etc.) should have minimal influence on an overall scattering estimate.

5.3. The Simple Model (Pearlite)

As has been discussed in the literature review section (section 3), many groups have contributed to the understanding of how to adequately model ultrasonic attenuation of complex microstructures. However there is one paper in particular [Du and Turner, 2014], which describes attenuation in a two phase (pearlite – consisting of ferrite and cementite lamellae) microstructure that provided the inspiration for the core principles explored during this project i.e. consideration of attenuation in martensitic power generation grade steels. The argument for using the pearlite model initially can be drawn from the work of Papadakis (as discussed in 3.3.2.). The argument stated that the total scattering of a microstructure with associated internal boundaries is the sum of the internal features individual scattering and the original grain scatter as a unit. Therefore, if this pearlite model holds, then a simple extension can be made to calculate the total scatter associated with martensitic microstructure.

The same notation as used in that paper is used throughout this work. The starting point is to define the contributions to total longitudinal and transverse attenuation, as shown in equations 5.21 and 5.22.

$$\alpha_{longitudinal} = \alpha_{LL} + \alpha_{LT} \tag{5.21}$$

$$\alpha_{transverse} = \alpha_{TT} + \alpha_{TL} \tag{5.22}$$

Here the subscripts L and T represent longitudinal and transverse waveforms respectively. The terms are represented in this form in order to indicate their wave-type, both before and after a scattering event have occurred. α_{LL} and α_{TT}therefore represent longitudinal and transverse waves which

remain unchanged. α_{LT} and α_{TL}account for mode conversion taking place. These individual contributions can be represented by eq 5.23-5.26 for simple, single phase interactions such as grain boundary scatter, originally calculated by [Weaver, 1990].

$$\alpha_{LL} = \frac{\pi^2\omega^4}{2{C_L}^8}\int_{-1}^{+1}\left[\tilde{\eta}_{LL(\theta_{PS})}N_{1(\theta_{PS})}\right]\mathrm{d}\left(cos_{(\theta_{PS})}\right) \tag{5.23}$$

$$\alpha_{TT} = \frac{\pi^2\omega^4}{2{C_T}^8}\int_{-1}^{+1}\left[\tilde{\eta}_{TT(\theta_{PS})}(N_{3(\theta_{PS})} - 2N_{2(\theta_{PS})} + N_{1(\theta_{PS})})\right]\mathrm{d}(cos_{(\theta_{PS})}) \tag{5.24}$$

$$\alpha_{LT} = \frac{\pi^2\omega^4}{2{C_L}^3{C_T}^5}\int_{-1}^{+1}\left[\tilde{\eta}_{LT(\theta_{PS})}(N_{2(\theta_{PS})} - N_{1(\theta_{PS})})\right]\mathrm{d}(cos_{(\theta_{PS})}) \tag{5.25}$$

$$\alpha_{TL} = \frac{{C_T}^2}{2{C_L}^2}\alpha_{LT} \tag{5.26}$$

The angle θ_{PS} is the angle used to represent the degree of deviation between the incoming incident wave and the subsequent scattered wave; they are represented by the unit vectors $\hat{\boldsymbol{p}}$ and $\hat{\boldsymbol{s}}$ respectively. $\tilde{\eta}$ is the spatial Fourier transform of the two-point autocorrelation function as described in section 3, this is the size estimate of the feature and has been calculated for a variety of feature shapes. The four combinations of $\tilde{\eta}$ are shown in equations 5.27-5.29, where $\tilde{\eta}_{LL(\theta_{PS})}$ (eq 5.27) is associated with longitudinal wave and $\tilde{\eta}_{TT(\theta_{PS})}$ (eq 5.28) with transverse wave, both with no mode conversion occurring. $\tilde{\eta}_{LT(\theta_{PS})} and\ \tilde{\eta}_{TL(\theta_{PS})}$ (eq 5.29) account for the respective mode conversion.

$$\tilde{\eta}_{LL(\theta_{PS})} = \frac{L^3}{\pi^2[1 + 2K_L^2L^2(1 - cos_{(\theta_{PS})})]^2} \tag{5.27}$$

$$\tilde{\eta}_{TT^{(\theta_{PS})}} = \frac{L^3}{\pi^2[1 + 2K_T^2L^2(1 - cos_{(\theta_{PS})})]^2} \tag{5.28}$$

$$\tilde{\eta}_{LT^{(\theta_{PS})}} = \tilde{\eta}_{TL^{(\theta_{PS})}} = \frac{L^3}{\pi^2[1 + K_L^2L^2 + K_T^2L^2 - 2K_LK_TL^2cos_{(\theta_{PS})}]^2} \tag{5.29}$$

$K_L$and K_T are the wavenumbers of the longitudinal and the transverse waves respectively and are given by dividing the angular frequency (ω) by the respective velocity (C_L or C_T). L is the spatial correlation length, also used in finding the two-point autocorrelation function; it is typically the length of the grain or other feature being investigated. $N_{1^{(\theta_{PS})}}$, $N_{2^{(\theta_{PS})}}$ and $N_{3^{(\theta_{PS})}}$ are the inner products of the eighth rank covariance tensor $\Xi_{ijkl}^{\alpha\beta\gamma\delta} = \langle C_{\alpha\beta\gamma\delta}C_{ijkl}\rangle - \langle C_{\alpha\beta\gamma\delta}\rangle\langle C_{ijkl}\rangle$, where the brackets indicate the ensemble average and $C_{\alpha\beta\gamma\delta}$ is the second order elastic moduli tensor. These inner products are determined by factors which take into account the crystallography of the material and so the particular symmetry should be specified. These equations have been formulated for cubic symmetry, as is appropriate for the materials considered as part of this work (with the exception of cementite as was the case in the reference paper), however other symmetries can be calculated and indeed have been as discussed previously in section 3. The inner products $N_{1^{(\theta_{PS})}}$, $N_{2^{(\theta_{PS})}}$ and $N_{3^{(\theta_{PS})}}$ are provided in equation 5.30-5.32.

$$N_{1^{(\theta_{PS})}} = \frac{\nu^2}{\rho^2}\left(\frac{9}{525} + \frac{6}{525}cos^2{}_{(\theta_{PS})} + \frac{1}{525}cos^4{}_{(\theta_{PS})}\right) \tag{5.30}$$

$$N_{2^{(\theta_{PS})}} = \frac{\nu^2}{\rho^2}\left(\frac{24}{525} + \frac{12}{525}cos^2{}_{(\theta_{PS})}\right) \tag{5.31}$$

$$N_{3^{(\theta_{PS})}} = \frac{\nu^2}{\rho^2}\left(\frac{63}{525} + \frac{21}{525}cos^2{}_{(\theta_{PS})}\right) \tag{5.32}$$

Here $\nu = c_{11} - c_{12} - 2c_{44}$ and represents the single crystal anisotropy factor, where c_{ij} are the single crystal moduli in the respective ij direction (these constants are specific to each material, although in practice certain reference values are commonly used). ρ represents the density of the material.

Du then extended this model by using the M-factor approach by Lobkis et al., as discussed in section 3, thereby extending the applicability of the model from the previous single-phase polycrystalline material to a dual-phase material. Here grains with two components (in the case considered colony and lamellae) are considered to be the primary and secondary phase respectively, the relative contributions of which are determined by the weighting factor which is denoted with M. Therefore the single-phase equations presented previously can be rewritten to become equations 5.33-5.36.

$$\alpha_{LL} = \frac{\pi^2\omega^4}{2{C_L}^8}\int_{-1}^{+1}\left[(1-M)\tilde{\eta}_{LL^{(\theta_{PS})}}{}^{(r)}N_{1^{(\theta_{PS})}}{}^{(r)} + M\tilde{\eta}_{LL^{(\theta_{PS})}}{}^{(w)}N_{1^{(\theta_{PS})}}{}^{(w)}\right]\mathrm{d}\left(cos_{(\theta_{PS})}\right) \tag{5.33}$$

$$\begin{aligned}\alpha_{TT} = \frac{\pi^2\omega^4}{2{C_T}^8}\int_{-1}^{+1}\Big[&(1-M)\tilde{\eta}_{TT^{(\theta_{PS})}}{}^{(r)}(N_{3^{(\theta_{PS})}}{}^{(r)} - 2N_{2^{(\theta_{PS})}}{}^{(r)} + N_{1^{(\theta_{PS})}}{}^{(r)}) \\ &+ M\tilde{\eta}_{TT^{(\theta_{PS})}}{}^{(w)}(N_{3^{(\theta_{PS})}}{}^{(w)} - 2N_{2^{(\theta_{PS})}}{}^{(w)} + N_{1^{(\theta_{PS})}}{}^{(w)}\Big]\mathrm{d}(cos_{(\theta_{PS})})\end{aligned} \tag{5.34}$$

$$\begin{aligned}\alpha_{LT} = \frac{\pi^2\omega^4}{2{C_L}^3{C_T}^5}\int_{-1}^{+1}\Big[&(1-M)\tilde{\eta}_{LT^{(\theta_{PS})}}{}^{(r)}(N_{2^{(\theta_{PS})}}{}^{(r)} - N_{1^{(\theta_{PS})}}{}^{(r)}) \\ &+ M\tilde{\eta}_{LT^{(\theta_{PS})}}{}^{(w)}(N_{2^{(\theta_{PS})}}{}^{(w)} - N_{1^{(\theta_{PS})}}{}^{(w)})\Big]\mathrm{d}(cos_{(\theta_{PS})})\end{aligned} \tag{5.35}$$

$$\alpha_{TL} = \frac{{C_T}^2}{2{C_L}^2}\alpha_{LT} \tag{5.36}$$

Where r and w denote the colony and lamellae respectively. The pearlitic colonies, which can be considered as equivalent grains in the single phase case, are considered equiaxed, and so spherical. This means the correlation function as used in the single-phase version is sufficient. However the lamellae structure within a pearlitic colony is typically long and thin, therefore an ellipsoidal approximation is more suitable. Details of the ellipsoidal correlation function and how it is formed can be found in the papers by Lobkis or Du, but the Fourier transform of the correlation function of the lamellae structure ($\tilde{\eta}_{ij^{(\theta_{PS})}}{}^{(w)}$) is given by equations 5.37-5.39.

$$\tilde{\eta}_{LL^{(\theta_{PS})}}{}^{(w)} = \frac{L^2 d}{\pi^2[1 + K_L^2(L^2 + d^2)\big(1 - cos_{(\theta_{PS})}\big)]^2} \tag{5.37}$$

$$\tilde{\eta}_{TT^{(\theta_{PS})}}{}^{(w)} = \frac{L^2 d}{\pi^2[1 + K_T^2(L^2 + d^2)\big(1 - cos_{(\theta_{PS})}\big)]^2} \tag{5.38}$$

$$\tilde{\eta}_{LT^{(\theta_{PS})}}{}^{(w)} = \tilde{\eta}_{TL^{(\theta_{PS})}}{}^{(w)} = \frac{L^2 d}{\pi^2[1 + (K_L^2 + K_T^2 - 2K_L K_T cos_{(\theta_{PS})})\frac{(L^2 + d^2)}{2}]^2} \tag{5.39}$$

Here d represents lamellae spacing, the parameter used to define the width of the elongated lamellae structure where L represents its length (typically the same as the colony size). Substituting equations 5.37-5.39 into the full scattering equations (5.33-5.36), the complete two-phase lamellae model is shown by equations 5.40-5.43.

$$\alpha_{LL} = \frac{\pi^2 \omega^4}{2{C_L}^8} \int_{-1}^{+1} \left[(1 - M) \frac{L^3}{\pi^2[1 + 2K_L^2 L^2\big(1 - cos_{(\theta_{PS})}\big)]^2} N_{1^{(\theta_{PS})}}{}^{(r)} + M \frac{L^2 d}{\pi^2[1 + K_L^2(L^2 + d^2)\big(1 - cos_{(\theta_{PS})}\big)]^2} N_{1^{(\theta_{PS})}}{}^{(w)} \right] \mathrm{d}\big(cos_{(\theta_{PS})}\big) \tag{5.40}$$

$$\alpha_{TT} = \frac{\pi^2\omega^4}{2{C_T}^8}\int_{-1}^{+1}\Bigg[(1-M)\frac{L^3}{\pi^2[1+2K_T^2L^2\left(1-cos_{(\theta_{PS})}\right)]^2}({N_{3^{(\theta_{PS})}}}^{(r)} - 2{N_{2^{(\theta_{PS})}}}^{(r)} + {N_{1^{(\theta_{PS})}}}^{(r)}) + M\frac{L^2d}{\pi^2[1+K_T^2(L^2+d^2)\left(1-cos_{(\theta_{PS})}\right)]^2}({N_{3^{(\theta_{PS})}}}^{(w)} - 2{N_{2^{(\theta_{PS})}}}^{(w)} + {N_{1^{(\theta_{PS})}}}^{(w)}\Bigg]\mathrm{d}(cos_{(\theta_{PS})}) \tag{5.41}$$

$$\alpha_{LT} = \frac{\pi^2\omega^4}{2{C_L}^3{C_T}^5}\int_{-1}^{+1}\Bigg[(1-M)\frac{L^3}{\pi^2[1+K_L^2L^2+K_T^2L^2-2K_LK_TL^2cos_{(\theta_{PS})}]^2}({N_{2^{(\theta_{PS})}}}^{(r)} - {N_{1^{(\theta_{PS})}}}^{(r)}) + M\frac{L^2d}{\pi^2[1+(K_L^2+K_T^2-2K_LK_Tcos_{(\theta_{PS})})\frac{(L^2+d^2)}{2}]^2}({N_{2^{(\theta_{PS})}}}^{(w)} - {N_{1^{(\theta_{PS})}}}^{(w)})\Bigg]\mathrm{d}(cos_{(\theta_{PS})}) \tag{5.42}$$

$$\alpha_{TL} = \frac{{C_T}^2}{2{C_L}^2}\alpha_{LT} \tag{5.43}$$

As the pearlitic microstructure here is also considered to have cubic symmetry (although the cementite is actually not), the same inner products (N) can be used, as identified in equations 5.30-5.32. For completeness, they can also be substituted into the overall equation, which results in a complex-appearing resulting equation, however once each element is identified eq 5.44-5.47 it can be used with relative ease.

$$\alpha_{LL} = \frac{\pi^2\omega^4}{2{C_L}^8}\int_{-1}^{+1}\Bigg[(1-M)\frac{L^3}{\pi^2[1+2K_L^2L^2\left(1-cos_{(\theta_{PS})}\right)]^2}\frac{\nu^2}{\rho^2}(\frac{9}{525}+\frac{6}{525}cos^2{}_{(\theta_{PS})} + \frac{1}{525}cos^4{}_{(\theta_{PS})}) + M\frac{L^2d}{\pi^2[1+K_L^2(L^2+d^2)\left(1-cos_{(\theta_{PS})}\right)]^2}\frac{\nu^2}{\rho^2}(\frac{9}{525} + \frac{6}{525}cos^2{}_{(\theta_{PS})} + \frac{1}{525}cos^4{}_{(\theta_{PS})})\Bigg]\mathrm{d}\left(cos_{(\theta_{PS})}\right) \tag{5.44}$$

$$\alpha_{TT} = \frac{\pi^2\omega^4}{2{C_T}^8}\int_{-1}^{+1}\Bigg[(1-M)\frac{L^3}{\pi^2\left[1+2K_T^2L^2\left(1-cos_{(\theta_{PS})}\right)\right]^2}\left(\frac{\nu^2}{\rho^2}\left(\frac{63}{525}+\frac{21}{525}cos^2{}_{(\theta_{PS})}\right)\right.$$
$$-2\frac{\nu^2}{\rho^2}\left(\frac{24}{525}+\frac{12}{525}cos^2{}_{(\theta_{PS})}\right)+\frac{\nu^2}{\rho^2}\left(\frac{9}{525}+\frac{6}{525}cos^2{}_{(\theta_{PS})}\right.$$
$$\left.+\frac{1}{525}cos^4{}_{(\theta_{PS})}\right))+M\frac{L^2d}{\pi^2[1+K_T^2(L^2+d^2)\left(1-cos_{(\theta_{PS})}\right)]^2}\left(\frac{\nu^2}{\rho^2}\left(\frac{63}{525}\right.\right.$$
$$\left.+\frac{21}{525}cos^2{}_{(\theta_{PS})}\right)-2\frac{\nu^2}{\rho^2}\left(\frac{24}{525}+\frac{12}{525}cos^2{}_{(\theta_{PS})}\right)$$
$$\left.+N_{1^{(\theta_{PS})}}{}^{(w)}\Bigg]\mathrm{d}(cos_{(\theta_{PS})})\right.$$
(5.45)

$$\alpha_{LT} = \frac{\pi^2\omega^4}{2{C_L}^3{C_T}^5}\int_{-1}^{+1}\Bigg[(1-M)\frac{L^3}{\pi^2\left[1+K_L^2L^2+K_T^2L^2-2K_LK_TL^2cos_{(\theta_{PS})}\right]^2}\left(\frac{\nu^2}{\rho^2}\left(\frac{24}{525}+\frac{12}{525}cos^2{}_{(\theta_{PS})}\right)-\right.$$
$$\left.\frac{\nu^2}{\rho^2}\left(\frac{9}{525}+\frac{6}{525}cos^2{}_{(\theta_{PS})}+\frac{1}{525}cos^4{}_{(\theta_{PS})}\right)\right)+$$
$$M\frac{L^2d}{\pi^2[1+(K_L^2+K_T^2-2K_LK_Tcos_{(\theta_{PS})})^{\frac{(L^2+d^2)}{2}}]^2}\left(\frac{\nu^2}{\rho^2}\left(\frac{24}{525}+\frac{12}{525}cos^2{}_{(\theta_{PS})}\right)-\frac{\nu^2}{\rho^2}\left(\frac{9}{525}+\right.\right.$$
$$\left.\left.\frac{6}{525}cos^2{}_{(\theta_{PS})}+\frac{1}{525}cos^4{}_{(\theta_{PS})}\right)\right)\Bigg]\mathrm{d}(cos_{(\theta_{PS})})$$
(5.46)

$$\alpha_{TL} = \frac{{C_T}^2}{2{C_L}^2}\alpha_{LT}$$
(5.47)

5.4. An extended Model of Complex Microstructure- induced Scattering

In addition to the work presented in the previous section, where an analytical model has been suggested for use in two-phase materials such as pearlite, this work aims to extend applicability of the model further still. The ultimate aim is to develop a model which is able to account for scatter induced by a wide array of complex microstructures. The model introduced here will focus on bainitic and martensitic microstructure alloys, as the assumptions and terms of the model, which depend on crystallographic symmetry conditions are largely transferable from the two phase model approach.

In much the same way as the single phase model has been extended to accommodate two-phase materials, here the model has been extended further in order to account for more complex microstructures.

$$\alpha_{LL} = \frac{\pi^2\omega^4}{2{C_L}^8}\int_{-1}^{+1}\left[M_1\tilde{\eta}_{LL^{(\theta_{PS})}}{}^{(r)}N_{1^{(\theta_{PS})}}{}^{(r)} + M_2\tilde{\eta}_{LL^{(\theta_{PS})}}{}^{(w)}N_{1^{(\theta_{PS})}}{}^{(w)} + M_3\tilde{\eta}_{LL^{(\theta_{PS})}}{}^{(l)}N_{1^{(\theta_{PS})}}{}^{(l)}\right]\mathrm{d}\left(cos_{(\theta_{PS})}\right) \tag{5.48}$$

$$\alpha_{TT} = \frac{\pi^2\omega^4}{2{C_T}^8}\int_{-1}^{+1}\left[M_1\tilde{\eta}_{TT^{(\theta_{PS})}}{}^{(r)}(N_{3^{(\theta_{PS})}}{}^{(r)} - 2N_{2^{(\theta_{PS})}}{}^{(r)} + N_{1^{(\theta_{PS})}}{}^{(r)}) + M_2\tilde{\eta}_{TT^{(\theta_{PS})}}{}^{(w)}(N_{3^{(\theta_{PS})}}{}^{(w)} - 2N_{2^{(\theta_{PS})}}{}^{(w)} + N_{1^{(\theta_{PS})}}{}^{(w)}) + M_3\tilde{\eta}_{TT^{(\theta_{PS})}}{}^{(l)}(N_{3^{(\theta_{PS})}}{}^{(l)} - 2N_{2^{(\theta_{PS})}}{}^{(l)} + N_{1^{(\theta_{PS})}}{}^{(l)})\right]\mathrm{d}\left(cos_{(\theta_{PS})}\right) \tag{5.49}$$

$$\alpha_{LT} = \frac{\pi^2\omega^4}{2{C_L}^3{C_T}^5}\int_{-1}^{+1}\left[M_1\tilde{\eta}_{LT^{(\theta_{PS})}}{}^{(r)}(N_{2^{(\theta_{PS})}}{}^{(r)} - N_{1^{(\theta_{PS})}}{}^{(r)}) + M_2\tilde{\eta}_{LT^{(\theta_{PS})}}{}^{(w)}(N_{2^{(\theta_{PS})}}{}^{(w)} - N_{1^{(\theta_{PS})}}{}^{(w)}) + M_3\tilde{\eta}_{LT^{(\theta_{PS})}}{}^{(l)}(N_{2^{(\theta_{PS})}}{}^{(l)} - N_{1^{(\theta_{PS})}}{}^{(l)})\right]\mathrm{d}\left(cos_{(\theta_{PS})}\right) \tag{5.50}$$

$$\alpha_{TL} = \frac{{C_T}^2}{2{C_L}^2}\alpha_{LT} \tag{5.51}$$

The difference here is the presence of three contributing terms to the overall equation, these consist of the prior austenite grain boundary (r), the packet boundary (w) and the lath boundary (l). For consistency the notation of the two contributory elements from equation 5.33-5.36 have been retained, but it should be noted the boundaries encountered in this context differ from the pearlitic case. The difference with the previous version of the model is the adaptation of the weighting factor (M); here they have been designed to indicate the ratio of significance of each term relative to the sum. Therefore the weighting factors must satisfy the condition in equation 5.52.

$$M_1 + M_2 + M_3 = 1 \tag{5.52}$$

The validity of this assumption is discussed in the results and discussion section (chapter 7) in the context of the experimental results.

Similarly to section 5.3, the same approach is used to substitute the terms associated with the inner products and the Fourier transform of the correlation function. Once again, the correlation is determined by the shape of the microstructural feature, in this case either spherical or ellipsoidal. As discussed in section 4.3.1, the assumption of cubic symmetry has been deemed adequate to use in the context of bainitic and martensitic materials. This decision is based on the expectation of a small degree of tetragonality (or deformation of the cubic lattice structure), due to low levels of carbon in solution, especially given the precipitation of carbides which further reduces the degree of tetragonality. Therefore the inner products used here will be the same as used in the previous model, equations 5.30-5.32. First by substituting $\tilde{\eta}$ into equations 5.48-5.51, the resulting form develops into equations 5.53-5.56.

$$\begin{aligned}\alpha_{LL} = \frac{\pi^2\omega^4}{2{C_L}^8}\int_{-1}^{+1}\Bigg[& M_1\frac{G^3}{\pi^2[1+2K_L^2G^2\big(1-cos_{(\theta_{PS})}\big)]^2}{N_1}^{(\theta_{PS})}(r) \\ & + M_2\frac{L^3}{\pi^2[1+2K_L^2L^2\big(1-cos_{(\theta_{PS})}\big)]^2}{N_1}^{(\theta_{PS})}(w) \\ & + M_3\frac{L^2d}{\pi^2[1+K_L^2(L^2+d^2)\big(1-cos_{(\theta_{PS})}\big)]^2}{N_1}^{(\theta_{PS})}(l)\Bigg]\mathrm{d}\big(cos_{(\theta_{PS})}\big)\end{aligned} \tag{5.53}$$

$$\alpha_{TT} = \frac{\pi^2\omega^4}{2{C_T}^8}\int_{-1}^{+1}\Bigg[M_1\frac{G^3}{\pi^2[1+2K_T^2G^2(1-cos_{(\theta_{PS})})]^2}({N_3}^{(\theta_{PS})(r)} - 2{N_2}^{(\theta_{PS})(r)} + {N_1}^{(\theta_{PS})(r)}) + M_2\frac{L^3}{\pi^2[1+2K_T^2L^2(1-cos_{(\theta_{PS})})]^2}({N_3}^{(\theta_{PS})(w)} - 2{N_2}^{(\theta_{PS})(w)} + {N_1}^{(\theta_{PS})(w)}) + M_3\frac{L^2d}{\pi^2[1+K_T^2(L^2+d^2)(1-cos_{(\theta_{PS})})]^2}({N_3}^{(\theta_{PS})(l)} - 2{N_2}^{(\theta_{PS})(l)} + {N_1}^{(\theta_{PS})(l)})\Bigg]\mathrm{d}(cos_{(\theta_{PS})}) \tag{5.54}$$

$$\alpha_{LT} = \frac{\pi^2\omega^4}{2{C_L}^3{C_T}^5}\int_{-1}^{+1}\Bigg[M_1\frac{G^3}{\pi^2\left[1+K_L^2G^2+K_T^2G^2-2K_LK_TG^2cos_{(\theta_{PS})}\right]^2}({N_2}^{(\theta_{PS})(r)} - {N_1}^{(\theta_{PS})(r)}) + M_2\frac{L^3}{\pi^2\left[1+K_L^2L^2+K_T^2L^2-2K_LK_TL^2cos_{(\theta_{PS})}\right]^2}({N_2}^{(\theta_{PS})(w)} - {N_1}^{(\theta_{PS})(w)}) + M_3\frac{L^2d}{\pi^2[1+(K_L^2+K_T^2-2K_LK_Tcos_{(\theta_{PS})})\frac{(L^2+d^2)}{2}]^2}({N_2}^{(\theta_{PS})(l)} - {N_1}^{(\theta_{PS})(l)})\Bigg]\mathrm{d}(cos_{(\theta_{PS})}) \tag{5.55}$$

$$\alpha_{TL} = \frac{{C_T}^2}{2{C_L}^2}\alpha_{LT} \tag{5.56}$$

Here the lengths G, L and d stand for grain (diameter), packet (diameter) and lath (width) size respectively. Once again the inner products shall also be substituted into equations 5.53-5.56 to illustrate the full form of the equation.

$$\alpha_{LL} = \frac{\pi^2\omega^4}{2{C_L}^8}\int_{-1}^{+1}\Bigg[M_1\frac{G^3}{\pi^2[1+2K_L^2G^2(1-cos_{(\theta_{PS})})]^2}\frac{\nu^2}{\rho^2}(\frac{9}{525}+\frac{6}{525}cos^2{}_{(\theta_{PS})} + \frac{1}{525}cos^4{}_{(\theta_{PS})}) + M_2\frac{L^3}{\pi^2[1+2K_L^2L^2(1-cos_{(\theta_{PS})})]^2}\frac{\nu^2}{\rho^2}(\frac{9}{525} + \frac{6}{525}cos^2{}_{(\theta_{PS})} + \frac{1}{525}cos^4{}_{(\theta_{PS})}) + M_3\frac{L^2d}{\pi^2[1+K_L^2(L^2+d^2)(1-cos_{(\theta_{PS})})]^2}\frac{\nu^2}{\rho^2}(\frac{9}{525}+\frac{6}{525}cos^2{}_{(\theta_{PS})} + \frac{1}{525}cos^4{}_{(\theta_{PS})})\Bigg]\mathrm{d}(cos_{(\theta_{PS})}) \tag{5.57}$$

$$\alpha_{TT} = \frac{\pi^2\omega^4}{2{C_T}^8}\int_{-1}^{+1}\Bigg[M_1\frac{G^3}{\pi^2[1+2K_T^2G^2(1-cos_{(\theta_{PS})})]^2}\Big(\frac{\nu^2}{\rho^2}\Big(\frac{63}{525}+\frac{21}{525}cos^2{}_{(\theta_{PS})}\Big) - 2\frac{\nu^2}{\rho^2}\Big(\frac{24}{525}+\frac{12}{525}cos^2{}_{(\theta_{PS})}\Big)+\frac{\nu^2}{\rho^2}\Big(\frac{9}{525}+\frac{6}{525}cos^2{}_{(\theta_{PS})} + \frac{1}{525}cos^4{}_{(\theta_{PS})}\Big)\Big) + M_2\frac{L^3}{\pi^2[1+2K_T^2L^2(1-cos_{(\theta_{PS})})]^2}\Big(\frac{\nu^2}{\rho^2}\Big(\frac{63}{525} + \frac{21}{525}cos^2{}_{(\theta_{PS})}\Big) - 2\frac{\nu^2}{\rho^2}\Big(\frac{24}{525}+\frac{12}{525}cos^2{}_{(\theta_{PS})}\Big)+\frac{\nu^2}{\rho^2}\Big(\frac{9}{525} + \frac{6}{525}cos^2{}_{(\theta_{PS})} + \frac{1}{525}cos^4{}_{(\theta_{PS})}\Big)\Big) + M_3\frac{L^2d}{\pi^2[1+K_T^2(L^2+d^2)(1-cos_{(\theta_{PS})})]^2}\Big(\frac{\nu^2}{\rho^2}\Big(\frac{63}{525}+\frac{21}{525}cos^2{}_{(\theta_{PS})}\Big) - 2\frac{\nu^2}{\rho^2}\Big(\frac{24}{525}+\frac{12}{525}cos^2{}_{(\theta_{PS})}\Big)+\frac{\nu^2}{\rho^2}\Big(\frac{9}{525}+\frac{6}{525}cos^2{}_{(\theta_{PS})} + \frac{1}{525}cos^4{}_{(\theta_{PS})}\Big)\Big)\Bigg]\mathrm{d}\big(cos_{(\theta_{PS})}\big) \tag{5.58}$$

$$\alpha_{LT} = \frac{\pi^2\omega^4}{2{C_L}^3{C_T}^5}\int_{-1}^{+1}\Bigg[M_1\frac{G^3}{\pi^2\big[1+K_L^2G^2+K_T^2G^2-2K_LK_TG^2cos_{(\theta_{PS})}\big]^2}\Big(\frac{\nu^2}{\rho^2}\Big(\frac{24}{525} + \frac{12}{525}cos^2{}_{(\theta_{PS})}\Big) - \frac{\nu^2}{\rho^2}\Big(\frac{9}{525}+\frac{6}{525}cos^2{}_{(\theta_{PS})}+\frac{1}{525}cos^4{}_{(\theta_{PS})}\Big)\Big) + M_2\frac{L^3}{\pi^2\big[1+K_L^2L^2+K_T^2L^2-2K_LK_TL^2cos_{(\theta_{PS})}\big]^2}\Big(\frac{\nu^2}{\rho^2}\Big(\frac{24}{525} + \frac{12}{525}cos^2{}_{(\theta_{PS})}\Big) - \frac{\nu^2}{\rho^2}\Big(\frac{9}{525}+\frac{6}{525}cos^2{}_{(\theta_{PS})}+\frac{1}{525}cos^4{}_{(\theta_{PS})}\Big)\Big) + M_3\frac{L^2d}{\pi^2[1+(K_L^2+K_T^2-2K_LK_Tcos_{(\theta_{PS})})\frac{(L^2+d^2)}{2}]^2}\Big(\frac{\nu^2}{\rho^2}\Big(\frac{24}{525} + \frac{12}{525}cos^2{}_{(\theta_{PS})}\Big) - \frac{\nu^2}{\rho^2}\Big(\frac{9}{525}+\frac{6}{525}cos^2{}_{(\theta_{PS})} + \frac{1}{525}cos^4{}_{(\theta_{PS})}\Big)\Big)\Bigg]\mathrm{d}\big(cos_{(\theta_{PS})}\big) \tag{5.59}$$

$$\alpha_{TL} = \frac{{C_T}^2}{2{C_L}^2}\alpha_{LT} \tag{5.60}$$

The equations developed here provide the foundation of the work conducted as part of this project. Therefore the subsequent results and discussion sections shall be largely focussed on either proving or disproving its applicability. In combination with this the work on the boundary reflection coefficient and the small feature size scatter shall also be used, with the intention of providing additional clarity to the situation. The intention is to incorporate these additional aspects into the main equation to improve the equation and to eliminate the experimentally obtained correction factors.

6. Microstructural analysis

6.1 Pearlite

The samples included as part of this section are generated from a single section of rail steel and heat-treated to generate a varied microstructure as outlined in section 4. The aim was to obtain suitable samples to compare with previously published work which extends the scattering model to pearlitic microstructures. A limitation of [Du and Turner, 2014] was the limited scope of microstructural analysis, with estimates of the expected microstructure used. This led to unrealistic microstructural features being applied to an as yet unproven model and a series of fitting parameters used to generate a trend line. Therefore, in order to avoid similar issues, it was deemed necessary to obtain sound microstructural data as the basis for this work. The following section is the summary of the microstructural analysis which is used to support the conclusions drawn as part of this work.

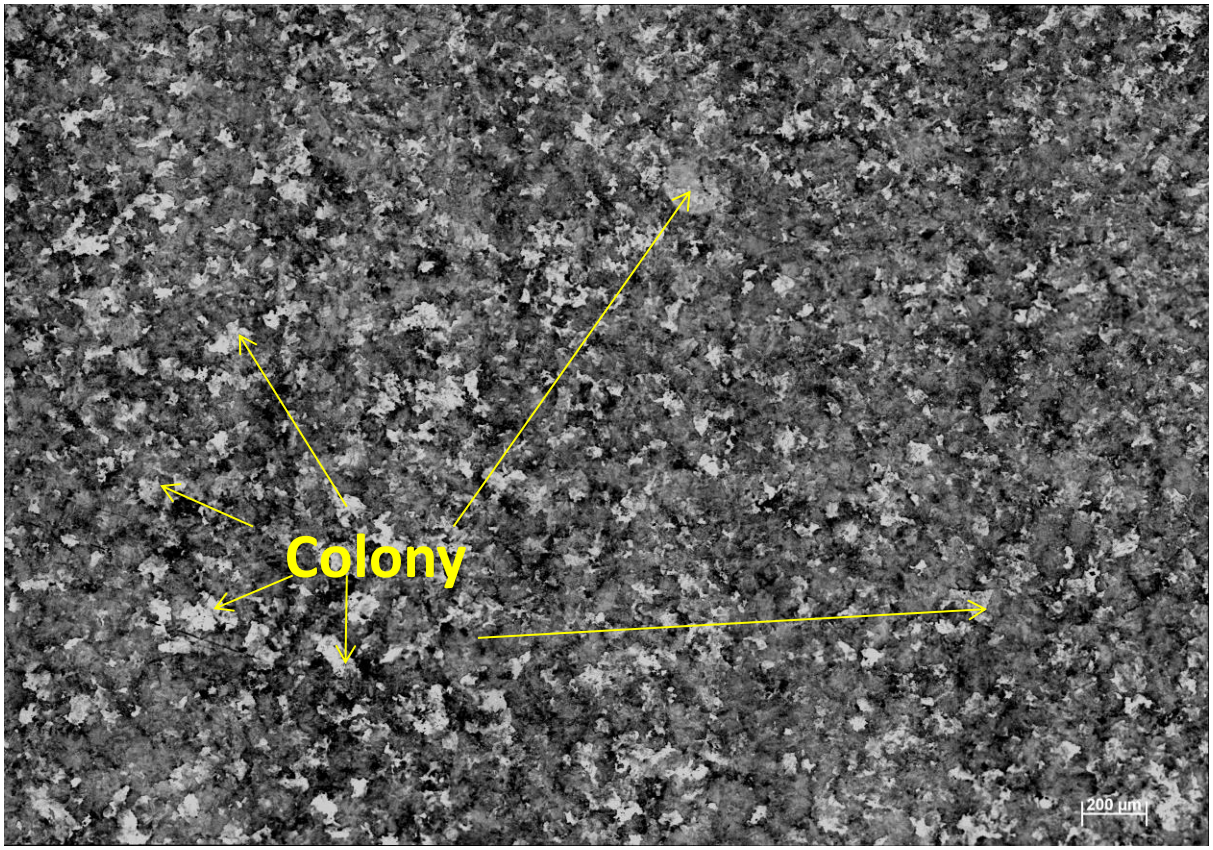

Figure 6.1: Optical micrograph showing the individual colonies of a pearlitic sample. Image taken of sample B1, but is representative of the entire sample range.

Figure 6.1 indicates individual colonies of a fully pearlitic sample; the sample is etched with a 2% nital solution in order to more easily distinguish the individual colonies. Figure 6.1 appears to show a degree of alignment/banding along the vertical axis of the image, this is likely to be the result of an earlier stage of processing (casting and rolling) [Dally, 2017; Watson, 2017; Kalinowski, 2017], but has not been investigated as part of this work. Figures 6.2 and 6.3 indicate the lamellar structure of these samples. Here the particular samples with the largest and smallest lamellae spacing have been presented in order to show the similarity in structures; the only real difference between them being the relative size of respective features. As is also evident from the images (Figures 6.2 and 6.3), there is a variation in the size of lamellae in individual colonies even across a single image, although it is unknown whether this is attributable to a genuine difference or a sectioning effect.

Therefore, the mean value of a significant number of measurements has been used, with the measurement technique, correction factor and standard error criteria detailed in Chapter 4.

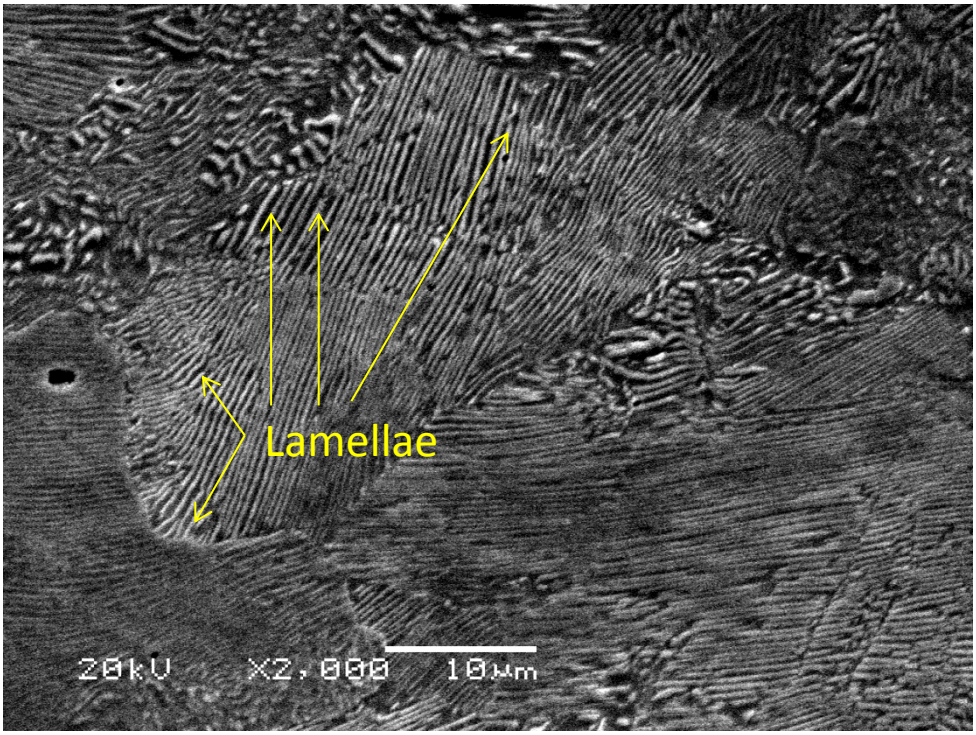

Figure 6.2: SEM image showing the lamellae structure of sample B, the sample with the largest lamellae spacing. Image indicates lamellar structure.

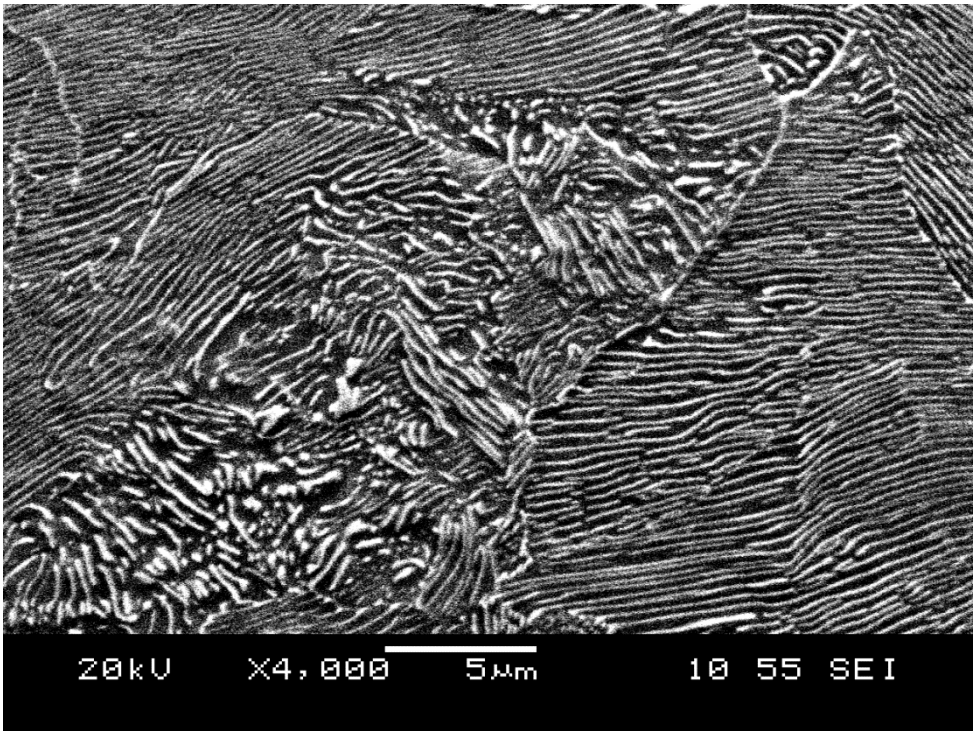

Figure 6.3: SEM image showing the lamellae structure of sample B1, the sample with the smallest lamellae spacing.

Table 6.1 quantifies the microstructures generated by the respective heat treatments of the pearlitic samples. The obtained microstructures are in line with the qualitative objectives for these samples as a range of colony sizes and lamellae spacing was desired and subsequently achieved. Samples A and B both have relatively large colony sizes but a significant difference in lamellae spacing, whereas samples A1 and B1 have smaller colony sizes and also a reasonable difference in lamellae spacing. The similar lamellae spacing's exhibited by samples A and B1 are reassuring, as these provide a comparable base to isolate the colony size contribution to ultrasonic scatter.

Table 6.1: Measured microstructures of generated pearlite samples along with a ± standard error in the mean

Sample name	Colony size (µm)	Lamellae spacing (µm)
A	108.6 ± 2.64	0.28 ± 0.003
A1	70.2 ± 1.85	0.35 ± 0.003
B	138.4 ± 3.42	0.51 ± 0.007
B1	89.0 ± 2.18	0.29 ± 0.003

Figure 6.4 shows the distribution of the colony size data (column 2 of table 6.1). The graph indicates the distribution of colony size is largely similar across the generated samples. Each distribution is characterised by a reasonably sharp increase in colony size frequency, and then a longer drawn out fall from this peak. The pattern approximately represents a log normal or skewed-right distribution curve. As would also be expected the samples with the larger average colony size (A and B) have a higher probability of unusually large measurements and have a frequency peak occurring for a larger colony size. Sample A appears to have a few larger colonies as outliers, whereas sample B is generally broader in distribution. A possible influence of these particularly large colonies is for them to exhibit a disproportionally large influence on ultrasonic scatter. Therefore, any uneven distribution within the sample, as associated with a tendency towards outliers, could result in a more inconsistent attenuation measurement across the sample. The distribution data as part of this graph have been normalised against relative area (an area percentage plot) in order to show a true comparison, rather than being dominated by number of measurements.

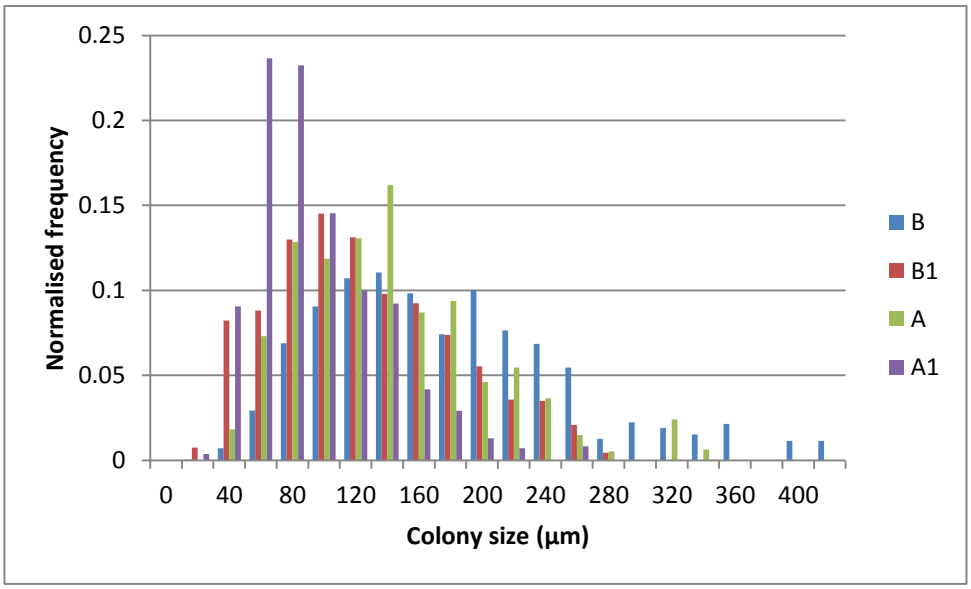

Figure 6.4: Measured pearlite sample colony size distributions

Figure 6.5 shows the distribution of pearlite sample lamellae spacing ranges. The distribution data as part of this graph have been normalised by number to show a true comparison (as a normalisation by area would not be appropriate here). The frequency of occurrence was used for normalisation as the area itself was not measured but rather the spacing, alternatively the data could be weighted by measured length and would show largely the same distribution pattern. The distribution data shown follow much the same distribution curves as those identified for colony size, that of a log-normal curve or skewed-right distribution. The data associated with sample B stand out in particular due to the significantly increased likelihood of large measurements and noticeably larger peak value than the other samples.

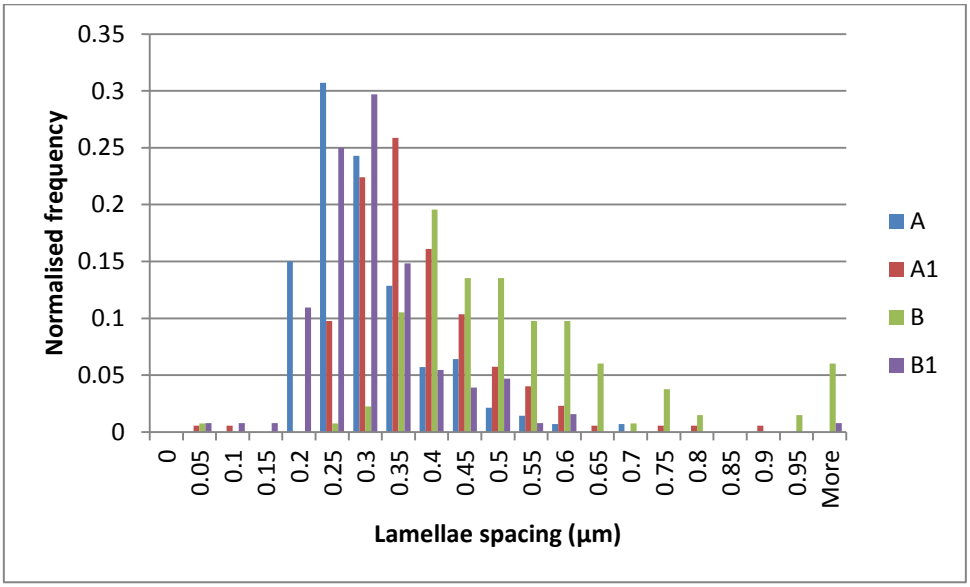

Figure 6.5: Measured pearlite sample lamellae spacing distributions

It is important to understand that austenite grain boundaries are an important part of pearlite phase transformation. Austenite grain boundaries are common nucleation sites for pearlite (either ferrite or cementite initially), and the average colony size increases with austenite grain size [Aranda et al., 2013]. Pearlite cannot typically grow across austenite grain boundaries. The colony size represents the crystallographic grain size in pearlite

[Bhadeshia, 2008], therefore measurements of the prior austenite grain size in pearlitic samples are not carried out. Although, having said that, a prior austenite grain boundary could partially coincide with a colony boundary. Several pearlite colonies are expected to form within a prior austenite grain boundary.

6.2 Mixed martensite and bainite

Figure 6.6 and Figure 6.7 both show the prior austenite grain boundaries of the mixed martensite and bainite samples, due to the hot picric etch used as described in chapter 4. Figure 6.6 is associated with sample C2, which has a far smaller prior austenite grain size than that of sample D (Figure 6.7); this result is as expected from the heat treatment procedure and is supported by quantitative analysis (table 6.2). It is also evident from the Figures (6.6 and 6.7) that a degree of banding is present, the light and dark streaks across the image. The lighter bands correspond to solute-rich areas and the darker bands to solute-poor areas, which suggest the microstructure is likely influenced by segregation. A previous study (currently under embargo) characterised the as-received material and found the segregation bands to be parallel to the rolling direction. As a consequence of this segregation, grain size and phase transformation can be influenced, which likely explains the mixed martensite and bainite microstructure as well as a banding effect of different grain size.

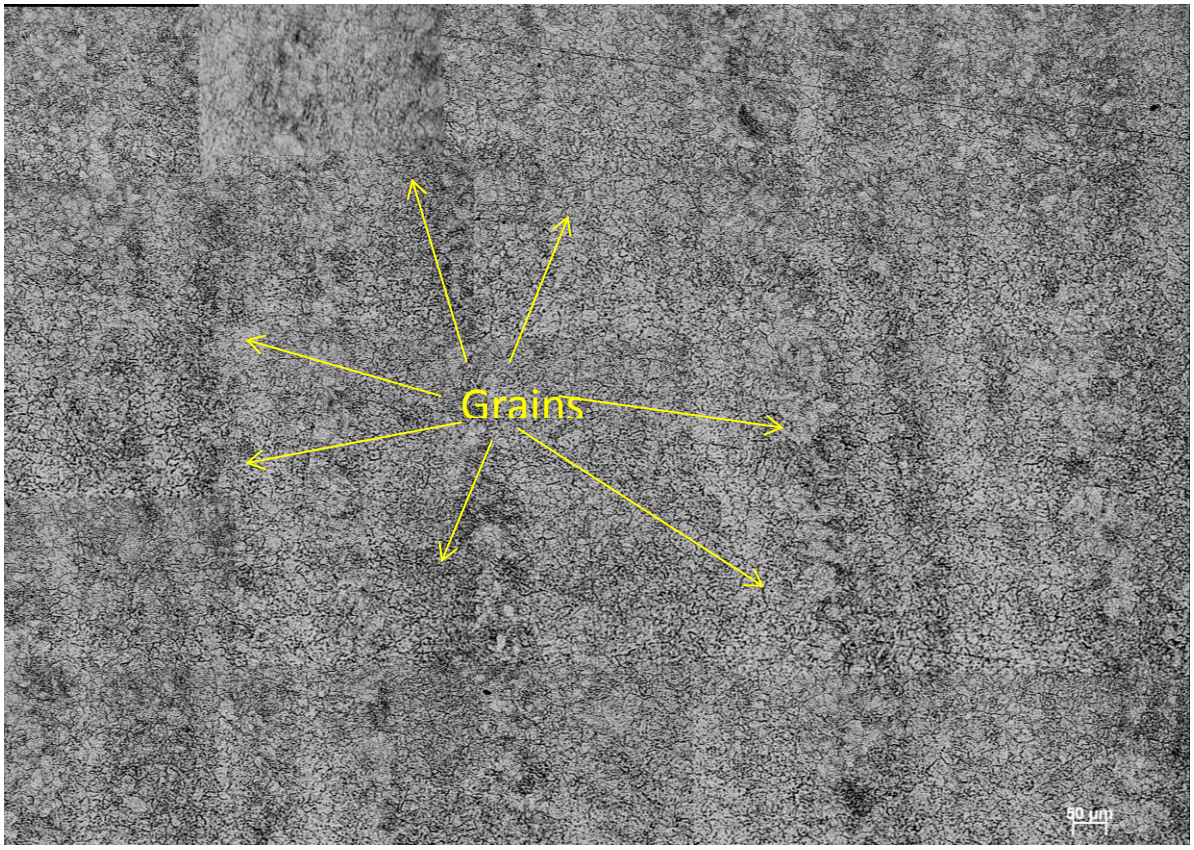

Figure 6.6: Mosaic of optical microscope images showing the prior austenite grain size of sample C2, the smallest measured average grain size.

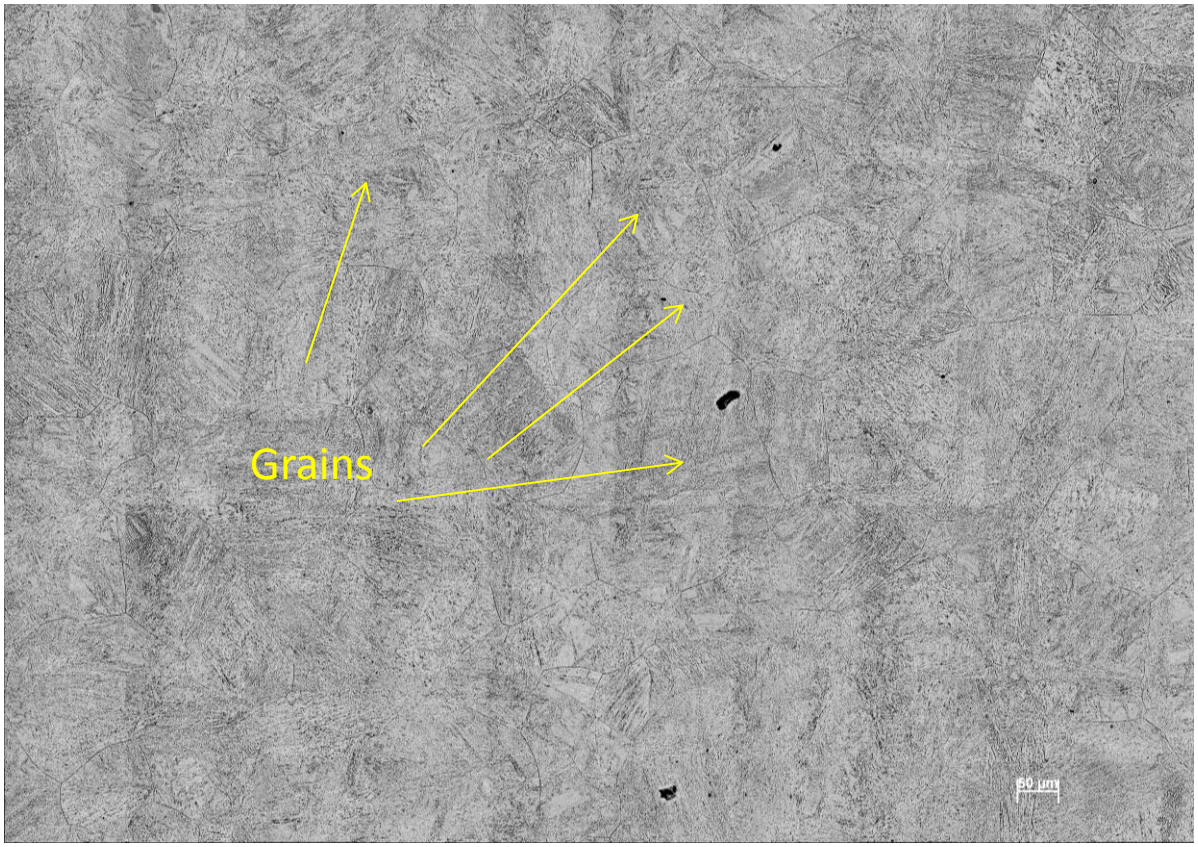

Figure 6.7: Mosaic of optical microscope images showing the prior austenite grain size of sample D, the largest measured average grain size.

Figure 6.8 shows the area normalised prior austenite grain size distributions of samples C, C2 and C3. The distributions are virtually identical, all following more of a normal distribution than the log-normal distribution (but still showing characteristics of both) and with the peak frequency in a similar place. The only difference being a slight tendency for sample C to have smaller peak grain size, which is expected as this is associated with the lowest heat-treatment temperature out of these samples. As the heat-treatment temperature would be expected to influence prior austenite grain size, a likely cause for the similar value of samples C, C2 and C3 is the reduced time at temperature for samples C2 and C3 which didn't allow for sufficient growth before re-austenitisation. This explanation is supported by the large prior austenite grain size of sample D (Figure 6.9), where the higher heat-treatment temperature coupled with the increased time at temperature (the same as for sample C), resulted in significant grain growth.

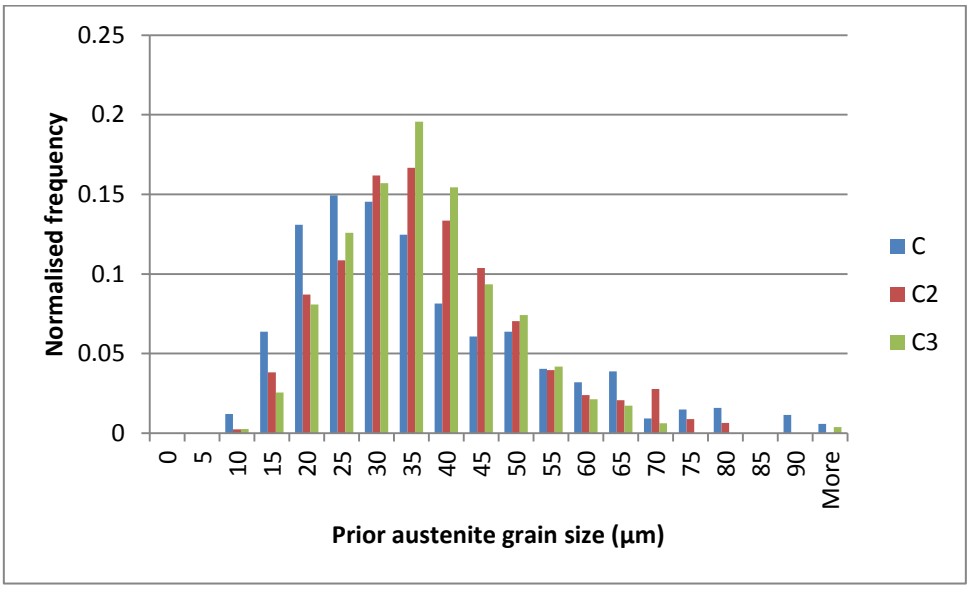

Figure 6.8: Measured mixed martensite and bainite samples (C, C2, C3) prior austenite grain size distributions

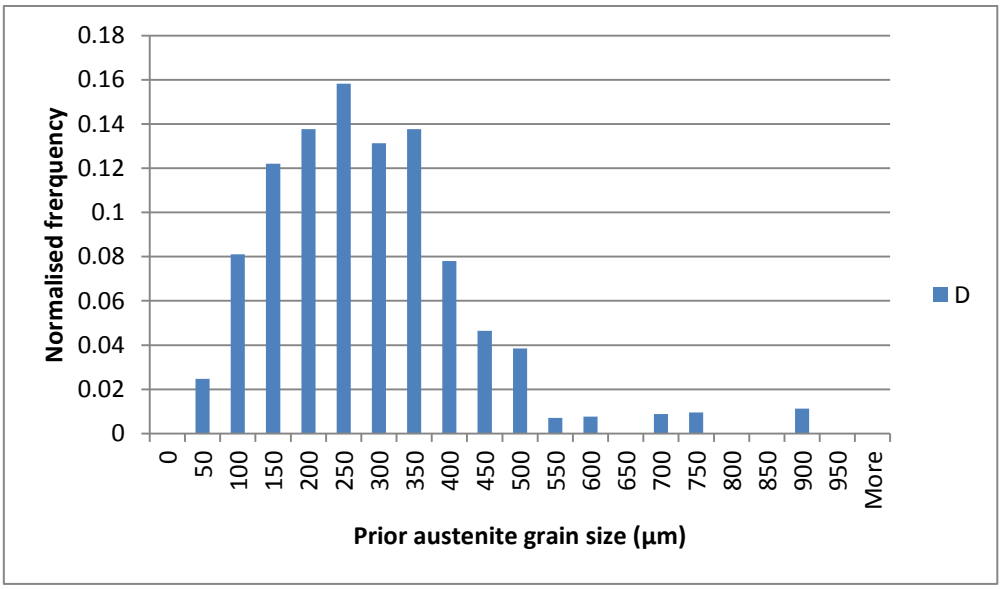

Figure 6.9: Measured mixed martensite and bainite sample (D) prior austenite grain size distribution

The data of Figure 6.9, sample D, are presented separately due to the significantly larger prior austenite grains size, to ensure an appropriate scaling.

The image shown in Figure 6.10 indicated the different phases present in these generated microstructures, the key differentiating factor being the carbides. Upper bainite is characterised by large carbides typically forming on the lath boundary, whereas lower

bainite would show smaller carbides forming in a single orientation throughout. Auto-tempered martensite would present very fine carbide formation, typically in three orientations, throughout the feature and untempered martensite would have no carbide formation. A detailed account of these microstructures can be found in “Steels-microstructure and properties” [Bhadeshia and Honeycomb, 2006].

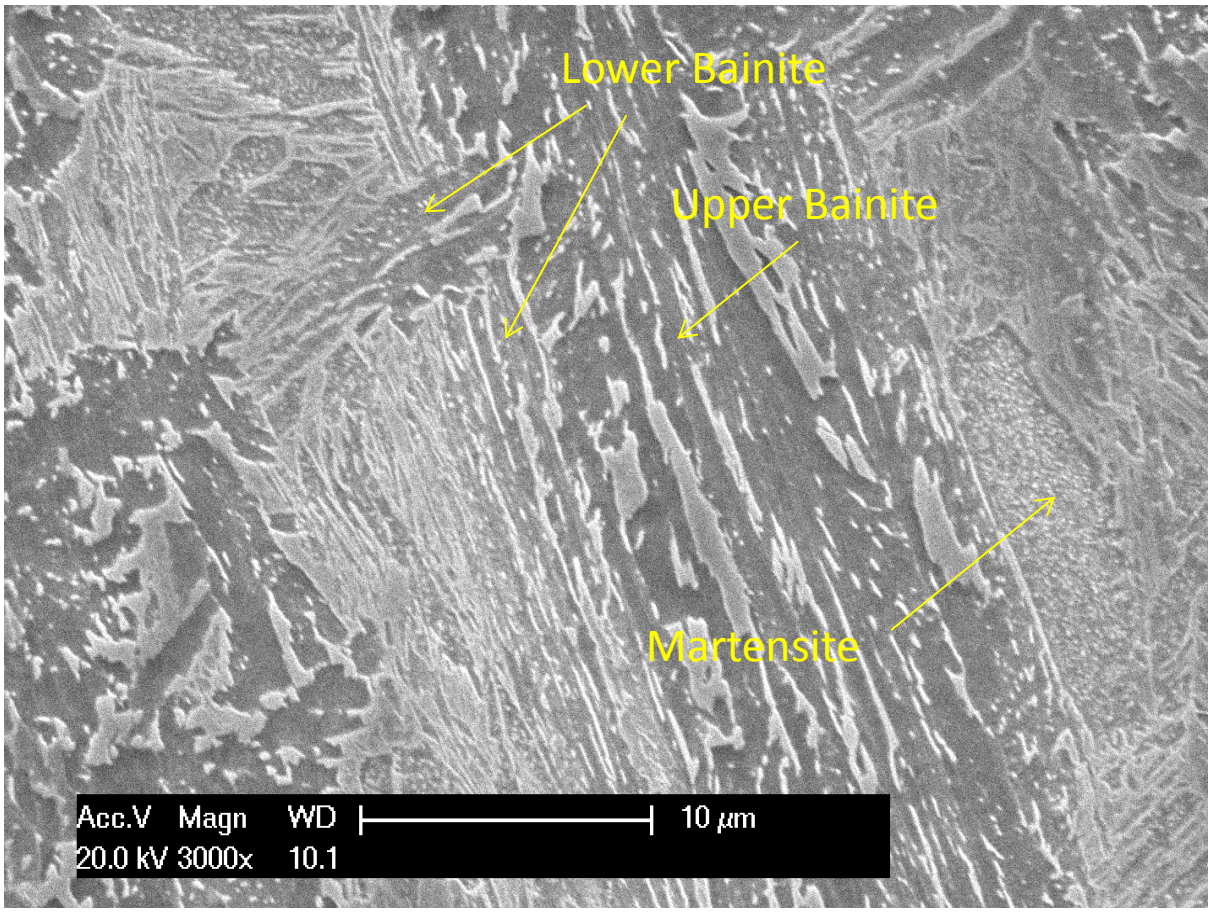

Figure 6.10: Micrograph showing the different phases forming as part of the same sample. Image taken of sample D but is representative of the microstructure across the range of samples

The distribution data from Figure 6.11 show similar lath size distributions across all of the mixed martensite and bainite samples. There is a slight tendency for sample C to have a smaller lath width and for C2 and C3 to have a slightly larger peak frequency, but such a small difference could be the result of a sampling effect or due to histogram bin size selection, and largely disappears in the averaged data (table 6.2). This is as expected as they

all have similar heat treatment without a secondary tempering stage, which would typically lead to an increase in lath width.

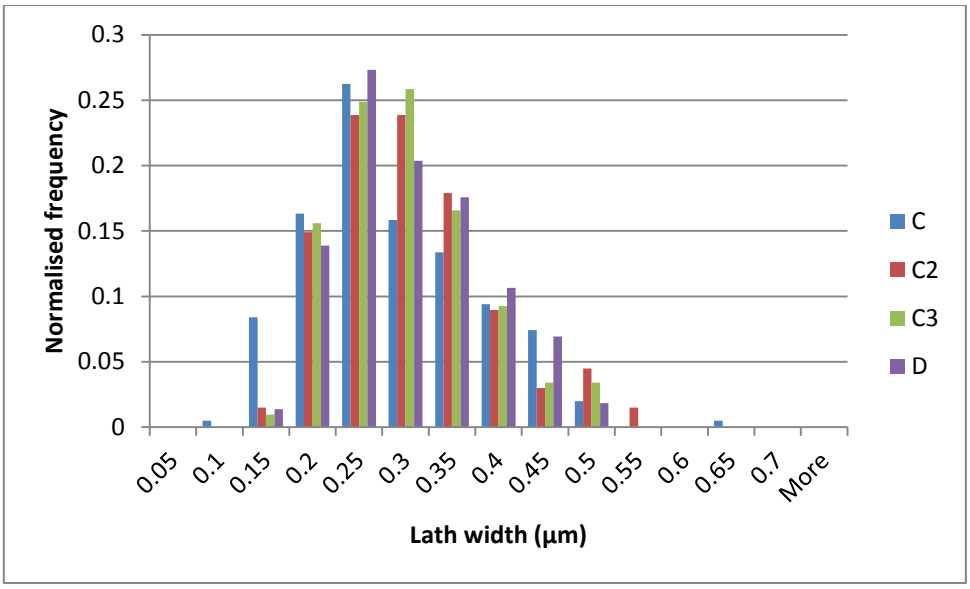

Figure 6.11: Measured mixed Martensitic and Bainitic samples (C, C2, C3, D) lath width distribution

Table 6.2: The measured microstructures associated with these mixed phase samples along with ± standard error of the mean

Sample name	Prior austenite grain size (µm)	Packet size (µm)	Lath width (µm)
C	27.8 ± 0.7	12.6 ± 5.0	0.26 ± 0.003
C2	30.5 ± 0.5	11.0 ± 3.8	0.28 ± 0.004
C3	30.2 ± 0.4	12.5 ± 4.4	0.27 ± 0.002
D	198.1 ± 6.9	16.2 ± 7.4	0.28 ± 0.002

6.3 Fully martensitic samples

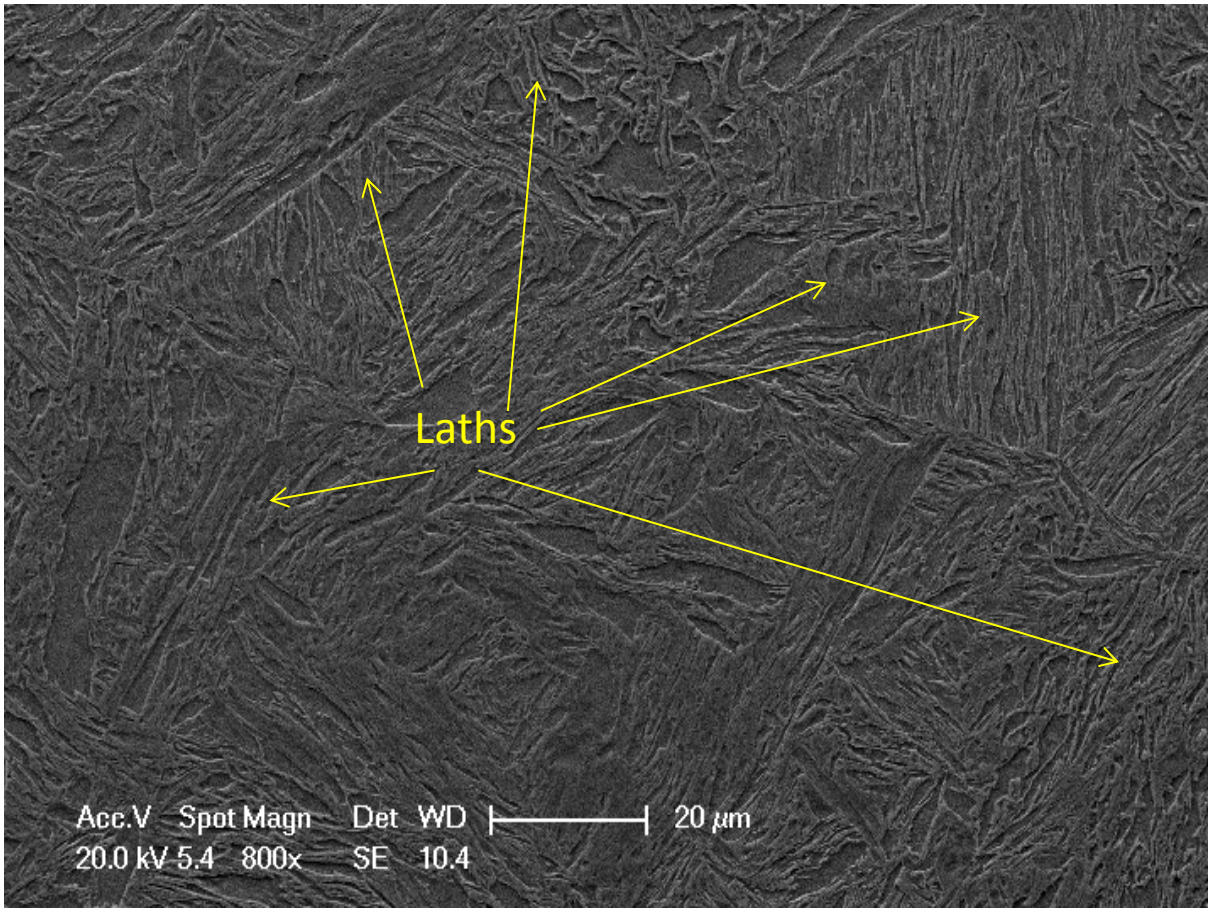

Figure 6.12: Micrograph showing the martensitic microstructure. Image taken of sample M4 (with the largest grain size) but is representative of the microstructure across the range of samples in this set

Figure 6.12 indicates the lath martensite structure associated with all of the fully martensitic samples. The sample used in Figure 6.12 (sample M4) represents the largest of all the sample prior austenite grain sizes, however the lath size is not too dissimilar to the other samples.

The data presented in Figure 6.13 show the distribution of prior austenite grain size for samples M1, M2, M3 and M7. These samples have been grouped together to show their similar distribution profiles. It is clear they each follow a log-normal distribution curve. The two samples which underwent a 900 °C heat-treatment cycle (samples M2 and M3) show

modal prior austenite grain size values of 15 µm, whereas the 1000 °C samples (M1 and M7) have modal values of 20 µm and 25 µm. This tendency for slightly larger grain size associated with the higher heat-treatment temperature is as expected. It is also likely that samples M1 and M7 have similar modal prior austenite grain size values and that they simply happen to fall into different histogram bins. The slight anomaly is the more widely spread distribution of sample M1; here there is an increased likelihood of larger grains and therefore a flatter peak and longer tail. The data in this graph have been normalised against area.

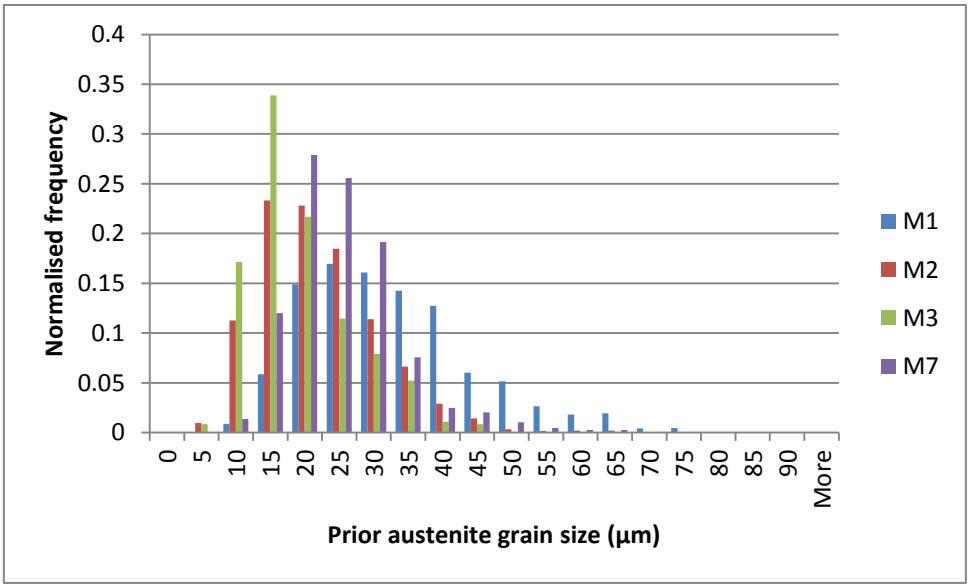

Figure 6.13: Measured martensitic sample (M1, M2, M3, M7) prior austenite grain size distributions

The data represented in Figure 6.14, normalised for area, show samples M4 and M5, which both have a very large grain size in comparison to the other samples and so have been represented separately. These very large grain sizes are completely in line with that of the parent samples (from the mixed martensite/bainite samples in chapter 6.2) and so is not a surprise. The distribution is also roughly as expected, showing a roughly log normal distribution. Although the ranges associated with both of these samples is equivalent, sample M5 shows a greater proportion of smaller grains relative to sample M4, there is no

immediately apparent explanation for this trend. The distribution could potentially be improved further by a combination of increased grain measurements and/or a change in the bin sizes. A limiting factor in the measurements of samples associated with such large grains is simply the lack of total grains to measure over a relatively small prepared sample surface.

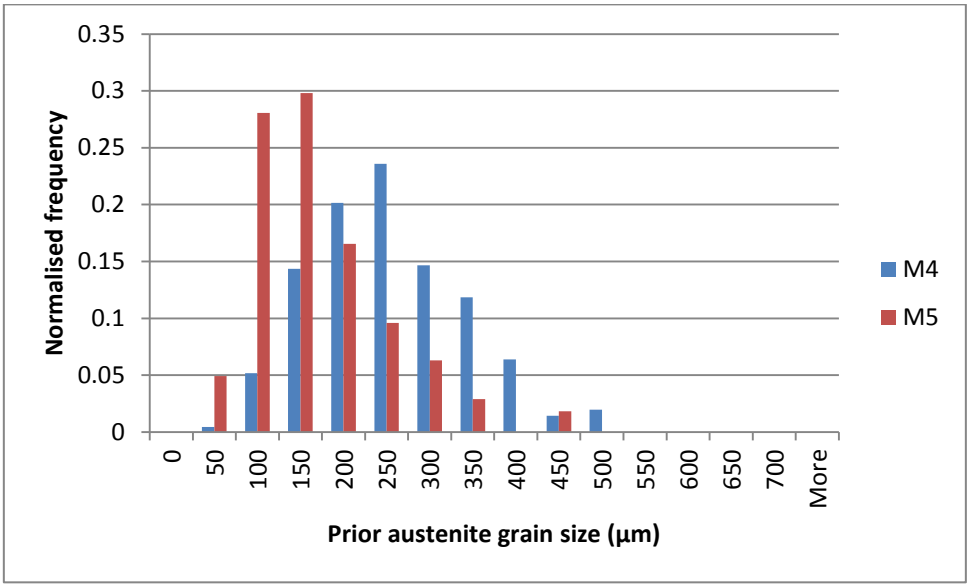

Figure 6.14: Measured martensitic sample (M4 and M5) prior austenite grain size distributions

The distribution data associated with sample M6 (Figure 6.15) have been presented separately as the grain size is roughly half way between the data presented in Figures 6.13 and 6.14, and so they would distort the chart if included in either of those sets of results. That point aside the data appear to nicely follow a log-normal distribution with a distribution shape largely similar to those of Figure 6.13. Table 6.3 provides a summary of all 7 martensitic sample prior austenite grain size variation against re-austenitising temperature. This is to clarify for the reader the influence that heat-treatment temperature has on grain growth. The data are as expected with higher re-austenitising temperature leading to larger prior austenite grain size and increased range. A slight anomaly is seen in samples M4 and M5 with large differences in mean values and modal groups, although the range of prior austenite grains is largely similar. This discrepancy was also encountered

during the mixed martensite/bainite sample preparation stage and so could point to initial sample variation or an unknown anomaly in initial heat-treatments.

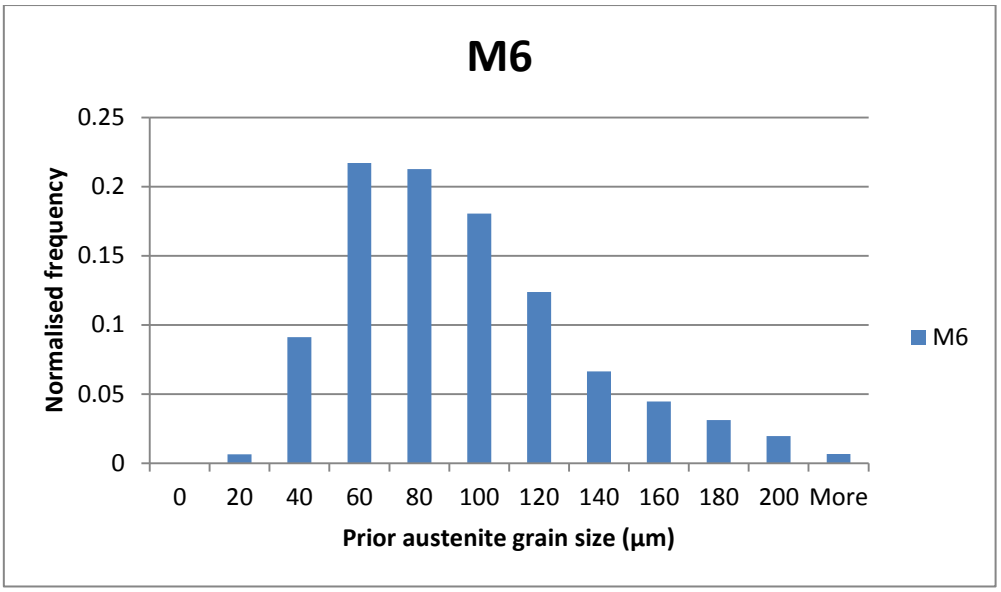

Figure 6.15: Measured martensitic sample (M6) prior austenite grain size distribution

Table 6.3: A summary of the modal, min/max group data alongside the re-austenitising temperature of the sample, to clarify the prior austenite grain size variation with sample preparation temperature.

Sample name	Modal group	Min group	Max group	Re-austenitising temperature (°C)
M1	25 – 30	10 – 15	75 – 80	1000
M2	15 – 20	5 – 10	50 – 55	900
M3	15 – 20	5 – 10	45 – 50	900
M4	250 – 300	50 – 100	500 – 550	1100
M5	150 – 200	50 – 100	450 – 500	1100
M6	60 – 80	20 – 40	220 +	1050
M7	20 – 25	10 – 15	65 – 70	1000

As is evident from Figures 6.16 and 6.17, the lath distributions among the martensitic samples appear to indicate a bi-modal distribution, which is likely as a result of the previously discussed segregation effects. M4, M5 and M6 being grouped separately as they show a tendency towards larger laths. The strange nature of the distribution in Figures 6.16 and 6.17, with two distinct peaks makes overall quantification challenging. As the overall lath width is very small, compared with the ultrasonic wavelength, both of these bi-modal peaks fall into the lower end of the Rayleigh scattering regime. Therefore the mean of all

measured laths shall still be used for further ultrasonic consideration; if the lath width proves to be an important consideration this shall be amended at a later point.

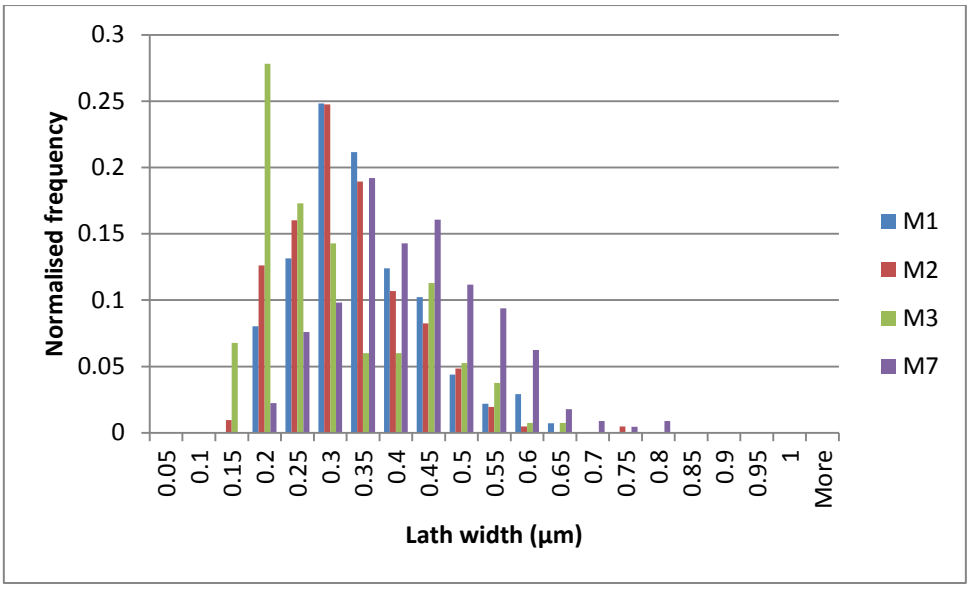

Figure 6.16: Measured martensitic samples (M1, M2, M3 and M7) lath width distribution, normalised by frequency of occurrence

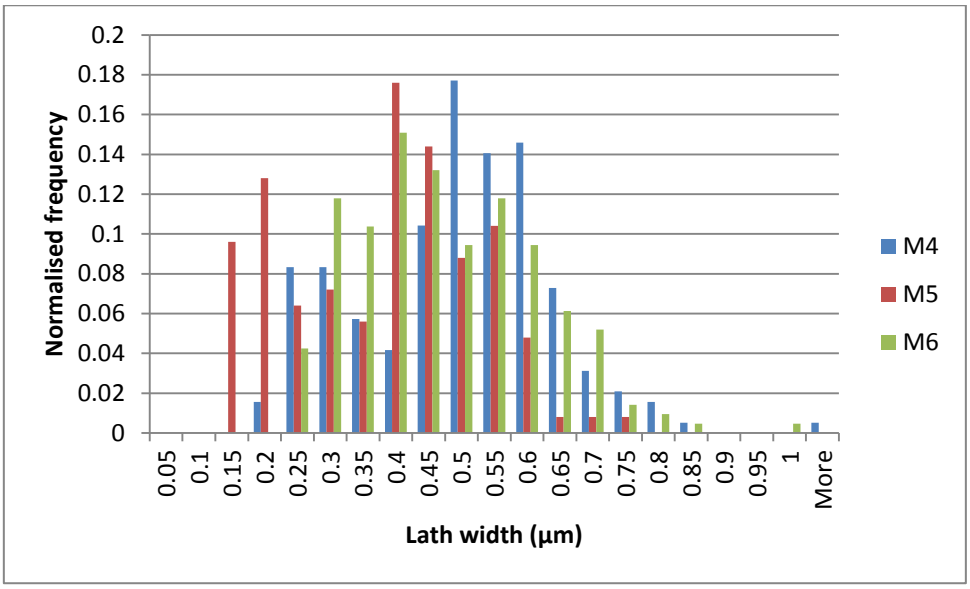

Figure 6.17: Measured martensitic samples (M4, M5 and M6) lath width distribution, normalised by frequency of occurrence

Table 6.4: The measured microstructures associated with the full martensitic samples along with ± standard error of the mean

Sample name	Prior austenite grain size (µm)	Packet size (µm)	Lath width (µm)
M1	26.3 ± 0.5	14.9 ± 4.7	0.33 ± 0.004
M2	16.4 ± 0.2	11.9 ± 3.5	0.30 ± 0.003
M3	14.2 ± 0.3	12.2 ± 4.6	0.28 ± 0.004
M4	198.3 ± 3.7	78.1 ± 44.6	0.47 ± 0.004
M5	115.7 ± 5.4	22.6 ± 9.2	0.36 ± 0.005
M6	69.8 ± 1.4	40.0 ± 18.2	0.45 ± 0.004
M7	20.7 ± 0.2	22.9 ± 6.3	0.40 ± 0.003

The data in table 6.4 indicate these sample microstructures are in fact very similar to that of the previous batch, that of table 6.2. This is precisely the desired outcome, as they have simply been reheated and quenched to ensure a fully martensitic transformation. This should allow for a reliable comparison between the two datasets and a subsequent comparison with literature results.

6.4. EBSD testing

EBSD is a useful technique to bridge the findings from chapter 5 with the data acquired from the physical samples (the beginning of chapter 6). An EBSD map can provide an insight into the actual boundaries, and their respective misorientations, found in the test samples. This, and particularly the differences between them, could prove valuable in explaining the scattering behaviours of the test samples. In so doing the crystallographic property anisotropy can be used in the development of a potential scatter model.

EBSD allows for a large variety of data visualisation which would otherwise not have been possible. Firstly, it allows for an automated methodology to be used to identify microstructural features associated with the sample. The advantage of using automated processing software based on specific physical measurements is of enormous benefit over the typical manual measurements applied previously. The software distinguishes features by comparing crystallographic orientations of a given area and comparing it to the neighbouring regions. Given a significant enough misorientation (above a pre-specified threshold) it is categorised as an independent feature. Using this precise measurement method a number of advantages become apparent when compared to the manual counterpart. Smaller feature sizes become distinguishable (although a minimum should be specified to avoid anomalous results); this allows for a far more representative dataset as the manual alternative requires them to be large enough and easily distinguishable. As an extension of this point, a more representative dataset would also result in a far larger dataset, as a significantly larger number of features should be distinguishable over a given area. This benefit of better feature identification, especially at lower size, should however be considered in light of the previous conclusion of small features simply being too small to positively influence the scattering calculation. Also, as discussed in previous sections, specific orientation relationships dictate which boundaries should present within specific misorientations between feature types. This allows the identified features to be categorised by boundary type, allowing for more detailed analysis.

Although all of the above points seem resoundingly positive attributes of using EBSD type analysis it is important to highlight a potential conflict, that of morphological and crystallographic packets. Whilst most definitions of these features would be the same, with

a number of laths having formed with an overall similar crystallographic orientation as to form a distinct unit – known as a packet, [Suikkanen et al., 2011] makes the distinction and suggests multiple morphological packets can form a single crystallographic packet. Although this distinction is largely inconsequential for many areas of research it is of particular importance here. Having established the importance of acoustic impedance variation with crystallographic orientation (chapter 5), a more appropriate measurement would be the crystallographic packet. However, taking this concept further still, it is important to note the possibility of a range of crystallographic misorientations within a single crystallographic packet. As the assessment of a packet, as measured from EBSD data, is defined by a misorientation above a given threshold (typically 10° or 15°) a scenario of progressive small misorientations could accumulate within a given packet. Therefore, in order to avoid any inadvertent categorisation issues which are caused purely by inappropriate labelling a more appropriate metric would be to simply use the term “misorientated region” as opposed to either crystallographic or morphological packet. This distinction makes little real difference, but simultaneously allows for the possibility of a misorientated region not necessarily coinciding with a packet, be that morphological or crystallographic. The large light blue region in the centre at the bottom of the image of Figure 6.18 also appears to be a likely candidate for a crystallographic packet which is of different size to a morphological packet.

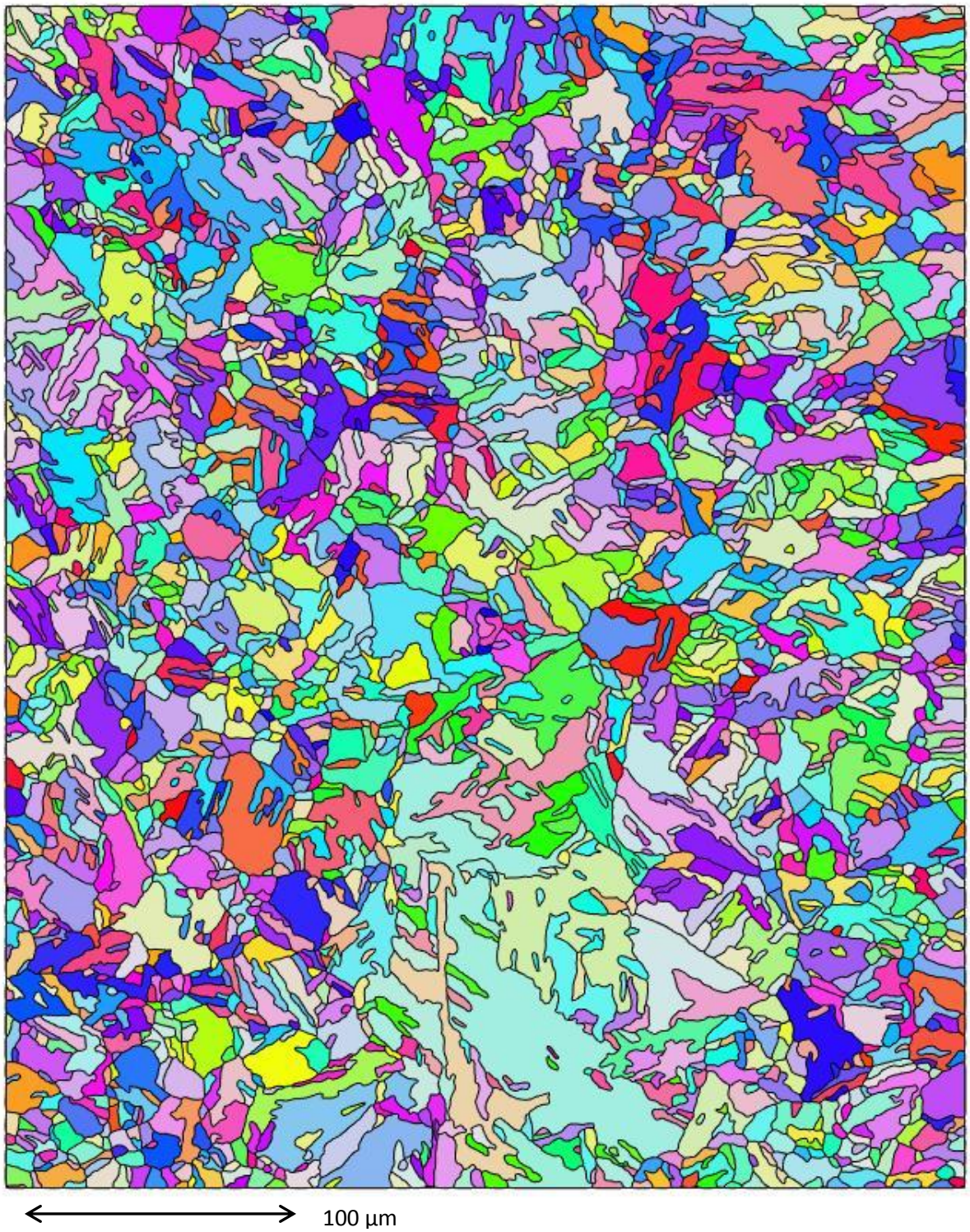

Figure 6.18: Example EBSD image from subsequent results (of sample M7) to indicate a "misorientated region" which likely highlights the difference between a crystallographic and morphologic packet (the large light blue region – bottom centre of the image). Generated with the mtex toolbox in Matlab

6.4.1. Sample C

Figure 6.19 shows an EBSD map of sample C. The image has been cleaned of non-indexed values but has otherwise been left unchanged. There is clear banding of different sized features, presenting with several “streaks” across the image, this has also been evident in some of the micrographs in the microstructural analysis section at the beginning of this chapter.

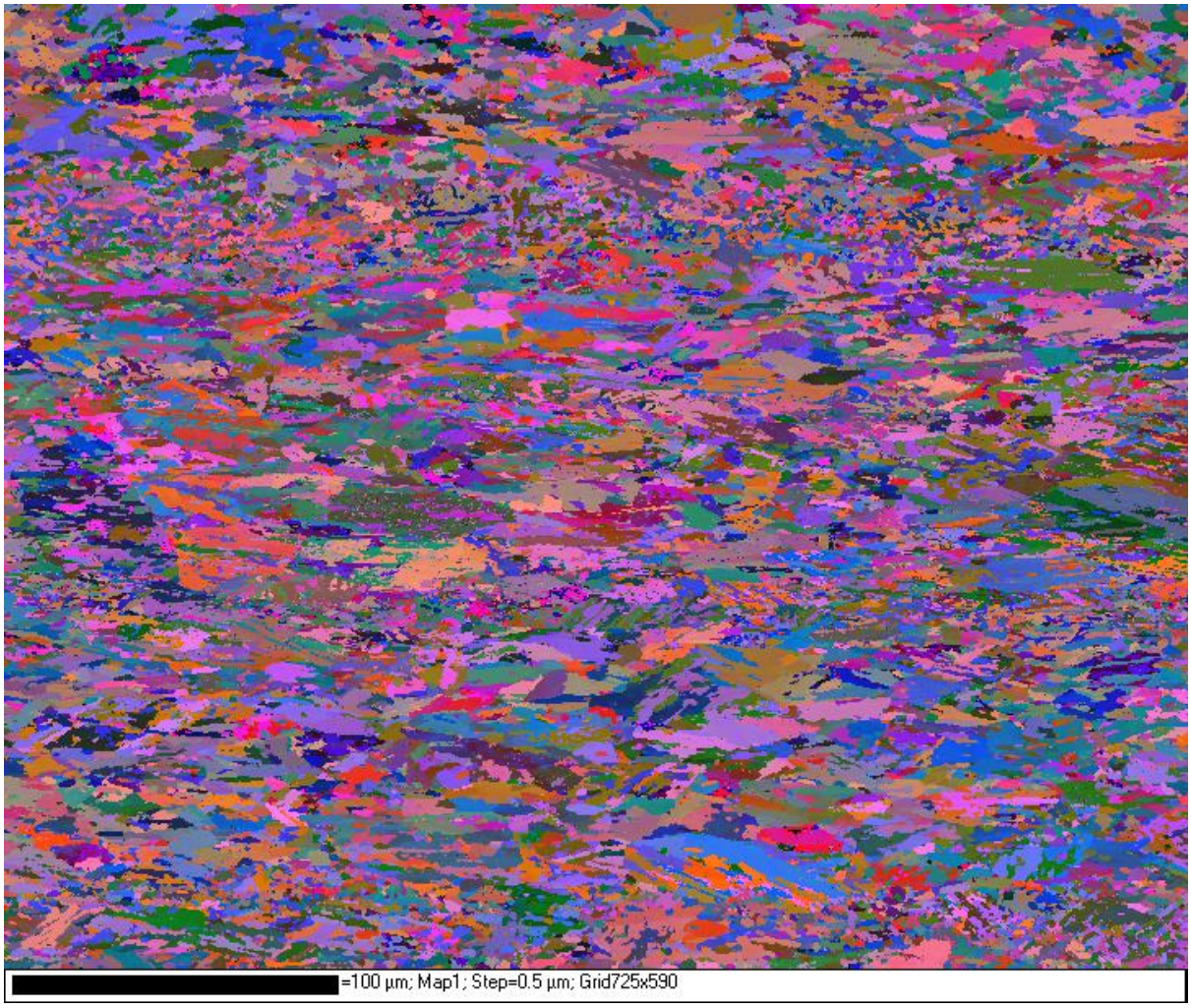

Figure 6.19: Original EBSD map of sample C with non-indexed solutions removed (Euler colouring).

Figure 6.20 has been generated using the mtex toolbox in Matlab (script in Appendix K). This toolbox has been designed specifically for texture analysis. It is important to clarify the

difference in axis orientation between Figures 6.19 and 6.20, which is due to the mtex software using inverted x-y axes as standard, this essentially results in the image having been rotated by 90°. Another difference between the two images is the colouring systems applied; Figure 6.19 uses Euler colouring whereas Figure 6.20 uses inverse pole-Figure (ipf) colouring. The ipf colouring system is advantageous in that it is more intuitive due to the similar colour representing a similar crystallographic orientation whereas that is not necessarily the case in Euler colouring. The ipf colour key as applied to all the images generated with the mtex toolbox is presented in Figure 6.21 and indicates how the individual colours relate to crystallographic orientation.

Figure 6.20 has also undergone further processing to Figure 6.19 with features under 10 individual measurements being smoothed out, thereby introducing a size criterion. The boundaries as applied to the image also have a minimum set point of a 10° misorientation, with the average orientation of the resultant feature being applied for the colouring. These minimum requirements result in a significantly simplified map with potential anomalous results removed, this can range from misidentified pixels to non-indexed values. It should however also be understood that this “smoothing” also potentially removes genuine data which is simply too small for the threshold criterion.

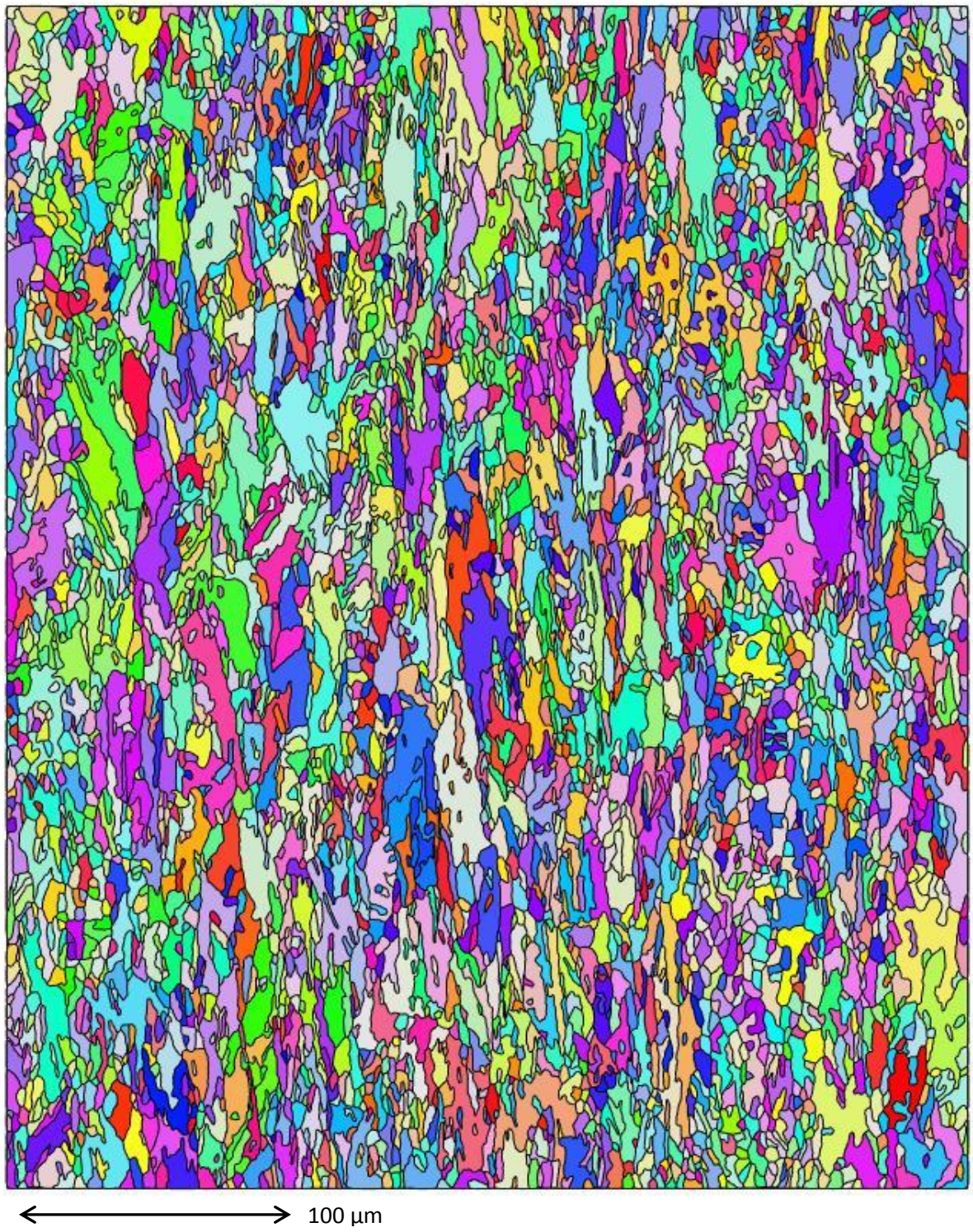

Figure 6.20: Smoothed EBSD map of sample C with IPF colouring. Generated with the mtex toolbox in Matlab – note the standard orientation is different in this toolbox hence the 90 degree rotation.

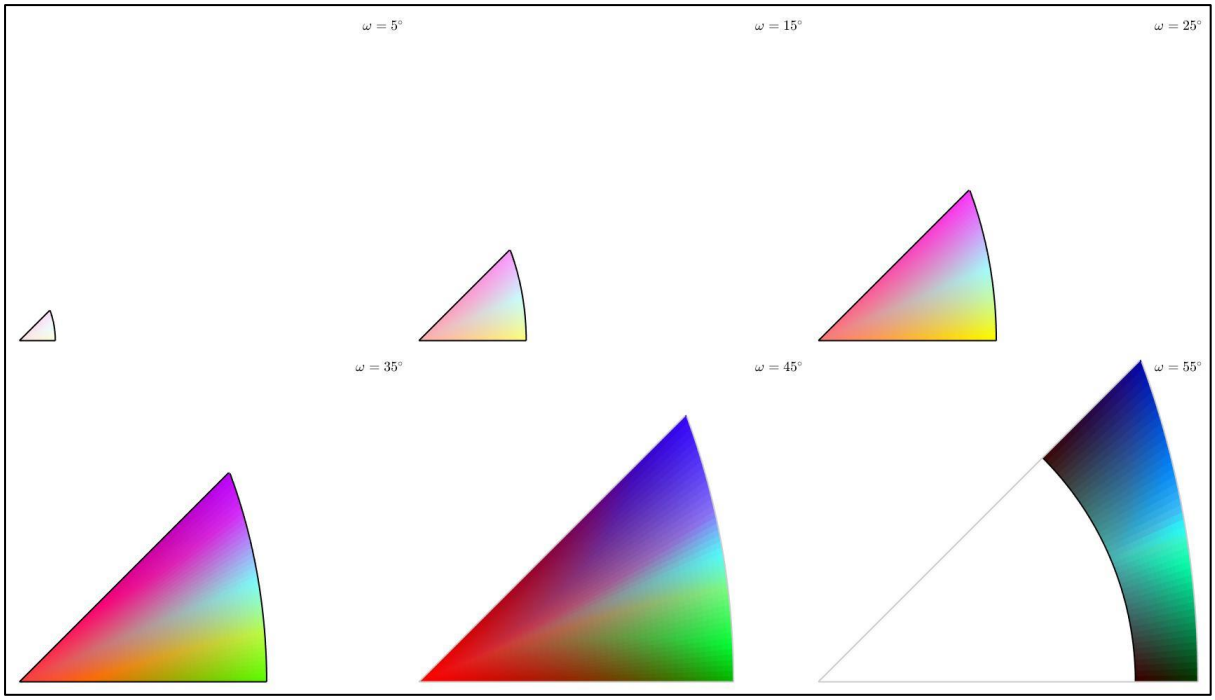

Figure 6.21: Representation of the IPF colour key used in the Matlab script to generate the EBSD maps.

Figure 6.22 is the same image as Figure 6.20 but with the additional detail of grain boundary misorientation applied. The boundaries of Figure 6.20 have been expanded and colour coded by misorientation angle between the features on either side of the boundary. Although it can initially appear somewhat messy the image presents the unique ability to intuitively visualise the boundary misorientations across an entire EBSD scan. Figure 6.23 also summarises this data in the form of a histogram grouped into 5° increments.

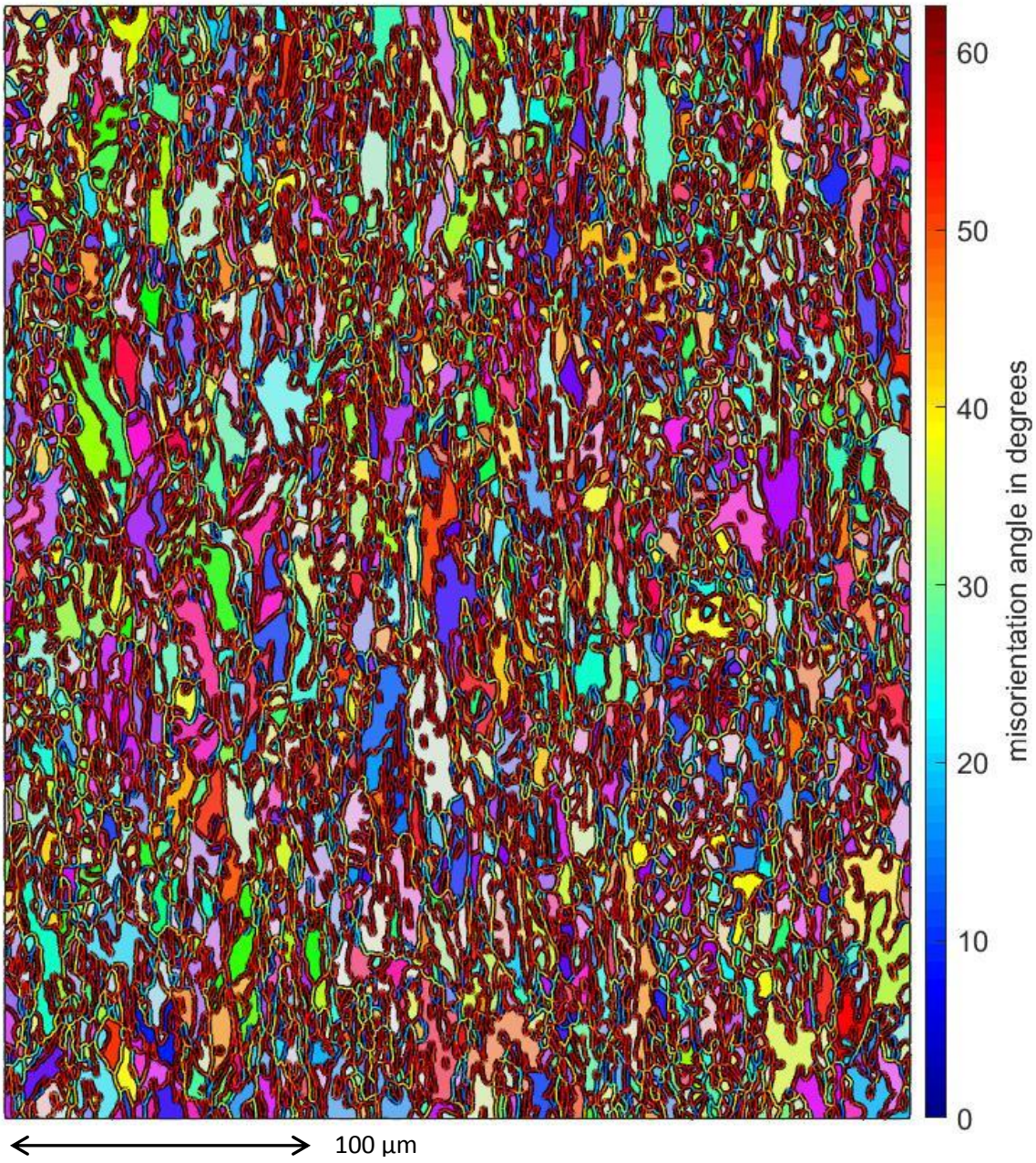

Figure 6.22: Same EBSD map of sample C with IPF colouring with grain boundary misorientation applied to the encountered boundaries. Generated with the mtex toolbox in Matlab.

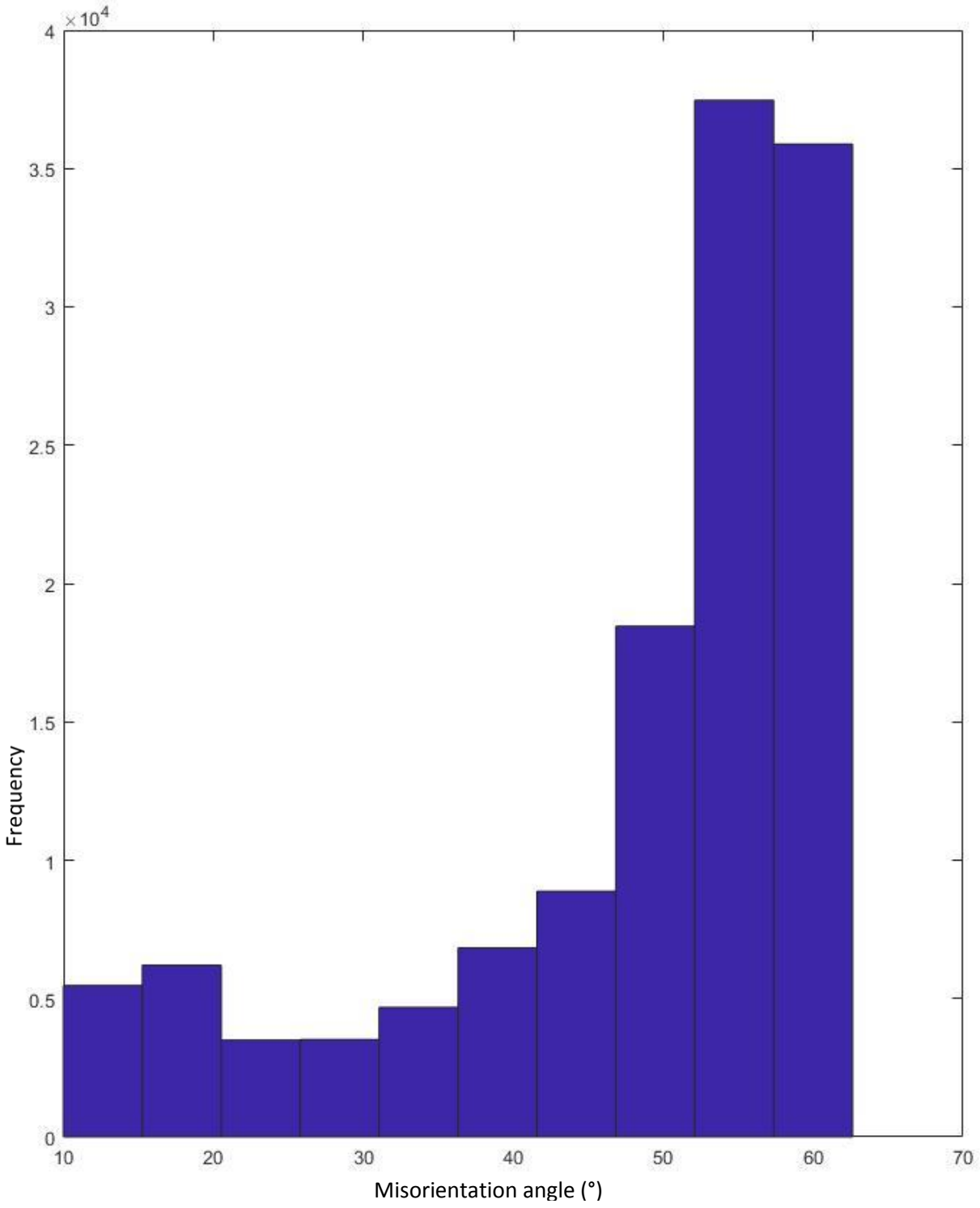

Figure 6.23: Histogram of the EBSD map of sample C with the grain boundary misorientation boundaries grouped by misorientation angle. Generated with the mtex toolbox in Matlab.

The data presented in Figures 6.22 and 6.23 show a clear tendency towards higher angle boundary misorientations. Although, as the histogram lists the frequency of occurrence, this could be skewed due to a large number of small features. This does at least partially appear

to be the case upon closer examination of Figure 6.22 with the majority of smaller features entirely contained by a larger feature exhibiting high angle boundary misorientation. It is important to also once again emphasize the absence of boundaries under 10°, as these would likely dominate had they not been filtered out.

The average of all misorientated regions of sample C, with an area above 10 indexed points, is equal to an equivalent circle diameter of 4.4 µm. The decision to express these values as an equivalent circle diameter was based on the expectation of approximately equiaxed structures, as described in the microstructural analysis technique section (chapter 4.3). This may appear strange for some of these EBSD images, however it must be emphasized that this is once again a two- dimensional representation of a three- dimensional structure, which manifests itself in a complex intertwined structure of laths, packets and grains. Therefore, the measurements taken are likely to be fragments of multiple different structures, which would appear to contradict this assumption. A common example of this would be laths from an adjacent packet breaking through the surface, appearing as multiple small circles or streaks.

6.4.2. Sample C3

Figure 6.24, the EBSD scan of sample C3, has undergone the same processing as Figure 6.20 of sample C.

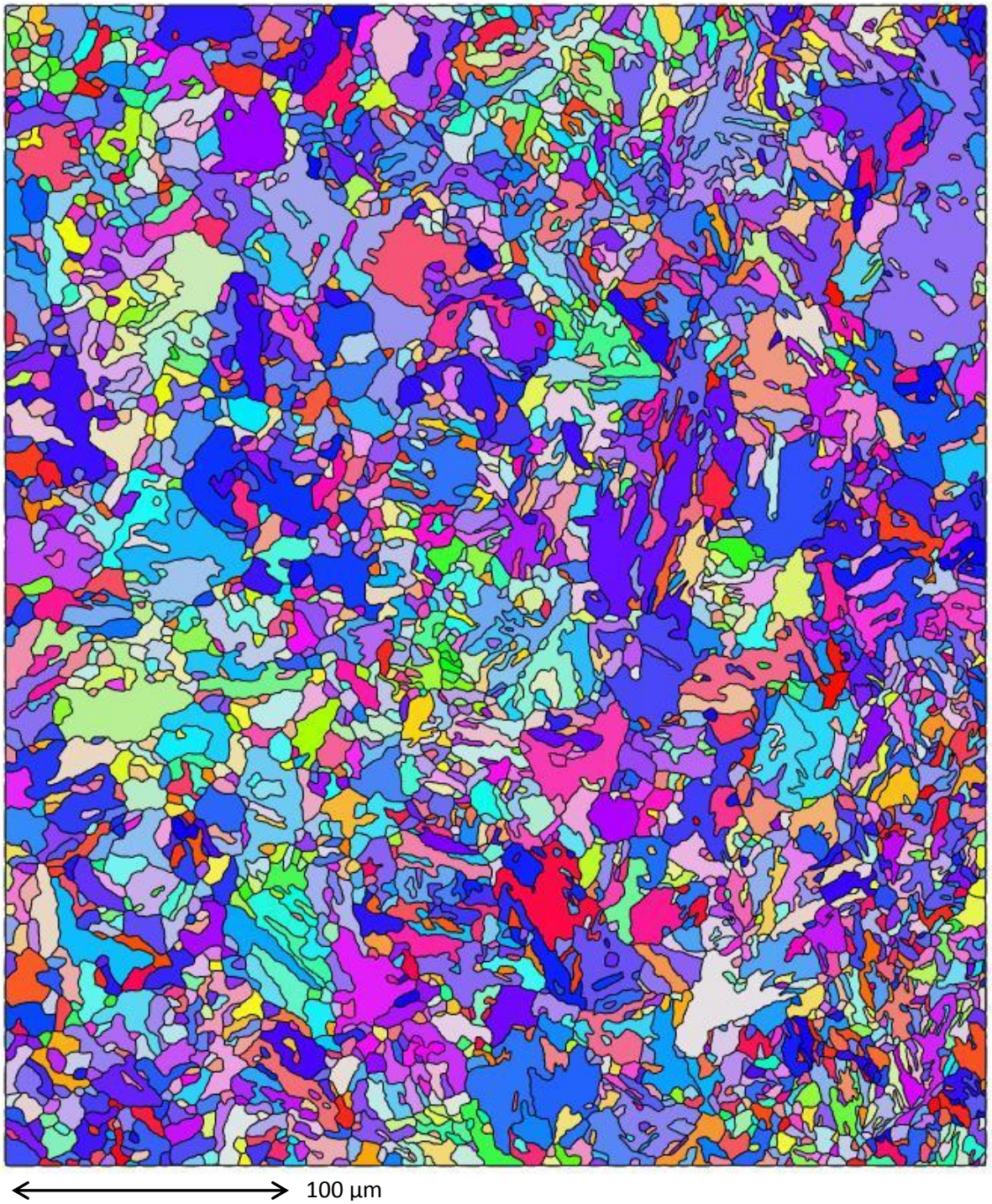

Figure 6.24: Smoothed EBSD map of sample C3 with IPF colouring. Generated with the mtex toolbox in Matlab – note the standard orientation is different in this toolbox hence the 90 degree rotation.

Figure 6.25 appears to show largely the same boundary misorientation as found in Figure 6.22. The tabulated data in Figure 6.26 do appear to show a reduced degree in the highest misorientation category (50 ° - 60 °) in comparison to sample C (Figure 6.23). There does not

appear to be any particularly obvious cause for this and could just be the result of random variation.

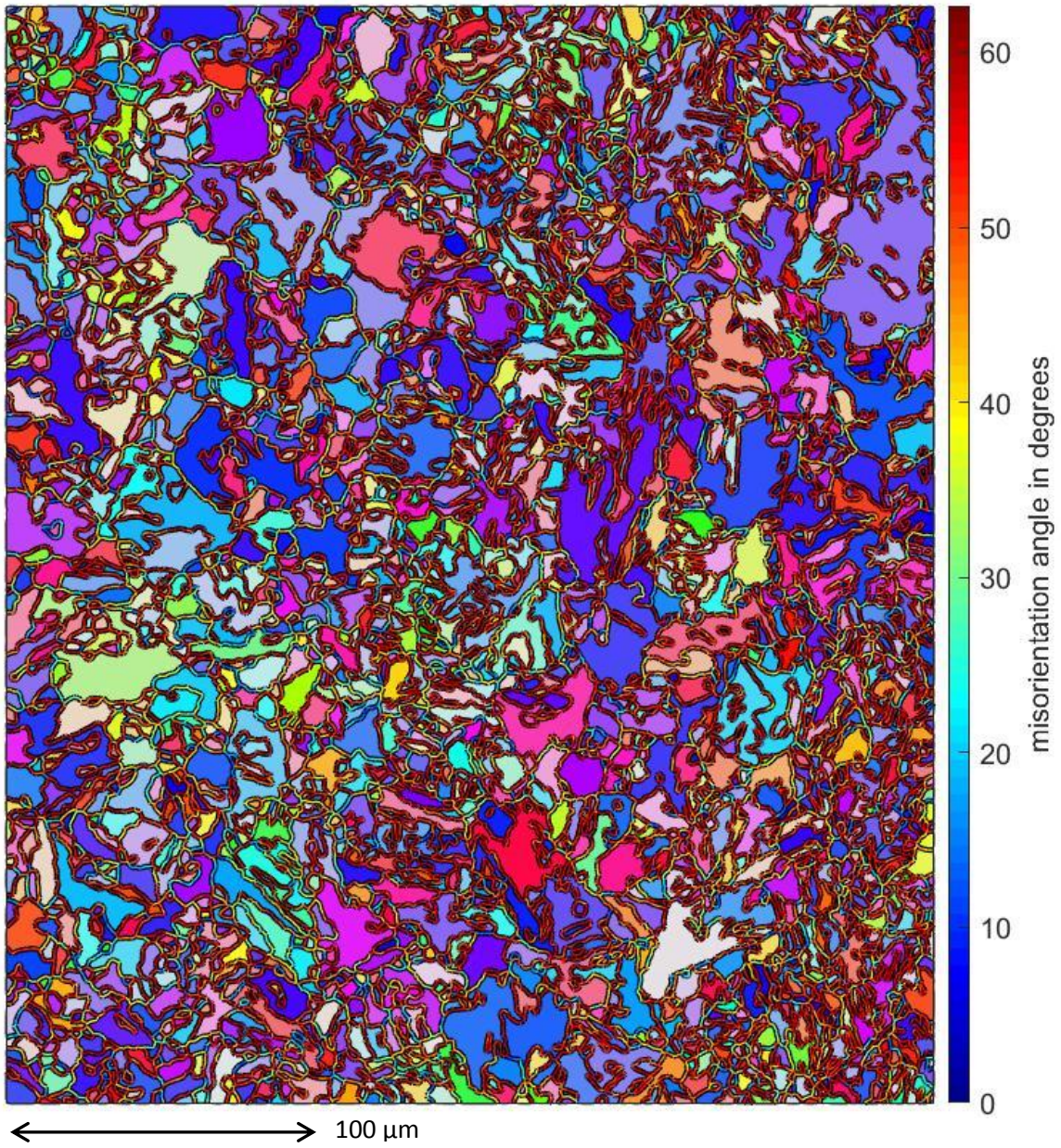

Figure 6.25: EBSD map of sample C3 with IPF colouring with grain boundary misorientation applied to the encountered boundaries. Generated with the mtex toolbox in Matlab.

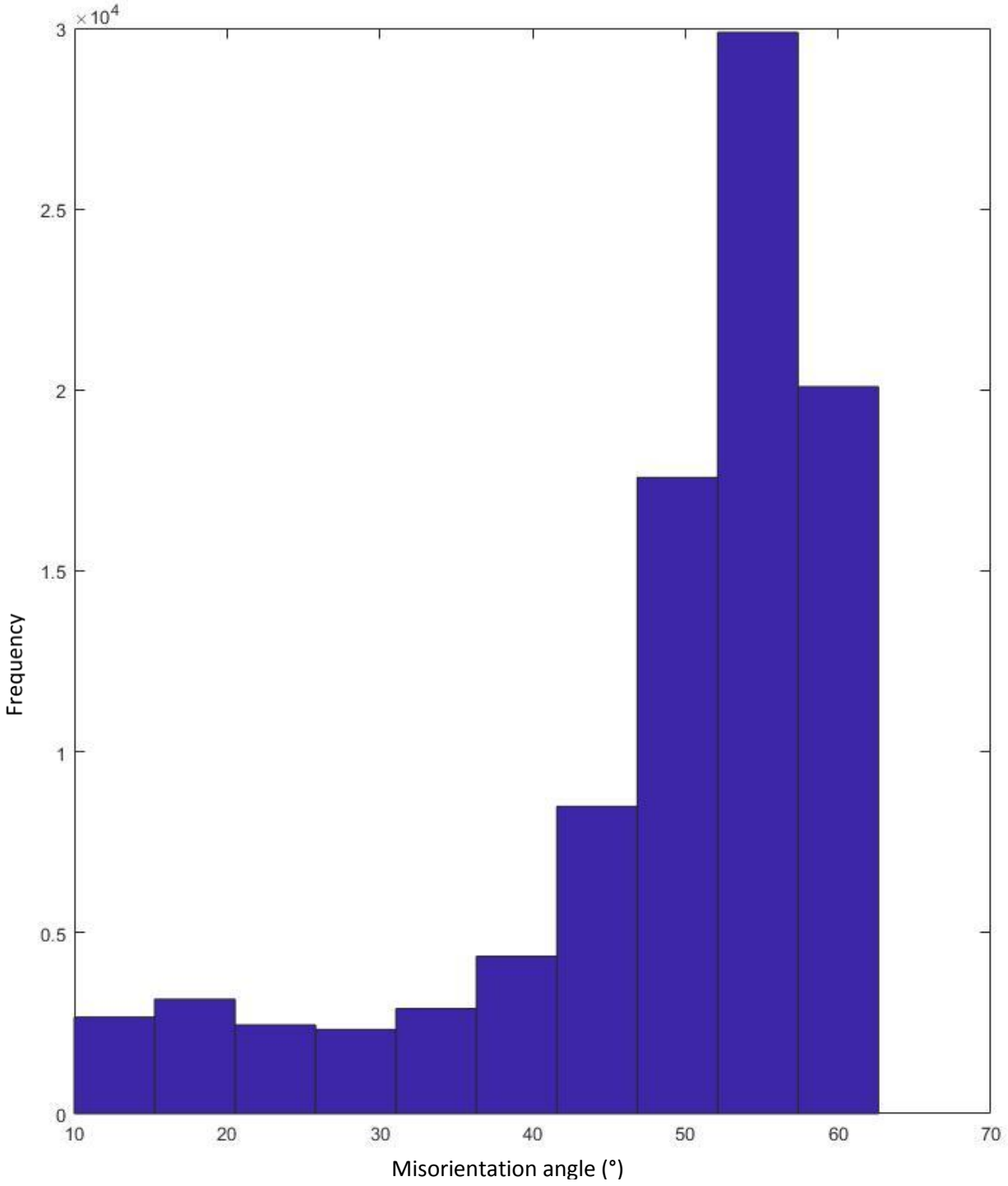

Figure 6.26: Histogram of the EBSD map of sample C3 with the grain boundary misorientation boundaries grouped by misorientation angle. Generated with the mtex toolbox in Matlab.

The average of all misorientated regions of sample C3, with an area above 10 indexed points, is equal to an equivalent circle diameter of 5.4 µm.

6.4.3. Sample D

Figures 6.27 - 6.30 represent the equivalent images for sample D as were used for sample C previously. Sample D exhibits a significantly greater prior austenite grain size however, with distinct grains visible on the EBSD scan (Figures 6.27 and 6.28). Figures 6.29 and 6.30 show a clear deviation from the pattern of the boundaries found in samples C and C3. There is a clear distinction in the distribution of grain boundary misorientation with the highest angle boundaries (50 ° - 60 °) presenting almost exclusively within the prior austenite grain, with very few instances of lower misorientation. Conversely, it is also apparent the prior austenite grain boundary consists almost exclusively of low-to mid- angle boundary misorientation. The misorientation distribution in Figure 6.30 is also heavily skewed towards the largest misorientation angles by the propensity for the boundaries found within the grain to fall in this region.

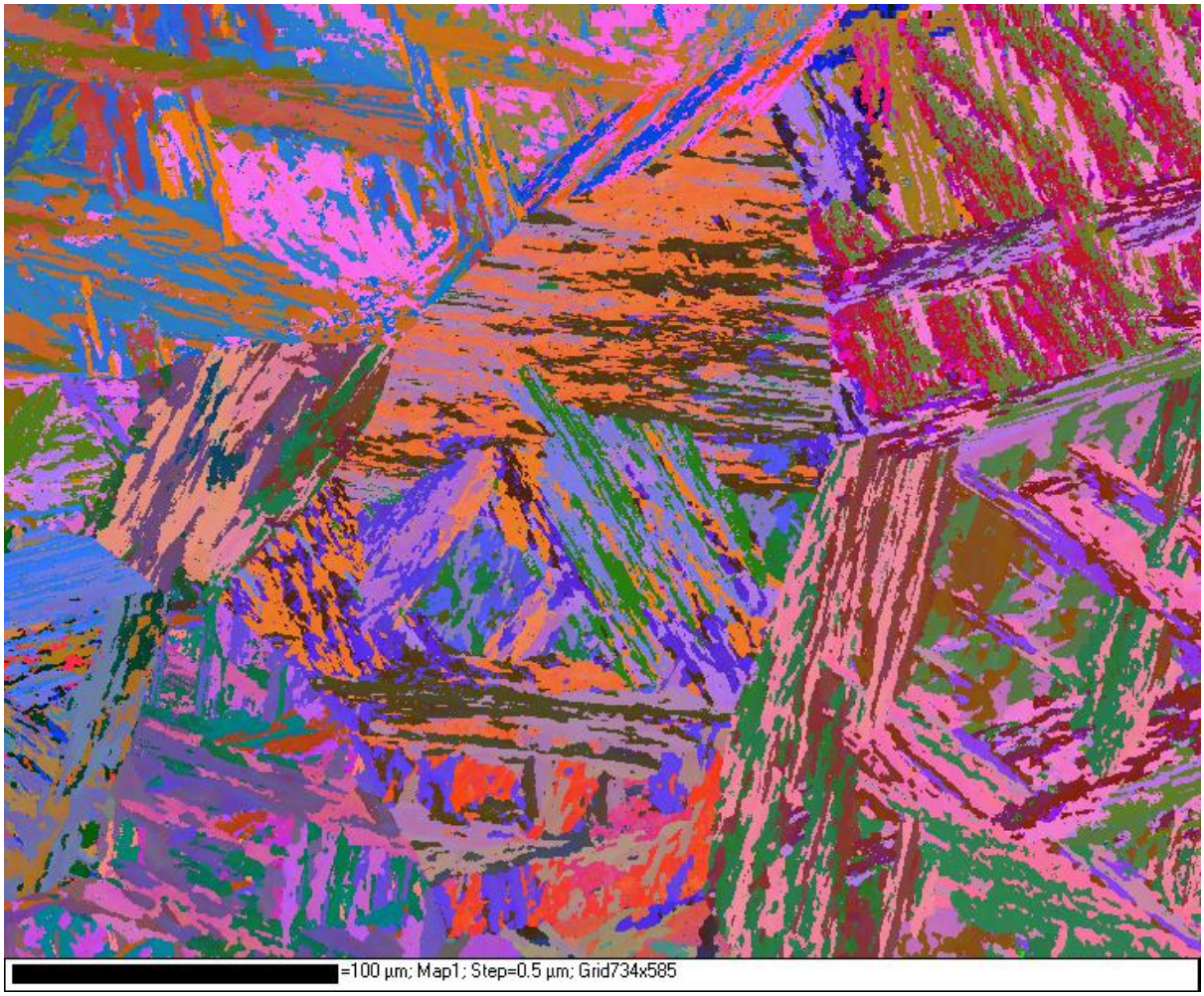

Figure 6.27: Original EBSD map of sample D with non-indexed solutions removed (Euler colouring).

Figure 6.28: Smoothed EBSD map of sample D with IPF colouring. Generated with the mtex toolbox in Matlab – note the standard orientation is different in this toolbox hence the 90 degree rotation.

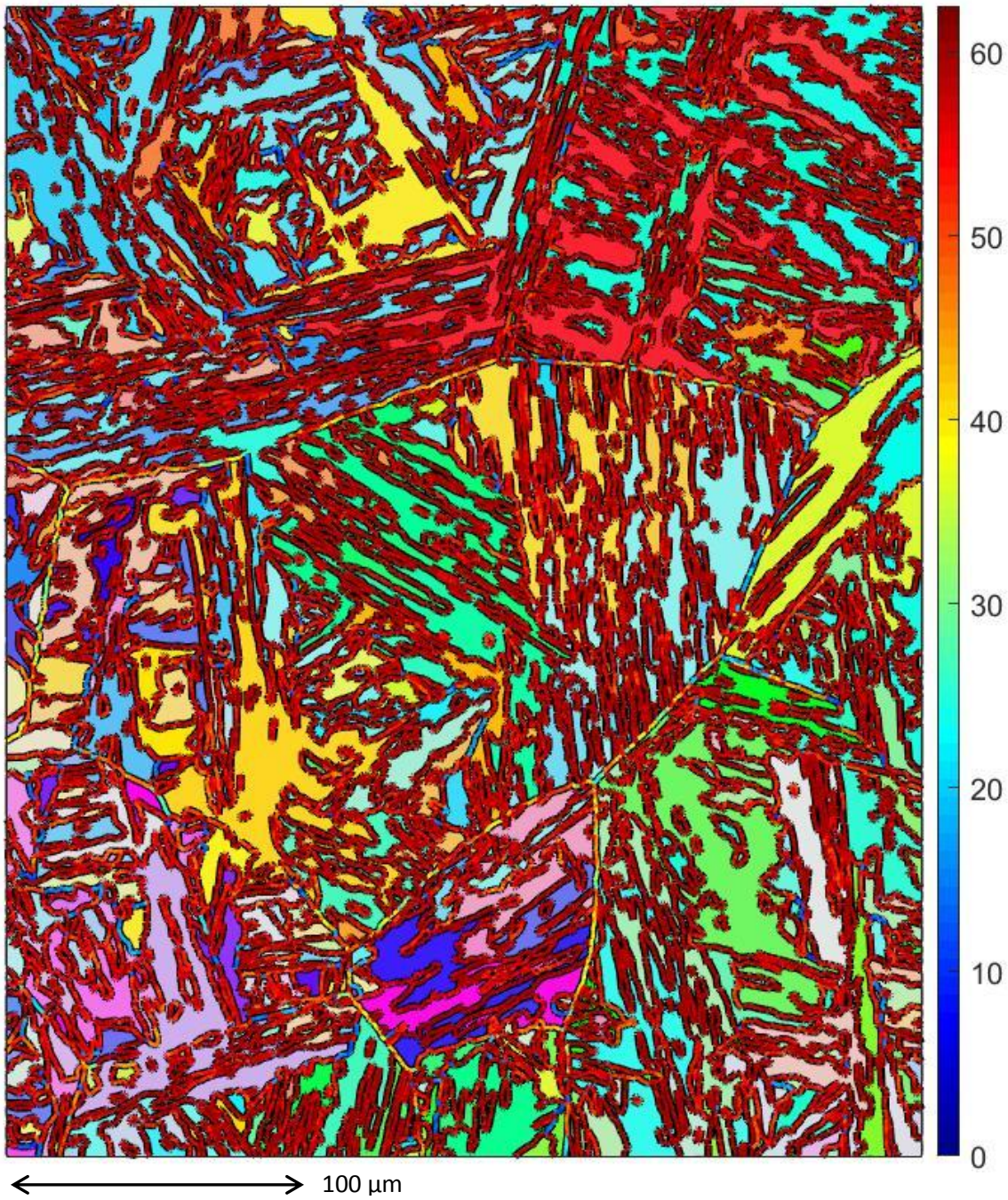

Figure 6.29: Same EBSD map of sample D with IPF colouring with grain boundary misorientation applied to the encountered boundaries. Generated with the mtex toolbox in Matlab.

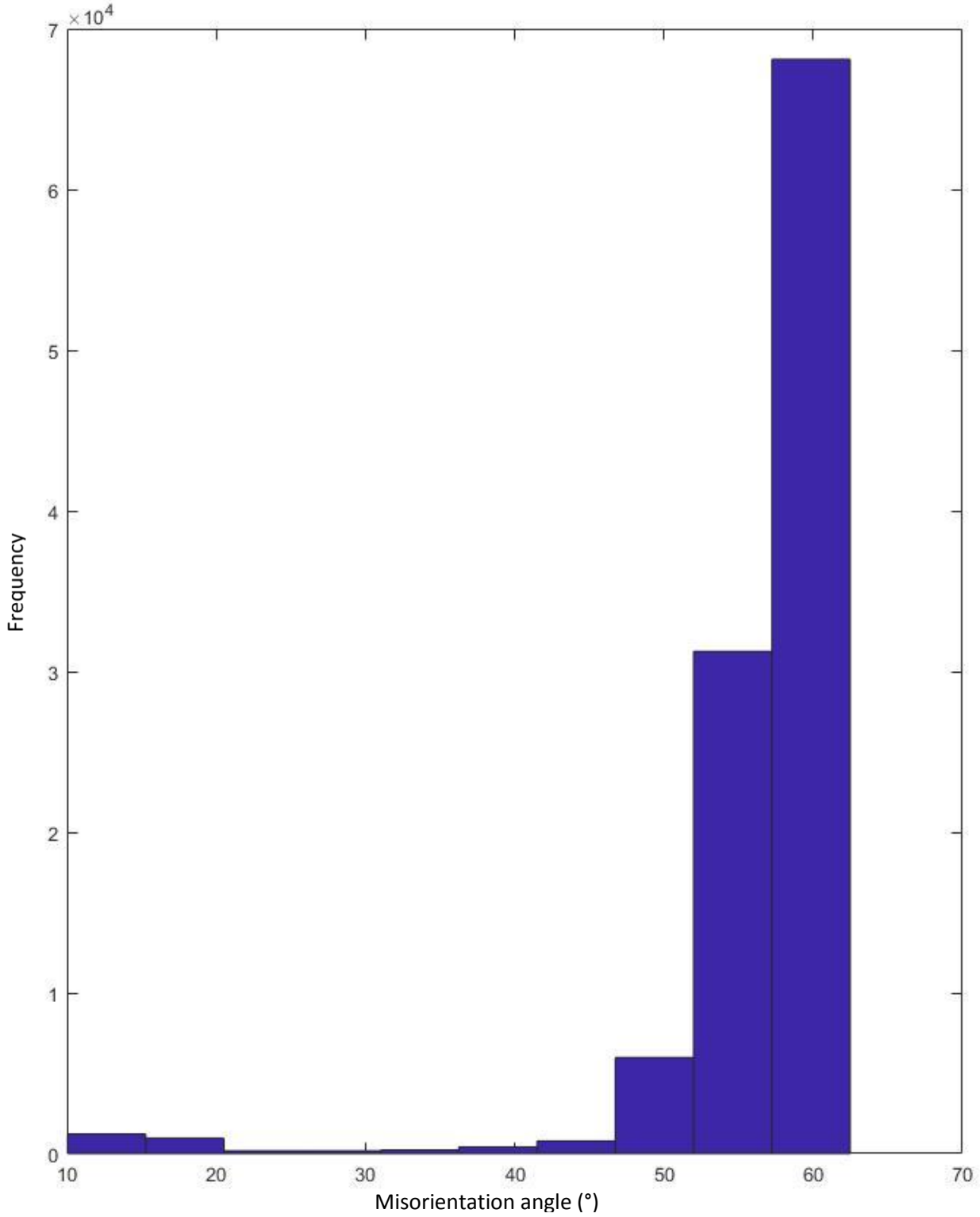

Figure 6.30: Histogram of the EBSD map of sample D with the grain boundary misorientation boundaries grouped by misorientation angle. Generated with the mtex toolbox in Matlab.

The average of all misorientated regions of sample D, with an area above 10 indexed points, is equal to an equivalent circle diameter of 9.3 µm.

6.4.4. Sample M4

As sample M4 is the same sample as sample D (having undergone a further heat-treatment to generate a fully martensitic microstructure), it is unsurprising that the images are very similar. As both have very large prior austenite grain sizes it is easy to distinguish the boundaries in these scans (Figures 6.31 and 6.32). There is once again a clear delineation of the highest angle boundaries within the grain and mainly low to mid angle boundaries for the prior austenite grain boundary, although it is interesting to note this tendency is a little less severe for this sample than in sample D. Figure 6.33 also indicates the distribution of boundary misorientation angles is more in line with the more even distributions of sample C and C3, which likely reflects the reduced number of boundaries within the prior austenite grain.

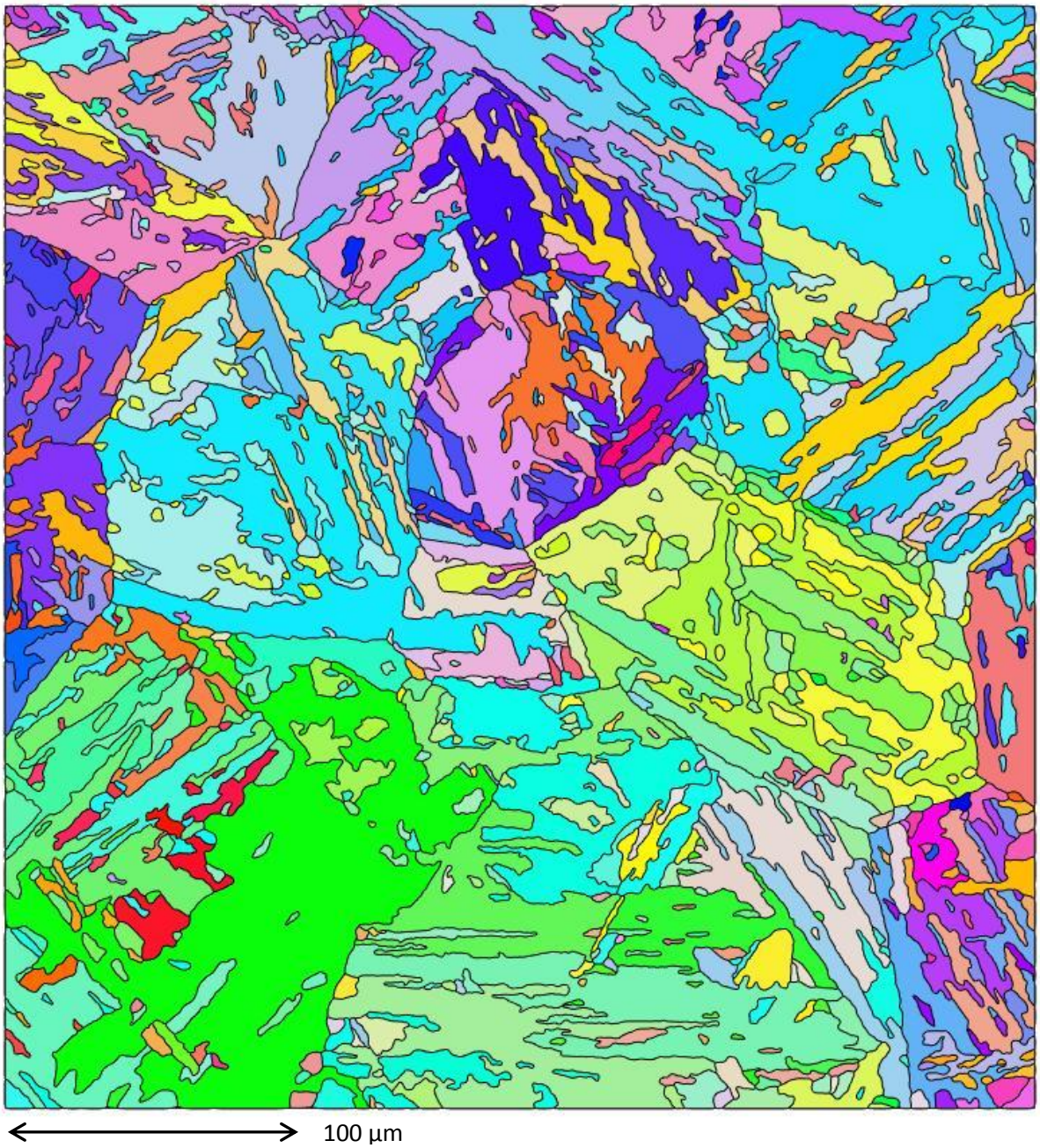

Figure 6.31: Smoothed EBSD map of sample M4 with IPF colouring. Generated with the mtex toolbox in Matlab – note the standard orientation is different in this toolbox hence the 90 degree rotation.

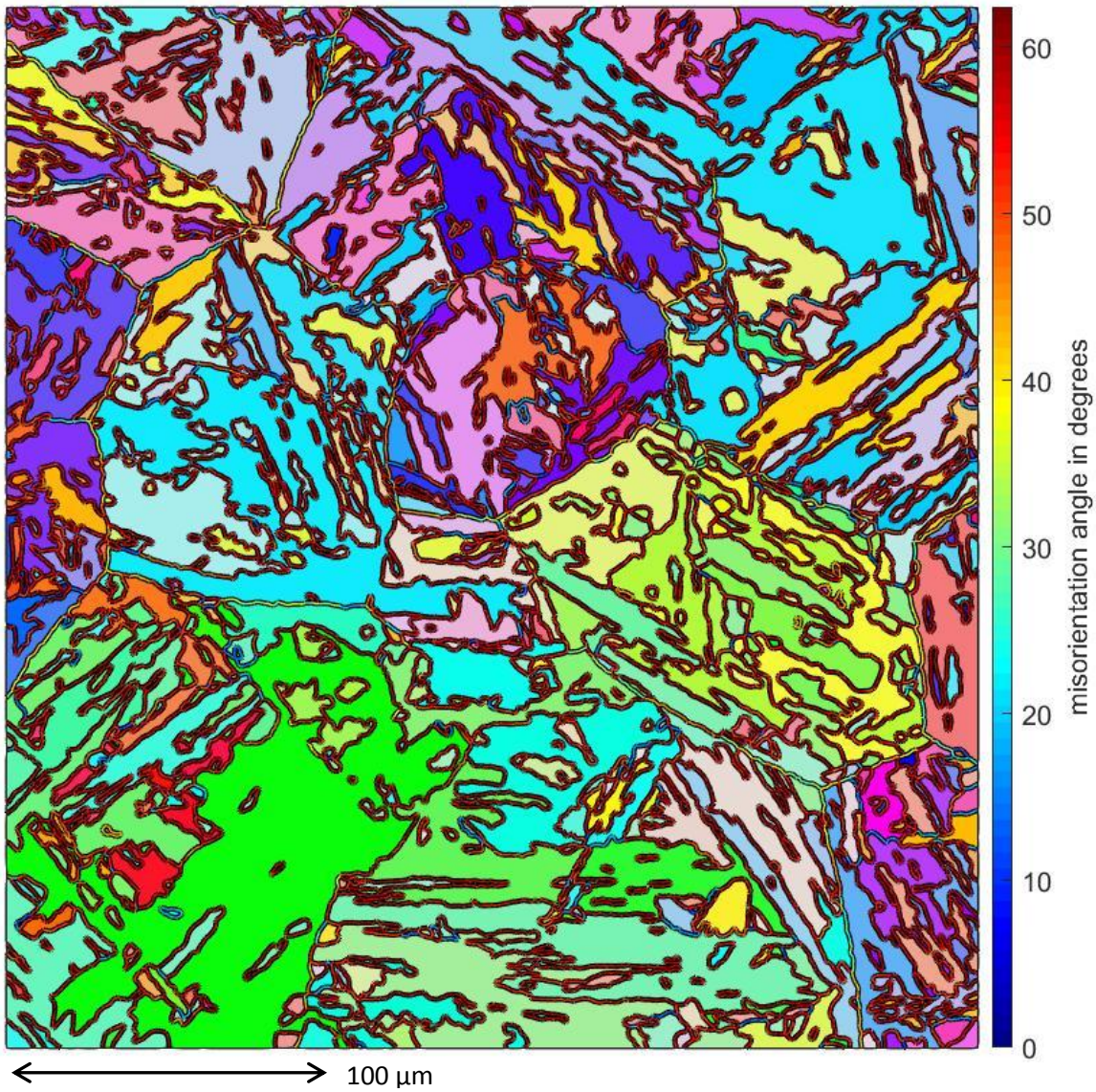

Figure 6.32: EBSD map of sample M4 with IPF colouring with grain boundary misorientation applied to the encountered boundaries. Generated with the mtex toolbox in Matlab.

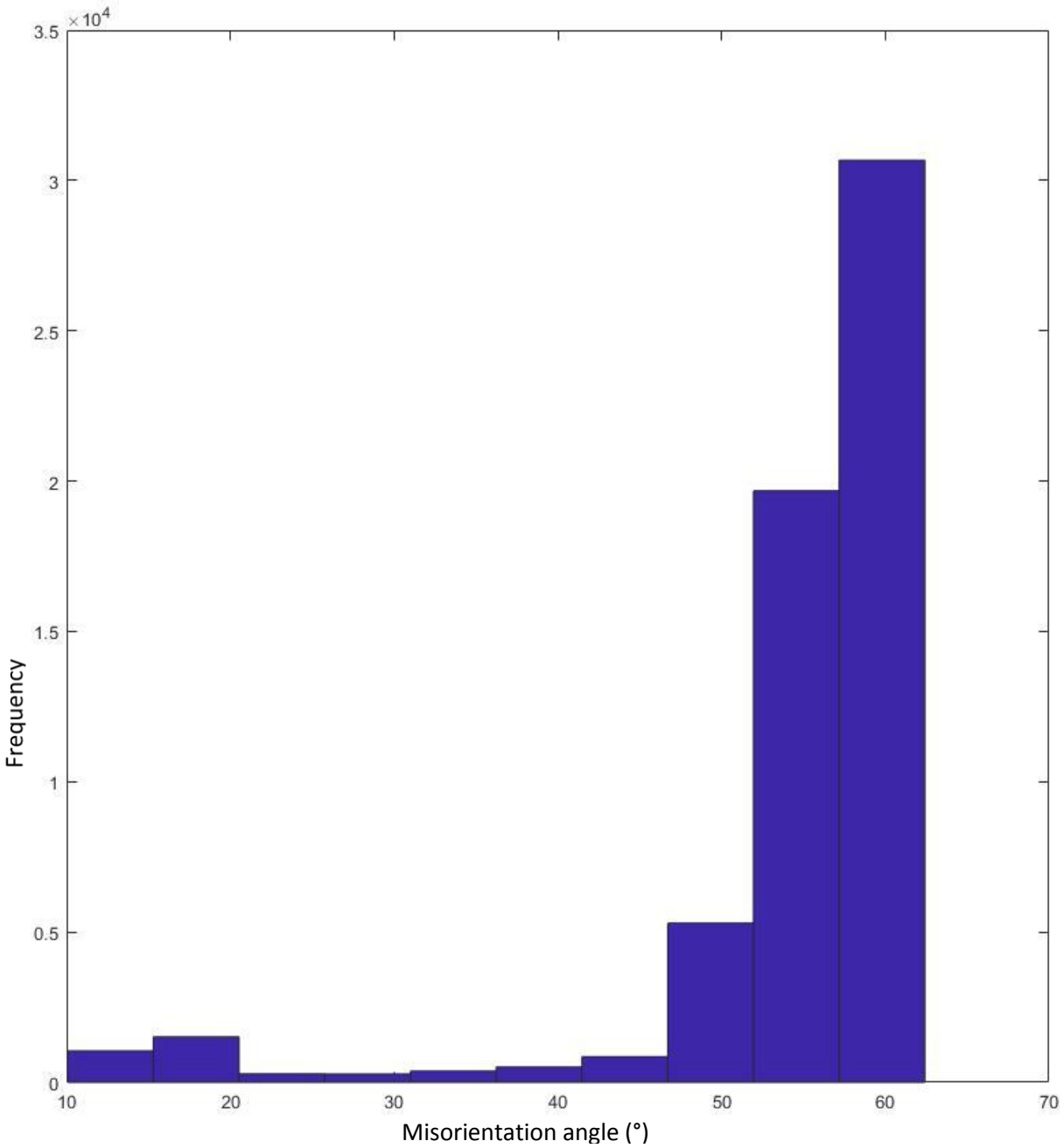

Figure 6.33: Histogram of the EBSD map of sample M4 with the grain boundary misorientation boundaries grouped by misorientation angle. Generated with the mtex toolbox in Matlab.

The average of all misorientated regions of sample M4, with an area above 10 indexed points, is equal to an equivalent circle diameter of 7.4 µm.

6.4.5. Sample M7

The images associated with sample M7 (Figure 6.34 – 6.36) appear largely similar to the results of samples C and C3, which is understandable given the similar prior austenite grain size. In Figure 6.34, the large light blue region in the centre at the bottom of the image also appears to be a likely candidate for a crystallographic packet which is of different size to a morphological packet. It would be unwise to assert this claim with any certainty given the smoothing and removal of small features however. There does appear to be some correlation with the previous trend of low to mid angle boundaries forming the prior austenite grain boundaries in Figure 6.35, although this is significantly harder to distinguish given their smaller relative size.

The variation observed across the boundary misorientation images presented here could simply be due to the fact that smaller grains simply have fewer boundaries within a grain of sufficient size so as not to be filtered out. As all of the scans are of roughly the same area and all of the same step size this could well be the defining aspect.

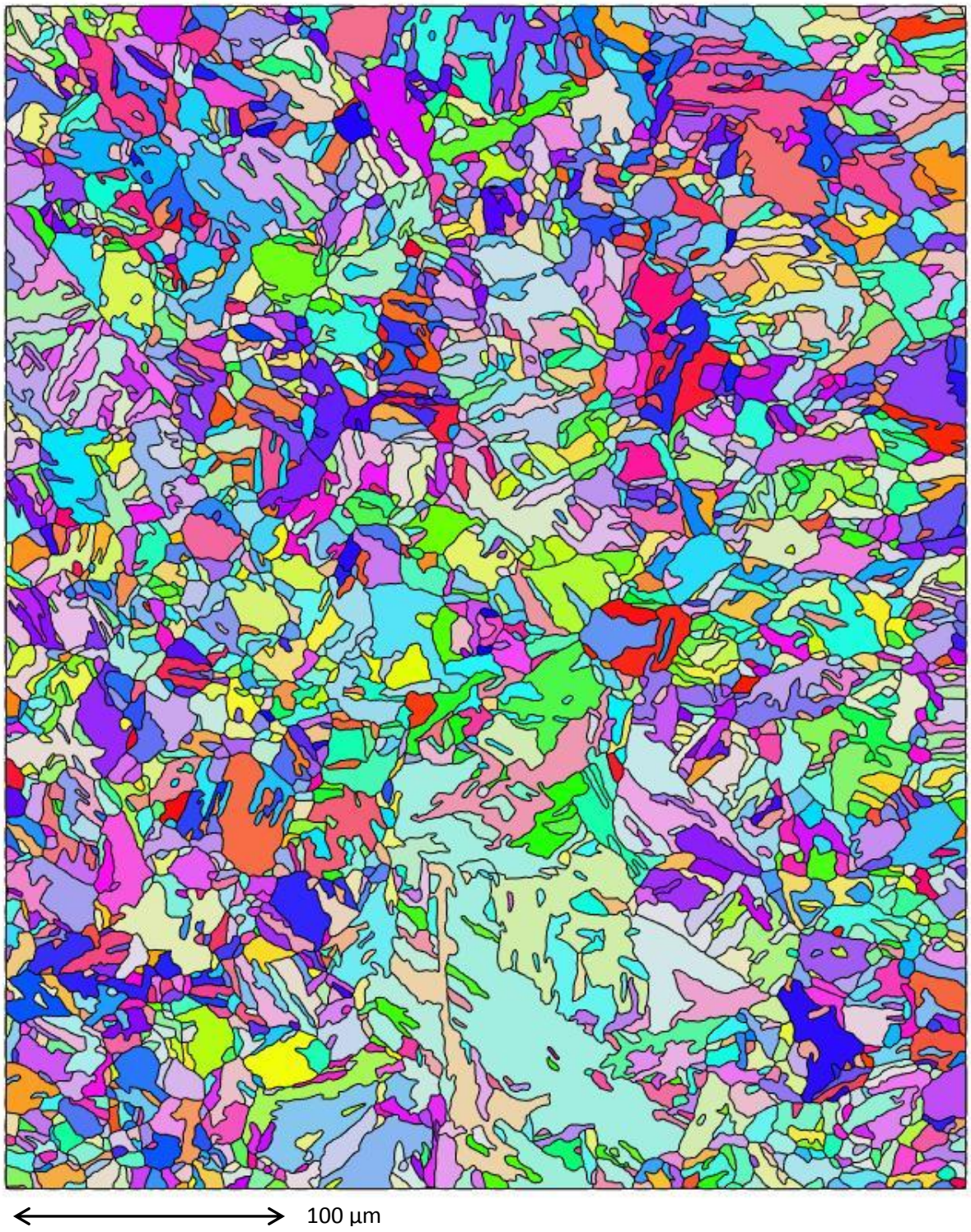

Figure 6.34: Smoothed EBSD map of sample M7 with IPF colouring. Generated with the mtex toolbox in Matlab – note the standard orientation is different in this toolbox hence the 90 degree rotation.

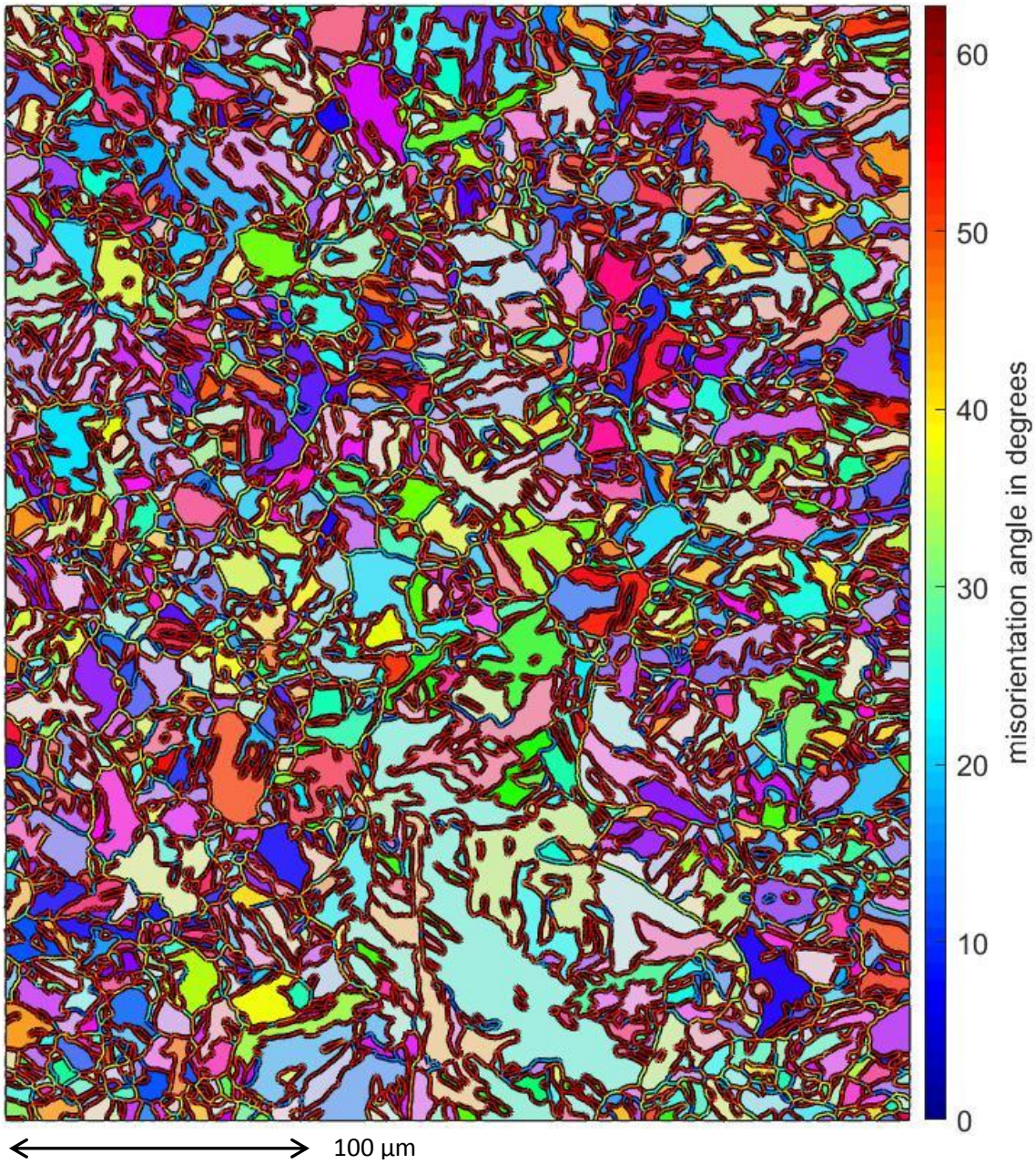

Figure 6.35: EBSD map of sample M7 with IPF colouring with grain boundary misorientation applied to the encountered boundaries. Generated with the mtex toolbox in Matlab.

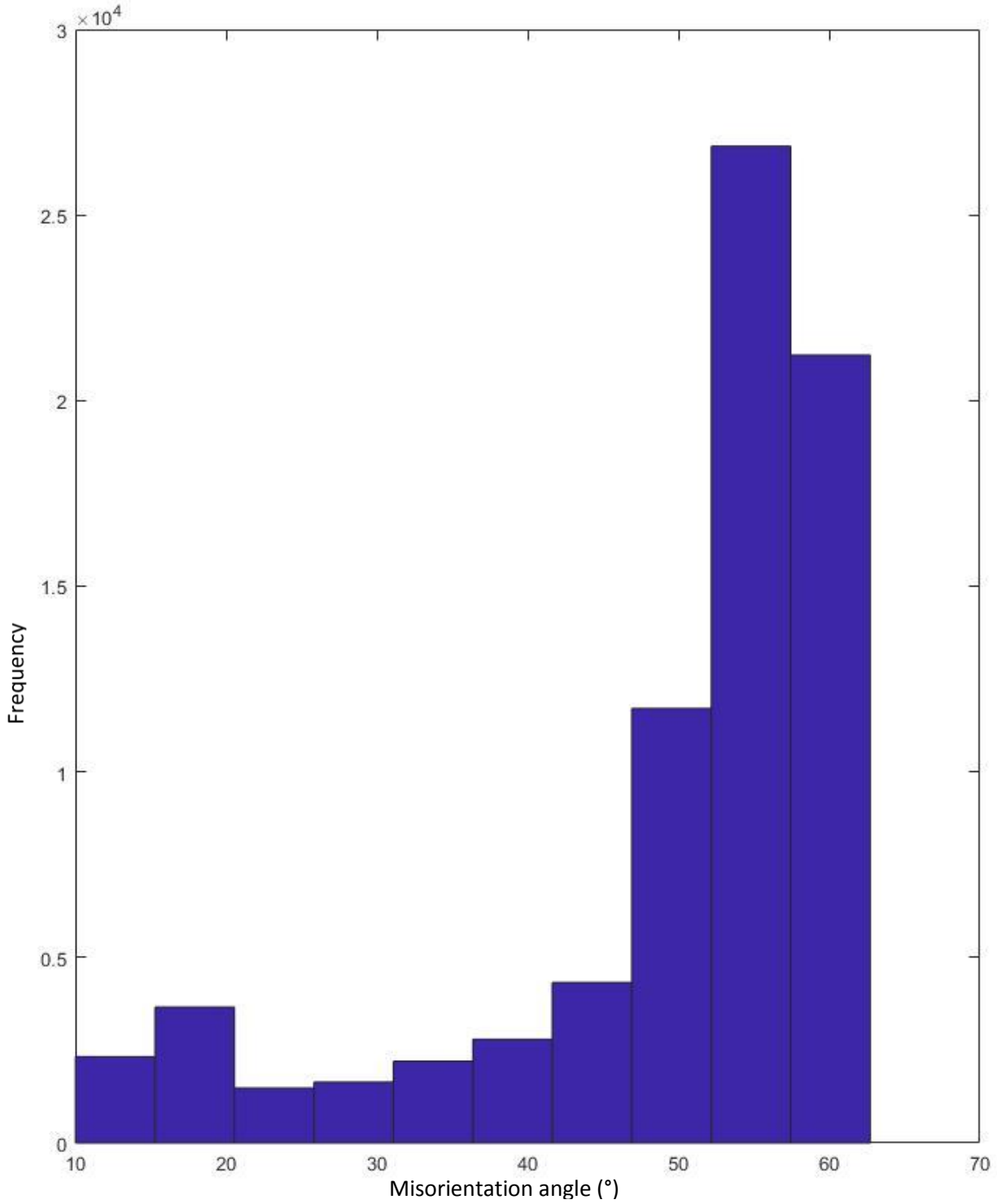

Figure 6.36: Histogram of the EBSD map of sample M7 with the grain boundary misorientation boundaries grouped by misorientation angle. Generated with the mtex toolbox in Matlab.

The average of all misorientated regions of sample M7, with an area above 10 indexed points, is equal to an equivalent circle diameter of 5.4 µm.

7. Results and discussion

7.1 Ultrasonic testing data

The ultrasonic testing data collected as part of this project involved a pulse/echo setup (details in chapter 4) using three distinct ultrasonic test frequencies. The centre frequencies of the transducers used were 10 MHz, 5 MHz and 2.25 MHz and were designed to provide data over a range of representative frequencies. A cursory examination of the attenuation values (tables 7.1, 7.2 and 7.3) across the ultrasonic test frequencies shows there is an issue. All ultrasonic attenuation models and calculations expect the attenuation to fall with reduced frequency, and yet here it does not. Trials with calibration blocks of different widths pointed to a side-wall interference issue. This is also supported by the far field beam spread calculation for transducers of different frequencies (chapter 4.4). Due to the restrictions on sample sizes and equipment used as part of this study, this unfortunately became an unavoidable obstacle. As the results associated with the lower frequency transducers (5 MHz and 2.25 MHz) were more influenced by the physical dimensions of the sample rather than the microstructure which is being investigated, they are of no further use to the development of a scattering model. Therefore they shall be omitted from the remainder of this chapter.

Table 7.1: Measured ultrasonic attenuation values of pearlitic samples with different frequencies (10 MHz, 5 MHz and 2.25 MHz). Measurement procedure and uncertainty detailed in chapter 4.

Sample name	10 MHz (Np/m)	5 MHz (Np/m)	2.25 MHz (Np/m)
A	27.1	22.3	-
A1	25.4	20.5	41.0
B	29.4	18.7	22.6
B1	22.3	20.6	44.3

Table 7.2: Measured ultrasonic attenuation values of mixed martensite and bainite samples with different frequencies (10 MHz, 5 MHz and 2.25 MHz). Measurement procedure and uncertainty detailed in chapter 4.

Sample name	10 MHz (Np/m)	5 MHz (Np/m)	2.25 MHz (Np/m)
C	13.8	11.6	19.6
C1	-	11.8	19.1
C2	10.4	11.1	21.1
C3	11.1	11.0	21.0
D	28.9	16.6	25.8
D1	25.1	15.9	23.5

Table 7.3: Measured ultrasonic attenuation values of martensitic samples with different frequencies (10 MHz, 5 MHz and 2.25 MHz). Measurement procedure and uncertainty detailed in chapter 4.

Sample name	10 MHz (Np/m)	5 MHz (Np/m)	2.25 MHz (Np/m)
M1	10.9	33.9	49.6
M2	17.5	35.9	52.2
M3	10.3	33.3	48.8
M4	28.8	48.0	64.2
M5	22.3	34.6	50.5
M6	21.2	38.6	56.0
M7	15.3	38.4	57.5

There appears to be a discrepancy between the severity of the side-wall interference issue across these attenuation values, which is likely linked to the dimensions of the individual sample.

7.2 Pearlite model

As the model was inspired by the work of [Du and Turner, 2014], it was decided to focus initial efforts on pearlitic microstructure steels. This choice of microstructure was made in order to specifically compare results to the paper and to cross verify the two sets of findings, especially as the paper is also the only source of published results which are directly comparable. It is also a method which can be used to validate the overall approach to modelling ultrasonic wave scattering from additional boundaries within the grain boundary itself.

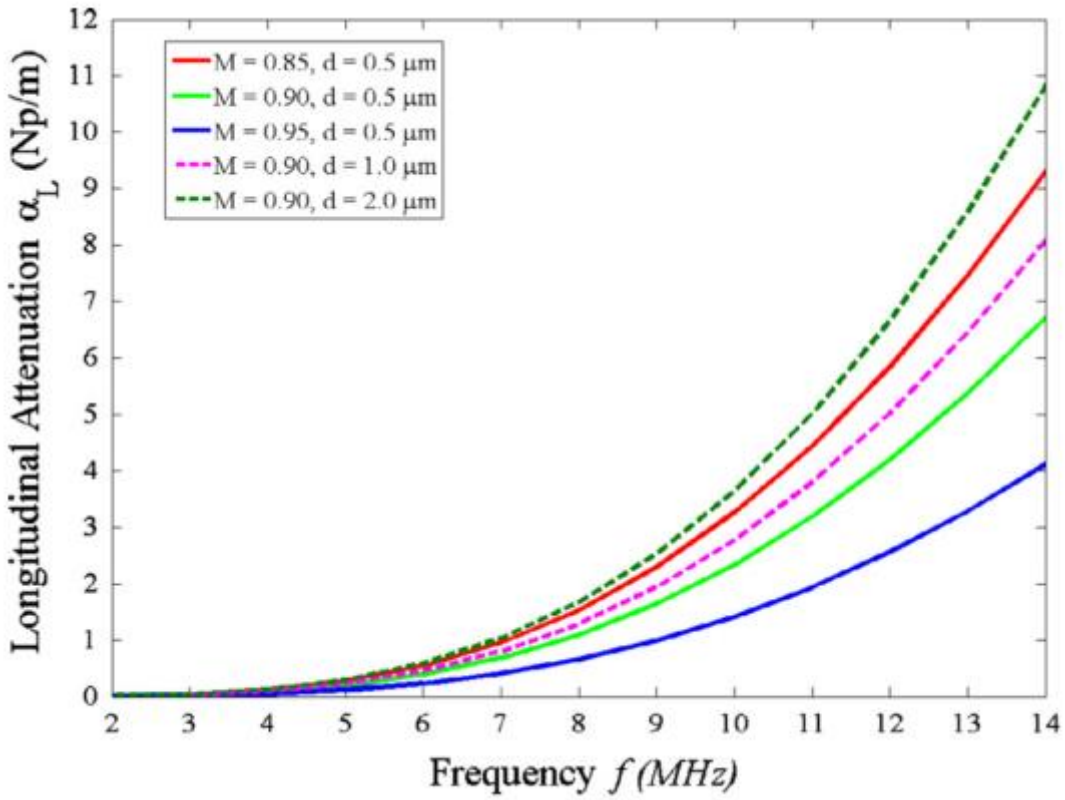

Figure 7.1: A Figure from [Du and Turner, 2014] predicting the levels of longitudinal attenuation associated with a range of different weighting factors (M), lamellae spacings (d) and frequency values (f)

The chart in Figure 7.1 shows the predictions made for the level of longitudinal attenuation across a combination of different weighting factors (M), lamellae spacings (d) and frequency values (f) as predicted by Du. In order to calibrate the maple script used to evaluate the respective model predictions (included in appendix I, J for pearlite and the equivalent for martensite in appendix G, H), this graph was independently successfully recreated with the respective input parameters.

Having established the script is recreating the intended results it is possible to link the observed experimental results against the theoretical prediction for the observed microstructure. The model paper concluded the best correlation between theoretical and experimental results was found to correspond with a weighting factor of M=0.9, and so this seems like a logical initial starting point. As previously stated the comparison will be made

against the 10 MHz longitudinal results as these provide the most robust dataset to compare against. A summary of the input data is provided in table 7.4.

Table 7.4: A comparison of the 10 MHz attenuation values against the microstructures of the generated pearlite samples. The 10 MHz ultrasonic dataset shall be used as it seems to be the most robust set of data available.

Sample name	Colony size (µm)	Lamellae spacing (µm)	Attenuation 10 MHz (Np/m)	Attenuation prediction 10 MHz (Np/m)
A	110.5	0.281	27.1	14.52614
A1	71.7	0.355	25.4	11.42129
B	142.9	0.514	29.4	15.88574
B1	90.5	0.288	22.3	13.28859

As is abundantly clear from the theoretical prediction presented in table 7.4 the data are a long way off from the actual experimental results. In fact the order of the predicted attenuation values does not follow the same trend as the tested samples. As a result it can be concluded there is likely to be a structural error with the model in its current form.

The model originally adopts the weighting associated with the individual terms, the M-factor, from another paper which considered the contribution of two completely independent phases (discussed in chapter 3.3.2.). By treating the individual terms as being independent, one is effectively being displaced by the other as their relative ratios change within the material. This, in turn, leads to the scattering contribution of one to change relative to the other, and so would be accounted for by the weighting factor.

This process would however not be an accurate way of describing the two terms in a pearlitic sample. As the lamellae structure cannot form independently of the colonies, as a colony is simply a number of lamellae oriented closely to a preferential direction. Therefore they do not displace one another from the scattering contributions, but rather form in addition to one another, in line with the argument of Papadakis (see chapter 3.3.2.). And so

it is suggested the terms should be calculated independently and then summed to form the resultant total.

Table 7.5 presents a set of weighting factors which at least recreate the order of attenuation as measured from the experimental test samples. However, this is clearly unrealistic. To generate an attenuation prediction which matches the order of the tested samples the weighting given to the lamellae had to be increased immensely, for which there is absolutely no justification. It also contradicts the expectations of small boundaries contributing little to scattering, as was discussed in chapter 5 (although lamellae were not specifically calculated). Therefore, there is likely to be a fundamental error in the approach to this model and that of [Du and Turner, 2014].

Table 7.5: Theoretical prediction using the amended model detailed above. Weighting is set to 0.09 for the colony and to 14 for the lamellae

Sample name	Colony size (µm)	Lamellae spacing (µm)	Attenuation prediction 10 MHz (Np/m)
A	110.5	0.281	23.81
A1	71.7	0.355	23.45
B	142.9	0.514	32.13
B1	90.5	0.288	23.14

A more likely scenario would be for the lamellae to contribute virtually nothing to overall scatter individually. This is drawn from the small feature calculation of chapter 6, with the estimates made for carbides being roughly representative given the same order of magnitude and similar acoustic impedance expected. Therefore the scattering should be dominated by colonies, as their relative size does not contradict this it seems reasonable. Furthermore, [Papadakis, 1964b] discussed a further f^2 contribution to attenuation, which he suggested could be due to dislocation damping, atomic relaxations or magnetic boundary effects. This seems like a reasonable argument given the unaccounted for differences that

are found between the samples which have undergone further heat-treatment and those which have not. This shall be explored more fully for the subsequent martensitic samples.

7.3 Bainite and martensite samples

As the foundation of the scattering models for these samples has already been disproven, it makes little sense to arbitrarily insert values to compare the outcomes. However the lessons learned as part of the boundary reflection calculation work can certainly be discussed here. Firstly, the individual contribution to scatter of lath boundaries is likely negligible. This statement is supported by the calculations made as part of chapter 5, where their small size resulted in a fraction of a percent of their already small scattering contribution being realised. Furthermore, as lath boundaries within a single packet are expected to tend towards low angles of misorientations, their contributions are reduced further still (as tables 5.5 and 5.7 shows a correlation between boundary misorientation and boundary reflection coefficient).

The EBSD scans indicate a tendency towards very high boundary misorientations within a prior austenite grain. This is likely the result of laths (or groups of laths) of a different packet partially breaking the EBSD scan surface. Although these features are mostly associated with a high boundary misorientation they should typically contribute very little to overall scattering given their small size. This would not necessarily be the case for the largest of these features, which are mostly found in samples associated with a large prior austenite grain size.

Therefore, for samples with small to medium size prior austenite grains the scattering contribution should be dominated by grain boundaries as described in the long established

models in the literature. However, this statement should be qualified by acknowledging the findings of [Papadakis, 1964b]. He found the internal structure of bainite and martensite disrupted the anisotropy of the grain, which reduces the contribution of a prior austenite grain to act as a scattering centre. This occurs as the result of the normally large acoustic impedance encountered at the grain boundary being broken up into smaller contributions. As was shown in chapter 5, these smaller segments simply become less effective scattering contributors. The end result of the summed contributions being significantly reduced in comparison to the original grain. This is also the case when the total acoustic impedance encountered as part of this internal structure is significantly larger than that of the grain boundary, as the size aspect of the scattering centre is so significant (D^3 in the Rayleigh regime).

Table 7.6: A summary of the data used to evaluate the model using 10 MHz data. The other frequency values are clearly erroneous and so will be discarded for now.

Sample name	Prior austenite grain size (µm)	Packet size (µm)	Lath width (µm)	Measured attenuation 10MHz (Np/m)
M1	26.3 ± 0.5	14.9 ± 4.7	0.33 ± 0.004	10.9
M2	16.4 ± 0.2	11.9 ± 3.5	0.30 ± 0.003	17.5
M3	14.2 ± 0.3	12.2 ± 4.6	0.28 ± 0.004	10.3
M4	198.3 ± 3.7	78.1 ± 44.6	0.47 ± 0.004	28.8
M5	115.7 ± 5.4	22.6 ± 9.2	0.36 ± 0.005	22.3
M6	69.8 ± 1.4	40.0 ± 18.2	0.45 ± 0.004	21.2
M7	20.7 ± 0.2	22.9 ± 6.3	0.40 ± 0.003	15.3

Looking through the data of table 7.6 with the understanding outlined above, the measured attenuation values are broadly in line with expectations. It however remains unclear as to why sample M1 is associated with a significantly lower attenuation than would be expected from the measured microstructure. It is interesting to note that sample M1 is the only

sample which was not a re-heated sample from the mixed martensitic and bainitic samples. Table 7.7 shows the measured hardness values of all of the martensitic samples and a mixed martensite and bainite sample used as a control. The hardness value of sample M1 is significantly lower than the other tested samples. This would support the statement by Papadakis that a further term (potentially f^2) contributes to the attenuation of these samples. As the scattering contribution is expected to be low for the samples with small prior austenite grain size, it is plausible that this other contribution dominates total attenuation.

Table 7.7: Vickers HV 20 values of the martensitic samples and a mixed martensite and bainite sample as a control.

Sample name	Vickers HV 20 value
M1	299.7 ± 3.9
M2	483.1 ± 14.9
M3	374.7 ± 6.3
M4	441.4 ± 7.7
M5	359.8 ± 5.1
M6	449.2 ± 12.0
M7	460.6 ± 7.7
C3	370.4 ± 12.5

The data in table 7.7 also show good agreement between the hardness of the samples which underwent a further tempering heat-treatment and those which did not. Samples M2, M4, M6, M7 and C3 did not involve a tempering heat-treatment cycle and reflect higher hardness values (C3 is expected to be lower given the mixed microstructure). Therefore the tempering heat-treatment appears to have led to sufficient carbide coarsening to be detrimental to overall hardness, which is in agreement with previous work on this material (work under embargo). [Pesicka et al., 2003] show the tendency towards very high dislocation densities in martensitic ferritic steels (such as power generation steels). This very high dislocation density results from the formation of the martensitic microstructure, and subsequent tempering and creep results in reduced dislocation densities, although it is still

high in comparison to other microstructures. Therefore, the measurement of carbide coarsening as identified by hardness values seems to be an ideal proxy which avoids the involved dislocation density measurement.

8. Conclusions

8.1 Summary

This thesis set out with the intention of better understanding the attenuation involved in ultrasonic testing of power generation steels, with a particular emphasis on scattering. Initially the operating conditions of modern power generation facilities were discussed, which led to the requirements placed on power generation materials and their failure mechanisms. Alloying elements, inclusions, microstructure formation and how these influence the desired creep characteristics of power generation steels were all discussed. Subsequently, the material processing route, segregation characteristics and ultrasonic testing in an industrial context were all discussed. Important aspects of ultrasonic testing were outlined in chapter 3, which led onto a discussion of attenuation and scattering models as developed in the literature. The chapter concluded by outlining the aspects which could be further developed and this work attempts to address. Experimental methods and error calculations were contained in chapter 4.

Chapter 5 developed the modelling portion of this work. A calculation to predict the boundary reflectivity (termed the boundary reflection coefficient), which was based on acoustic theory calculations as discussed in the literature, was developed based on acoustic impedance calculations from the expected anisotropy within the grain. This was coupled with the long established orientation relationships, associated with these microstructural transformations (martensite). A further development was introduced to estimate the significance of a particular boundary related to the size of the feature (relative to wavelength). This was based on work in the literature which investigated the reflection associated with a thin air gap between two bounding layers of the same type. The parallel

would therefore be to approximate each microstructural feature individually between two layers of steel, which are described by the averaged bulk properties of steel. This aspect is an unrealistic assumption intended to simplify the modelling and provide an adequate comparison between boundaries. Furthermore, an extension was made to a literature model which predicts scattering associated with pearlitic microstructure. The argument was made that if that model is appropriate then a simple extension could account for the complex microstructure of martensite, as used in power generation components.

Chapter 6 presented the characterised microstructures of the generated samples. Here a combination of optical microscopy, scanning electron microscopy and electron back scatter diffraction were used. This led to the quantification of microstructure feature size, and an understanding of crystallographic orientation to be developed. An understanding of the frequency and distribution of boundary misorientation within the sample were established.

This was all brought together in the final results and discussion chapter (chapter 7). Here attempts were made to verify the literature model with attenuation of generated pearlitic samples. As there appeared to be large discrepancies between the predicted and measured attenuations, attempts were made to adjust the literature model. Ultimately, the model itself proved to be inappropriate for predicting scatter associated with pearlitic microstructures, this assertion was supported by other authors made in the literature. As a result of invalidating the pearlitic model, the model extension which aimed to predict martensitic scatter was also disproven. Therefore, lessons learned from previous chapters were used to clarify the significance of the individual boundary types associated with martensitic microstructure. A discrepancy between the quantified microstructure and measured attenuation was encountered for samples of small prior austenite grain size and

was clarified with hardness data. This trend, as identified by hardness values, appeared to validate a suggested contribution based on dislocation damping as made by Papadakis in previous work. The revised discussion appeared to be in agreement with other qualitative arguments in the literature, principally the work of Papadakis.

8.2 Contributions of this work

This work failed to establish a quantitative scattering model for martensitic microstructure as was the main objective of this work. There were however still valuable contributions made, even if these were not the originally intended outcomes. Firstly, the model for scattering in pearlitic microstructure, as established in the literature, was shown to be inappropriate experimentally (and with it the extension to martensitic microstructure). An argument was made as to why this is the case supported by an analysis of individual scattering contributions.

An analytical model was established which compares the reflectivity of features based on relative acoustic impedance differences and size. This is based on acoustic theory and provides a first principles approach rather than experimentally obtained fitting factors, as was the case in the literature. The experimental work proved to be in general agreement with qualitative discussion in the literature, and appeared to support a secondary attenuation contribution which appears to dominate during low scattering scenarios. The hardness tests appear to support the theory that this is the result of dislocation damping as it is influenced by the tempering heat-treatment procedures.

8.3 Improvements and future work

It is unfortunate that many elements of this thesis did not have the intended outcome. However, this section shall give a brief description of potential areas for improvement and how to develop the topic in the future.

An obvious area for improvement is the size selection of the testing samples. The use of bigger samples, which avoids the side wall reflection issue as encountered with the lower frequency transducers as part of this work. By using a variety of frequencies a greater understanding of the attenuation contributions can be gained, thereby fully validating the theories of Papadakis for example.

Taking this work to its full potential, a numerical model could be used to simulate a full component as used in the power generation industry. A ray tracing model could be a possible option for this but as it is still an approximation a finite element (FE) or finite difference (FD) model could be more appropriate. This would require the full quantification of boundary reflection for all orientation relationship variants across all incident wave angles, as could be encountered in the component. The refraction behaviour at each boundary would need to be incorporated, along with any associated mode conversion. This would likely require a huge amount of computing power, especially if the model of a full component is created; however the foundations for achieving this type of model have already been established, both here and elsewhere, as discussed in this thesis.

Appendix

Appendix A – ReadLeCroyBinaryWaveform.m

Conversion script to read a binary data file from a Lecroy Oscilloscope. Details of contributors listed in the first section of the code.

```
% ReadLeCroyBinaryWaveform -  read binary waveform file created by a LeCroy
Oscilloscope
%     waveform = LeCroyBinaryWaveform(FILENAME) loads the waveform file
into the workspace variable W.
%     FILENAME can either be a variable or a string constant enclosed by
quotes.
%
%     The return value "waveform" is a record containing four elements:
%     waveform.INFO   Waveform information, in readable formats. For
example Oscilloscope ID, sampling time and settings
%     waveform.DESC   Waveform information used for further calculations.
For example Sampling rate
%     waveform.Y      Values sampled by the oscilloscope
%     waveform.X      Array of time values corresponding to waveform.Y.
Time '0' marks the trigger event
%
%     The routine was tested with files generated by a WavePro7300 and
WaveRunner64Xi, Template LECROY_2_3
%
% See also LCPLOT LCPLOTEXT
%
%-------------------------------------------------------
% Original version (c)2001 Hochschule fï¿½r Technik+Architektur Luzern
% Fachstelle Elektronik
% 6048 Horw, Switzerland
% Slightly modified by Alan Blankman, LeCroy Corporation, 2006
% July 2007; added decoding of TrigTime_array so that sequence mode
waveforms decode correctly
% Slightly modified by Jean-Daniel Deschênes, Universite Laval, 2010
% Added support for sequence mode, even if RECORD_TYPE says "single_sweep"
% (seen on a WavePro 7 Zi).  Output will be a MxN matrix, where M is the
% number of points in each segment, and N is the number of segments.  X
% vector also update to include offset of each trigger.

function wave=ReadLeCroyBinaryWaveform(fn)
%%
%-------------------------------------------------------------------------
-------------
% Open File
%-------------------------------------------------------------------------
-------------
fid=fopen(fn,'r');
if fid==-1
   disp (sprintf('ERROR: file not found: %s', fn));
   return
end;

%-------------------------------------------------------------------------
-------------
% Seek offset in the header block
%-------------------------------------------------------------------------
-------------
```

```
data=fread(fid,50);
WAVEDESC=findstr('WAVEDESC', char(data(1:50)'))-1;
   % subtract 1 because:
   %        - 1st byte in the File = Index [0]
   %        - 1st byte in the Matlab-Array = Index[1]

%-------------------------------------------------------------------------
-------------
% Define the addresses of the various informations in the file
% These addresses are valid for the template LECROY_2_3 and are subject to
change in
% future revisions of the LeCroy firmware. Testing to this template version
% has been disabled to facilitate decoding of waveforms from scopes
% utilizing version 2_2 of the template.
%-------------------------------------------------------------------------
-------------
TESTED_TEMPLATE = 'LECROY_2_3';

%Addresses (WAVEDESC + address as stated in the LECROY template)
aTEMPLATE_NAME      = WAVEDESC+ 16;
aCOMM_TYPE          = WAVEDESC+ 32;
aCOMM_ORDER         = WAVEDESC+ 34;
aWAVE_DESCRIPTOR    = WAVEDESC+ 36; % length of the descriptor block
aUSER_TEXT          = WAVEDESC+ 40; % length of the usertext block
aTRIGTIME_ARRAY     = WAVEDESC+ 48;
aWAVE_ARRAY_1       = WAVEDESC+ 60; % length (in Byte) of the sample array
aINSTRUMENT_NAME    = WAVEDESC+ 76;
aINSTRUMENT_NUMBER  = WAVEDESC+ 92;
aTRACE_LABEL        = WAVEDESC+ 96;
aWAVE_ARRAY_COUNT   = WAVEDESC+ 116;
aSUBARRAY_COUNT     = WAVEDESC+ 144;
aVERTICAL_GAIN      = WAVEDESC+ 156;
aVERTICAL_OFFSET    = WAVEDESC+ 160;
aNOMINAL_BITS       = WAVEDESC+ 172;
aHORIZ_INTERVAL     = WAVEDESC+ 176;
aHORIZ_OFFSET       = WAVEDESC+ 180;
aVERTUNIT           = WAVEDESC+ 196;
aHORUNIT            = WAVEDESC+ 244;
aTRIGGER_TIME       = WAVEDESC+ 296;
aRECORD_TYPE        = WAVEDESC+ 316;
aPROCESSING_DONE    = WAVEDESC+ 318;
aTIMEBASE           = WAVEDESC+ 324;
aVERT_COUPLING      = WAVEDESC+ 326;
aPROBE_ATT          = WAVEDESC+ 328;
aFIXED_VERT_GAIN    = WAVEDESC+ 332;
aBANDWIDTH_LIMIT    = WAVEDESC+ 334;
aVERTICAL_VERNIER   = WAVEDESC+ 336;
aACQ_VERT_OFFSET    = WAVEDESC+ 340;
aWAVE_SOURCE        = WAVEDESC+ 344;



%-------------------------------------------------------------------------
-------------
% determine the number storage format HIFIRST / LOFIRST     (big endian /
little endian)
%-------------------------------------------------------------------------
-------------

fseek(fid,aCOMM_ORDER,'bof');
```

```
COMM_ORDER=fread(fid,1,'int16');

fclose(fid);
% reopen the data file using the correct HIFIRST/LOFIRST format
if COMM_ORDER==0
   fid=fopen(fn,'r','ieee-be');     % HIFIRST
else
   fid=fopen(fn,'r','ieee-le');     % LOFIRST
end;

%--------------------------------------------------------------------------
-------------
% Get the waveform information
%--------------------------------------------------------------------------
-------------
% Check the template revision  (Commented out to facilitate decoding of 2_2
% files
TEMPLATE_NAME       = ReadString(fid, aTEMPLATE_NAME);
if ~strcmp( deblank(TEMPLATE_NAME), TESTED_TEMPLATE)
  disp (sprintf ('WARNING!\n %s %s %s\n %s %s %s',...
            'This function has been written for the LeCroy-Template',...
            TESTED_TEMPLATE, '.',...
            'The current file contains information created with the
template',...
            TEMPLATE_NAME, '.'));
end

% Instrument
wave.info.INSTRUMENT_NAME   = ReadString(fid, aINSTRUMENT_NAME);
wave.info.INSTRUMENT_NUMBER = ReadLong  (fid, aINSTRUMENT_NUMBER);
wave.info.Filename          = fn;

% Channel
wave.info.TRIGGER_TIME      = ReadTimestamp(fid, aTRIGGER_TIME);

tmp=['channel 1';'channel 2';'channel 3';'channel 4';'unknown  '];
wave.info.WAVE_SOURCE           = tmp (1+ ReadWord(fid, aWAVE_SOURCE),:);

tmp=['DC_50_Ohms'; 'ground    ';'DC 1MOhm  ';'ground    ';'AC 1MOhm  '];
wave.info.VERT_COUPLING     = deblank (tmp (1+ ReadWord(fid,
aVERT_COUPLING),:));

tmp=['off'; 'on '];
wave.info.BANDWIDTH_LIMIT   = deblank (tmp (1+ ReadWord(fid,
aBANDWIDTH_LIMIT),:));

tmp=[
   'single_sweep      ';    'interleaved       '; 'histogram         ';
   'graph             ';    'filter_coefficient'; 'complex           ';
   'extrema           ';    'sequence_obsolete '; 'centered_RIS      ';
   'peak_detect       '];
wave.info.RECORD_TYPE       = deblank (tmp (1+ ReadWord(fid,
aRECORD_TYPE),:));

tmp=[
   'no_processing';   'fir_filter   '; 'interpolated ';   'sparsed      ';
   'autoscaled   ';   'no_result    '; 'rolling      ';   'cumulative   '];
wave.info.PROCESSING_DONE       = deblank (tmp (1+ ReadWord(fid,
aPROCESSING_DONE),:));
```

```
% Vertical settings
FIXED_VERT_GAIN         = ReadFixed_vert_gain(fid, aFIXED_VERT_GAIN);
PROBE_ATT               = ReadFloat (fid, aPROBE_ATT);
VERTICAL_GAIN           = ReadFloat (fid, aVERTICAL_GAIN);
VERTICAL_OFFSET         = ReadFloat (fid, aVERTICAL_OFFSET);
wave.info.NOMINAL_BITS  = ReadWord  (fid, aNOMINAL_BITS);
wave.info.Gain_with_Probe = strcat
(Float_to_Eng(FIXED_VERT_GAIN*PROBE_ATT), 'V/div');

% Horizontal settings
HORIZ_INTERVAL          = ReadFloat(fid, aHORIZ_INTERVAL);
HORIZ_OFFSET            = ReadDouble(fid, aHORIZ_OFFSET);
wave.info.TIMEBASE  = strcat (Float_to_Eng (ReadTimebase(fid,aTIMEBASE)),
's/div');
wave.info.SampleRate    = strcat (Float_to_Eng(1/HORIZ_INTERVAL) ,
'S/sec');
wave.desc.Ts            = HORIZ_INTERVAL;
wave.desc.fs            = 1/HORIZ_INTERVAL;

%-------------------------------------------------------------------------
-------------
% Read samples array (Plain binary ADC values)
%-------------------------------------------------------------------------
-------------
COMM_TYPE           = ReadWord(fid, aCOMM_TYPE);
WAVE_DESCRIPTOR     = ReadLong(fid, aWAVE_DESCRIPTOR);
USER_TEXT           = ReadLong(fid, aUSER_TEXT);
WAVE_ARRAY_1        = ReadLong(fid, aWAVE_ARRAY_1);
WAVE_ARRAY_COUNT    = ReadLong(fid, aWAVE_ARRAY_COUNT);
TRIGTIME_ARRAY      = ReadLong(fid, aTRIGTIME_ARRAY);

% returns number of segments in acquisition
wave.info.nbSegments      = ReadLong(fid, aSUBARRAY_COUNT);


if wave.info.nbSegments > 1
    % for sequence mode only

    %-------------------------------------------------------------------------
-----------------
    % Read contents of TRIGTIME_ARRAY, which is an interleaved array
    %-------------------------------------------------------------------------
-----------------

    % Take from X-Stream oscilloscopes remote control manual, appendix II:
    % <  0>          TRIGGER_TIME: double     ; for sequence acquisitions,
    %                                         ; time in seconds from first
    %                                         ; trigger to this one
    % <  8>          TRIGGER_OFFSET: double   ; the trigger offset is in
seconds
    %                                         ; from trigger to zeroth data
point
    fseek(fid, WAVEDESC + WAVE_DESCRIPTOR + USER_TEXT, 'bof');
    trigtime_array_temp = fread(fid, 2*wave.info.nbSegments, 'double');
    % We need to de-interleave the trigger_time and trigger_offset data.
    wave.trigger_time = trigtime_array_temp(1:2:end);
    wave.trigger_offset = trigtime_array_temp(2:2:end);
```

```
    if WAVE_ARRAY_1/wave.info.nbSegments ~=
WAVE_ARRAY_1/wave.info.nbSegments
        % if this condition happens, MATLAB will pad the rest of the output
        % matrix with zeros, so the file is still readable, but this could
        % signify another error (in this m-file?)
        warning('While reading segment file: Total number of points is not
a multiple of the number of segments');
    end

    %--------------------------------------------------------------------
----------------
    % Read the ADC values into a matrix
    %--------------------------------------------------------------------
----------------
    % since this is a sequence acquisition, we will return a
    % (WAVE_ARRAY_COUNT/nbSegments)x(nbSegments) matrix, where each column
is one segment.
    fseek(fid, WAVEDESC + WAVE_DESCRIPTOR + USER_TEXT + TRIGTIME_ARRAY,
'bof');
    if COMM_TYPE == 0  % byte
       wave.y = fread(fid, [WAVE_ARRAY_COUNT/wave.info.nbSegments
wave.info.nbSegments], 'int8');
    else    %   word
       wave.y = fread(fid, [WAVE_ARRAY_COUNT/wave.info.nbSegments
wave.info.nbSegments], 'int16');
    end;

    %--------------------------------------------------------------------
----------------
    % Create corresponding matrix of time, with correction for each trigger
time
    %--------------------------------------------------------------------
----------------
    wave.x = repmat(wave.trigger_time.',
WAVE_ARRAY_COUNT/wave.info.nbSegments, 1) +
repmat((0:WAVE_ARRAY_COUNT/wave.info.nbSegments-1)'*HORIZ_INTERVAL +
HORIZ_OFFSET, 1, wave.info.nbSegments);

else

    fseek(fid, WAVEDESC + WAVE_DESCRIPTOR + USER_TEXT + TRIGTIME_ARRAY,
'bof');
    if COMM_TYPE == 0  % byte
       wave.y=fread(fid,WAVE_ARRAY_1, 'int8');
    else    %   word
       wave.y=fread(fid,WAVE_ARRAY_1, 'int16');
    end;

    %--------------------------------------------------------------------
----------------
    % Create corresponding array of time
    %--------------------------------------------------------------------
----------------
    wave.x = (0:WAVE_ARRAY_COUNT-1)'*HORIZ_INTERVAL + HORIZ_OFFSET;

end

%--------------------------------------------------------------------------
-------------
```

```
% Transform the ADC values to voltages
%------------------------------------------------------------------------
------------
wave.y = VERTICAL_GAIN * wave.y - VERTICAL_OFFSET;

%------------------------------------------------------------------------
------------
% close the waveform file
%------------------------------------------------------------------------
------------
fclose(fid);

%========================================================================
============
% Support functions
%========================================================================
============

%------------------------------------------------------------------------
------------
% Read 8Bit signed Byte (not used)
%------------------------------------------------------------------------
------------
function b=ReadByte(fid, Addr)
    fseek(fid,Addr,'bof');
    b=fread(fid,1,'int8');

%------------------------------------------------------------------------
------------
% Read 16Bit signed Word
%------------------------------------------------------------------------
------------
function w=ReadWord(fid, Addr)
    fseek(fid,Addr,'bof');
    w=fread(fid,1,'int16');

%------------------------------------------------------------------------
------------
% Read 32Bit signed Long
%------------------------------------------------------------------------
------------
function l=ReadLong(fid, Addr)
    fseek(fid,Addr,'bof');
    l=fread(fid,1,'int32');

%------------------------------------------------------------------------
------------
% Read 32Bit IEEE Float
%------------------------------------------------------------------------
------------
function f=ReadFloat(fid, Addr)
    fseek(fid,Addr,'bof');
    f=fread(fid,1,'float32');

%------------------------------------------------------------------------
------------
% Read 64Bit IEEE Double
%------------------------------------------------------------------------
------------
function d=ReadDouble(fid, Addr)
```

```
    fseek(fid,Addr,'bof');
    d=fread(fid,1,'float64');

%-------------------------------------------------------------------------------
-------------
% Read string (up to 16 characters)
%-------------------------------------------------------------------------------
-------------
function s=ReadString(fid, Addr)
    fseek(fid,Addr,'bof');
    s=fgets(fid,16);

%-------------------------------------------------------------------------------
-------------
% Read timestamp
%-------------------------------------------------------------------------------
-------------
function t=ReadTimestamp(fid, Addr)
    fseek(fid,Addr,'bof');
    seconds = fread(fid,1,'float64');
   minutes  = fread(fid,1,'int8');
   hours        = fread(fid,1,'int8');
   days     = fread(fid,1,'int8');
   months   = fread(fid,1,'int8');
   year     = fread(fid,1,'int16');

   t=sprintf('%i.%i.%i, %i:%i:%2.0f', days, months, year, hours, minutes,
seconds);
%-------------------------------------------------------------------------------
-------------
% Timebase aus dem File lesen
%-------------------------------------------------------------------------------
-------------
function t=ReadTimebase(fid, Addr)
    fseek(fid,Addr,'bof');
    e=fread(fid,1,'int16');

   tmp=[1 2 5];
   mant = tmp( 1+ mod(e,3));
   ex  = floor (e / 3)-12;

   t=mant*10^ex;
%-------------------------------------------------------------------------------
-------------
% fixed Vertical Gain aus dem File lesen
%-------------------------------------------------------------------------------
-------------
function t=ReadFixed_vert_gain(fid, Addr)
    fseek(fid,Addr,'bof');
    e=fread(fid,1,'int16');

   tmp=[1 2 5];
   mant = tmp( 1+ mod(e,3));
   ex  = floor (e / 3)-6;

   t= mant*10^ex;
%-------------------------------------------------------------------------------
-------------
% Transform a Float to the Engineering-Format (returns a string)
```

```
%-------------------------------------------------------------------------
-------------
function s=Float_to_Eng (f)
   ex= floor(log10(f));
    exeng=ex-mod(ex,3);
   if exeng<-18; exeng=-18; end
   if exeng>18; exeng=18; end;
   mant=f/10^exeng;

   prefix=('afpnum kMGPE'); %prefixes (u=micro, m=milli, k=kilo, ...)
   s=sprintf('%g%s',mant, prefix( (exeng+18)/3 +1));
```

Appendix B – General_Masterscript.m

```
clear all
%Part 1 - User inputs section

%This section is designed with the intention of keeping all necessary
inputs
%in a simple to use format in the same section of the code. The subsequent
%sections will require no user inputs and will contain both the
calculations
%them selves as well as the outputs necessary to compare/interpret the
%data.

%%%%%%%%%%%%%%%%%%%%%%%%%%%%%%%%%%%%%%%%%%%%%%%%%%%%%%%%%%%%%%%%%%%%%%%
load('M1 5MHz 110 Width test 10.mat')
Fs=2000000000; %Scope sampling rate (in Hz)
F=05000000; %transducer frequency (in Hz)
h= 0.02669; %sample depth (front surface to back surface) (in m)
a= 0.006; %transducer diameter (in m)


N=10; %number of segments (needs to have an echo in each segment)


Cl=5700;
Ct=3200;
Cw=1500;

Rho_w=10; %FIND VALUE
Rho_s=10; %FIND VALUE
%%%%%%%%%%%%%%%%%%%%%%%%%%%%%%%%%%%%%%%%%%%%%%%%%%%%%%%%%%%%%%%%%%%%%%%

%Part 2 - Calculation section

%This section is designed to be a self-contained part of the program which
%is not required to be understood by the eventual user. All the
%calculations will be conducted in this section. Need to ensure all of the
%alterations necessary for different data sets can be made from simple
%choices in the first section, therefore it is necessary to automate any
%adjustments required.

CH1=ans.y;
T=1/Fs;
n=numel(CH1);
time = (0:n-1)*T;
```

```
multiplier=1/(2*h);
R=(Rho_s*Cl-Rho_w*Cw)/(Rho_s*Cl+Rho_w*Cw);

Figure(50)
subplot(2,1,1)
plot(time,CH1);
xlabel('\itTime Axis \rightarrow');
ylabel('\itAmplitude \rightarrow');
title('\itOriginal signal');
%CH1dc=deconv(CH1,freq1)



NFFT = 2^nextpow2(n);
Y = fft(CH1,NFFT)/n;
%Y1=abs(fft(CH1))
%Y=Y1(1:n/2);
f = Fs/2000000*linspace(0,1,NFFT/2+1);
%f=Fs*(0:n/2-1)/n
subplot(2,1,2)
plot(f,2*abs(Y(1:NFFT/2+1)))
%axis([xmin xmax ymin ymax])
xlabel('\itFrequency (MHz) \rightarrow');
ylabel('\it|CH1(f)| \rightarrow');
title('\itSingle-Sided Amplitude Sepectrum')
xlim([0 50])

%Beam spread calculation
lambda=Cl/F; %Wavelength calculated from transverse velocity and wave
frequency
n1=round(n/10);
n1=n1*10;
echo=n1/N; %number of datapoints for each individual pulse
k=n1/echo;
c=1;
AlphaStarTot=0;
while c<k-1
s=(2*c*h*lambda)/(a^2); %intermediate term to calculate the dispersion
correction term for the nth echo
snew=2*pi/s; %multiplied to fit into equation correctly

J0=besselj(snew,0);
J1=besselj(snew,1);
C=cos(snew);
S=sin(snew);
A=(C-J0)^2;
B=(S-J1)^2;
D_echo= sqrt(A+B); %dispersion correction for nth echo
pulse=CH1((c*n1/k)-((n1/k)/2):((c+1)*n1/k)-((n1/k)/2));
int_echo=max(pulse); %signal intensity for nth echo


%individual pulse
Figure(c)
subplot(2,1,1)
time_pulse=time((c*n1/k)-((n1/k)/2):((c+1)*n1/k)-((n1/k)/2));
plot(time_pulse,pulse);
xlabel('\itTime Axis \rightarrow');
ylabel('\itAmplitude \rightarrow');
%title('\itPulse 1 Original signal');
```

```
%ylim([-2 2])

num=numel(pulse);
NFFT1 = 2^nextpow2(num);
Y1 = fft(pulse,NFFT1)/num;
f1 = Fs/2000000*linspace(0,1,NFFT1/2+1);
subplot(2,1,2)
plot(f1,2*abs(Y1(1:NFFT1/2+1)))
xlim([0 50])
%ylim([0 0.6])
xlabel('\itFrequency (MHz) \rightarrow');
ylabel('\it|CH1(f)| \rightarrow');
title('\itSingle-Sided Amplitude Sepectrum')

c=c+1;

s=(2*c*h*lambda)/(a^2); %intermediate term to calculate the dispersion
correction term for the nth echo
snew=2*pi/s; %multiplied to fit into equation correctly

J0=besselj(snew,0);
J1=besselj(snew,1);
C=cos(snew);
S=sin(snew);
A=(C-J0)^2;
B=(S-J1)^2;
D_echo_2= sqrt(A+B); %dispersion correction for n+1th echo
pulse2=CH1((c*n1/k)-((n1/k)/2):((c+1)*n1/k)-((n1/k)/2));
int_echo_2=max(pulse2); %sigvnal intensity for n+1th echo
int_ratio=int_echo/int_echo_2; %The ratio between the nth and n+1th echo
int_ratio_cor=(int_echo*R^2)/int_echo_2;
D_ratio=D_echo_2/D_echo; %ratio between the nth and n+1th dispersion
correction term
ln_int_ratio=log(int_ratio);%natural logorithm of echo intensity ratio
ln_int_ratio_cor=log(int_ratio_cor);
log_int_ratio_cor=log10(int_ratio_cor);
log_int_ratio=log10(int_ratio);
ln_D_ratio=log(D_ratio);%natural logorithm of dispersion correction ratio
log_D_ratio=log10(D_ratio);

%BetaStar(:,c-1)=(int_ratio*D_ratio);
%AlphaStar(:,c-1)=(log(BetaStar(:,c-1)))*multiplier;

%All values in Nepers/m, multiply by 20 and replace ln with log for dB/m

AlphaStar(:,c-1)=(ln_int_ratio+ln_D_ratio)*multiplier;
AlphaPrime(:,c-1)=ln_int_ratio*multiplier;
Alpha(:,c-1)=(ln_int_ratio_cor+ln_D_ratio)*multiplier;

 if(AlphaStar(:,c-1)<10)
AlphaStarCor(:,c-1)=0
    else AlphaStarCor(:,c-1)=(AlphaStar(:,c-1))
    end
end



AlphaStarTot=sum(AlphaStarCor)
```

Appendix C – rotVecAroundArbAxis.m

Function used to calculated a rotation around an arbitrary axis. Source and contributors listed in the texts.

```
function rotatedUnitVector =
rotVecAroundArbAxis(unitVec2Rotate,rotationAxisUnitVec,theta)
%% Purpose:
%
%  This routine will allow a unit vector, unitVec2Rotate, to be rotated
%  around an axis defined by the RotationAxisUnitVec.  This is performed by
%  first rotating the unit vector around it's own cartesian axis (in this
%  case we will rotate the vector around the z-axis, [0 0 1]) corresponding
%  to each rotation angle specified by the user via the variable theta ...
%  this rotated vector is then transformed around the user defined axis of
%  rotation as defined by the rotationAxisUnitVec variable.
%
%
%% References:
%  Murray, G. Rotation About an Arbitrary Axis in 3 Dimensions. 06/06/2013.
%  http://inside.mines.edu/fs_home/gmurray/ArbitraryAxisRotation/
%
%% Inputs:
%  unitVec2Rotate               [N x 3]                Unit Vector in
%                                                      Cartesian
%                                                      Coordinates to
%                                                      rotate
%                                                      [x,y,z]
%
%
%  rotationAxisUnitVec          [N x 3]                Unit Vector with
%                                                      respect to the same
%                                                      cartesian
coordinates
%                                                      used for
unitVec2Rotate
%                                                      [x,y,z]
%
%  theta                        [N x 1]                Angle in degrees
%                                                      in which to rotate
%                                                      the unitVec2Rotate
%                                                      about the Z-axis
%                                                      before transforming
%                                                      it to the
%
RotateionAxisUnitVec
%                                                      This rotation is
%                                                      counter clockwise
%                                                      when theta is
%                                                      positive, clockwise
%                                                      when theta is
%                                                      negative.
%
%% Outputs:
%  rotatedUnitVector            [N x 3]                Resulting vector
%                                                      of rotating the
%                                                      unitVec2Rotate
%                                                      about the z-axis
```

```
%                                                       described by the
%                                                       angle theta, then
%                                                       transforming the
%                                                       rotated vectors
%                                                       with respect to the
%
rotateionAxisUnitVec
%
%% Revision History:
%  Darin C. Koblick                                 (c)  03-03-2015
%
%  Darin C. Koblick      Fixed order of rotations          07-30-2015
%% ---------------------- Begin Code Sequence -----------------------------
if nargin == 0
         unitVec2Rotate = [1 0 1]./norm([1 0 1]);
    rotationAxisUnitVec = [1 1 1]./norm([1 1 1]);
    theta = (0:5:360)';
    rotatedUnitVector =
rotVecAroundArbAxis(unitVec2Rotate,rotationAxisUnitVec,theta);
    %Show a graphical representation of the rotated vector:
    Figure('color',[1 1 1]);

quiver3(zeros(numel(theta),1),zeros(numel(theta),1),zeros(numel(theta),1),
...

rotatedUnitVector(:,1),rotatedUnitVector(:,2),rotatedUnitVector(:,3),'k','l
inewidth',2);
    hold on;
    quiver3(0,0,0,rotationAxisUnitVec(1), ...
                  rotationAxisUnitVec(2), ...
                  rotationAxisUnitVec(3), ...
                  'r','linewidth',5);
    axis equal;
    return;
end
%Check the dimensions of the input vectors to see if we need to repmat
%them:
if size(unitVec2Rotate,1) == 1
   unitVec2Rotate = repmat(unitVec2Rotate,[numel(theta) 1]);
end
if size(rotationAxisUnitVec,1) == 1
   rotationAxisUnitVec = repmat(rotationAxisUnitVec,[numel(theta) 1]);
end
%% Step One: take the unit vector rotation axis and rotate into z:
R2Z = vecRotMat(rotationAxisUnitVec,repmat([0 0
1],[size(rotationAxisUnitVec,1) 1]));
unitVectortoRotateAboutZ =Dim33Multiply(unitVec2Rotate,R2Z);
% Rotate the unit vector about the z-axis:
rotatedAboutZAxisUnitVec = bsxRz(unitVectortoRotateAboutZ,theta.*pi/180);
%% Step Two: Find the rotation Matrix to transform the z-axis to
rotationAxisUnitVec
R = vecRotMat(repmat([0 0 1],[size(rotationAxisUnitVec,1)
1]),rotationAxisUnitVec);
%% Step Three: Apply the Rotation matrix to the rotatedAboutZAxisUnitVec
vectors
rotatedUnitVector =Dim33Multiply(rotatedAboutZAxisUnitVec,R);
end

function a = Dim33Multiply(a,b)
%% Purpose:
% Given a, an [N x 3] matrix, use b, an [3 x 3 x N] rotation matrix to come
```

```
% up with a vectorized solution to b*a
%
%% Inputs:
%  a            [N x 3]                                          N x 3 vector
%
%  b            [3 x 3 x N]                                      3 x 3 x N
%                                                                matrix
%
%% Outputs:
%  a            [N x 3]                                          vectorized
%                                                                solution
%                                                                a = b*a
%
%% Revision History:
% Created by Darin C. Koblick   (C)                                        2013
%% ---------------------- Begin Code Sequence -----------------------------
a =cat(1,sum(permute(bsxfun(@times,b(1,:,:),permute(a,[3 2 1])),[2 3
1]),1), ...
         sum(permute(bsxfun(@times,b(2,:,:),permute(a,[3 2 1])),[2 3
1]),1), ...
         sum(permute(bsxfun(@times,b(3,:,:),permute(a,[3 2 1])),[2 3
1]),1))';
end

function R = vecRotMat(f,t)
%% Purpose:
%Commonly, it is desired to have a rotation matrix which will rotate one
%unit vector, f,  into another unit vector, t. It is desired to
%find R(f,t) such that R(f,t)*f = t.
%
%This program, vecRotMat is the most
%efficient way to accomplish this task. It uses no square roots or
%trigonometric functions as they are very computationally expensive.
%It is derived from the work performed by Moller and Hughes, which have
%suggested that this method is the faster than any previous transformation
%matrix methods tested.
%
%
%% Inputs:
%f                      [N x 3]                          N number of vectors
%                                                        in which to
%                                                        transform into
%                                                        vector t.
%
%t                      [N x 3]                          N number of vectors
%                                                        in which it is
%                                                        desired to rotate
%                                                        f.
%
%
%% Outputs:
%R                      [3 x 3 x N]                      N number of
%                                                        rotation matrices
%
%% Source:
% Moller,T. Hughes, F. "Efficiently Building a Matrix to Rotate One
% Vector to Another", 1999. http://www.acm.org/jgt/papers/MollerHughes99
%
%% Created By:
% Darin C. Koblick (C) 07/17/2012
% Darin C. Koblick     04/22/2014       Updated when lines are close to
```

```
%                                        parallel by checking
%% ---------------------- Begin Code Sequence -----------------------------
%It is assumed that both inputs are in vector format N x 3
dim3 = 2;
%Declare function handles for multi-dim operations
normMD = @(x,y) sqrt(sum(x.^2,y));
anyMD  = @(x) any(x(:));
% Inputs Need to be in Unit Vector Format
if anyMD(single(normMD(f,dim3)) ~= single(1)) ||
anyMD(single(normMD(t,dim3)) ~= single(1))
   error('Input Vectors Must Be Unit Vectors');
end
%Pre-Allocate the 3-D transformation matrix
R = NaN(3,3,size(f,1));

v = permute(cross(f,t,dim3),[3 2 1]);
c = permute(dot(f,t,dim3),[3 2 1]);
h = (1-c)./dot(v,v,dim3);

idx  = abs(c) > 1-1e-13;
%If f and t are not parallel, use the following computation
if any(~idx)
%For any vector u, the rotation matrix is found from:
R(:,:,~idx) = ...
    [c(:,:,~idx) +
h(:,:,~idx).*v(:,1,~idx).^2,h(:,:,~idx).*v(:,1,~idx).*v(:,2,~idx)-
v(:,3,~idx),h(:,:,~idx).*v(:,1,~idx).*v(:,3,~idx)+v(:,2,~idx); ...

h(:,:,~idx).*v(:,1,~idx).*v(:,2,~idx)+v(:,3,~idx),c(:,:,~idx)+h(:,:,~idx).*
v(:,2,~idx).^2,h(:,:,~idx).*v(:,2,~idx).*v(:,3,~idx)-v(:,1,~idx); ...
     h(:,:,~idx).*v(:,1,~idx).*v(:,3,~idx)-
v(:,2,~idx),h(:,:,~idx).*v(:,2,~idx).*v(:,3,~idx)+v(:,1,~idx),c(:,:,~idx)+h
(:,:,~idx).*v(:,3,~idx).^2];
end
%If f and t are close to parallel, use the following computation
if any(idx)
     f = permute(f,[3 2 1]);
     t = permute(t,[3 2 1]);
     p = zeros(size(f));
     iidx = abs(f(:,1,:)) <= abs(f(:,2,:)) & abs(f(:,1,:)) < abs(f(:,3,:));
     if any(iidx & idx)
        p(:,1,iidx & idx) = 1;
     end
     iidx = abs(f(:,2,:)) < abs(f(:,1,:)) & abs(f(:,2,:)) <= abs(f(:,3,:));
     if any(iidx & idx)
        p(:,2,iidx & idx) = 1;
     end
     iidx = abs(f(:,3,:)) <= abs(f(:,1,:)) & abs(f(:,3,:)) < abs(f(:,2,:));
     if any(iidx & idx)
        p(:,3,iidx & idx) = 1;
     end
     u = p(:,:,idx)-f(:,:,idx);
     v = p(:,:,idx)-t(:,:,idx);
     rt1 = -2./dot(u,u,dim3);
     rt2 = -2./dot(v,v,dim3);
     rt3 = 4.*dot(u,v,dim3)./(dot(u,u,dim3).*dot(v,v,dim3));
     R11 = 1 +
rt1.*u(:,1,:).*u(:,1,:)+rt2.*v(:,1,:).*v(:,1,:)+rt3.*v(:,1,:).*u(:,1,:);
     R12 =
rt1.*u(:,1,:).*u(:,2,:)+rt2.*v(:,1,:).*v(:,2,:)+rt3.*v(:,1,:).*u(:,2,:);
```

```
     R13 =
rt1.*u(:,1,:).*u(:,3,:)+rt2.*v(:,1,:).*v(:,3,:)+rt3.*v(:,1,:).*u(:,3,:);
     R21 =
rt1.*u(:,2,:).*u(:,1,:)+rt2.*v(:,2,:).*v(:,1,:)+rt3.*v(:,2,:).*u(:,1,:);
     R22 = 1 +
rt1.*u(:,2,:).*u(:,2,:)+rt2.*v(:,2,:).*v(:,2,:)+rt3.*v(:,2,:).*u(:,2,:);
     R23 =
rt1.*u(:,2,:).*u(:,3,:)+rt2.*v(:,2,:).*v(:,3,:)+rt3.*v(:,2,:).*u(:,3,:);
     R31 =
rt1.*u(:,3,:).*u(:,1,:)+rt2.*v(:,3,:).*v(:,1,:)+rt3.*v(:,3,:).*u(:,1,:);
     R32 =
rt1.*u(:,3,:).*u(:,2,:)+rt2.*v(:,3,:).*v(:,2,:)+rt3.*v(:,3,:).*u(:,2,:);
     R33 = 1 +
rt1.*u(:,3,:).*u(:,3,:)+rt2.*v(:,3,:).*v(:,3,:)+rt3.*v(:,3,:).*u(:,3,:);
     R(:,:,idx) = [R11 R12 R13; R21 R22 R23; R31 R32 R33];
end
end

function m = bsxRz(m,theta)
%% Purpose:
% Perform a rotation of theta radians about the z-axis on the vector(s)
% described by m.
%
%% Inputs:
% m         [N x 3]                                              vector matrix
%                                                                in which you
%                                                                would like to
%                                                                rotate with the
%                                                                x,y,z
%                                                                components
%                                                                specified along
%                                                                a specific
%                                                                dimension
%
% theta     [N x 1]                                              Rotation Angle
%                                                                about z-axis
%                                                                in radians
%
%% Outputs:
% m         [N x 3]
%
%% Revision History:
%  Darin C Koblick (C)                                 Initially Created 2013
%% ---------------------- Begin Code Sequence -----------
%Assemble the rotation matrix
Rz = zeros(3,3,size(m,1));
Rz(1,1,:) = cos(theta);  Rz(1,2,:) = -sin(theta);
Rz(2,1,:) = sin(theta);  Rz(2,2,:) =  cos(theta);
Rz(3,3,:) = 1;
%Dim33Multiply
m = Dim33Multiply(m,Rz);
end
```

Appendix D – Matrix_rotation_final.m

```
clear all

%Elastic constant used to calculate compliance tensor

C11=229.3; %100
C12=134.1; %110
C44=116.7; %111

S11=(C11+C12)/((C11^2)+(C11*C12)-2*(C12^2));
S12=(-C12)/((C11^2)+(C11*C12)-2*(C12^2));
S44=1/C44;

RotAxis=[-0.71 0.70 0.12]
Vec= [0 -0.17 0.99]
unitVec2Rotate=Vec/norm(Vec)
rotationAxisUnitVec=RotAxis/norm(RotAxis)



for theta=0:360
i=0
rotatedUnitVector =
rotVecAroundArbAxis(unitVec2Rotate,rotationAxisUnitVec,theta)

RotVec=rotatedUnitVector
% %Calculation of the rotation matrix with respect to theta {x y z}
%
% x=5;
% y=5;
% z=4;
%
% axis=[x;y;z];
%
% theta=10;  %in degrees
%
% c=cosd(theta);
% s=sind(theta);
% t=1-c;
%
% a1=(t*(x^2))+c;
% a2=(t*x*y)-(s*z);
% a3=(t*x*z)-(s*y);
%
% b1=(t*x*y)+(s*z);
% b2=(t*(y^2))+c;
% b3=(t*y*z)-(s*x);
%
% c1=(t*x*z)-(s*y);
% c2=(t*y*z)+(s*x);
% c3=(t*(z^2))+c;
%
% Mat=[a1,a2,a3;b1,b2,b3;c1,c2,c3]
% %normalized_Mat = Mat/norm(Mat)
%
% %<u v w> is the axis which is being rotated in the plane by matrix Mat
%
% u=-2;
```

```
% v=-2;
% w=5;
%
% vec=[u;v;w];
%
% RotVec=Mat*vec
%
% %[az,el,r]=cart2sph(RotVec(1),RotVec(2),RotVec(3))
%
% %XYPlaneNorm=[0;0;1]
% %Zplane
%
% %RotVecX=[RotVec(1);RotVec(2);0];
% %RotVecY=[RotVec(1);RotVec(2);0];
% %RotVecZ=[RotVec(1);RotVec(2);RotVec(3)];
%
% %normalized_V = RotVec/norm(RotVec)
% %normalized_V = RotVec/norm(RotVec,1)

xaxis=[1;0;0];
yaxis=[0;1;0];
zaxis=[0;0;1];

norm(RotVec)
norm(xaxis)
l=dot(RotVec,xaxis)/(norm(RotVec).*norm(xaxis))
%l=l(1)

m=dot(RotVec,yaxis)/(norm(RotVec).*norm(yaxis))
%m=m(2)

n=dot(RotVec,zaxis)/(norm(RotVec).*norm(zaxis))
%n=n(3)

%xRot=vrrotvec(RotVecX,xaxis)
%l=cos(xRot(4))

%yRot=vrrotvec(RotVecY,yaxis)
%m=cos(yRot(4))

%zRot=vrrotvec(RotVecZ,zaxis)
%n=cos(zRot(4))

%Effective Young's modulus in an arbitrary direction to the known elastic
%compliances simplifies to the following for cubic symmetry, full equation
%in notebook.

t1=(l^4)*S11;
t2=(m^4)*S11;
t3=(n^4)*S11;
t4=2*(l^2)*(m^2)*(S12+S44/2);
t5=2*(l^2)*(n^2)*(S12+S44/2);
t6=2*(m^2)*(n^2)*(S12+S44/2);

E=1/(t1+t2+t3+t4+t5+t6)



% ans=dot(axis,RotVec)
```

```
% Cro=cross(vec,RotVec)
% check=dot(axis,vec)

Values(theta+1)=E;
angle(theta+1)=theta;
end

plot(angle,Values)
xlabel('rotation angle (deg)');
ylabel('Effective elastic modulous value (GPa)');
title('{1 1 0}<0 0 1>')

V=(0.0001602*Values*1000000000);
Velocity = V.^(0.5);

Figure(2)
plot(angle,Velocity)
xlabel('rotation angle (deg)');
ylabel('Effective longitudinal velocity (m/s)');
title('{1 1 0}<0 0 1>')
```

Appendix E – Rotation_function_test.m

```
clear all%Similar script to Misorientation_calc_full.m but with the N-W
variants listed


%Misorientation_calc_full.m

%Elastic constant used to calculate compliance tensor

%Input Variants (axis)

Variant1Axis=[-0.71 0.70 0.12];
Variant2Axis=[-0.71 0.12 0.70];
Variant3Axis=[0 0.99 -0.17];
Variant4Axis=[-0.71 0.99 -0.17];
Variant5Axis=[-0.70 0.12 0.71];
Variant6Axis=[-0.17 0.99 0];
Variant7Axis=[-0.70 0.71 0.12];
Variant8Axis=[-0.12 0.71 0.70];
Variant9Axis=[-0.99 0.17 0];
Variant10Axis=[-0.12 0.70 0.71];
Variant11Axis=[-0.12 0.70 0.71];
Variant12Axis=[-0.99 0 0.17];

%Input Variants (vector)

Variant1Vector=[0 -0.17 0.99];
Variant2Vector=[0.71 -0.12 0.70];
Variant3Vector=[-0.71 0.12 0.70];
Variant4Vector=[0 0.169 0.99];
Variant5Vector=[0.70 -0.12 0.71];
Variant6Vector=[-0.70 -0.12 0.70];
Variant7Vector=[0.17 0 0.99];
Variant8Vector=[-0.12 -0.71 0.70];
```

```
Variant9Vector=[-0.12 -0.70 0.71];
Variant10Vector=[-0.17 0 0.99];
Variant11Vector=[0.12 -0.70 0.71];
Variant12Vector=[0.12 -0.71 0.70];

%Primary material constants

C11=229.3; %100
C12=134.1; %110
C44=116.7; %111

Axis1 = Variant1Axis; %The axis is normal to the plane in question
Vector1 = Variant1Vector; %the orientation direction on said plane

AngleOfRot=53.7;  %Set angle between primary and secondary media (used for
set
%orientation relations otherwise set to zero) [Note: in degrees]
AxisOfRot=[-0.68 0.22 0.70];%Misorientation axis


UnitAxisOfRot=AxisOfRot/norm(AxisOfRot);

Density1=7870;

%Secondary material constants

D11=229.3; %100
D12=134.1; %110
D44=116.7; %111

Axis2 = Variant12Axis;
Vector2 = Variant12Vector;

Density2=7870;

Const1= 0.0001602*Density1;
Const2= 0.0001602*Density2;

S11=(C11+C12)/((C11^2)+(C11*C12)-2*(C12^2));
S12=(-C12)/((C11^2)+(C11*C12)-2*(C12^2));
S44=1/C44;

T11=(D11+D12)/((D11^2)+(D11*D12)-2*(D12^2));
T12=(-D12)/((D11^2)+(D11*D12)-2*(D12^2));
T44=1/D44;

RotAxis=Axis1
Vec= Vector1
unitVec2Rotate=Vec/norm(Vec)
rotationAxisUnitVec=RotAxis/norm(RotAxis)



for theta=0:360
i=0
rotatedUnitVector =
rotVecAroundArbAxis(unitVec2Rotate,rotationAxisUnitVec,theta)
```

```
RotVec=rotatedUnitVector
% %Calculation of the rotation matrix with respect to theta {x y z}
%
% x=5;
% y=5;
% z=4;
%
% axis=[x;y;z];
%
% theta=10;  %in degrees
%
% c=cosd(theta);
% s=sind(theta);
% t=1-c;
%
% a1=(t*(x^2))+c;
% a2=(t*x*y)-(s*z);
% a3=(t*x*z)-(s*y);
%
% b1=(t*x*y)+(s*z);
% b2=(t*(y^2))+c;
% b3=(t*y*z)-(s*x);
%
% c1=(t*x*z)-(s*y);
% c2=(t*y*z)+(s*x);
% c3=(t*(z^2))+c;
%
% Mat=[a1,a2,a3;b1,b2,b3;c1,c2,c3]
% %normalized_Mat = Mat/norm(Mat)
%
% %<u v w> is the axis which is being rotated in the plane by matrix Mat
%
% u=-2;
% v=-2;
% w=5;
%
% vec=[u;v;w];
%
% RotVec=Mat*vec
%
% %[az,el,r]=cart2sph(RotVec(1),RotVec(2),RotVec(3))
%
% %XYPlaneNorm=[0;0;1]
% %Zplane
%
% %RotVecX=[RotVec(1);RotVec(2);0];
% %RotVecY=[RotVec(1);RotVec(2);0];
% %RotVecZ=[RotVec(1);RotVec(2);RotVec(3)];
%
% %normalized_V = RotVec/norm(RotVec)
% %normalized_V = RotVec/norm(RotVec,1)

xaxis=[1;0;0];
yaxis=[0;1;0];
zaxis=[0;0;1];

norm(RotVec)
norm(xaxis)
l=dot(RotVec,xaxis)/(norm(RotVec).*norm(xaxis))
%l=l(1)
```

```
m=dot(RotVec,yaxis)/(norm(RotVec).*norm(yaxis))
%m=m(2)

n=dot(RotVec,zaxis)/(norm(RotVec).*norm(zaxis))
%n=n(3)

%xRot=vrrotvec(RotVecX,xaxis)
%l=cos(xRot(4))

%yRot=vrrotvec(RotVecY,yaxis)
%m=cos(yRot(4))

%zRot=vrrotvec(RotVecZ,zaxis)
%n=cos(zRot(4))

%Effective Young's modulus in an arbitrary direction to the known elastic
%compliances simplifies to the following for cubic symmetry, full equation
%in notebook.

t1=(l^4)*S11;
t2=(m^4)*S11;
t3=(n^4)*S11;
t4=2*(l^2)*(m^2)*(S12+S44/2);
t5=2*(l^2)*(n^2)*(S12+S44/2);
t6=2*(m^2)*(n^2)*(S12+S44/2);

E=1/(t1+t2+t3+t4+t5+t6)



% ans=dot(axis,RotVec)
% Cro=cross(vec,RotVec)
% check=dot(axis,vec)

Values(theta+1)=E;
angle(theta+1)=theta;
end

% plot(angle,Values)
% xlabel('rotation angle (deg)');
% ylabel('Effective elastic modulous value (GPa)');
% title('{1 1 0}<0 0 1>')

V1=(Const1/Density1*Values*1000000000);
Velocity1 = V1.^(0.5);
Z1=Velocity1*Density1;


%%%%%%%Second part of code! Repeated script for the secondary material
%%%%%%%constants

Vec= Vector2;
unitVec2Rotate=Vec/norm(Vec);

rotatedUnitVector =
rotVecAroundArbAxis(unitVec2Rotate,UnitAxisOfRot,AngleOfRot);
```

```
RotAxis=Axis2;
Vec= rotatedUnitVector;
unitVec2Rotate=Vec/norm(Vec);
rotationAxisUnitVec=RotAxis/norm(RotAxis);



for theta=0:360
i=0
rotatedUnitVector =
rotVecAroundArbAxis(unitVec2Rotate,rotationAxisUnitVec,theta)

RotVec=rotatedUnitVector
% %Calculation of the rotation matrix with respect to theta {x y z}
%
% x=5;
% y=5;
% z=4;
%
% axis=[x;y;z];
%
% theta=10;  %in degrees
%
% c=cosd(theta);
% s=sind(theta);
% t=1-c;
%
% a1=(t*(x^2))+c;
% a2=(t*x*y)-(s*z);
% a3=(t*x*z)-(s*y);
%
% b1=(t*x*y)+(s*z);
% b2=(t*(y^2))+c;
% b3=(t*y*z)-(s*x);
%
% c1=(t*x*z)-(s*y);
% c2=(t*y*z)+(s*x);
% c3=(t*(z^2))+c;
%
% Mat=[a1,a2,a3;b1,b2,b3;c1,c2,c3]
% %normalized_Mat = Mat/norm(Mat)
%
% %<u v w> is the axis which is being rotated in the plane by matrix Mat
%
% u=-2;
% v=-2;
% w=5;
%
% vec=[u;v;w];
%
% RotVec=Mat*vec
%
% %[az,el,r]=cart2sph(RotVec(1),RotVec(2),RotVec(3))
%
% %XYPlaneNorm=[0;0;1]
% %Zplane
%
% %RotVecX=[RotVec(1);RotVec(2);0];
```

```
% %RotVecY=[RotVec(1);RotVec(2);0];
% %RotVecZ=[RotVec(1);RotVec(2);RotVec(3)];
%
% %normalized_V = RotVec/norm(RotVec)
% %normalized_V = RotVec/norm(RotVec,1)

xaxis=[1;0;0];
yaxis=[0;1;0];
zaxis=[0;0;1];

norm(RotVec)
norm(xaxis)
l=dot(RotVec,xaxis)/(norm(RotVec).*norm(xaxis))
%l=l(1)

m=dot(RotVec,yaxis)/(norm(RotVec).*norm(yaxis))
%m=m(2)

n=dot(RotVec,zaxis)/(norm(RotVec).*norm(zaxis))
%n=n(3)

%xRot=vrrotvec(RotVecX,xaxis)
%l=cos(xRot(4))

%yRot=vrrotvec(RotVecY,yaxis)
%m=cos(yRot(4))

%zRot=vrrotvec(RotVecZ,zaxis)
%n=cos(zRot(4))

%Effective Young's modulus in an arbitrary direction to the known elastic
%compliances simplifies to the following for cubic symmetry, full equation
%in notebook.

p1=(l^4)*T11;
p2=(m^4)*T11;
p3=(n^4)*T11;
p4=2*(l^2)*(m^2)*(T12+T44/2);
p5=2*(l^2)*(n^2)*(T12+T44/2);
p6=2*(m^2)*(n^2)*(T12+T44/2);

E=1/(p1+p2+p3+p4+p5+p6)



% ans=dot(axis,RotVec)
% Cro=cross(vec,RotVec)
% check=dot(axis,vec)

Values(theta+1)=E;
angle(theta+1)=theta;
end

% plot(angle,Values)
% xlabel('rotation angle (deg)');
% ylabel('Effective elastic modulous value (GPa)');
% title('{1 1 0}<0 0 1>')
```

```
V2=(Const2/Density2*Values*1000000000);
Velocity2 = V2.^(0.5);
Z2=Velocity2*Density2;

for theta=0:360
    theta=theta+1;
Reflection(theta)= ((Z2(theta)-Z1(theta)).^2)./((Z2(theta)+Z1(theta)).^2);
end

plot(angle,Reflection)
xlabel('rotation angle (deg)');
ylabel('Boundary reflection coefficient');
title('Variation across all angles between V1 and V12 of the N-W OR')

Misorientation = mean(abs(Reflection)) %modulus and mean of all reflection
terms, therefore giving the average of all potential rotations
```

Appendix E (2) – KS_rotation_function_test.m

```
clear all

%This code is the same as Rotation_function_test.m but with variants
%changed for K-S OR instead of N-W OR

%Misorientation_calc_full.m

%Elastic constant used to calculate compliance tensor

%Input Variants (axis)

Variant1Axis=[-0.075 -0.167 0.983];
Variant2Axis=[-0.650 0.167 0.742];
Variant3Axis=[-0.742 0.167 0.650];
Variant4Axis=[0.075 -0.167 0.983];
Variant5Axis=[0.667 0.075 0.742];
Variant6Axis=[-0.667 0.075 0.742];
Variant7Axis=[0.167 -0.650 0.742];
Variant8Axis=[-0.167 -0.075 0.983];
Variant9Axis=[0.075 -0.667 0.742];
Variant10Axis=[0.075 -0.742 0.667];
Variant11Axis=[-0.167 0.075 0.983];
Variant12Axis=[-0.742 -0.167 0.650];
Variant13Axis=[0.167 -0.075 0.983];
Variant14Axis=[-0.167 -0.650 0.742];
Variant15Axis=[-0.167 -0.742 0.650];
Variant16Axis=[0.167 0.075 0.983];
Variant17Axis=[-0.075 -0.742 0.667];
Variant18Axis=[-0.075 -0.667 0.742];
Variant19Axis=[-0.742 -0.075 0.667];
Variant20Axis=[-0.667 -0.075 0.742];
Variant21Axis=[-0.075 0.167 0.983];
Variant22Axis=[-0.650 -0.167 0.742];
Variant23Axis=[0.650 -0.167 0.742];
Variant24Axis=[0.075 0.167 0.983];

%Input Variants (vector)
```

```
Variant1Vector=[0.742 0.650 0.167];
Variant2Vector=[0.167 0.983 -0.074];
Variant3Vector=[0.667 0.075 0.742];
Variant4Vector=[0.667 0.742 0.075];
Variant5Vector=[0.075 0.983 -0.167];
Variant6Vector=[0.742 0.167 0.650];
Variant7Vector=[0.983 0.167 -0.075];
Variant8Vector=[0.650 0.742 0.167];
Variant9Vector=[0.167 0.742 0.650];
Variant10Vector=[0.983 0.167 0.075];
Variant11Vector=[0.742 0.667 0.075];
Variant12Vector=[0.667 -0.075 0.742];
Variant13Vector=[0.742 0.667 -0.075];
Variant14Vector=[0.075 0.742 0.667];
Variant15Vector=[0.983 -0.075 0.167];
Variant16Vector=[0.650 0.742 -0.167];
Variant17Vector=[0.167 0.650 0.742];
Variant18Vector=[0.983 0.075 0.167];
Variant19Vector=[0.650 0.167 0.742];
Variant20Vector=[0.075 0.983 0.167];
Variant21Vector=[0.667 0.742 -0.075];
Variant22Vector=[0.742 0.075 0.667];
Variant23Vector=[0.167 0.983 0.075];
Variant24Vector=[0.742 0.650 -0.167];

%Primary material constants

C11=229.3; %100
C12=134.1; %110
C44=116.7; %111

Axis1 = Variant1Axis; %The axis is normal to the plane in question
Vector1 = Variant1Vector; %the orientation direction on said plane

AngleOfRot=57.21;  %Set angle between primary and secondary media (used for
set
%orientation relations otherwise set to zero) [Note: in degrees]
AxisOfRot=[-0.246 -0.628 -0.738];%Misorientation axis


UnitAxisOfRot=AxisOfRot/norm(AxisOfRot);

Density1=7870;

%Secondary material constants

D11=229.3; %100
D12=134.1; %110
D44=116.7; %111

Axis2 = Variant23Axis;
Vector2 = Variant23Vector;

Density2=7870;

Const1= 0.0001602*Density1;
Const2= 0.0001602*Density2;
```

```
S11=(C11+C12)/((C11^2)+(C11*C12)-2*(C12^2));
S12=(-C12)/((C11^2)+(C11*C12)-2*(C12^2));
S44=1/C44;

T11=(D11+D12)/((D11^2)+(D11*D12)-2*(D12^2));
T12=(-D12)/((D11^2)+(D11*D12)-2*(D12^2));
T44=1/D44;

RotAxis=Axis1
Vec= Vector1
unitVec2Rotate=Vec/norm(Vec)
rotationAxisUnitVec=RotAxis/norm(RotAxis)



for theta=0:360
i=0
rotatedUnitVector =
rotVecAroundArbAxis(unitVec2Rotate,rotationAxisUnitVec,theta)

RotVec=rotatedUnitVector
% %Calculation of the rotation matrix with respect to theta {x y z}
%
% x=5;
% y=5;
% z=4;
%
% axis=[x;y;z];
%
% theta=10;  %in degrees
%
% c=cosd(theta);
% s=sind(theta);
% t=1-c;
%
% a1=(t*(x^2))+c;
% a2=(t*x*y)-(s*z);
% a3=(t*x*z)-(s*y);
%
% b1=(t*x*y)+(s*z);
% b2=(t*(y^2))+c;
% b3=(t*y*z)-(s*x);
%
% c1=(t*x*z)-(s*y);
% c2=(t*y*z)+(s*x);
% c3=(t*(z^2))+c;
%
% Mat=[a1,a2,a3;b1,b2,b3;c1,c2,c3]
% %normalized_Mat = Mat/norm(Mat)
%
% %<u v w> is the axis which is being rotated in the plane by matrix Mat
%
% u=-2;
% v=-2;
% w=5;
%
% vec=[u;v;w];
%
% RotVec=Mat*vec
```

```
%
% %[az,el,r]=cart2sph(RotVec(1),RotVec(2),RotVec(3))
%
% %XYPlaneNorm=[0;0;1]
% %Zplane
%
% %RotVecX=[RotVec(1);RotVec(2);0];
% %RotVecY=[RotVec(1);RotVec(2);0];
% %RotVecZ=[RotVec(1);RotVec(2);RotVec(3)];
%
% %normalized_V = RotVec/norm(RotVec)
% %normalized_V = RotVec/norm(RotVec,1)

xaxis=[1;0;0];
yaxis=[0;1;0];
zaxis=[0;0;1];

norm(RotVec)
norm(xaxis)
l=dot(RotVec,xaxis)/(norm(RotVec).*norm(xaxis))
%l=l(1)

m=dot(RotVec,yaxis)/(norm(RotVec).*norm(yaxis))
%m=m(2)

n=dot(RotVec,zaxis)/(norm(RotVec).*norm(zaxis))
%n=n(3)

%xRot=vrrotvec(RotVecX,xaxis)
%l=cos(xRot(4))

%yRot=vrrotvec(RotVecY,yaxis)
%m=cos(yRot(4))

%zRot=vrrotvec(RotVecZ,zaxis)
%n=cos(zRot(4))

%Effective Young's modulus in an arbitrary direction to the known elastic
%compliances simplifies to the following for cubic symmetry, full equation
%in notebook.

t1=(l^4)*S11;
t2=(m^4)*S11;
t3=(n^4)*S11;
t4=2*(l^2)*(m^2)*(S12+S44/2);
t5=2*(l^2)*(n^2)*(S12+S44/2);
t6=2*(m^2)*(n^2)*(S12+S44/2);

E=1/(t1+t2+t3+t4+t5+t6)



% ans=dot(axis,RotVec)
% Cro=cross(vec,RotVec)
% check=dot(axis,vec)

Values(theta+1)=E;
angle(theta+1)=theta;
```

```
end

% plot(angle,Values)
% xlabel('rotation angle (deg)');
% ylabel('Effective elastic modulous value (GPa)');
% title('{1 1 0}<0 0 1>')

V1=(Const1/Density1*Values*1000000000);
Velocity1 = V1.^(0.5);
Z1=Velocity1*Density1;


%%%%%%%Second part of code! Repeated script for the secondary material
%%%%%%%constants

Vec= Vector2;
unitVec2Rotate=Vec/norm(Vec);

rotatedUnitVector =
rotVecAroundArbAxis(unitVec2Rotate,UnitAxisOfRot,AngleOfRot);


RotAxis=Axis2;
Vec= rotatedUnitVector;
unitVec2Rotate=Vec/norm(Vec);
rotationAxisUnitVec=RotAxis/norm(RotAxis);



for theta=0:360
i=0
rotatedUnitVector =
rotVecAroundArbAxis(unitVec2Rotate,rotationAxisUnitVec,theta)

RotVec=rotatedUnitVector
% %Calculation of the rotation matrix with respect to theta {x y z}
%
% x=5;
% y=5;
% z=4;
%
% axis=[x;y;z];
%
% theta=10;  %in degrees
%
% c=cosd(theta);
% s=sind(theta);
% t=1-c;
%
% a1=(t*(x^2))+c;
% a2=(t*x*y)-(s*z);
% a3=(t*x*z)-(s*y);
%
% b1=(t*x*y)+(s*z);
% b2=(t*(y^2))+c;
% b3=(t*y*z)-(s*x);
%
% c1=(t*x*z)-(s*y);
% c2=(t*y*z)+(s*x);
```

```
% c3=(t*(z^2))+c;
%
% Mat=[a1,a2,a3;b1,b2,b3;c1,c2,c3]
% %normalized_Mat = Mat/norm(Mat)
%
% %<u v w> is the axis which is being rotated in the plane by matrix Mat
%
% u=-2;
% v=-2;
% w=5;
%
% vec=[u;v;w];
%
% RotVec=Mat*vec
%
% %[az,el,r]=cart2sph(RotVec(1),RotVec(2),RotVec(3))
%
% %XYPlaneNorm=[0;0;1]
% %Zplane
%
% %RotVecX=[RotVec(1);RotVec(2);0];
% %RotVecY=[RotVec(1);RotVec(2);0];
% %RotVecZ=[RotVec(1);RotVec(2);RotVec(3)];
%
% %normalized_V = RotVec/norm(RotVec)
% %normalized_V = RotVec/norm(RotVec,1)

xaxis=[1;0;0];
yaxis=[0;1;0];
zaxis=[0;0;1];

norm(RotVec)
norm(xaxis)
l=dot(RotVec,xaxis)/(norm(RotVec).*norm(xaxis))
%l=l(1)

m=dot(RotVec,yaxis)/(norm(RotVec).*norm(yaxis))
%m=m(2)

n=dot(RotVec,zaxis)/(norm(RotVec).*norm(zaxis))
%n=n(3)

%xRot=vrrotvec(RotVecX,xaxis)
%l=cos(xRot(4))

%yRot=vrrotvec(RotVecY,yaxis)
%m=cos(yRot(4))

%zRot=vrrotvec(RotVecZ,zaxis)
%n=cos(zRot(4))

%Effective Young's modulus in an arbitrary direction to the known elastic
%compliances simplifies to the following for cubic symmetry, full equation
%in notebook.

p1=(l^4)*T11;
p2=(m^4)*T11;
p3=(n^4)*T11;
p4=2*(l^2)*(m^2)*(T12+T44/2);
```

```
p5=2*(l^2)*(n^2)*(T12+T44/2);
p6=2*(m^2)*(n^2)*(T12+T44/2);

E=1/(p1+p2+p3+p4+p5+p6)



% ans=dot(axis,RotVec)
% Cro=cross(vec,RotVec)
% check=dot(axis,vec)

Values(theta+1)=E;
angle(theta+1)=theta;
end

% plot(angle,Values)
% xlabel('rotation angle (deg)');
% ylabel('Effective elastic modulous value (GPa)');
% title('{1 1 0}<0 0 1>')

V2=(Const2/Density2*Values*1000000000);
Velocity2 = V2.^(0.5);
Z2=Velocity2*Density2;

for theta=0:360
    theta=theta+1;
Reflection(theta)= ((Z2(theta)-Z1(theta)).^2)./((Z2(theta)+Z1(theta)).^2);
r(theta)=abs(Z2(theta)/Z1(theta));
end

plot(angle,Reflection)
xlabel('rotation angle (deg)');
ylabel('Boundary reflection coefficient');
title('Variation across all angles between V1 and V8 of the K-S OR')

Misorientation = mean(abs(Reflection)) %modulus and mean of all reflection
terms
r_ratio=mean(r) %Average impedance ratio across all angles
V=mean(Velocity2) %Average velocity across all angles
```

Appendix F – Carbide_calc.m

```
clear all%Size significance script. Currently calculating V1-V23 of K-S OR
(in m)

r=1.0569; %impedance ratio of main medium relative to secondary

f=1000000; %in Hz
V=5510; %in m/s
dMax=0.001350000;%in m
dMin=0.00000001;%in m
Inc=0.00000001;%in m
i=1;
```

```
k=(2*pi*f/V);%wavenumber of the secondary (gap) medium

for d=dMin:Inc:dMax



%kd=k*d;
%check=sin(k*d)

Rflec_ratio=(0.25*((r-(1/r))^2)*(sin(k*d))^2)/(1+0.25*((r-
(1/r))^2)*(sin(k*d))^2);

Values(i)=Rflec_ratio*100;
Size(i)=d;%*(f/1000);
i=i+1;
end

Max_Values=max(Values);
Scaled_Values=Values/Max_Values;
plot(Size,Scaled_Values)
xlabel('d*f (m*MHz)');
ylabel('Ratio of maximum reflection');
title('Proportion of maximum boundary reflection against frequency and
size')
```

Appendix G – Martensite LL

```
> restart;
```

$M1 := 4.2;$

$$M1 := 4.2$$

$M2 := 2.3;$

$$M2 := 2.3$$

$M3 := 80;$

$$M3 := 80$$

$L := 0.0002002$

$$L := 0.0002002$$

$l := 0.0000816$

$$l := 0.0000816$$

$d := 0.000001280$

$$d := 1.280\,10^{-6}$$

$v := -138200000000$

$$v := -138200000000$$

$p := 7850$

$$p := 7850$$

$f := 10000000$

$$f := 10000000$$

$$A := \frac{2\cdot\pi\cdot f}{5973}$$

$$A := \frac{20000000\,\pi}{5973}$$

$$Grain := \frac{M1\cdot L^3}{\left(1+2\cdot A^2\cdot L^2\cdot(1-x)\right)^2}\cdot\left(\frac{v^2}{p^2}\right)\cdot\left(\frac{9}{525}+\frac{6}{525}\cdot x^2+\frac{1}{525}\cdot x^4\right)$$

$$Grain := \frac{10445.23661\left(\frac{3}{175}+\frac{2}{175}x^2+\frac{1}{525}x^4\right)}{(9.870188504-8.870188504\,x)^2}$$

$$a := int(Grain, x)$$

$$a := 0.08428921817\,x^3+0.2813752397\,x^2+2.456495996\,x+4.770080181\ln(-1.233773563\,10^9+1.108773563\,10^9\,x)-\frac{5.036116434\,10^9}{-1.233773563\,10^9+1.108773563\,10^9\,x}$$

$$P1 := subs(x=1,a)-subs(x=-1,a);$$

$$P1 := 43.22065552+4.770080181\ln(-1.25000000\,10^8)-4.770080181\ln(-2.342547126\,10^9)$$

$$Packet := \frac{M2\cdot l^3}{\left(1+2\cdot A^2\cdot l^2\cdot(1-x)\right)^2}\cdot\left(\frac{v^2}{p^2}\right)\cdot\left(\frac{9}{525}+\frac{6}{525}\cdot x^2+\frac{1}{525}\cdot x^4\right)$$

$$Packet := \frac{387.3246035\left(\frac{3}{175}+\frac{2}{175}x^2+\frac{1}{525}x^4\right)}{(2.473618349-1.473618349\,x)^2}$$

$$P2 := subs(x=1,int(Packet,x))-subs(x=-1,int(Packet,x));$$

$$P2 := 22.69897404+13.27104174\ln(-1.000000000\,10^9)-13.27104174\ln(-3.947236698\,10^9)$$

$$Lath := \frac{M3\cdot d\cdot l^2}{\left(1+A^2\cdot\left(l^2+d^2\right)\cdot(1-x)\right)^2}\cdot\left(\frac{v^2}{p^2}\right)\cdot\left(\frac{9}{525}+\frac{6}{525}\cdot x^2+\frac{1}{525}\cdot x^4\right)$$

$$Lath := \frac{211.3280018\left(\frac{3}{175}+\frac{2}{175}x^2+\frac{1}{525}x^4\right)}{(1.736990473-0.7369904730\,x)^2}$$

$$P3 := subs(x=1,int(Lath,x))-subs(x=-1,int(Lath,x));$$

$$P3 := 57.90239356+59.76971190\ln(-1.000000000\,10^9)-59.76971190\ln(-2.473980946\,10^9)$$

$$eval\left(\frac{(P1+P2+P3)\cdot A^4}{2\cdot(5973)^4},\pi\right.$$
$$= 3.14159265358979323846264338327950288419716939937510582097494459230781640628620899862803482534211706798214\left.8\right)$$

$$180.2804853+0.\,I$$

Appendix H – Martensite LT

```
> restart;
M1 := 4.2;
```

$$M1 := 4.2$$

```
M2 := 2.3;
```

$$M2 := 2.3$$

```
M3 := 80;
```

$$M3 := 80$$

```
L := 0.0002002
```

$$L := 0.0002002$$

```
l := 0.0000817
```

$$l := 0.0000817$$

```
d := 0.000001280
```

$$d := 1.280\,10^{-6}$$

```
B := 2·π·f/3250
```

$$B := \frac{\pi f}{1625}$$

```
v := -138200000000
```

$$v := -138200000000$$

```
p := 7850
```

$$p := 7850$$

```
f := 10000000
```

$$f := 10000000$$

```
A := 2·π·f/5973
```

$$A := \frac{20000000\,\pi}{5973}$$

```
Grain := M1·L^3/(1+B^2·L^2+A^2·L^2-2·A·B·L^2·x)^2·(v^2/p^2)·(9/525+6/525·x^2+1/525·x^4)
```

$$Grain := \frac{10445.23661\left(\frac{3}{175}+\frac{2}{175}x^2+\frac{1}{525}x^4\right)}{(-16.30204182\,x+20.41541668)^2}$$

```
int(Grain, x)
```

$$0.02495477844\,x^3+0.09375430494\,x^2+0.8014179388\,x-\frac{1.273498717\,10^9}{8.15102091\,10^8\,x-1.020770834\,10^9}+1.713195700\ln\left(8.15102091\,10^8\,x-1.020770834\,10^9\right)$$

```
P1 := subs(x = 1, int(Grain, x)) - subs(x = -1, int(Grain, x));
```

$$P1 := 7.151060268 + 1.713195700\ln(-2.05668743\,10^{8}) - 1.713195700\ln(-1.835872925\,10^{9})$$

$$Packet := \frac{M2\cdot l^3}{\left(1 + B^2\cdot l^2 + A^2\cdot l^2 - 2\cdot A\cdot B\cdot l^2\cdot x\right)^2}\cdot\left(\frac{v^2}{p^2}\right)\cdot\left(\frac{9}{525} + \frac{6}{525}\cdot x^2 + \frac{1}{525}\cdot x^4\right)$$

$$Packet := \frac{388.7503368\left(\frac{3}{175} + \frac{2}{175}x^2 + \frac{1}{525}x^4\right)}{(-2.714925832\,x + 4.233424186)^2}$$

$P2 := subs(x = 1, int(Packet, x)) - subs(x = -1, int(Packet, x));$

$$P2 := 6.878847414 + 3.403346401\ln(-7.59249177\,10^{8}) - 3.403346401\ln(-3.474175009\,10^{9})$$

$$Lath := \frac{M3\cdot d\cdot l^2}{\left(1 + \left(B^2 + A^2 - 2\cdot A\cdot B\cdot x\right)\cdot\frac{\left(l^2 + d^2\right)}{2}\right)^2}\cdot\left(\frac{v^2}{p^2}\right)\cdot\left(\frac{9}{525} + \frac{6}{525}\cdot x^2 + \frac{1}{525}\cdot x^4\right)$$

$$Lath := \frac{211.8462800\left(\frac{3}{175} + \frac{2}{175}x^2 + \frac{1}{525}x^4\right)}{\left(2.617108927 - 0.1375735095\,\pi^2\,x\right)^2}$$

$P3 := subs(x = 1, int(Lath, x)) - subs(x = -1, int(Lath, x));$

$$P3 := 14.92135247 + 11.33168055\ln(-2.518625624\,10^{9}) - 11.33168055\ln(-7.949810084\,10^{9})$$

$$eval\left(\frac{(P1 + P2 + P3)\cdot A^4}{2\cdot(5973)^4}, \pi\right)$$

$= 3.14159265358979323846264338327950288419716939937510582097494459230781640628620899862803482534211706798214$8)

$$33.67170119 + 0.\,I$$

Appendix I – Pearlite LT

```
> restart;
M := 14;
```

$$M := 14$$

```
L := 0.0001105
```

$$L := 0.0001105$$

```
d := 0.000000281
```

$$d := 2.81\,10^{-7}$$

```
v := -138200000000
```

$$v := -138200000000$$

$$-138200000000$$

```
p := 7850
```

$$p := 7850$$

$f := 10000000$

$$f := 10000000$$

$A := \frac{2 \cdot \pi \cdot f}{5973}$

$$A := \frac{20000000\,\pi}{5973}$$

$Grain := \frac{0 \cdot L^3}{\left(1 + 2 \cdot A^2 \cdot L^2 \cdot (1 - x)\right)^2} \cdot \left(\frac{v^2}{p^2}\right) \cdot \left(\frac{9}{525} + \frac{6}{525} \cdot x^2 + \frac{1}{525} \cdot x^4\right)$

$$Grain := 0.$$

$int(Grain, x)$

$$0.$$

$h := int(Grain, x)$

$$h := 0.$$

$subs(x = 1, h);$

$$0.$$

$subs(x = -1, h);$

$$0.$$

$P1 := subs(x = 1, h) - subs(x = -1, h);$

$$P1 := 0.$$

$Lam := \frac{M \cdot L^2 \cdot d}{\left(1 + A^2 \cdot \left(L^2 + d^2\right) \cdot (1 - x)\right)^2} \cdot \left(\frac{v^2}{p^2}\right) \cdot \left(\frac{9}{525} + \frac{6}{525} \cdot x^2 + \frac{1}{525} \cdot x^4\right)$

$$Lam := \frac{14.88797683\left(\frac{3}{175} + \frac{2}{175}x^2 + \frac{1}{525}x^4\right)}{(2.351145353 - 1.351145353\,x)^2}$$

$int(Lam, x);$

$$0.005177868090\,x^3 + 0.02703022396\,x^2 + 0.2343085435\,x + 0.6517519637 \ln\left(-2.351145353\,10^9 + 1.351145353\,10^9\,x\right) - \frac{7.626402716\,10^8}{-2.351145353\,10^9 + 1.351145353\,10^9\,x}$$

$g := int(Lam, x);$

$$g := 0.005177868090\,x^3 + 0.02703022396\,x^2 + 0.2343085435\,x + 0.6517519637 \ln\left(-2.351145353\,10^9 + 1.351145353\,10^9\,x\right) - \frac{7.626402716\,10^8}{-2.351145353\,10^9 + 1.351145353\,10^9\,x}$$

$subs(x = 1, g);$

$$1.029156907 + 0.6517519637 \ln\left(-1.000000000\,10^9\right)$$

$subs(x = -1, g);$

$$-0.0064647266 + 0.6517519637 \ln\left(-3.702290706\,10^9\right)$$

$P2 := subs(x = 1, g) - subs(x = -1, g);$

$$P2 := 1.035621634 + 0.6517519637 \ln\left(-1.000000000\,10^9\right) - 0.6517519637 \ln\left(-3.702290706\,10^9\right)$$

$P1 + P2$

$$0.18250977 + 0.\,I$$

$$eval\left(\frac{(P1+P2)\cdot A^4}{2\cdot(5973)^4},\pi = 3.14159265358979323846264338327950288419716939937510582097494459230781640628620899862803482534211706798214\right)$$

$$0.8778806525 + 0.\,\mathrm{I}$$

Appendix J – Pearlite LT

```
> restart;
```

$M := 14;$

$$M := 14$$

$L := 0.0001105$

$$L := 0.0001105$$

$d := 0.000000281$

$$d := 2.81\,10^{-7}$$

$v := -138200000000$

$$v := -138200000000$$

$p := 7850$

$$p := 7850$$

$f := 10000000$

$$f := 10000000$$

$B := \frac{2\cdot\pi\cdot f}{3250}$

$$B := \frac{80000\,\pi}{13}$$

$A := \frac{2\cdot\pi\cdot f}{5973}$

$$A := \frac{20000000\,\pi}{5973}$$

$$GrainLT := \frac{0.09\cdot L^3}{\left(1+B^2\cdot L^2+A^2\cdot L^2-2\cdot A\cdot B\cdot L^2\cdot x\right)^2}\cdot\left(\frac{v^2}{p^2}\right)\cdot\left(\frac{15}{525}+\frac{6}{525}\cdot x^2-\frac{1}{525}\cdot x^4\right)$$

$$GrainLT := \frac{37.63623019\left(\frac{1}{35}+\frac{2}{175}x^2-\frac{1}{525}x^4\right)}{(-4.966362462\,x+6.914841691)^2}$$

$int(GrainLT, x)$

$$-0.0009688325750\,x^3-0.004046819337\,x^2+0.0005353982942\,x + 0.01718121593\ln\left(4.966362462\,10^9\,x-6.914841691\,10^9\right) - \frac{3.301715102\,10^8}{4.966362462\,10^9\,x-6.914841691\,10^9}$$

$h := int(GrainLT, x)$

$$h := -0.0009688325750\,x^3 - 0.004046819337\,x^2 + 0.0005353982942\,x + 0.01718121593\ln\left(4.966362462\,10^9\,x - 6.914841691\,10^9\right) - \frac{3.301715102\,10^8}{4.966362462\,10^9\,x - 6.914841691\,10^9}$$

$subs(x = 1, h);$

$$0.1649706213 + 0.01718121593\ln\left(-1.948479229\,10^9\right)$$

$subs(x = -1, h);$

$$0.02417601289 + 0.01718121593\ln\left(-1.188120415\,10^{10}\right)$$

$P1 := subs(x = 1, h) - subs(x = -1, h);$

$$P1 := 0.1407946084 + 0.01718121593\ln\left(-1.948479229\,10^9\right) - 0.01718121593\ln\left(-1.188120415\,10^{10}\right)$$

$$DupLT := \frac{M\cdot L^2\cdot d}{\left(1 + \left(B^2 + A^2 - 2\cdot A\cdot B\cdot x\right)\cdot\frac{\left(L^2 + d^2\right)}{2}\right)^2}\cdot\left(\frac{v^2}{p^2}\right)\cdot\left(\frac{15}{525} + \frac{6}{525}\cdot x^2 - \frac{1}{525}\cdot x^4\right)$$

$$DupLT := \frac{14.88797683\left(\frac{1}{35} + \frac{2}{175}\,x^2 - \frac{1}{525}\,x^4\right)}{\left(3.957439971 - 0.2516004886\,\pi^2\,x\right)^2}$$

$int(DupLT, x);$

$$-0.001532966538\,x^3 - 0.007447998778\,x - 0.007329207884\,x^2 + 0.01349045684\ln\left(1.241598645\,10^{10}\,x - 1.978719986\,10^{10}\right) - \frac{1.358306224\,10^9}{1.241598645\,10^{10}\,x - 1.978719986\,10^{10}}$$

$g := int(DupLT, x);$

$$g := -0.001532966538\,x^3 - 0.007447998778\,x - 0.007329207884\,x^2 + 0.01349045684\ln\left(1.241598645\,10^{10}\,x - 1.978719986\,10^{10}\right) - \frac{1.358306224\,10^9}{1.241598645\,10^{10}\,x - 1.978719986\,10^{10}}$$

$subs(x = 1, g);$

$$0.1679615536 + 0.01349045684\ln\left(-7.37121341\,10^9\right)$$

$subs(x = -1, g);$

$$0.04383100674 + 0.01349045684\ln\left(-3.220318631\,10^{10}\right)$$

$P2 := subs(x = 1, g) - subs(x = -1, g);$

$$P2 := 0.1241305469 + 0.01349045684\ln\left(-7.37121341\,10^9\right) - 0.01349045684\ln\left(-3.220318631\,10^{10}\right)$$

$P1 + P2$

$$0.2139716390 + 0.\,I$$

$$eval\left(\frac{(P1+P2)\cdot B^4}{2\cdot(5973)^3\cdot 3250},\pi = 3.14159265358979323846264338327950288419716939937510582097494459230781640628620899862803482534211706798214808651328230664709384460955058223172535940812848111745028410270193852110555964462294895493038196\right)$$

$$21.57999512 + 0.\mathrm{I}$$

Appendix K – mtex_working_script.m

Requires the mtex toolbox and loaded EBSD data. This script is mostly adapted from examples on the mtex website (link in references).

```
%plot(ebsd)% visualize the whole data set

% segmentation angle typically 10 to 15 degrees that seperates to grains
seg_angle = 10;

% minimum indexed points per grain between 5 and 10
min_points = 10;

% restrict to indexed only points
[grains,ebsd.grainId,ebsd.mis2mean] =
calcGrains(ebsd('indexed'),'angle',seg_angle*degree);

% remove small grains with less than min_points indexed points
grains = grains(grains.grainSize > min_points);

% re-calculate grain model to cleanup grain boundaries with less than
% minimum index points used ebsd points within grains having the minium
% indexed number of points (e.g. 10 points)
ebsd = ebsd(grains);
[grains,ebsd.grainId,ebsd.mis2mean] =
calcGrains(ebsd('indexed'),'angle',seg_angle*degree);

% smooth grains
grains = smooth(grains,4);

plot(grains('indexed'),grains('indexed').meanOrientation,'micronbar','off',
'figSize','large')
hold on
plot(grains.boundary)
hold off

 %oM = ipfColorKey(ori_variable_name) [Note not currently working need to
 %change ori_variable_name]
 % plot(oM)

 % define the linewidth
lw = 1; %reduced from 6 otherwise the image is dominated by boundaries

% consider on Fo-Fo boundaries
gB = grains.boundary('indexed','indexed');

% The following command reorders the boundary segments such that they are
```

```
% connected. This has two advantages:
% 1. the plots become more smooth
% 2. you can consider every third line segment as we do in the next
paragraph
gB = gB.reorder;

% visualize the misorientation angle
% draw the boundary in black very thick
hold on
plot(gB,'linewidth',lw+2);

% and on top of it the boundary colorized according to the misorientation
% angle
hold on
plot(gB,gB.misorientation.angle./degree,'linewidth',lw);
hold off
mtexColorMap jet
mtexColorbar('title','misorientation angle in degrees')

mAngle = gB.misorientation.angle./ degree;
title('Frequency of misorientation angle occurance')
hist(mAngle)

[~,id] = histc(mAngle,0:30:120);
```

References

[Abe, 2004]Abe F. (2004). "Bainitic and martensitic creep-resistant steels." Current Opinion in Solid State and Materials Science **8**.

[Abe, 2008]Abe F. (2008). "Precipitate design for creep strengthening of 9% Cr tempered martensitic steel for ultra-supercritical power plants." SCIENCE AND TECHNOLOGY OF ADVANCED MATERIALS **9**.

[Abe, 2014a]Abe F. (2014a). Development of creep-resistant steels and alloys for use in power plants. Structural Alloys for Power Plants, Woodhead Publishing Series in Energy.

[Abe, 2014b]Abe F. (2014b). Grade 91 heat- resistant martensitic steel Coal Power Plant Materials and Life Assessment Developments and Applications. https://doi.org/10.1533/9780857097323.1.3, Elsevier Ltd.

[Abe, 2017]Abe F. (2017). "New martensitic steels." Materials for Ultra-Supercritical and Advanced Ultra-Supercritical Power Plants. **Chapter 10**.

[Ahmed and Thompson, 1995] Ahmed S., Thompson R.B. (1995). Influence of Columnar Microstructure on Ultrasonic Backscattering. Review of Progress in Quantitative Nondestructive Evaluation. https://doi.org/10.1007/978-1-4615-1987-4_207, Springer, Boston, MA.

[Ahmed and Thompson, 1996]Ahmed S., Thompson R. B. (1996). "Propagation of elastic waves in equiaxed stainless-steel polycrystals with aligned [001] axes." The Journal of the Acoustical Society of America **99**.

[Arakawa et al., 1985]Arakawa T., Hirose S., Senda T. (1985). "The detection of weld cracks using ultrasonic testing." NDT INTERNATIONAL **18**(1).

[Aranda et al., 2013]Aranda M. M., Kim B., Rementeria R., Capdevila C., García de Andrés C. (2013). "Effect of prior austenite grain size on pearlite transformation in a hypo-euctectoid Fe-C-Mn steel." Metallurgical and Materials Transactions A **45A**(4).

[backdiffusion, Sentesoftware]. "Modelling Dendritic Solidification with Back Diffusion." 2019, from https://www.sentesoftware.co.uk/site-media/backdiffusion.

[Bai et al., 2018]Bai X., Tie B., Schmitt J.-H., Aubry D. (2018). "Finite element modeling of grain size effects on the ultrasonic microstructural noise backscattering in polycrystalline materials." Ultrasonics **87**.

[Beckermann, 2001]Beckermann C. (2001). Macrosegregation. Encyclopedia of Materials: Science and Technology (Second Edition). https://doi.org/10.1016/B0-08-043152-6/00824-X, Elsevier Ltd**:** Pages 4733-4738.

[Betteridge and Shaw, 1987]Betteridge W., Shaw S. W. K. (1987). "Development of superalloys." Materials Science and Technology **3**(9).

[Bhadeshia and Christian, 1990]Bhadeshia H. K. D. H., Christian J. W. (1990). "Bainite in steels." Metallurgical transactions A **21A**.

[Bhadeshia and Honeycomb, 2006] Bhadeshia H.K.D.H., Honeycomb R. (2006). Steels: Microstructure and Properties Butterworth-Heinemann

[Bhadeshia, 2001a]Bhadeshia H. K. D. H (2001a). "Design of Creep-resistant Steels." ISIJ (The Iron and Steel Institute of Japan) **41**(6).

[Bhadeshia, 2001b]Bhadeshia H. K. D. H (2001b). Worked examples in the Geometry of Crystals, The Institute of Metals.

[Bhadeshia, 2002]Bhadeshia H. K. D. H (2002). "Martensite and Martensitic Phase Transformations." from https://www.phase-trans.msm.cam.ac.uk/2002/martensite.html.

[Bhadeshia, 2008]Bhadeshia H. K. D. H (2008). "Interpretation of the Microstructure of Steels." from https://www.phase-trans.msm.cam.ac.uk/2008/Steel_Microstructure/SM.html.

[Bhadeshia, 2015]Bhadeshia H. K. D. H (2015). Bainite in Steels Theory and practice http://www.phase-trans.msm.cam.ac.uk/bainite.html, Maney Publishing

[Bhatia, 1959]BHATIA A. B. (1959). "Scattering of High-Frequency Sound Waves in Polycrystalline Materials " The Journal of the Acoustical Society of America **31**.

[Blaes et al., 2003]Blaes N., Schönfeld K.H., Bokelmann D. (2003). High temperature steel forgings for power generation machinery. 15th International Forgemasters Meeting. Kobe, Japan**:** 219-226.

[Blaes et al., 2011]Blaes N., Donth B., Diwo A., Bokelmann D. (2011). Advanced forgings for highly efficient fossil power plants. Advances in materials technology for fossil power plants proceedings from the sixth international conference

[Blugel, 2012]Blugel S. (2012). Scattering Theory: Born Series. Lecture Notes of the 43rd IFF Spring School "Scattering Methods for Condensed Matter Research: Towards Novel Applications at Future Sources", Forschungszentrum Julich.

[Bogdan, 2018]Bogdan O. (2018). "Optimization of ingot geometry, casting technology and chemical composition of a 20 tons 42CrMo4 ingot to minimize A-segregation and increase material homogeneity.".

[Bontempo and Manna, 2019]Bontempo R., Manna M. (2019). "Work and efficiency optimization of advanced gas turbine cycles." Energy Conversion and Management **195**.

[Brebbia and Dominguez, 1992]Brebbia C. A., Dominguez J. (1992). Boundary Elements An Introductory Course. Boston, Southampton WIT Press/Computational Mechanics Publications.

[Breeze, 2016]Breeze P. (2016). Gas Turbines. Gas-Turbine Power Generation. http://dx.doi.org/10.1016/B978-0-12-804005-8.00004-5, Elsevier Ltd.

[Breeze, 2019]Breeze P. (2019). Natural Gas-Fired Gas Turbine and Combined Cycle Power Plants. Power Generation Technologies. https://doi.org/10.1016/B978-0-08-102631-1.00004-3, Elsevier Ltd.

[Bunge, 1982]Bunge H.J. (1982). Texture Analysis in Materials Science Butterworth & Co (publishers).

[Charlesworth and Temple, 2001]Charlesworth J. P.,Temple J. A. G. (2001). Engineering Applications of Ultrasonic Time-of-Flight DiffractionResearch Studies Press LTD.

[Cipolla, 2010]Cipolla L (2010). Conversion of MX Nitrides to Modified Z-Phase in 9-12%Cr Ferritic Steels. PhD Thesis, Technical University of Denmark.

[Clark and Chaskelis, 1981]Clark A.V., Chaskelis H.H. (1981). "Measurement of ultrasound reflected from ultra-thin defects." Ultrasonics **19**.

[Clark and Chaskelis, 1982]Clark A.V., Chaskelis H.H. (1982). "The effect of surface cleanness of thin defects on the reflection of ultrasound." Ultrasonics **20**.

[Connolly, 2009]Connolly G. D. (2009). MODELLING OF THE PROPAGATION OF ULTRASOUND THROUGH AUSTENITIC STEEL WELDS. Doctor of Philosophy, Imperial College London.

[Cowen et al., 2012]Cowen C. J., Hawk J. A., Holcomb G. R., Jablonski P. D. (2012). Materials Development for USC & Advanced USC Combustion. 25th Annual Fossil Energy Materials Conference 27 April 2012.

[Dahmen, 1982]Dahmen U. (1982). "ORIENTATION RELATIONSHIPS IN PRECIPITATION SYSTEMS " Acta Metall. **30**.

[Dally, 2017]Dally R. (2017). Modelling and simulation of the microstructure of ESR ingots for power generation forgings, University of Birmingham.

[Danielsen, 2015] Danielsen, H. K. (2016). "Review of Z phase precipitation in 9–12 wt-%Cr steels." Materials Science and Technology **32**(2).

[Davis et al., 2008] Davis C. L., Mukhopadhyay P., Strangwood M.,Potter M., Dixon S., Morris P. F. (2008). "Comparison between elastic modulus and ultrasonic velocity anisotropy with respect to rolling direction in steels." Ironmaking and Steelmaking **35**.

[DeLuca, 2001]DeLuca D.P. (2001). "Understanding Fatigue." ASME International Gas Turbine Institute.

[Di Gianfrancesco et al., 2008]Di Gianfrancesco A., Cipolla L., Venditti D., Neri S., Calderini M. (2008). Creep behaviour and microstructural analysis of FB2 trial rotor steel. Advances in materials technology for fossil power plants proceedings from the fifth international conference 366-376.

[Donth et al., 2011]Donth B., Blaes N., Bokelmann D. (2011). Manufacturing of advanced Rotor Forgings for Highly Efficient Fossil Power Plants. 8th International Charles Parsons Turbine Conference.
Portsmouth, UK, 2011 Saarschmiede GmbH Freiformschmiede.

[Du and Turner, 2014]Du H., Turner J. A. (2014). "Ultrasonic attenuation in pearlitic steel." Ultrasonics **54**: 6.

[Du et al., 2013]Du H., Lonsdale C., Oliver J., Wilson B. M., Turner J. A. (2013). "Evaluation of Railroad Wheel Steel with Lamellar Duplex Microstructures Using Diffuse Ultrasonic Backscatter." J Nondestruct Eval **32**.

[Dudko et al., 2012]Dudko V, Belyakov A., Kaibyshev R. (2012). "Effect of Tempering on Mechanical Properties and Microstructure of a 9% Cr Heat Resistant Steel." Materials Science Forum Vols **706-709**.

[Dugmore et al., 2002]Dugmore K., Jonson D., Walker M. (2002). "A comparison of signal consistency of common ultrasonic couplants used in the inspection of composite structures." Composite Structures **58**.

[Dupont-Marillia et al., 2017]Dupont-Marillia F., Jahazi M., Lafreniere S., Belanger P. (2017). "Influence of local mechanical properties of high strength steel from large size forged ingot on ultrasonic wave velocities." 43rd Annual Review of Progress in Quantitative Nondestructive Evaluation **36**.

[El-Ali, 2011]El-Ali S. (2011). "Ultrasonic Wave Propagation Review." first accessed 2014, from http://96.64.46.169/ti/news/technical/Ultrasonic-Wave-Propagation-Review.

[Ennis and Cyzrska-Filemonowicz, 2002]Ennis P. J., Czyrska-Filemonowicz A. (2002). "Recent Advances in Creep Resistant Steels for Power Plant Applications." Operation Maintenance and Materials Issue **1**(1).

[Ennis and Czyrska-Filemonowicz, 2003]Ennis P. J., Czyrska-Filemonowicz A. (2003). "Recent advances in creep-resistant steels for power plant applications." Sadhana **28**.

[Fadok, 2010]FADOK J. (2010). Advanced gas turbine materials, design and technology. Advanced Power Plant Materials, Design and Technology.
https://doi.org/10.1533/9781845699468.1.3, Woodhead Publishing Series in Energy.

[Flemings and Nerco, 1967]Flemings M. C., Nereo G. E. (1967). "MACROSEGREGATION. PT. 1." Trans. TMS-AIME **239**.

[Flemings and Nerco, 1968a]Flemings M. C., Nereo G. E. (1968a). Trans. TMS-AIME **242**.

[Flemings and Nerco, 1968b]Flemings M. C., Nereo G. E. (1968b). Trans. TMS-AIME **242**.

[Flemings, 1974]Flemings M. C. (1974). Solidification Processing. McGraw-Hill, New York.

[Flemings, 2000]FLEMINGS M. C. (2000). "Our Understanding of Macrosegregation: Past and Present." ISIJ International **40**(9).

[Fooladi and Kundu, 2019]Fooladi S., Kundu T. (2019). "Distributed point source modeling of the scattering of elastic waves by a circular cavity in an anisotropic half-space." Ultrasonics **94**.

[Fujii et al., 1979]Fujii T., Poirier D. R., Flemings M. C. (1979). Metall., Trans. **10B**.

[Fusfeld, 1950]FUSFELD H. I. (1950). "Apparatus for Rapid Measurement of Internal Friction " Review of Scientific Instruments **21**.

[Ganesh et al., 2011]Ganesh B. J., Raju S., Rai A. K., Mohandas E., Vijayalakshmi M., Rao K. B. S., Raj B. (2011). "Differential scanning calorimetry study of diffusional and martensitic phase transformations in some 9 wt-%Cr low carbon ferritic steels." Materials Science and Technology **27**(2).

[Garcin, 2016]Garcin T. (2016). In-situ Laser Ultrasonic grain size measurement in superalloy Inconel 718. LUM 2016 Workshop. The University of British Columbia, Canada

[Ge et al., 2018a]Ge H., Ren F., Li J., Hu Q., Xia M., Li J. (2018a). "Modelling of ingot size effects on macrosegregation in steel castings." Journal of Materials Processing Technology **252**.

[Ge et al., 2018b]Ge H., Ren F., Cai D., Hao J., Li J., Li J. (2018b). "Gradual-cooling solidification approach to alleviate macrosegregation in large steel ingots." Journal of Materials Processing Technology **262**.

[Gemant, 1943]GEMANT A. (1943). "Frictional Phenomena. XIII." Journal of Applied Physics **14**.

[Ghosh, 2001]GHOSH A. (2001). "Segregation in cast products." Sadhana **26**.

[Goni and Rousseau, 2014]Goñi M. A., Rousseau C.-E. (2014). "On the validity and improvement of the ultrasonic pulse-echo immersion technique to measure real attenuation." Ultrasonics **54**.

[Guo, 2003]Guo Y. (2003). "Effects of material microstructure and surface geometry on ultrasonic scattering and flaw detection." Digital Repository @ Iowa State University **PhD Thesis**.

[Gusarova et al., 2015]Gusarova T., Schulze S., Runge A., Reifferscheid M. (2015). Ultrasonic testing for the internal quality evaluation of cast steel products. METEC & 2nd ESTAD. Düsseldorf.

[Gustafson, 1978]Gustafson S. C. (1978). Ultrasonic Interactions With Thin Air Layers in Solids. First international symposium on ultrasonic materials characterization. Gaithersburg, Md.

[Hald and Korcakova, 2003]Hald J., Korcakova L. (2003). "Precipitate stability in creep resistant ferritic steels – experimental investigations and modelling." ISIJ (The Iron and Steel Institute of Japan) **43**(3).

[Hald, 2008]Hald J. (2008). "Microstructure and long-term creep properties of 9–12% Cr steels." International Journal of Pressure Vessels and Piping **85**.

[He and Zheng, 2001]He P., Zheng J. (2001). "Acoustic dispersion and attenuation measurement using both transmitted and reflected pulses." Ultrasonics **39**.

[He, 1999]He P. (1999). "Direct measurement of ultrasonic dispersion using a broadband transmission technique." Ultrasonics **37**.

[Hirsekorn, 1982]Hirsekorn S. (1982). "The scattering of ultrasonic waves by polycrystals." The Journal of the Acoustical Society of America **72**.

[Hirsekorn, 1985]Hirsekorn S. (1985). "The scattering of ultrasonic waves in polycrystalline materials with texture." The Journal of the Acoustical Society of America **77**.

[Hirsekorn,1986]Hirsekorn S. (1986). "Directional dependence of ultrasonic propagation in textured polycrystals." The Journal of the Acoustical Society of America **79**.

[Hu, 2012]Hu Z.-F. (2012). Heat-Resistant Steels, Microstructure Evolution and Life Assessment in Power Plants Thermal Power Plants 195-226.

[Huang et al., 2005]Huang X., Yin H. (2005). A Data-Driven Approach to Extract Shear And Compressional Slowness From Dispersive Waveform Data. 2005 SEG Annual Meeting.

[Huang et al., 2019]Huang Y., Turner J. A., Song Y., Ni P., Li X. (2019). "Enhanced ultrasonic detection of near-surface flaws using transverse-wave backscatter." Ultrasonics **98**.

[Huygens' principle, Mathpages.com]. "Huygens' Principle." 2019, from https://www.mathpages.com/home/kmath242/kmath242.htm.

[Inoue et al., 1970]Inoue T., Matsuda S., Okamura Y., Aoki K. (1970). "The fracture of a low carbon tempered martensite." Trans. JIM **11**.

[Joseph et al., 2016]Joseph J., Sathyanarayanan S., Vigney K.,Prasad B. V. S. S. S., Biswas D.,

Jimbo T. (2016). "Thermodynamic wetness loss calculation in a steam turbine rotor tip section: nucleating steam flow." Journal of Physics: Conference Series **745**.

[Kalinowski, 2017]Kalinowski P. (2017). RECRYSTALLISATION AND GRAIN SIZE DEVELOPMENT DURING FORGING IN POWER GENERATION STEELS, University of Birmingham.

[Kang et al., 2005]Kang S.-T., Kim D.-S. , Kim K.-C., Kim M.-S., Ryu S.-H., Kim J.-T. (2005). "MANUFACTURING AND MECHANICAL & METALLURGICAL PROPERTIES OF 9 ~ 12%CR ROTOR FORGINGS STEEL FOR ADVANCED STEAM TURBINE " Doosan Heavy Industries Co., Ltd., Korea.

[Karal and Keller, 1964]Karal F. C., Jr, Keller J . B. (1964). "Elastic, Electromagnetic, and Other Waves in a Random medium." J. Math. Phys. **5**.

[Kim et al., 2016]Kim H.-H., Kim H.-J., Song S.-J., Kim K.-C. , Kim Y.-B. (2016). "Simulation Based Investigation of Focusing Phased Array Ultrasound in Dissimilar Metal Welds." Nuclear Engineering and Technology **48**.

[Kitahara et al., 2006]Kitahara H., Ueji R., Tsuji N., Minamino Y. (2006). "Crystallographic features of lath martensite in low-carbon steel." Acta Materialia **54**.

[Klotz et al., 2008]Klotz U. E., Solenthaler C, Uggowitzer P. J. (2008). "Martensitic–austenitic 9–12% Cr steels—Alloy design, microstructural stability and mechanical properties." Materials Science and Engineering A **476**.

[Klueh, 2005]Klueh R. L (2005). "Elevated temperature ferritic and martensitic steels and their application to the future nuclear reactors." International Materials Reviews **50**(5).

[Krakow et al., 2017]Krakow R., Bennett R. J., Johnstone D. N., Vukmanovic Z., Solano-Alvarez W., Lainé S. J., Einsle J. F., Midgley P. A., Rae C. M. F., Hielscher R. (2017). "On three-dimensional misorientation spaces." Proc. R. Soc. A **473**.

[Kral, 2012]Kral M. V. (2012). Proeutectoid ferrite and cementite transformations in steels. Phase transformations in steels, Woodhead Publishing Limited.

[Krautkramer and Krautkramer, 1990]Krautkramer J., Krautkramer H. (1990). Ultrasonic Testing of Materials 4th Fully Revised Edition Springer-Verlag Berlin Heidelberg GmbH

[Kube et al., 2017]Kube C. M., Arguelles A. P., Turner J. A. (2017). "Ultrasonic backscatter from elongated grains using line focused ultrasound." Ultrasonics.

[Kube et al., 2018]Kube C. M., Arguelles A. P., Turner J. A. (2018). "Ultrasonic backscatter from elongated grains using line focused ultrasound." Ultrasonics **82**.

[LeVeque, 2002]LeVeque R. J. (2002). Finite-volume methods for hyperbolic problems, Cambridge University Press.

[Li and Rokhlin, 2015]Li J., Rokhlin S. I. (2015). "Propagation and scattering of ultrasonic waves in polycrystals with arbitrary crystallite and macroscopic texture symmetries." WaveMotion **58**.

[Li et al., 2012a]Li J., Wua M., Hao J., Ludwig A. (2012a). "Simulation of channel segregation using a two-phase columnar solidification model – Part I: Model description and verification." Computational Materials Science **55**.

[Li et al., 2012b]Li J., Wua M., Hao J., Kharicha A., Ludwig A. (2012b). "Simulation of channel segregation using a two-phase columnar solidification model – Part II: Mechanism and parameter study." Computational Materials Science **55**.

[Li et al., 2014a]Li L, Li Y, Xie X., Li J. (2014a). "Quantitative evaluation of wetness losses in steam turbines based on three-dimensional simulations of non-equilibrium condensing flows." Proc IMechE Part A: J Power and Energy **228**(6).

[Li et al., 2014b]Li J., Yang L., Rokhlin S.I. (2014b). "Effect of texture and grain shape on ultrasonic backscattering in polycrystals." Ultrasonics **54**.

[Li et al., 2016]Li J., Rokhlin S. I. (2016). "Elastic wave scattering in random anisotropic solids." International Journal of Solids and Structures **78**.

[Lobkis and Rokhlin, 2010]Lobkis O. I., Rokhlin S. I. (2010). "Characterization of polycrystals with elongated duplex microstructure by inversion of ultrasonic backscattering data." Applied Physics Letters **96**: 3.

[Lobkis et al., 2012]Lobkis O.I., Yang L., Li J., Rokhlin S. I. (2012). "Ultrasonic backscattering in polycrystals with elongated single phase and duplex microstructures." Ultrasonics **52**.

[Louhenkilpi, 2014]Louhenkilpi S. (2014). "Continuous Casting of Steel " Treatise on Process Metallurgy **3**.

[Lun Wang, 2010]Lun Wang B. S (2010). Development of Predictive Formulae for the A1 Temperature in Creep Strength Enhanced Ferritic Steels. Master of Science Thesis, The Ohio State University.

[Lyons and Prettyman, 1948]LYONS W. J., PRETTYMAN I. B. (1948). "Method for the Absolute Measurement of Dynamic Properties of Linear Structures at Sonic Frequencies." Journal of Applied Physics **19**.

[Ma et al., 2019]Ma Y., Liu Y, Zhang J., Jiang Xu, Liu C. (2019). "Effect of Tempering Temperature on the Precipitation Behavior and Mechanical Properties of a Martensite Ferritic Steel." Journal of Materials Engineering and Performance **28**.

[Maduriya and Yadav, 2018]Maduriya B., Yadav N. P. (2018). "Prediction Of Solidification Behaviour Of Alloy Steel Ingot Casting." Materials Today: Proceedings **5**.

[Maki et al., 1980]Maki T., Tsuzaki T., Tamura I. (1980). "The morphology of microstructure composed of lath martensite in steels." Transactions of the Iron and Steel Institute of Japan **20**.

[Maki, 2012]Maki T. (2012). Morphology and substructure of martensite in steels. Phase Transformations in Steels Diffusionless Transformations, High Strength Steels, Modelling and Advanced Analytical Techniques. https://doi.org/10.1533/9780857096111.1.34, Woodhead Publishing Limited. **Volume 2 in Woodhead Publishing Series in Metals and Surface Engineering**.

[Marder and Marder, 1969]Marder J.M., Marder A.R. (1969). "The morphology of iron-nickel massive martensite." Trans. ASM **62**.

[Mason and McSkimin, 1947]MASON W. P., MCSKIMIN H. J. (1947). "Attenuation and Scattering of High Frequency Sound Waves in Metals and Glasses." The Journal of the Acoustical Society of America **19**.

[Masuyama, 2001]Masuyama F, (2001). "History of Power Plants and Progress in Heat Resistant Steels." ISIJ (The Iron and Steel Institute of Japan) International **41**(6).

[Matsuda et al., 1972]Matsuda S., Inoue T., Mimura H., Okamura Y. (1972). "Toughness and effective grain size in heat-treated low-alloy high strength steels." Trans. ISIJ **12**.

[Mayer and Masuyama, 2008]Mayer K. H., Masuyama F. (2008). The development of creep resistance in creep resistant steels, Abington Publishing**:** 15-77.

[Mayer et al., 1993]Mayer K. H. , Berger C. , Gnirss G., Heinrich D., Prestel W. (1993). "Investigations by non-destructive inspection to determine the size of natural defects in large forgings of turbogenerators." Nuclear Engineering and Design **144**.

[Mayer et al., 1996]Mayer K. H., Prestel W., Weber D., Weiss M. (1996). "IN-SERVICE INSPECTION AND DEFECT ASSESSMENT OF STEAM TURBINE ROTORS." Int. J. Pres. Ves. & Piping **66**.

[Mcdonald and Hunt, 1970]McDonald R.J., Hunt J.D. (1970). "Convective fluid motion within the interdendritic liquid of a casting." Metallurgical and Materials Transactions B **1**(6).

[McNab and Campbell, 1987]McNab A., Campbell M.J. (1987). "Ultrasonic phased arrays for nondestructive testing." NDT International **20**(6).

[Medina et al., 2004]MEDINA M., DU TERRAIL Y., DURAND F. , FAUTRELLE Y. (2004). "Channel Segregation during Solidification and the Effects of an Alternating Traveling Magnetic Field." METALLURGICAL AND MATERIALS TRANSACTIONS B **35B**.

[Mikami et al., 2000]Mikami M., Morinaka K., Okamura Y., Tanimoto S., Wakeshima Y., Magoshi R., et al. (2000). Manufacturing of 12%Cr rotor forgings for high temperature steam turbines from electro slag hot topped ingot. 14th International Forgemasters Meeting

Conference Proceedings. Wiesbaden, Germany**:** 295-300.

[Morton and Mayers, 2005]Morton K. W., Mayers D. F. (2005). Numerical solution of partial differential equations : an introduction, Cambridge University Press.

[MTEX website]. "MTEX publications." 2019, from https://mtex-toolbox.github.io/publications.

[Nde-ed]. "Introduction to ultrasonic testing." Ultrasound Retrieved June, 2017, from https://www.nde-ed.org/EducationResources/CommunityCollege/Ultrasonics/cc_ut_index.htm.

[Nolze and Hielscher, 2016]Nolze G., Hielscher R. (2016). "Orientations – perfectly colored." J. Appl. Cryst. **49**.

[Nomoto, 2017]Nomoto H. (2017). Solid particle erosion analysis and protection design for steam turbines. Advances in Steam Turbines for Modern Power Plants. http://dx.doi.org/10.1016/B978-0-08-100314-5.00010-5, Elsevier Ltd.

[Nowers et al., 2016]Nowers O., Duxbury D. J., Drinkwater B. W. (2016). "Ultrasonic array imaging through an anisotropic austenitic steel weld using anefficient ray-tracingalgorithm." NDT&E International **79**.

[Nowotnik et al., 2014]NOWOTNIK A., KUBIAK K., SIENIAWSKI J., ROKICKI P., PĘDRAK P., MRÓWKA-NOWOTNIK G. (2014). "Development of Nickel Based Superalloys for Advanced Turbine Engines." Materials Science Forum **783**.

[Nozu et al., 2003]Nozu S., Morinaka K., Naruse H., Muraoka T. (2003). Manufacturing technology of 12%Cr steel alloyed with boron large ingot for power generator. 15th International Forgemasters Meeting. Kobe, Japan 276-281.

[Ohji and Haraguchi, 2017]Ohji A., Haraguchi M. (2017). Steam turbine cycles and cycle design optimization: the Rankine cycle, thermal power cycles, and IGCC power plants. Advances in Steam Turbines for Modern Power Plants. http://dx.doi.org/10.1016/B978-0-08-100314-5.00002-6, Elsevier Ltd.

[Osgerby, 2014]Osgerby S. (2014). Steam turbines: operating conditions, components and material requirements. Structural Alloys for Power Plants.

[Packo, 2013]Paćko P. (2013). Numerical Simulation of Elastic Wave Propagation. Advanced Structural Damage Detection: From Theory to Engineering Applications. https://doi.org/10.1002/9781118536148.ch2, John Wiley & Sons, Ltd.

[Papadakis and Reed, 1961]PAPADAKIS E. P. , REED E. L. (1961). "Ultrasonic Detection of Changes in the Elastic Properties of a 70-30 Iron-Nickel Alloy upon Heat Treatment " Journal of Applied Physics **32**.

[Papadakis, 1961]Papadakis E. P. (1961). J. Acoust. Soc. Am **33**.

[Papadakis, 1964a]Papadakis E. P. (1964a). J. Appl. Phys. **35**.

[Papadakis, 1964b]Papadakis E. P. (1964b). "Ultrasonic Attenuation and Velocity in Three Transformation Products in Steel " Journal of Applied Physics **35**.

[Papadakis, 1981]Papadakis E. P. (1981). Scattering in polycrystalline media. Methods of experimental physics, Academic press, inc. **19**.

[Pesicka et al., 2003]Pesicka J., Kuzel R., Dronhofer A., Eggeler G. (2003). "The evolution of dislocation density during heat treatmentand creep of tempered martensite ferritic steels." Acta Materialia **51**.

[Pickering and Bhadeshia, 2014]Pickering E. J., Bhadeshia H. K. D. H. (2014). "Macrosegregation and Microstructural Evolution in a Pressure-Vessel Steel." Metallurgical and Materials Transactions A **45**(7).

[Pickering, 2014]Pickering E. J. (2014). Macrosegregation in Steel Ingots. Doctor of Philosophy, University of Cambridge.

[Povey, 1997]Povey M. J. W. (1997). "Ultrasonic Techniques for Fluids Characterization." Academic Press, San Diego, CA: 24.

[Raju et al., 2010]Raju S., Jeya Ganesh B., Kumar Rai A., Mythili R., Saroja S., Raj B. (2010). "A study on martensitic phase transformation in 9Cr–1W–0.23V–0.063Ta–0.56Mn–0.09C–0.02N (wt.%) reduced activation steel using differential scanning calorimetry." Journal of Nuclear Materials **405**.

[Rayleigh, 1877]Strutt J. W., Baron Rayleigh (1877). "The theory of sound." London, Macmillan and co. **Volume 1**.

[Rayleigh, 1878]Strutt J. W., Baron Rayleigh (1878). "The theory of sound " London, Macmillan and co. **Volume 2**.

[Reed, 2006]Reed R. C. (2006). The Superalloys Fundamentals and Applications. https://doi.org/10.1017/CBO9780511541285, Cambridge University Press

[Roderick and Truell, 1952]RODERICK R. L., TRUELL R. (1952). "The Measurement of Ultrasonic Attenuation in Solids by the Pulse Technique and Some Results in Steel." Journal of Applied Physics **23**.

[Rogers and Van Buren, 1974] Rogers P. H., Van Buren A. L. (1974). "An exact expression for the Lommel diffraction correction integral." J. Acoust. Soc. Am **55**.

[Rübenkönig, 2006]Rübenkönig O. (2006). "The finite difference method: an introduction." Albert-Ludwigs University of Freiburg.

[Saad et al., 2013]Saad A. A., Hyde T. H., Sun W., Hyde C. J., Tanner D. W. J. (2013). "Characterization of viscoplasticity behaviour of P91 and P92 power plant steels." International Journal of Pressure Vessels and Piping **111-112**.

[Sang et al., 2010]Sang B., Kang X., Li D. (2010). "A novel technique for reducing macrosegregation in heavy steel ingots." J. Mater. Process. Technol. **210**.

[Sarazin and Hellawell, 1988]SARAZIN J.R., HELLAWELL A. (1988). "Channel Formation in Pb-Sn, Pb-Sb, and Pb-Sn-Sb Alloy Ingots and Comparison with the System NH4CI-H20." METALLURGICAL TRANSACTIONS A **19A**.

[Sarnet, 2009]Sarnet J. (2009). On the analysis of cast structure and its changes during hot working of forging ingots. Doctor Thesis, Royal Institute of Technology (KTH).

[Sawada et al., 2008]Sawada K., Suzuki K., Kushima H., Tabuchi M., Kimura K. (2008). "Effect of tempering temperature on Z-phase formation and creep strength in 9Cr–1Mo–V–Nb–N steel." Materials Science and Engineering A **480**: 558–563.

[Scalzo and Bannister, 1994]Scalzo, A. J., Bannister, R. L. (1994). "Evolution of heavy duty power generation and industrial combustion turbines in the United States." ASME 94-GT-488.

[Shrestha et al., 2015]Shrestha T., Alsagabi S. F., Charit I., Potirniche G. P., Glazoff M. V. (2015). "Effect of Heat Treatment on Microstructure and Hardness of Grade 91 Steel." Metals **5**.

[Silk and Lidington, 1975]Silk M. G. , Lidington B. H. (1975). "The potential of scattered or diffracted ultrasound in the determination of crack depth." NON-DESTRUCTIVE TESTING.

[Singh, 2016]Singh R. (2016). "Ultrasonic Testing." Applied Welding Engineering (Second Edition) **Chapter 6**.

[Sklenička et al. 2003]Sklenicka V., Kucharova K., Svoboda M., Kloc L., Bursık J., Kroupa A. (2003). "Long-term creep behavior of 9–12%Cr power plant steels." Materials Characterization **51**.

[Smith, 2017]Smith R. W. (2017). Steam turbine cycles and cycle design optimization: combined cycle power plants. Advances in Steam Turbines for Modern Power Plants. http://dx.doi.org/10.1016/B978-0-08-100314-5.00004-X, Elsevier Ltd.

[Sonatest 350M](June 2009). Masterscan 350 User's guide, Sonatest.

[Stanke and Kino, 1984]Stanke F. E., Kino G. S. (1984). "A unified theory for elastic wave propagation in polycrystalline materials." The Journal of the Acoustical Society of America **75**.

[Stanke, 1986]Stanke F. E. (1986). "Spatial autocorrelation functions for calculations of effective propagation constants in polycrystalline materials." Acoustical Society of America

80.

[Steven and Haynes, 1956]Steven W., Haynes A. G. (1956). "The Temperature of Formation of Martensite and Bainite in Low-Alloy Steels." Journal of the Iron and Steel Institute **183**(8).

[Strang and Fix, 1973]Strang G., Fix G. J. (1973). An analysis of the finite element method, Englewood Cliffs.

[Strangwood, 2012]Strangwood M. (2012). Fundamentals of ferrite formation in steels. Phase Transformations in Steels Fundamentals and Diffusion-Controlled Transformations, Woodhead Publishing Series in Metals and Surface Engineering. **1**.

[Struers preparation guide]. "Grinding and Polishing." Struers - Ensuring Certainty, 2018, from https://www.struers.com/en/Knowledge/Grinding-and-polishing#grinding-polishing-how-to.

[Suikkanen et al., 2011]Suikkanen P. P., Cayron C., DeArdo A. J., Karjalainen L. P. (2011). "Crystallographic Analysis of Martensite in 0.2C-2.0Mn-1.5Si-0.6Cr Steel using EBSD." J. Mater. Sci. Technol. **27**.

[Swindman and Klueh, 1977] Swindman R. W., Klueh R. L (1977). "Relaxation behaviour of 2 ¼ Cr-1 Mo Steel Under Multiple Loading." Oak Ridge National Laboratory.

[Szilard, 1963]Szilard J. (1963). Ultrasound Penetration Through Very Thin Gas Layers Embedded in Solid Bodies. 4th Int. Conf. NDT. Butterworth, London**:** 159-161.

[Tanuma, 2017]Tanuma T. (2017). Introduction to steam turbines for power plants. Advances in Steam Turbines for Modern Power Plants. http://dx.doi.org/10.1016/B978-0-08-100314-5.00001-4, Elsevier Ltd.

[Tarndczy, 1956]Tarndczy H. (1956). On the Propagation of Ultrasonic Energy Through Thin Air Layers. 2nd Conf. Ultrasonics. Warsaw, Poland**:** 91-94.

[Temple, 1993] Temple, J. A. G. (1993). "Diffraction coefficients for flat-bottomed holes from 3-D finite difference calculations." Ultrasonics **31**(1): 3-12.

[Tominaga, 2017]Tominaga J. (2017). Steam turbine cycles and cycle design optimization: advanced ultra-supercritical thermal power plants and nuclear power plants. Advances in Steam Turbines for Modern Power Plants. http://dx.doi.org/10.1016/B978-0-08-100314-5.00003-8, Elsevier Ltd.

[Totemeier et al., 2006]TOTEMEIER T.C., TIAN H., SIMPSON J.A. (2006). "Effect of Normalization Temperature on the Creep Strength of Modified 9Cr-1Mo Steel." METALLURGICAL AND MATERIALS TRANSACTIONS **37A**.

[Turner, 1999]Turner J. A. (1999). "Elastic wave propagation and scattering in heterogeneous, anisotropic media: Textured polycrystalline materials." The Journal of the Acoustical Society of America **106**.

[Underwood, 1970]Underwood E. E. (1970). Quantitative Stereology. Reading, Mass., Addison-Wesley Pub. Co.

[Van Pamel et al, 2017]Van Pamel A, Sha G, Rokhlin SI, Lowe MJS (2017). "Finite-element modelling of elastic wave propagation and scattering within heterogeneous media." Proc. R. Soc. A **473**.

[Van Pamel, 2015]Van Pamel A. (2015). ULTRASONIC INSPECTION OF HIGHLY SCATTERING MATERIALS. Doctor of Engineering, Imperial College London.

[Vander Voort, 1984]VANDER VOORT G. F. (1984). "Measurement of the Interlamellar Spacing of Pearlite." METALLOGRAPHY **17**.

[Vanstone et al., 2013]Vanstone R., Chilton I., Jaworski P. (2013). "Manufacturing Experience in an Advanced 9%CrMoCoVNbNB Alloy for Ultra-Supercritical Steam Turbine Rotor Forgings and Castings." Journal of Engineering for Gas Turbines and Power **135**.

[Voigt et al., 2004]Voigt R. C., Charles, M., Deskevich N., Varkey V., Wollenburg A. (2004). Heat Treatment Procedure Qualification for Steel Castings. doi:10.2172/836878, Pennsylvania State Univ., University Park, PA (United States).

[Vrana et al., 2016]VRANA J., ZIMMER A., LOHMANN H.-P., HEINRICH W. (2016). Evolution of the Ultrasonic Inspection over the Past Decades on the Example of Heavy Rotor Forgings. 19th World Conference on Non-Destructive Testing 2016.

[Wang et al., 2018]Wang X., Wang X., Luo B., Guo J. (2018). "Analysis of cavity evolution in 9%Cr heat-resistant steel welded joint during creep." Engineering Fracture Mechanics **202**.

[Wang et al., 2019]Wang X., Wang X., Luo B., Hu X.-L. , Yuan T.-B. (2019). "Creep degradation assessment in 9%Cr heat-resistant steel welded joints using ultrasonic methods." Results in Physics **12**.

[Watson, 2017]Watson C. (2017). Modelling high integrity steel forgings for turbine application in the power generation industry, University of Birmingham.

[Weaver, 1990]WEAVER R. L. (1990). "DIFFUSIVITY OF ULTRASOUND IN POLYCRYSTALS." J. Mrch. Phys. Solids **38**.

[Wegel and Walther, 1935]WEGEL R. L., WALTHER H. (1935). "Internal Dissipation in Solids for Small Cyclic Strains " Physics **6**.

[Wiskel et al., 2016]WISKEL J. B., KENNEDY J., VASUDEV K., IVEY D. G. , HENEIN H (2016). Measurement and Modelling of Through Thickness Ultrasonic Velocity in X70 Pipeline Steel. 19th World Conference on Non-Destructive Testing 2016. Munich, Germany.

[Yamaguchi et al., 2007]Yamaguchi M, Nishiyama Y., Kaburaki H. (2007). "Decohesion of iron

grain boundaries by sulfur or phosphorous segregation: First-principles calculations." Phys. Rev. B **78**.

[Yang and Rokhlin, 2013] Yang L., Rokhlin S. I. (2013). "Ultrasonic Backscattering in Cubic Polycrystals with Ellipsoidal Grains and Texture." Journal of Nondestructive Evaluation **32**.

[Yang et al., 2007]Yang L., Turner J. A., Li Z. (2007). "Ultrasonic characterization of microstructure evolution during processing." Acoustical Society of America **121**.

[Yang et al., 2011a]Yang L., Lobkis O.I., Rokhlin S.I. (2011a). "Explicit model for ultrasonic attenuation in equiaxial hexagonal polycrystalline materials." Ultrasonics **51**.

[Yang et al., 2011b]Yang L., Lobkis O.I., Rokhlin S.I. (2011b). "Shape effect of elongated grains on ultrasonic attenuation in polycrystalline materials." Ultrasonics **51**.

[Yang et al., 2012]Yang L., Lobkis O.I., Rokhlin S.I. (2012). "An integrated model for ultrasonic wave propagation and scattering in a polycrystalline medium with elongated hexagonal grains." Wave Motion **49**.

[Yang et al., 2013]Yang L., Li J., Rokhlin S. I. (2013). "Ultrasonic scattering in polycrystals with orientation clusters of orthorhombic crystallites." Wave Motion **50**.

[Yoshino et al., 2008]Yoshino M., Mishima Y., Toda Y., Kushima H., Sawada K., Kimura K. (2008). "Influence of normalizing heat treatment on precipitation behaviour in modified 9Cr–1Mo steel." Materials at High Temperatures **25**(3).

[Zaloznik and Combeau, 2010]Zaloznik M, Combeau H. (2010). "Thermosolutal flow in steel ingots and the formation of mesosegregates." International Journal of Thermal Sciences **49**.

[Zeiler, 2017]Zeiler G. (2017). Martensitic steels for rotors in ultra-supercritical power plants. Materials for Ultra-Supercritical and Advanced Ultra-Supercritical Power Plants. http://dx.doi.org/10.1016/B978-0-08-100552-1.00006-3, Elsevier Ltd.

[Zhang et al., 2019]Zhang Y., Lai P., Jia H., Ju X., Cui G. (2019). "Investigation of Test Parameters on EBSD Analysis of Retained Austenite in TRIP and Pipeline Steels." Metals **9**(94).

[Zhao et al., 2005]Zhao B., Basir O.A., Mittal G.S. (2005). "Estimation of ultrasound attenuation and dispersion using short time Fourier transform." Ultrasonics **43**.

[Zienkiewicz, 1973]Zienkiewicz O. C. (1973). Introductory lectures on the finite element method, Springer-Verlag.

[Zimmer et al., 2010]Zimmer A., Vrana J., Meiser J., Maximini W., Blaes N. (2010). "Evolution of the Ultrasonic Inspection of Heavy Rotor Forgings Over the Last Decades." Review of quantitative nondestructive evaluation **29**.